ABSTRACT

Title of Dissertation: EXCITED STATES IN MONOLAYER TRANSITION METAL DICHALCOGENIDES

Julia C. Sell
Doctor of Philosophy, 2022

Dissertation Directed by: Professor Mohammad Hafezi
Department of Physics

Monolayer two-dimensional transition metal dichalcogenides (2D TMDs) represent a class of atomically thin semiconductors with unique optical properties. Similar to graphene, but with a three-layer (staggered) honeycomb lattice, TMDs host direct-gap transitions at their ±K valleys that exhibit circular-dichroism due to their finite Berry curvature. The reduced dimensionality of materials in this system, combined with large effective carrier masses, leads to enhanced Coulomb interaction and extremely tightly bound excitons ($E_\mathrm{B} \approx 150 - 300\,\mathrm{meV}$). Here, we seek to exploit the unusually tight binding of the excitons to probe two different types of higher energy exciton species in TMDs.

First, we experimentally probe the magneto-optical properties of $2s$ Rydberg exciton species in WSe_2. The magnetic response of excitons gives information on their spin and valley configurations, nuanced carrier interactions, and insight into the underlying band structure. Recently, there have been several reports of $2s$/$3s$ charged excitons in TMDs, but very little is still known about their response to external magnetic fields.

Using photoluminescence excitation spectroscopy, we verify the $2s$ charged exciton and report for the first time its response to an applied magnetic field. We benchmark this response against the neutral exciton and find that both the $2s$ neutral and charged excitons exhibit similar behavior with g-factors of $\mathrm{g}_{\mathrm{X}_0^{2s}}$=-5.20$\pm 0.11$ μ_B and $\mathrm{g}_{\mathrm{X}_-^{2s}}$=-4.98$\pm 0.11$ μ_B, respectively.

Second, via theoretical calculations, we investigate the exciton spectrum generated in 2D semiconductors under illumination by twisted light. Twisted light carries orbital angular momentum (OAM) which can act as an additional tunable degree of freedom in the system. We demonstrate that twisted light does not have the ability to modify the exciton spectrum and induce dipole-forbidden excitons, in contrast to atoms. This result stems from the fact that the additional OAM is transferred preferentially to the center-of-mass (COM) of the exciton, without modifying the relative coordinate which would allow dipole-forbidden, higher energy excitons to form.

EXCITED STATES IN MONOLAYER TRANSITION METAL DICHALCOGENIDES

by

Julia C. Sell

Dissertation submitted to the Faculty of the Graduate School of the
University of Maryland, College Park in partial fulfillment
of the requirements for the degree of
Doctor of Philosophy
2022

Advisory Committee:
Professor Mohammad Hafezi, Chair/Advisor
Professor Sunil Mittal
Professor Glenn Solomon
Professor Ichiro Takeuchi
Professor You Zhou

Dedication

To my grandfather, who inspired me to pursue my Ph.D. from the time I was a little girl. To my parents, for their unwavering support through all of my years of school. To Garrett and Layla for all of the love, encouragement, and tail-wags that fueled me through the finish line.

Acknowledgments

I would like to thank my advisor, Dr. Mohammad Hafezi, for his kind support throughout graduate school. He has built a group unlike any other, where experimentalists and theorists coexist and collaborate within the group; it fosters a wonderful sense of scientific community and curiosity. This model allowed to step out of my comfort zone and try new projects, like some theoretical modeling. I found this work to be extremely rewarding and believe it helped me grow as a scientist in the later years of my doctorate. Mohammad also "talks physics" better than just about anyone I have met, with an uncanny ability to break down extremely difficult problems into simple terms. I strive to one day be able to communicate my thoughts so succinctly; I'm extremely grateful that he took a chance on me at the end of my second year and let me join such a wonderful group.

I was lucky enough to have quite a few mentors in graduate school who were not my advisor. My first was Rodney Snyder, who was the senior graduate student who helped me through my first semester. He turned out to be one my best friends in graduate school as well and made the journey much more enjoyable. I also received wonderful council on both science and the business of being a scientist from Dr. Utso Bhattarcharya, Dr. Tobias Graß, Dr. Sunil Mittal, Dr. Daniel Suárez-Forero, and Dr. Glenn Solomon. They taught me so much, and I'm a better scientist for having known them; thank you all. I would also like to thank Dr. Ichiro Takeuchi and Dr. You Zhou for taking the time to serve as

committee members, I greatly appreciate it!

I would also like to thank the other group members: Jon Vannucci (who also put a huge amount of work in to making the contents of this thesis a reality), Deric Session, and Bin Cao. In no particular order: Sandy, Zach, Natalia, Christie, Liz, Phil, Harry, Kristi, and Brittany - I'm lucky to have met all of you through graduate school. Outside of the university, I also received wonderful support over the years from Irene, Caroline, Aurora, Jackie, and all my NOVA friends. Shelby, who was my roommate for three years of graduate school, is the best Ph.D. soul-sister I could've ever asked for and I'm so grateful to have her in my life.

I would like to thank Berry Jonker's group at the Naval Research Laboratory who we collaborated with for samples and sample material. On campus, I would like to sincerely thank the clean room staff - Tom, Mark, and John - who taught me so much about fabrication and working in a clean room environment. Additionally, I would like to thank Dr. Karen Gaskell, who is the caretaker of the AFM on campus and was always game to try whatever crazy AFM technique I read about but wasn't quite sure how to actually execute.

I would like to thank Dr. Tom O'Haver for his assistance in understanding and implementing signal processing techniques. His book was extremely helpful, and he was kind enough to correspond with me and provide insight on some fitting issues I encountered while analyzing magnetic field data. Though the project I originally contacted him about was scrapped, his expert advice proved to be invaluable and helped me hone my processing techniques for other data that did make the cut for this thesis.

I was fortunate to be supported by the National Science Foundation Graduate Research

Fellowship Program (NSF GRFP) from 2015-2020 and the ARCS MWC Scholar program from 2020-2022, for which I am eternally grateful.

Last, but not least I would like to thank my parents, my wonderful partner, and our dog. My parents have provided so much unwavering support to me since I announced that I wanted a Ph.D. when I was 6. Though the field has changed (paleobotany turned out to not be my thing), their support never has and I'm so grateful to have a family that understands this journey that I have been on. As for Garrett, I strongly feel that it takes a special person to be willing to walk the path of a Ph.D. with someone in their relationship. It was a commitment that I made before we met, but he has really taken it on as his burden to share. Garrett has been such a wonderful partner while I work towards accomplishing my goals, doing everything from taking on extra household chores when I'm busy to answering random programming syntax questions. He has been my emotional rock when research has been hard, and I appreciate everything he has done so much. Our dog, Layla, was my pandemic work-from-home buddy while the university was closed. I really missed her when I returned to working on campus, but she's always at the door wagging and happy to see me after a long day.

Table of Contents

List of Figures

List of Abbreviations

2D	two-dimensional
2DEG	two-dimensional electron gas
AFM	atomic force microscopy
BZ	Brillouin zone
CPL	circularly polarized light
CVD	chemical vapor deposition
DI	deionized
DOF	degree of freedom
DOS	density of states
EBL	electron beam lithography
EEA	exciton-exciton annihilation
hBN	hexagonal boron nitride
HOPG	highly oriented pyrolitic graphite
IPA	isopropanol
LCPL	left circularly polarized light
LG	Laguerre-Gauss
NA	numerical aperture
OAM	orbital angular momentum
PC	poly(Bisphenol A carbonate)
PDMS	polydimethylsiloxane
PL	photoluminescence
PLE	photoluminescence excitation
PMMA	poly(methyl methacrylate)
PPC	poly(propylene carbonate)
RCPL	right circularly polarized light
SEM	scanning electron microscopy
TMD	transition metal dichalcogenide
QE	quantum emitters
QHE	quantum Hall effect
FQHE	fractional quantum Hall effect
vdW	van der Waals

Chapter 1: Introduction

1.1 Motivation

Traditional electronics are at a crossroads; while our thirst for increased computational power to tackle larger problems is ever growing, the semiconductor industry is struggling to keep pace. In recent years, the rate of computational power increases has diverged from the expectations of Moore's Law as development of new chips is hindered by minimum component (transistor) size constraints and electronic Joule heating arising from the increasing density of transistors on functional computer chips. Photonics – which relies on photons to transmit information instead of electrons – can circumvent these issues and has the potential to bridge the gap between conventional electronics and our computational needs.

Currently, most commercially available optoelectronic components are constructed from Si or GaAs because there is well established large-scale manufacturing for both materials. However, both materials have their drawbacks. Si is inefficient at emitting light due to its indirect band gap, while GaAs is toxic to manufacture and confined to the infrared regime. There exists a need for other materials that circumvent these issues, especially ones that emit in the visible spectrum. Within this thesis, we discuss a family of two-dimensional (2D) semiconductors that have the potential to fill this hole: the transition metal dichalcogenides (TMDs).

1.2 The Rise of Two-Dimensional Materials

The study of 2D materials dates back nearly 100 years. Many experimentalists tried to synthesize these materials to no avail. Theory backed up their lack of success; both Landau and Peierls published work arguing that the thermal fluctuations in the lattice of a 2D crystal would be so large that atomic displacement could take place on the scale of the lattice rendering the whole system unstable [157, 158, 228]. Over the years, clever scientists managed to grow monolayers of material on top of lattice-matched, single-crystal bulk materials. No one thought that it would be experimentally feasible for 2D materials to exist in a free-standing form until Geim and Novosolev surprised the world with their isolation of graphene in 2004 from larger highly oriented pyrolytic graphite (HOPG) crystals [217]. This discovery earned them the Nobel prize in 2010.

The isolation of graphene sparked a revolution in science, where more than 15 years later the number of papers per year on graphene is still on the rise and new, ground-breaking discoveries come nearly yearly. In the early days of graphene research, the physics accessible was hampered by the quality of the material available and the size of the sheets that researchers were able to extract. However, improvements in bulk crystal synthesis, exfoliation, and fabrication techniques have opened up a huge range of possible physics to study. Due to the special Dirac nature of graphene, the presence of massless Dirac fermions in the system allows for carriers densities researchers previously couldn't even dream of (200,000 cm^2/Vs), and with it astonishing discoveries [27, 41, 219]. Not only could researchers see the quantum Hall effect (QHE), they could see it at room temperature [220, 351]. Along with this came the measurement of the more exotic fractional quantum Hall effect (FQHE) [28], and the chance to probe Hofstadter's butterfly in a condensed matter system [60, 116, 234]. The measurement of Hofstadter's butterfly sparked further interest in moiré lattices formed with graphene, which led to the discovery of unconventional superconductivity in twisted bilayer graphene [34].

However, for all of its many interesting properties, one of graphene's strengths is also one of its weaknesses: graphene doesn't have a band gap. Practically speaking, our understanding of how to make electronics hinges upon using the band gap present in semiconductors (currently predominantly Si) to act as a switch. Researchers have successfully been able to produce semimetallic graphene, through artificially inducing very small band gaps. However, as the name suggests, these materials are still more similar in their electronic properties to a metal than a semiconductor, which makes control in both the electronic and optoelectronic regimes difficult [4, 258, 328, 336].

In the mid-2000s, as researchers were trying to make semimetallic graphene, interest arose in another group of 2D materials: the TMDs. Similar in structure to graphene – both in terms of the (staggered) honeycomb lattice and the fact that the layers are held together by weak van der Waals attraction – it offered a simple way to extend the 2D materials family. Like HOPG, studies of these materials in bulk had existed for many years [322]. Interestingly, the first report of monolayer TMDs is actually from the 1980s, with few layer thick studies dating even earlier, but these works were lost to time until the renewed interest in the 2000s [83, 124]. Materials in this family are of the chemical form MX_2, where M is the transition metal atom and X is the chalcogen atom. Despite having this similar chemical structure, different degrees of filling in the non-bonding d bands of the transition metal result in a family of ~ 60 different materials that range from

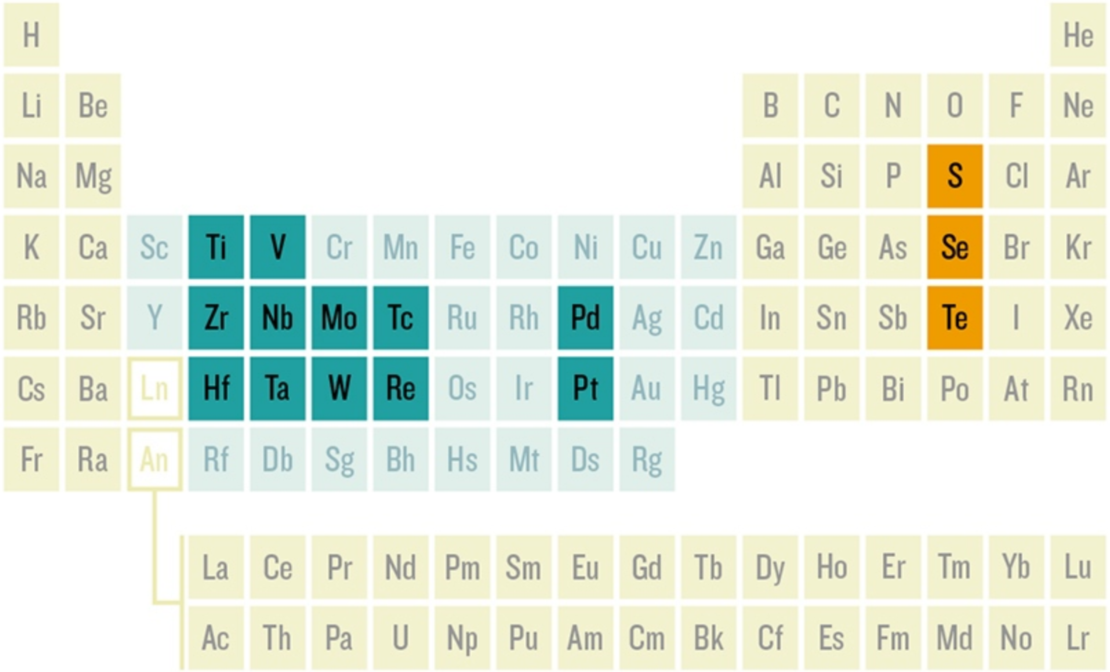

Figure 1.1: Table of elements capable of forming TMDs. TMDs are of the chemical form MX_2, where M is the transition metal atom and X is the chalcogen atom. The chalcogen atoms are highlighted in orange and the transition metals are highlighted in teal. Figure from Ref. [90].

insulators and semiconductors to superconductors with competing charge density waves. This variety has opened a new field that allows researchers to study nearly every electronic system in the extreme quantum limit of 2D. Figure 1.1 shows all of the transition metals and chalcogens that can form TMDs.

Over the last decade, the semiconducting TMDs have become an extremely promising platform for photonics research as it allows us to study light-matter interaction in truly the quantum limit. In bulk, these materials possess indirect band gaps, but in the monolayer limit they undergo an electronic band structure transition that leads to the formation of a direct band gap [197, 287]. Applying strain allows researchers to tune this gap deterministically, introducing a simple means for band gap engineering to suit different

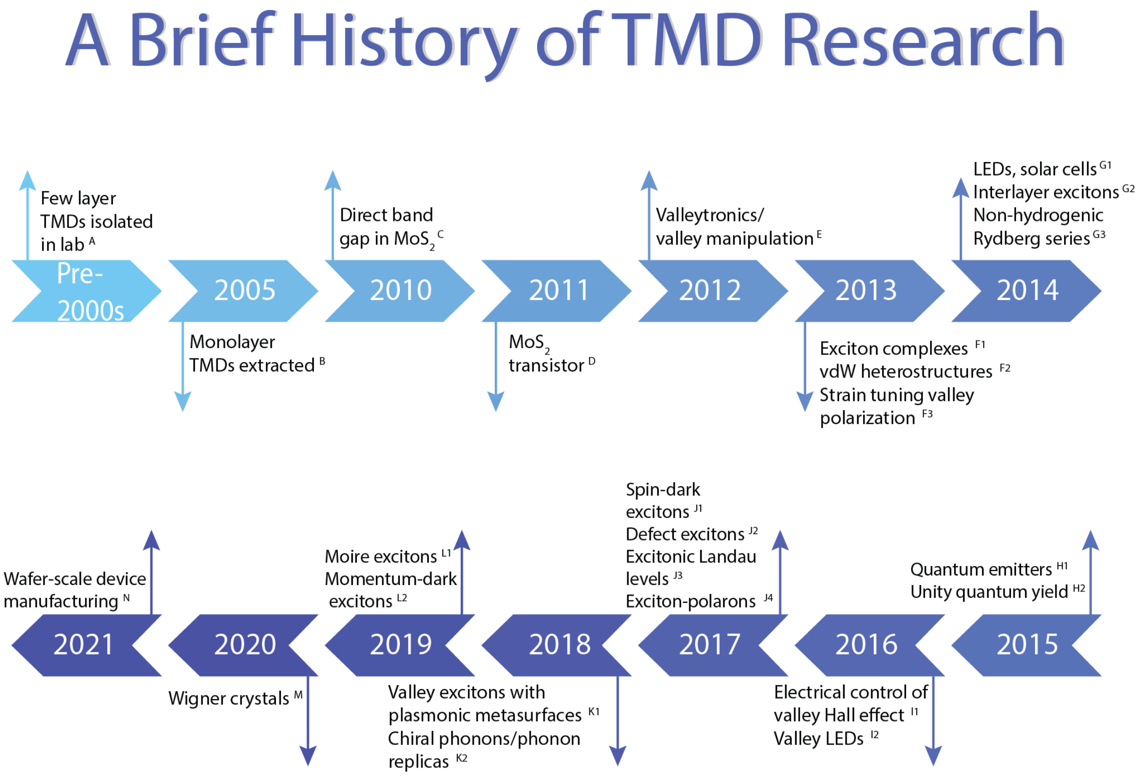

Figure 1.2: A brief, and ever-evolving history of a discoveries in semiconducting TMDs. The references included: A: [83, 124], B: [218], C: [197], D: [241], E: [195, 344], F1: [257], F2: [89], F3: [357], G1: [188, 235, 256], G2: [246], G3: [46], H1: [109, 288, 300], H2: [8], I1: [163], I2: [334], J1: [208, 350], J2: [42], J3: [319], J4: [15], K1: [48], K3: [358], L1: [303], L2: [304], M: [243, 283, 356], N: [45, 265].

device needs [14, 252, 357].

Along with the direct band gap, the broken inversion symmetry and strong spin-orbit interaction gives rise to spin-valley polarized excitons in the system that are selectively addressable with circularly polarized light. This is effectively a naturally occurring on-off switch and makes these materials of great interest for both optoelectronics [199, 315] and valleytronics. The strong 2D confinement in the monolayer sheets and large carrier mass leads to exceptionally tightly bound excitons (bound electron-hole pairs with $E_B \approx 100 - 300$meV) which makes it possible to observe them even at room temperature [19, 190, 196, 257]. This alluring combination means that many desirable and interesting quantum effects can be observed without expensive and cumbersome cryogenic equipment, which is a boon for industrial scaling of cutting edge technology. It also results in a semiconductor platform where many exciton species, including multi-particle states like trions [191, 289], biexcitons (both neutral and charged) [44, 172, 181, 290], and most recently exciton-polarons [15, 69, 91, 275] can all coexist with distinct energetic signatures. Further state tuning has recently become experimentally accessible with the advent of moiré lattices [303], leaving us with seemingly endless possibilities to tune these systems to fit many needs.

TMDs have also attracted interest in the field of quantum computation. The valleys in the material have the capacity to form a qubit and the planar nature of the materials has the potential to lend itself to large-scale integration of qubits in a way that trapped ions currently do not [307]. Beyond that, dark exciton states have been found to exist in TMDs [19]. Due to the fact that these states require a second-order process to recombine, and therefore have long lifetimes, they are a promising candidate in the field quantum photonic memory research [110, 120, 262]. A brief, and ever-evolving timeline of discoveries in TMDs is shown in Fig. 1.2. This figure highlights breakthroughs most relevant to the semiconducting TMDs and this work.

1.3 Goals of this Work

The focus of this thesis is on higher energy exciton species in TMDs, which we define here as those with principle quantum number $n > 1$. As n increases, the binding energy of the exciton species decreases. This makes observing higher n exciton species difficult in most traditional semiconductor systems, since the binding energy of the $n = 1$ exciton is small to start with *e.g.* $E_\mathrm{B} \approx 10$ meV in GaAs. However, the large binding energy in TMDs gives us a unique opportunity to probe higher energy exciton dynamics. In this work, we study two types of higher energy species:

(EI) In analogy to the hydrogen atom, excitons are also known to form higher energy Rydberg series [128]. However, until its recent discovery in TMDs, a similar series for trion-like particles was thought to be energetically impossible. We, for the first time, explore the magneto-optical properties of the $2s$ charged state in WSe_2 via observation of the valley Zeeman effect and extract a g-factor for this $2s$ charged exciton. Origins of the observed g-factor are discussed.

(EII) The excitons in (EI) are all s exciton species with orbital quantum number $l = 0$. However, also in analogy to the hydrogen atom, it is possible for excitons to form higher energy states with non-zero orbital quantum number l. A typical example of this are $2p$ excitons, which have been observed in many different semiconductor systems including TMDs. However, because of the additional angular momentum, these states are dipole-forbidden and therefore require a nonlinear optical process – like two-photon spectroscopy – to access them. Here, we theoretically examine if light that carries additional orbital angular momentum (OAM) ℓ can modify the exciton spectrum and, for example, allow transitions beyond the dipole approximation. We explicitly determine if the OAM carried by the light is transferred to the internal degree of freedom of the exciton where is could create a p exciton or if it would instead transfer to the center-of-mass (COM) of the exciton where it could induce vortex-like motion or dispersion.

1.4 Outline of this Work

We begin this thesis in Ch. 2 with an overview of the properties of the semiconducting TMDs. Here, the physical crystal structure is discussed, as well as the various types of exciton species that can be optically generated along with their selection rules; this also includes a comparison of single-particle and many-body interaction. Next, in Ch. 3 we explore different experimental methods for TMD sample fabrication. Following sample preparation techniques, in Ch. 4, we discuss measuring light-matter interaction and the experimental "knobs" that are at our disposal. As a primer for understanding our experimental findings regarding (EI), in Ch. 5 we examine the different effects that a magnetic field can have on excitons with a specific emphasis on the Zeeman effect. Based on this context, we then discuss our work on magneto-optical characterization of the $2s$ charged exciton in WSe_2 (EI) in Ch. 6. Following this, we review the fundamentals of OAM in Ch. 7 as a primer for our theoretical findings regarding (EII); those findings are highlighted in Ch. 8. Finally, a summary of this work and prospective direction of future study is presented in Ch. 9.

Chapter 2: Review of Transition Metal Dichalcogenide Fundamental Properties and Exciton Species

This section is meant to discuss the physical and electronic properties of TMDs. In bulk form, TMDs have been studied extensively. However, in monolayer form they are truly in the atomic limit and their properties are distinctly different than their bulk counterparts. Their reduced dimensionality, paired with strong Coulomb interaction, supports a wide variety of stable, optically accessible exciton species that remain difficult to traditional semiconductors systems like Si and GaAs [15,191,198,290,293].

Before we dive into the formalism, it is instructive to look at the crystal structure of TMDs. TMD monolayers, unlike their graphene counterparts, are actually three atomic layers thick and comprised of a plane of transition metal atoms between two sheets of chalcogen atoms. These monolayer sheets come in two phases: trigonal prismatic and octahedral. In both cases, the transition metal atom is six-fold coordinated, but the positions of the chalcogen atoms are different: in trigonal prismatic monolayers the chalcogens are directly over one another, while in octahredal monolayers they are staggered. Which structure a given TMD monolayer takes depends mostly on the d orbital filling, with the naturally occurring Mo- and W- based (semiconducting) TMDs falling into trigonal prismatic category [137]. Modification of the structure is possible,

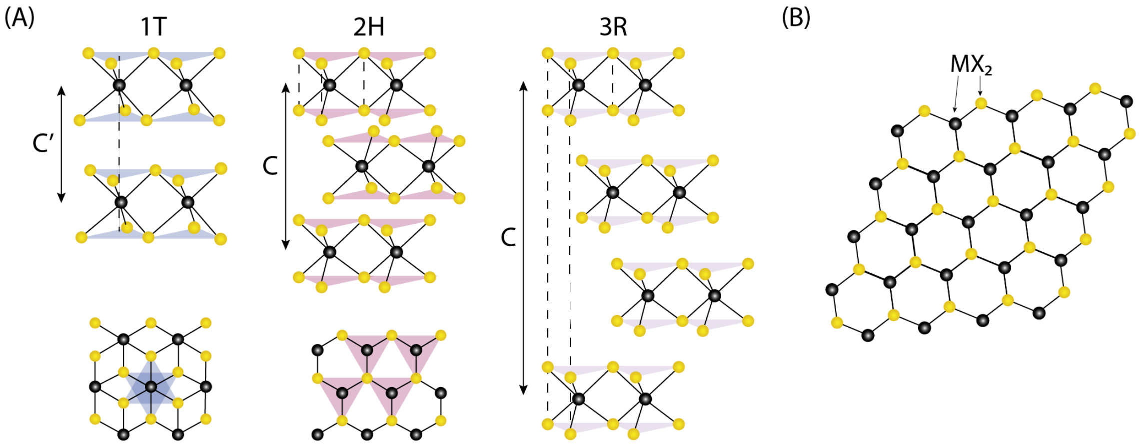

Figure 2.1: (A) An illustration of stacking periodicity and coordination of the different TMD polytypes. C is the unit repeat in the $\hat{z}$ direction. In this labeling scheme, the number denotes the monolayers in the unit cell and T, H, and R correspond to trigonal, hexagonal, and rhombohedral respectively [145]. (B) An illustration of a monolayer TMD lattice extracted from a 2H crystal from a top-down view. In both panels, the black atoms correspond to the transition metal atoms and the yellow atoms correspond to the chalcogen atoms. This figure is adapted with some modification from Ref. [137]

but usually require significant engineering to do so, and usually results in some lattice distortion [284, 340].

Fig. 2.1(A) shows the three common polytypes – referred to as 1T, 2H and 3R based on their respective unit cell geometries. 1T crystals are comprised of octahedral monolayers with the top-down view showing effect of the staggered chalcogens. Both 2H and 3R crystals are comprised of trigonal prismatic monolayers, and are the type used within our work that result in the honeycomb-like lattice. Though beyond the scope of this thesis, it is worth noting that though the underlying monolayers are the same, the difference in stacking between 2H and 3R can lead to different electronic and optical properties of homobilayer systems [169, 206]. This highlights the important role that the underlying structure plays in the physics observed. Fig. 2.1(B) shows a larger, top-down view of a trigonal prismatic monolayer.

2.1 Band Structure

One of the very interesting properties that the semiconducting TMDs exhibit is an indirect-to-direct band gap transition as the material is thinned from bulk to monolayer form. This was originally observed in 2010 by Mak *et al.* in MoS_2 and has since been observed experimentally countless times in the the group VIB TMDs [146,197,287,315] and the origins of this phenomenon confirmed with first principle density function theory (DFT) calculations [337]. An important consequence of this property is that, compared to its bulk form, the monolayer TMDs are optically very bright since this direct transition enhances our ability to access states without having to provide additional momentum.

Referring to Fig. 2.2 for an illustration, when the TMD is in monolayer form the direct band gap is formed at the two inequivalent, high symmetry points (±K) which correspond to the corners of the BZ. Though they are inequivalent, ±K do constitute a time-reversed pair, which is important to a variety of phenomena in the system. Similar to graphene, we call these points *valleys*, and since they are inequivalent they act as another degree of freedom within the system. Manipulation of this degree of freedom forms the basis for *valleytronics* in the system and allows for manipulation of the population of each valley independently [261,307]. We will discuss this more explicitly in relation to selection rules in the next section and also look at the origin of the valley Hall effect in the system.

In 2H TMDs, the unit cell is comprised of two monolayers that are rotated in-plane by 180°with respect to the other. This means if the crystal is thinned to a monolayer unit, the resulting 2D piece lacks inversion symmetry. This leads to spin-splitting of

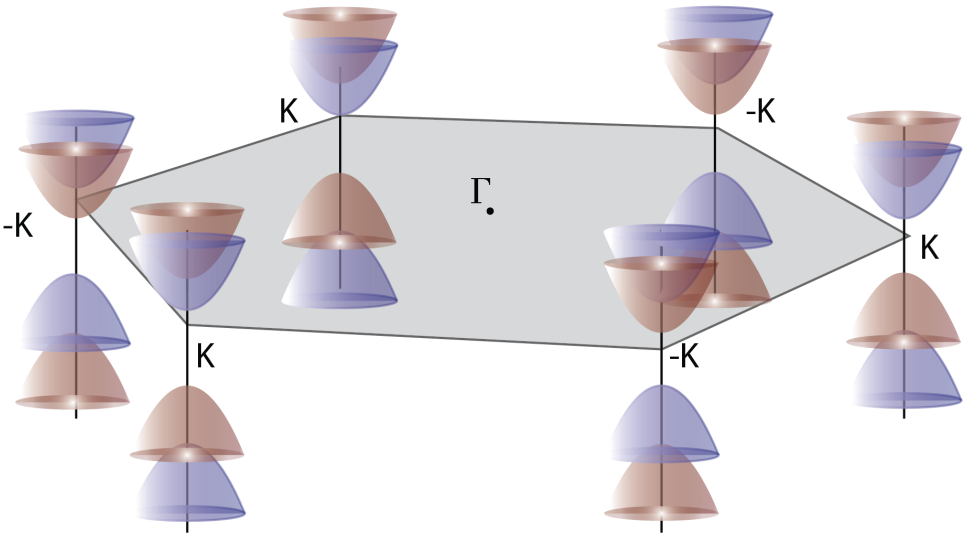

Figure 2.2: Transition metal dichalcogenide band structure schematic of the band edges showing the spin splitting of the valence band/conduction band at the ±K valleys. The schematic is not to scale. The figure is derived from Reference [327].

the bands that is a manifestation of strong spin-orbit interaction in the system; thus, it is present even with no applied magnetic field. Both the conduction band and valence band at the ±K points are spin-split, though the there is roughly an order of magnitude difference between the magnitudes with the valence band splitting in the 100s of meV and the conduction band splitting is generally 10s of the meVs [141, 142, 186]. As a general rule of thumb, the magnitude of the spin-splitting in both the valence and conduction band increases with the mass of the transition metal (*e.g.* $\Delta E_{\mathrm{Mo}} < \Delta E_{\mathrm{W}}$), and then for a given transition metal the splitting increases further with increasing mass of the chalcogen (*e.g.* $\Delta E_{\mathrm{S}} < \Delta E_{\mathrm{Se}} < \Delta E_{\mathrm{Te}}$). This can be understood in the context spin-splitting resulting from the spin-orbit coupling is a *relativistic effect*. It is therefore felt more strongly with increasing nuclear mass; as is the case with the heavy transition metals with their valence d orbitals [201].

Because ±K constitute a time-reversed pair, the spin-splitting between the two valleys is opposite, which implies that the spin and valley degrees of freedom are *coupled*, or rather the system is *spin-valley polarized* [33, 195, 198, 199, 326, 327, 339, 344]. In fact, the coupling is so robust that it has even been observed to translate to the Landau level (LL) structure in the quantum Hall regime [98, 166, 185, 231, 319]. In the next section, we will discuss the implications of the band structure on optical selection in more quantitative detail. Later in the chapter, we will explore the important role of the spin-valley polarization in the formation of different exciton species under optical excitation.

2.2 Selection Rules

To describe the 2H-TMDs we will use two terms,

$$\mathcal{H} = \mathcal{H}_{\mathrm{MD}} + \mathcal{H}_{\mathrm{SOC}}. \tag{2.1}$$

The first term, $\mathcal{H}_{\mathrm{MD}}$ is the *massive Dirac* Hamiltonian which serves as the most basic model for low-energy electronic properties and yields the well-known valley coupled selection rules. Recalling from the previous section that the *spin-orbit coupling* plays an important role in this system, the second term $\mathcal{H}_{\mathrm{SOC}}$ corrects the energies from $\mathcal{H}_{\mathrm{MD}}$ to account for spin-splitting. Additional terms that correct this Hamiltonian become relevant in specific cases – for example in the case of magnetic impurities one must add an exchange term [38] – but these two terms suffice to understand our elementary selection rules. Here, we also ignore Coulomb interaction, but we later include it when explicitly looking at exciton formation.

2.2.1 Massive Dirac Hamiltonian

Graphene, the first of the aptly named “Dirac material” is gapless (i.e. metallic) and described with well known massless Dirac equation. The TMDs, as we noted earlier, have a similar honeycomb lattice and a gapped band structure. The gap implies that the particles in the system are massive, so it is not a stretch to think that the massive Dirac equation would describe our system well [327]. The massive Dirac Hamiltonian is given as,

$$\hat{\mathcal{H}}_{\mathrm{MD}}(\mathbf{k}) = \hbar v_{\mathrm{F}}(\tau_z k_x \hat{\sigma}_x + k_y \hat{\sigma}_y) + \frac{\Delta}{2}\hat{\sigma}_z. \tag{2.2}$$

Here v_{F} is the Fermi velocity, τ_z is the valley index and can take the values ± 1, $\mathbf{k} = (k_x, k_y)$ are the electron wave-vectors, $\sigma_{x,y,z}$ are the Pauli matrix elements, and Δ is the direct band gap energy [327]. Note that the fermi velocity $v_{\mathrm{F}} = \frac{at}{\hbar}$ where a is the lattice constant and t is the hopping parameter. We can rewrite Eqn. (2.2) in matrix form using the sub-lattice sigma basis as,

$$\begin{pmatrix} \frac{\Delta}{2} & \hbar v_{\mathrm{F}}(\tau k_x - i k_y) \\ \hbar v_{\mathrm{F}}(\tau k_x + i k_y) & -\frac{\Delta}{2} \end{pmatrix} \tag{2.3a}$$

$$= \begin{pmatrix} \frac{\Delta}{2} & \hbar v_{\mathrm{F}} k e^{-i\tau\phi_{\mathbf{k}}} \\ \hbar v_{\mathrm{F}} k e^{i\tau\phi_{\mathbf{k}}} & -\frac{\Delta}{2}. \end{pmatrix} \tag{2.3b}$$

Here, tan($\phi_{\mathbf{k}}$) = k$_y$/k$_x$. Diagonalizing Eqn. (2.3b) to solve for the eigenvalues, we get

$$\pm\lambda = \pm\frac{1}{2}\sqrt{\Delta^2 + 4(\hbar v_{\mathrm{F}} k)^2} = E_{c/v}(\mathbf{k}). \tag{2.4}$$

We can solve for the corresponding eigenvectors and find that,

$$|c, \mathbf{k}\rangle_\tau = \begin{pmatrix} \cos\left(\frac{\theta_k}{2}\right) \\ \sin\left(\frac{\theta_k}{2}\right) e^{i\tau\phi_{\mathbf{k}}} \end{pmatrix} \tag{2.5a}$$

$$|v, \mathbf{k}\rangle_\tau = \begin{pmatrix} \sin\left(\frac{\theta_k}{2}\right) e^{-i\tau\phi_{\mathbf{k}}} \\ -\cos\left(\frac{\theta_k}{2}\right) \end{pmatrix}. \tag{2.5b}$$

Here, $\cos(\theta_k) \equiv \frac{\Delta}{2\lambda}$ [93, 348]. We now have the eigenvectors corresponding to the conduction and valence bands, and in the next section we will use them to find the selection rules for forming a bound pair (exciton) between the bands.

2.2.1.1 Light-Matter Interaction

Suppose now that we illuminate the TMD with circularly polarized light (CPL); applying minimal coupling ($\mathbf{p} \to \mathbf{p} + e\mathbf{A}$) and assuming that the frequency of the light $\hbar\nu \approx \Delta$ so that we can make the rotating wave approximation, the light-matter interaction Hamiltonian can be written as,

$$\hat{\mathcal{H}}_{\mathrm{LM}} = e\hbar v_{\mathrm{F}} A(\mathbf{r})[\tau\hat{\sigma}_x A_x + \hat{\sigma}_y A_y]. \tag{2.6}$$

Where in the circularly polarized basis $A_x = \frac{1}{2}\left(A^+ + A^-\right)$ and $A_y = -\frac{i}{2}\left(A^+ - A^-\right)$. We can rewrite Eqn. (2.6) as

$$\begin{aligned}\hat{\mathcal{H}} &= e\hbar v_{\mathrm{F}} A(\mathbf{r}) \begin{pmatrix} 0 & (\tau+1)A^+ + (\tau-1)A^- \\ (\tau-1)A^+ + (\tau+1)A^- & 0 \end{pmatrix} \\ &= \tau\hbar e v_{\mathrm{F}} A(\mathbf{r}) \begin{pmatrix} 0 & A^\tau \\ A^{-\tau} & 0 \end{pmatrix}.\end{aligned} \tag{2.7}$$

With this, we can write the amplitude $\mathcal{P}(\mathbf{k}_{\mathrm{e}}, \mathbf{k}_{\mathrm{h}})$ of creating an electron-hole pair – or rather an exciton, which we will discuss more extensively in the next section – in the valley with associated index τ,

$$\begin{aligned}\mathcal{P}_\tau(\mathbf{k}_{\mathrm{e}}, \mathbf{k}_{\mathrm{h}}) &=_\tau \langle c, \mathbf{k}_{\mathrm{e}} | \, \mathbf{r}\rangle \langle \mathbf{r} | \, \mathcal{H}_{\mathrm{LM}} \, | \mathbf{r}\rangle \langle \mathbf{r} | \, v, \mathbf{k}_{\mathrm{h}}\rangle_\tau \\ &= \tau\hbar(e v_{\mathrm{F}}) \left[-\cos^2\left(\frac{\theta_k}{2}\right) A^\tau + e^{-2\mathrm{i}\tau\phi_{\mathrm{k}}} \sin^2\left(\frac{\theta_k}{2}\right) A^{-\tau} \right] \frac{1}{S} \underbrace{\int d^2 r A(\mathbf{r}) e^{i\mathbf{r}\cdot(\mathbf{k}_{\mathrm{e}} - \mathbf{k}_{\mathrm{h}})}}_{=constant}.\end{aligned} \tag{2.8}$$

We note that the portion of Eqn. (2.8) with the underbrace is equal to a constant because CPL has no spatial profile. Here S is the area of the system. From this we can find our selection rules: s excitons couple to A^τ light and d excitons couple to $A^{-\tau}$ light. However, the coupling strength is vastly different. Recall that $\cos(\theta_k) \equiv \frac{\Delta}{2\lambda}$. Near the ±K points, where the band gap is direct, $2\lambda \approx \Delta$ which means that the $\cos^2\left(\frac{\theta_k}{2}\right) \gg \sin^2\left(\frac{\theta_k}{2}\right)$. This implies that the s exciton formation process with A^τ light is near 1 and the d exciton amplitude with $A^{-\tau}$ is roughly zero. In the dipole approximation, the d excitons should be completely dark – i.e. there should not be a non-zero transition amplitude associated with them. This amendment to traditionally expected results for selection rules is due to the *winding number w* of the Bloch bands, which is a topological quantity; here w =1 [348]. There are is another additional correction due to reducing the symmetry of the system from C_∞ to C_3 to reflect the true symmetry of the crystal lattice which is referred to as *trigonal warping*. Though we will not explore it here, it also brightens dipole forbidden transitions. The curious reader can find an excellent overview in the article by Gong *et al.* [93].

2.2.1.2 Polarization

The selection rules we have derived above let us finally show a property that we have already alluded to: valley polarization. We define the polarizability as

$$\begin{aligned}\eta(\mathbf{k}) &= \frac{|\mathcal{P}_\tau(\mathbf{k}_\mathrm{e},\mathbf{k}_\mathrm{h})|^2 - |\mathcal{P}_{-\tau}(\mathbf{k}_\mathrm{e},\mathbf{k}_\mathrm{h})|^2}{|\mathcal{P}_\tau(\mathbf{k}_\mathrm{e},\mathbf{k}_\mathrm{h})|^2 + |\mathcal{P}_{-\tau}(\mathbf{k}_\mathrm{e},\mathbf{k}_\mathrm{h})|^2} \\ &= \frac{|\sim 1|^2 - |\sim 0|^2}{|\sim 1|^2 + |\sim 0|^2} \\ &\approx 1.\end{aligned} \tag{2.9}$$

Thus, we see that from theory we would expect that there is near unity coupling of the +K valley to right CPL and similarly between the -K valley and left CPL. Sadly, in experimental practice, researchers do not observe near unity polarization in the TMDs without taking great pains [212]. A typical laboratory experiment see somewhere between 20-70% polarization [102,150,195,259,325,344]. According to research done by McCreary *et al.* this is largely attributable to the fact that is it desirable to have samples with strong and sharp photoluminescence (PL) response for performing experiments, but this correlates with long radiative lifetimes. The longer the radiative lifetime, the higher the chance the exciton will experience a decoherence event (i.e. intervalley phonon scattering) and lose polarization leading to an overall lower degree of polarization in the system. Conversely, systems with short non-radiative lifetimes experience fewer decoherence events and have higher overall polarization [205].

2.2.1.3 Valley Hall Effect

While we are on the topic of valley properties related to the massive Dirac Hamiltonian, it is worth taking a brief look at the Berry curvature in each valley. The Berry curvature can be generically written as,

$$\mathbf{\Omega}(\mathbf{k}) = i \sum_{j \neq n} \left[\frac{\left\langle u_{n,k} \left| \frac{\partial \mathcal{H}}{\partial k_x} \right| u_{j,k} \right\rangle \left\langle u_{j,k} \left| \frac{\partial \mathcal{H}}{\partial k_y} \right| u_{n,k} \right\rangle}{(E_j - E_n)^2} - c.c. \right]. \tag{2.10}$$

Here, E_n and u_n are the energy and wavefunction of the nth band, respectively [40, 289, 327]. In our case, we have a two-band model and can apply our massive Dirac Hamiltonian and associated energy eigenvalues/eigenvectors and find that the Berry curvature in the conduction band is,

$$\mathbf{\Omega}_{\mathrm{c}}(\mathbf{k}) = -\tau \frac{2\hbar^2 v_{\mathrm{F}}^2 \Delta}{\left(\Delta^2 + 4\hbar^2 v_{\mathrm{F}}^2 k^2 \right)^{3/2}} \hat{}. \tag{2.11}$$

Note that we can do a similar calculation for the valence band and we find that

$\mathbf{\Omega}_\mathrm{v}(\mathbf{k}) = -\mathbf{\Omega}_\mathrm{c}(\mathbf{k})$. Additionally, we see that Eqn. (2.11) has a τ dependence indicating that the magnitude of the Berry phase in each valley is the same, but the signs are different between the ±K valleys. The Berry phase is commonly described as a pseudomagnetic field occurring in k-space and, as such, can be used to drive Hall effect physics. Specifically, if there is an electronic bias in the system the difference in Berry curvature between the two valleys can drive the *valley Hall effect* (VHE). Similar to the classical Hall effect, in the VHE electrons and holes from the same valley will move in opposite directions, but it requires no applied magnetic field; the motion is instead induced by the Berry curvature. It is worth noting that because the resulting current would be equal in magnitude, but opposite in sign for the two valleys in equilibrium, in order to observe the VHE the system needs to be driven our of equilibrium. This is easy to achieve experimentally by preferentially pumping on one valley with circularly polarized light [198]. Researchers are very interested in this phenomenon for its applications in valleytronics [198, 307]

2.2.2 Spin-Orbit Coupling

As we can see in the above section, the massive Dirac Hamiltonian described there is a simple two-band model that does not take into account the spin-splitting that occurs in the conduction and valence band through spin-orbit coupling. As we discussed in the previously in Section 2.1, this interaction is far from negligible in TMDs and as such should be included in order to understand the full selection in this system. We have,

$$\hat{\mathcal{H}}_\mathrm{SOC} = \tau \frac{\lambda_c(\mathbb{1} + \hat{\sigma}_z) + \lambda_v(\mathbb{1} - \hat{\sigma}_z)}{2} s_z. \tag{2.12}$$

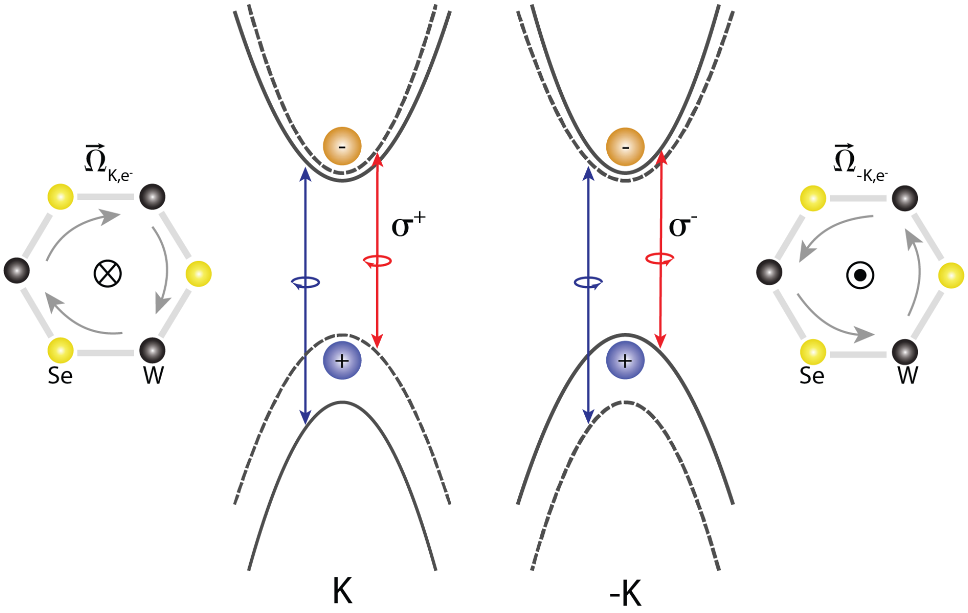

Figure 2.3: Valley- and spin-selection rules in TMDs the polarization to excite each valley is denoted ($\sigma^{\pm}$) and the dipole allowed transitions are denoted with blue (higher energy, “B” excitons) and red (lower energy,“A” excitons) transitions. Spin up is denoted with the dashed line and spin down is denoted with the solid line. On the outside the Berry curvature in each valley is depicted. This figure is derived with modification from Ref. [198]

Here, similar to the definition in the massive Dirac equation, $2\lambda_{c/v}$ are the respective conduction and valence band splittings and $s_z = \pm 1$ is the spin index labeling spin-up (+1)/spin-down (-1) [38]. Then, the whole Hamiltonian thus far is equal to,

$$\begin{aligned}\hat{\mathcal{H}}_{\mathrm{tot-MD/SOC}} &= \mathbb{I} \otimes \hat{\mathcal{H}}_{\mathrm{MD}} + \hat{\mathcal{H}}_{\mathrm{SOC}} \\ &= \begin{pmatrix} \frac{\Delta}{2} + \lambda_c \tau & \hbar v_{\mathrm{F}} k e^{-i\tau\phi_{\mathbf{k}}} & 0 & 0 \\ \hbar v_{\mathrm{F}} k e^{i\tau\phi_{\mathbf{k}}} & -\frac{\Delta}{2} + \lambda_v \tau & 0 & 0 \\ 0 & 0 & \frac{\Delta}{2} - \lambda_c \tau & \hbar v_{\mathrm{F}} k e^{-i\tau\phi_{\mathbf{k}}} \\ 0 & 0 & \hbar v_{\mathrm{F}} k e^{i\tau\phi_{\mathbf{k}}} & -\frac{\Delta}{2} - \lambda_v \tau \end{pmatrix}.\end{aligned} \tag{2.13}$$

We can see in Eqn. (2.13) that the additional of spin-orbit interaction lifts the spin-degeneracy of the valence and conduction band and transforms our two-band model into a four-band model. We are not overly concerned here with the specifics of solving this Hamiltonian, the more interesting correction here is to the energy of the system. Noting that Eqn. (2.12) bares a striking resemblance to Eqn. (2.2), we can add a correction to the band gap that with spin-orbit coupling included is

$$E_{\mathrm{gap}}^{\tau, s_z} = \Delta + \tau s_Z(\lambda_c - \lambda_v) = \Delta'. \tag{2.14}$$

Calling this new quantity Δ' we can solve but analogy the eigenvalues and we see that here,

$$\begin{aligned}\pm\lambda_{\mathrm{MD+SOC}} &= \pm\frac{1}{2}\sqrt{\Delta'^2 + 4(\hbar v_{\mathrm{F}} k)^2} \\ &= \pm\frac{1}{2}\sqrt{(\Delta + \tau s_z(\lambda_c - \lambda_v))^2 + 4(\hbar v_{\mathrm{F}} k)^2}.\end{aligned} \tag{2.15}$$

From this we can see that between the outer ± and inner τ and s_z we now have four distinct energy eigenvalues. Additionally, because we can see that the splitting depends on τ we expect that the ordering of the levels with spin will be reversed between the ±K valleys. An illustration of this, along with the Berry curvature we discussed in the previous section, is shown in Fig. 2.3. In the diagram we see that we can select the valley with the polarization and by tuning the energy of the light we can access excitation associated with each spin state separately. This is commonly referred to as *spin-valley polarization*. Note that the energy of the blue and red transition are degenerate, so this is technically two degenerate Kramer doublets. This degeneracy can be broken with an applied magnetic field and lead to an extremely large degree of polarization, which will be discussed further in Ch. 5.

2.3 Exciton Species

Now that we understand the band structure and resulting selection rules in TMDs, we will look at the different species of optically generated excitons that result from them. This section is broken down into two models for describing these species: single-particle and many-body states. The single-particle interpretation, which describes exciton species as a finite number of electrons and holes bound together, is the simplest picture to understand and we capture most of the basic underlying physics. The many-body interpretation, on the other hand, treats all of the electrons and holes in the system as an interacting ensemble which makes the description more complete. It has been successfully used to describe optical excitations in TMDs when there are a large number of free carriers

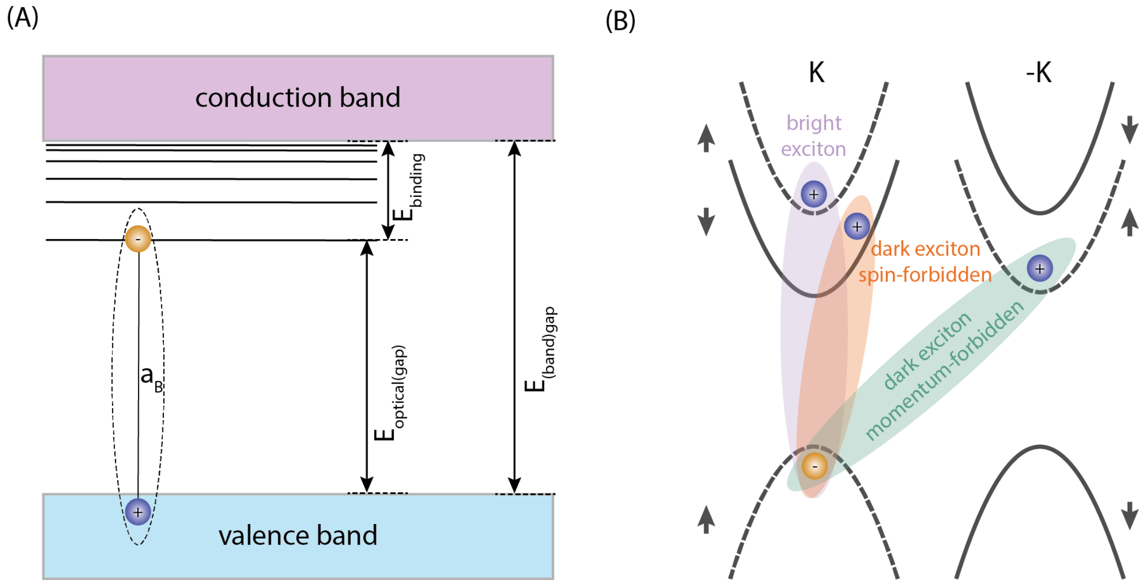

Figure 2.4: (A) An illustration of the general energy configuration for excitons as mid-gap states in semiconductors. (B) An illustration of the different kinds of exciton species possible within the TMDs. Here, we ignore the lower valence band due the energy discrepancy between the two bands (>100 meV). Excitations originating with with a hole in the lower valence band make up the B series of excitons in TMDs. Panel (A) is adapted with modification from Ref. [132].

present in the system.

2.3.1 Single-Particle Models

Excitons are bound electron-hole pairs that are created in semiconductors when a photon excites an electron from the valence band to a mid-gap "defect"-like state below the conduction band. They have been studied in semiconductors for many years, but the TMD system has allowed researchers to push the boundaries of exciton physics. As discussed earlier in this chapter in the band structure section (Section 2.1), the TMDs undergo an indirect-to-direct band gap transition when the crystal is thinned from bulk to monolayer form [197, 287]. The direct gap strongly enhances the oscillator strength of the bright exciton, which makes the study of the exciton states more readily accessible from optical measurements.

Since that discovery, researchers have found quite a number of interesting and sometimes exotic excitonic states in the TMDs. Not only are traditional bright excitons visible, but many-particle phenomenon like biexcitons [16, 290, 342] and trions [18, 181, 190, 196, 257] have also been observed. Owing to band inversion in some TMDs, spin-forbidden dark excitons have been observed in W-based TMDs [19, 120, 181, 208, 350, 355], and intervalley momentum-forbidden dark excitons are also possible under the right conditions [229, 304]. Localized excitons within the gap of the material have been host to quantum emitters (QE) [39, 109, 139, 288, 300]. A visual representation of these excitons can be found in Fig. 2.4(B). This section will serve to provide further explanation of these phenomenon.

Though beyond the scope of this work, it is worth mentioning that the wealth of excitons is even richer in the realm of traditional vdW heterostructures and Moiré physics. It is not only possible to get interlayer excitons [74, 246], but more recently so-called "Moiré excitons" have been found to exist in Moiré heterostructures and exhibit properties different than their more "traditional" (if one can truly use that word in a field still so new) interlayer excitonic states [268, 303].

2.3.1.1 Bright Excitons

Excitons are typically discussed in analogy to the hydrogen atom since they are also a bound pair consisting of a negatively and positively charged particle. Thus, the distance between the electron and hole is called the exciton Bohr radius, a_B. The energy of the state is sometimes called the optical gap, and is defined as:

$$E_{\mathrm{X}} = E_{\mathrm{(optical)gap}} = E_{\mathrm{bandgap}} - E_{\mathrm{binding}} \tag{2.16}$$

The selection rules discussed in the previous section apply to "bright" excitons found in TMDs (see Fig. 2.4(B)). Bright excitons are a bound $\mathrm{e}^-/\mathrm{h}^+$ pair where the e^- and h^+ both are in bands with the same electron spin. They are thus a dipole-allowed transition which recombine and emit light readily, leading to the moniker that they are "bright." In this case, the dipole is in-plane and thus the bright exciton emits in the out-of-plane direction. The ease with which they recombine lends itself to a short lifetime ($<$ 10ps).

The exciton spectrum of a material depends strongly on the dimensionality of the system. Because many materials are well described with a hydrogenic approach, a good jumping off point for describing excitons is the Rydberg model.In general, for a α-dimensional space, the Rydberg series is given as,

$$E^{n}_{\mathrm{binding}} = -\frac{E_0}{\left(n + \frac{\alpha - 3}{2}\right)^2}. \tag{2.17}$$

Here, $\mathrm{E}^{n}_{\mathrm{binding}}$ is the binding energy of the n-th level, n is the principal quantum number, α is the dimensionality of the system, and E_0 is the Rydberg energy. If we for a moment ignore any dielectric effects, we see from Equation 2.17 that the energy of the lowest energy state will be four times larger in 2D than in 3D. An illustration of excitons, Eqn. 2.16, and the Rydberg states is shown in Fig. 2.4. The Rydberg series is particularly

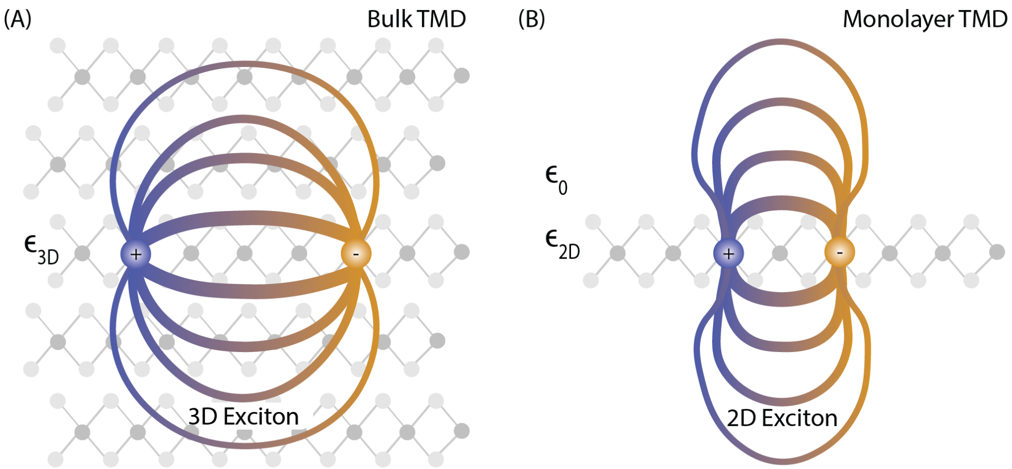

Figure 2.5: (A) exciton formed in a bulk TMD. The entire exciton is contained within the same dielectric environment, $\epsilon_{3\mathrm{D}}$. (B) exciton formed in a monolayer TMD. Much of the field associated with the exciton extends out of the TMD dielectric environment, $\epsilon_{2\mathrm{D}}$, into the surrounding atmosphere, ϵ_0. This leads to reduced dielectric screening on 2D excitons. Figure is adapted from Ref. [46].

prolific in TMDs because of the strong 2D confinement, and have been observed through a variety of different optical techniques up to n =11 [44,46,94,292,293,317].

However, there are other effects to take into account when discussing the structure of the exciton series in TMDs. In the atomically thin limit, i.e. in the monolayer regime, the dielectric screening is reduced substantially as the electric field between the bound $\mathrm{e}^-/\mathrm{h}^+$ pair forming the exciton extends outside of the monolayer and into the surrounding atmosphere (generally air or vacuum, which has a lower dielectric constant than the semiconductor). This is unlike bulk excitons, in which the field emanating from the bound $\mathrm{e}^-/\mathrm{h}^+$ pair is all contained within the same, bulk dielectric environment. An illustration of this effect can seen in Fig. 2.5. This also means that the excitons themselves are strongly confined within the plane of the monolayer sheet.

These two factors – increased binding energy and reduced dielectric screening –

have major implications for the behavior of excitons within TMDs. First, the optical gap is expected to increase in monolayer TMDs. Second, the binding energy of the excitons is also expected to increase (beyond the 4x factor from reduced dimensionality) due to enhanced electron-hole interaction from the confinement [46]. In fact, this phenomenon results in such a strong confinement of the exciton, that the binding energy of the exciton is on the order of 100-300 meV, which is much larger than the thermal energy provided at room temperature ($\approx$ 25 meV) [292, 293]. This means that researchers observe robust bright excitons in the in TMDs without ever having to cool their samples to cryogenic temperatures, which is typically required to study this kind of physics [36, 187, 189, 323].

To dive in to this a little more, let's rewrite Eqn. 2.17,

$$E_n = \frac{\mu e^4}{2\hbar^2 \epsilon^2 (n - 1/2)^2}. \tag{2.18}$$

Here μ is the reduced exciton mass, $\hbar$ is Planck's constant/2π, e is the charge of the electron, and ϵ is the effective dielectric constant. In practice, when experimentalists measure the Rydberg series they are measuring difference in energy that is actually E_g^{qp} - E_n where E_g^{qp} is the quasiparticle gap. Thus, experimentally both the binding energy for the nth state and the quasiparticle gap can be obtained if the series behaves in a hydrogenic fashion.

As mentioned briefly, another quantity used to describe excitons are their Bohr radius. For hydrogen, $a_{\mathrm{B}}^{\mathrm{H}}$ = 0.529 Å but the radius scales with n like the energy does. As with the binding energy, if we again account for the mass and dielectric environment difference of the exciton, we can define the exciton Bohr radius as

$$a_{\mathrm{B}}^{n} = \frac{m_e \epsilon a_{\mathrm{B}}^{\mathrm{H}} n^2}{\mu}. \tag{2.19}$$

Here, all previously defined symbols retain their meanings.

To throw a wrench in this formalism, researchers mapping the Rydberg series in TMDs have found that they behave in a non-hydrogenic fashion with respect to the the energy spacing between the levels in the series [46, 107]. In essence, researchers found that the energy scaling is weaker with respect to n; in particular when n=1 and n=2. For n=3-5, the spacing is much closer to what would be expected for a hydrogenic series and this allows researchers to still extract physical information about the exciton binding energy, etc. However, this still does not explain the diversion from the hydrogenic model. If we recall Fig. 2.5, we see that the field from the exciton extends outside of the dielectric environment of the monolayer itself. As the radius of the exciton extends with increasing n, the charge separation leads to a larger portion of the electric field exists in this low-dielectric region outside of the TMD. This gives rise to what researchers refer to as "anti-screening," whereby the dielectric screening is reduced and leads to non-hydrogenic-like behavior [46].

2.3.1.2 Dark Excitons

An exciton, like those discussed above, is said to be "bright" if it has a one photon, dipole-allowed transition (i.e. has even parity). If we refer back to Fig. 2.4(B) from earlier in this section, we see that there are two "dark" kinds of excitons: spin-forbidden (intra-valley) and momentum-forbidden (inter-valley).

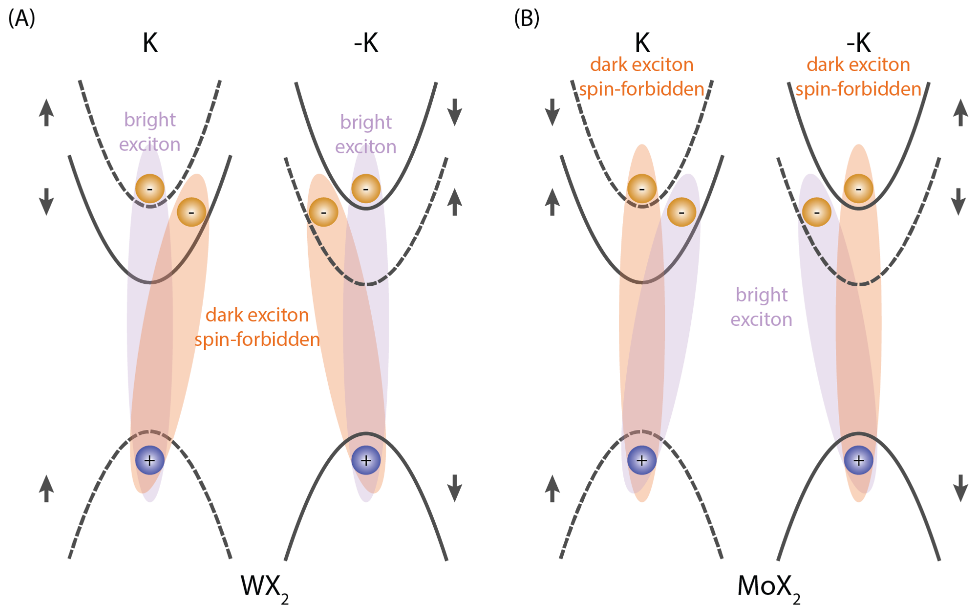

Figure 2.6: Comparison of the bright/dark states in (A) W-based TMDs and (B) Mo-based TMDs. Due to d-orbital chemistry in the W-based TMDs the conduction band orbitals are inverted compared with the conduction band in Mo-based TMDs.

2.3.1.3 Spin-Dark Excitons

As discussed in the previous section, bright excitons are formed from a e^-/h^+ pair that comes from bands with the *same* spin. Spin-forbidden dark excitons, on the other hand, are formed from an e^-/h^+ pair in bands with the *opposite* spin. This means that in order to recombine a second-order process (spin-flip) must occur. This leads to significantly longer lifetimes than for bright excitons, with lifetimes >100 ps vs. fs scale in bright states [249].

Not all TMDs form dark excitons readily. In particular, TMDs with W as the transition metal have highly populated dark states. Turning our attention to Fig. 2.6, let us examine why. In W-based TMDs resulting d-orbital hybridization in the heavier system ($6d$ in W vs. $5d$ in Mo) leads to a *band inversion* in the conduction band [141, 142, 144, 186]. Thus, when we look at this in Fig. 2.6 (A), we see that the bright state (same spin) is *higher* in energy than the dark state (opposite spin) in this system. The electrons can undergo an intervalley exchange interaction via phonon and relax down in the lower energy state, thus populating the dark state and leaving a large reservoir of dark excitons trapped there due to the long lifetimes. On the other hand, we can see in Fig. 2.6 (B) that in Mo-based TMDs the bright state is *lower* in energy than in the dark state. Therefore, while it is possible to form a dark exciton, the bright state is much more energetically favorable and will populate in the same manner that the dark state does in W-based TMDs [19].

The dark state was first observed indirectly in temperature resolved PL measurements [11, 313, 349]. Researchers found that as the temperature was increased, so did the PL intensity of the $1s$ state. Since the dark state is lower energy than the bright state, as the system is cooled the electrons are more likely to non-radiatively thermalize into the dark state, thereby quenching the emission and lowering the intensity. After this initial work, researchers set about trying to determine how to "brighten" the dark states and interact with it in a controlled fashion. In contrast to the bright state, the dark state has an out-of-plane dipole transition which means that if it emits light it does so in the plane of the monolayer which makes detecting signatures difficult in common laboratory setups [67, 249, 299, 349]. Naturally, upon experimental evidence of it's existence the research community set about determine how to best probe it.

The most obvious method is simply to collect light from the in-plane direction by rotating the objective used to collect the light by 90°in order to have it aligned with the edge of the monolayer plane. Wang *et. al* did just this and successfully observed the dark

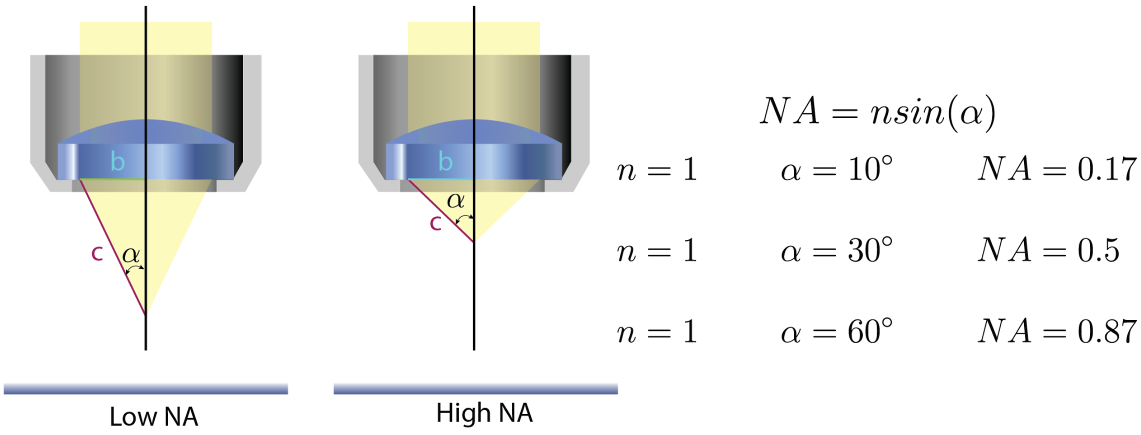

Figure 2.7: Illustration of low NA and high NA configuration showing the difference in the light collected. Additionally, there are some different NA values calculated on the right side of the illustration to show the correlation between angle and NA more clearly. In our experiments, we need NA > 0.6 to see dark excitons. Figure is adapted with some modification from Ref. [59]

state directly in-plane [312]. Though rotating the setup like this may seem trivial, for many groups performing their measurements at low temperatures in fixed cryostats it's simply not achievable depending on their optical access. Remarkably though, Wang *et al.* also showed that with the correct common-place lenses it was possible to observe the dark state emission (albeit weakly) without having to flip the setup.

Referring to Fig. 2.7, we see that the numerical aperture (NA) of a lens is defined as

$$NA = n_{\text{med}} sin(\alpha). \tag{2.19}$$

Here, n_{med} in the refractive index of the medium through which the light travels and α is the collection angle of the light. Thus, for low NA lenses, almost all of the light we collect is emitted in the out-of-plane direction. However, with increasing NA we collected progressively more and more light that is emitted in-plane. In W-based TMDs, especially at low temperatures, the dark state population becomes so large that even though the lifetime of the dark state is long and the amount of in-plane light collected is small, we can capture enough in-plane emission with a high NA lens to directly observe the dark exciton even when the optics is aligned perpendicular to the sample. In fact, this is how we observe dark state within our experimental work.

Though the high-NA lens method is popular, it does have the drawback of producing a relatively weak signal. For those who still want to measure the state directly, a slightly more refined method has become popular as it is easier to implement in existing measurement setups. This method relies on high magnetic fields that are generally already accessible in many measurement systems. Because of its reliance on a magnetic field, this technique is referred to as "magnetic brightening."

The premise of magnetic brightening is simple: applying an in-plane (parallel) magnetic field **B** = (B$_x$, B$_y$) in the plane of the monolayer TMD results in a Zeeman interaction that mixes the spin states in both the valence and conduction band which results in a small, but non-zero, tunable emission in the out-of-plane direction of the dark exciton. Diving into the math, we see how this mixing occurs,

$$\mathcal{H}_Z = \frac{1}{2} g_c \mu_B (\sigma_x B_x + \sigma_y B_y), \tag{2.20}$$

μ_B is the Bohr magneton, $\sigma_{x,y}$ are the Pauli matrices, and here g_c is the in-plane Landé g-factor for the conduction band. For the remainder of this section we will be working in the basis of $\{|\tau, b\rangle, |\tau, d\rangle\}$, where τ is still our valley index and b/d represent the bright and dark states within the material.

In this formalisn, the Hamiltonian for the unperturbed bright and dark states is,

$$\mathcal{H}_0 = \begin{bmatrix} E_b & 0 \\ 0 & E_d \end{bmatrix}. \tag{2.21}$$

Here, E_b and E_d are the energies of the bright and dark states, respectively, and E_b - E_d = ΔE^c_{SO}. ΔE^c_{SO} is our chosen form for the difference in energy between the bright and dark states in the conduction band that are split due to spin-orbit coupling.

We know that the combined Hamiltonian accounting for interaction of the applied parallel field is $\mathcal{H}^{B_{||}}_{int} = \mathcal{H}_0 + \mathcal{H}_Z$, so combining Equations 2.20 and 2.21 and applying the matrix form of the Pauli matrices we get,

$$\mathcal{H}^{B_{||}}_{int} = \begin{bmatrix} E_b & \frac{g_c\mu_B}{2}(B_x - iB_y) \\ \frac{g_c\mu_B}{2}(B_x + iB_y) & E_d \end{bmatrix} \tag{2.22a}$$

$$= \begin{bmatrix} E_b & \frac{1}{2}g_c\mu_B B_{-\tau} \\ \frac{1}{2}g_c\mu_B B_{+\tau} & E_d \end{bmatrix}. \tag{2.22b}$$

To simplify matters, $B_\pm$ = $B_x \pm iB_y$ is introduced in Equation 2.22b. With our Hamiltonian in place, we can solve for our eigenvectors through the usual process and that,

$$|\tau, b\rangle^{B_{||}}_{int} = \frac{1}{1+\gamma/2}\,|\tau, b\rangle - \sqrt{\gamma}B_{+\tau}\,|\tau, d\rangle \tag{2.23a}$$

and

$$|\tau, d\rangle^{B_{||}}_{int} = \frac{1}{1+\gamma/2}\,|\tau, d\rangle + \sqrt{\gamma}B_{-\tau}\,|\tau, b\rangle \tag{2.23b}$$

where, γ = $g_c^2\mu_B^2B^2/(4\Delta E_{SO}^2)$. Since $\gamma \ll 1$, the perturbed states in Equations 2.23a and 2.23b are very close to those of the original bright and dark states in the system. We can see easily from this that the bright state now has a non-negligible mixture of the dark state attached, making it possible to detect signatures of the dark state in out-of-plane PL measurements. From Equation 2.23a we can easily read off some information about the intensity of the PL signal from such a dark state,

$$I_d \propto n_d I_b \gamma \propto n_d I_b B^2. \tag{2.24}$$

Here, n_d is the is the population of the dark exciton state and I_b is the intensity of the bright exciton emission without the applied external field.

Even with the magnetic brightening method, which is limited by the field strengths readily available in a lab setting, the intensity of this dark state is still very small. However, it has been successfully measured and the preceding derivation is based on the work presented by these successful experiments [29, 208, 350]. Other groups have since found more creative methods as well to measure and interact with the dark states, such as chiral phonons and through use of waveguides [184, 299, 355].

2.3.1.4 Momentum-Dark Excitons

Momentum-dark excitons, as the same suggests, occur when an exciton pair is formed between and electron and a hole that are at distinctly different points in momentum space. Most commonly, this phrase references an exciton formed between a hole in the ±K valley and an electron in the ∓K valley (see Fig. 2.4(B)). Researchers have found that there is a prominent phonon-assisted decay path that allows for electron in the upper conduction band in one valley to undergo intervalley scattering and end up in the lower conduction band of the other valley (spin/valley degree of freedom are retained here) [131, 170]. This is then considered a dark transition since another phonon is needed to allow the electron to move back to the correct momentum in order to radiatively recombine.

Similar to the spin-dark exciton, the momentum-dark energy is lower energetically than the bright exciton. However, it lies in between the spin-dark and bright excitons. In a naïve model, one would expect that the spin-dark and momentum-dark excitons would be energetically degenerate. After all, they are both formed because a hole in the upper valence band and an electron in the lower conduction band. However, in this naïve model, there is no accounting for the exchange effect on an exciton species formed between two valleys. This intervalley exchange effect is rather substantial and raises the energy of the momentum-dark exciton by $7-10$ meV – depending on the TMD – from the spin-dark exciton energy [180]. The recombination can be observed directly, as well as additional signature of a chiral phonon replica – which comes from the chiral phonon required for the exciton to recombine – in PL measurements [170, 180, 358].

Ongoing research has found evidence of many different kinds of momentum-dark excitons betwen the ±K valleys and different symmetry points within the band structure. This is rapidly developing area of research and outside of the scope of this work. For the curious reader, please see References 30, 76, 179, 194, 229, 304.

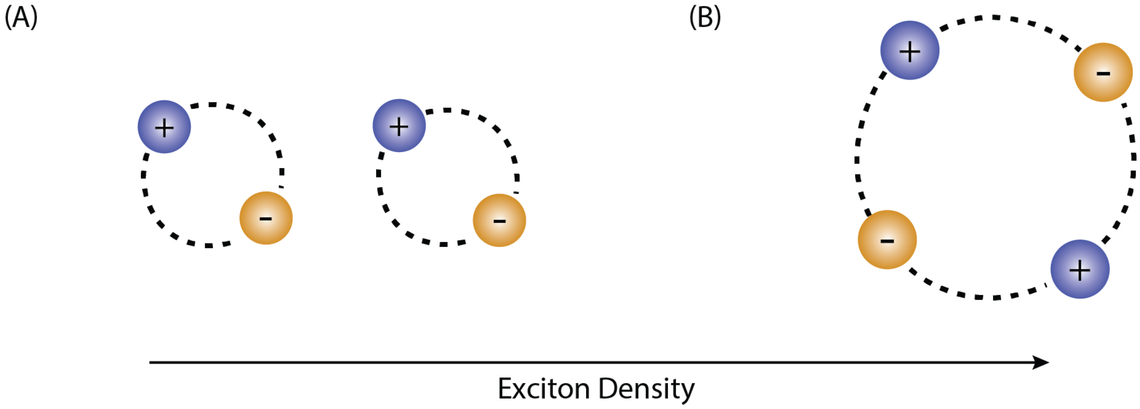

Figure 2.8: (A) shows two excitons, which are higher densities will interact and form a biexciton compound (B)

2.3.1.5 More Exotic Pairings: Biexcitons and Trions

2.3.1.5.1 *Biexcitons* So far we have only discussed a single exciton in a TMD, but what happens when there are many excitons in a TMD sample? One possibility is that as the incident excitation power density increases, two excitons will undergo a 4-body interaction where their energy/momentum is transferred and results in the creation of energetic free carriers (so-called hot carriers) through the destruction of the exciton pairs. This is known as exciton-exciton annihilation (EEA). This is a well-known process in many semiconducting systems and several groups have reported EEA in TMDs in the literature [55, 147, 211, 341]. The interest in this particular mechanism is two-fold: first, the destruction of excitons results in loss of optical signal which is undesirable in many experiments [8, 316] and second, on the flip side, research has shown that the efficient of generation of hot-carriers from this project could be an excellent means of energy generation in photovoltaics [24, 100, 178, 200].

In a process quite opposite of EEA, as the exciton density increases in the monolayer, excitons in close proximity can bind together into a larger complex referred to as a biexciton (Fig. 2.8). Biexcitons have been studied extensively in bulk semiconductors as well as in other quantum systems – like quantums wells, nanowires, and quantum dots [**?**, 210]. Since the biexciton consists of two holes and two electrons, it can be modeled similarly to positronium. In bulk,

$$E^b_{\mathrm{XX}}(\mathbf{k}) = 2E_{\mathrm{X}} - E_{\mathrm{XX}} + \frac{\hbar^2\mathbf{k}^2}{2\mu_{\mathrm{X}}}. \tag{2.25}$$

Here, $\mathrm{E}^b_{\mathrm{XX}}(\mathbf{k})$ is the biexciton binding energy as a function of momentum, E_X is the energy of the exciton, E_{XX} is the energy of the biexciton, and μ_{X} is the reduced mass of the exciton ($2\mu_X$ = μ_{XX}) [135]. In systems with reduced dimensionality, research has shown that this manifest as increasing biexciton binding energy with increasing confinement [134, 226, 280].

Biexcitons have been studied extensively in the semiconducting TMD systems [16, 104, 233, 276, 291, 306, 342]. As an illustration, we will discuss results in $\mathrm{WSe_2}$ since that is our system of interest. The biexciton was the subject of controversy in the TMD community for several years. Based on theoretical numerical simulations, the expected binding energy of the biexciton in $\mathrm{WSe_2}$ is $\sim$ 20 meV [149, 204, 297, 345]. However, in early experimental measurements, researchers have found that it is actually closer to $\sim$ 50 meV [342]. The theoretical and experimental results were later reconciled when the researchers determined that there were *two* biexciton complexes that had formed in the material: a neutral biexciton with a binding energy of $\sim$ 17 meV (in good agreement with the numerical simulations) as well as the a negatively charged biexciton residing at the first reported position with a binding energy of ~ 50 meV [172]. Since then, further work has revealed biexciton fine structure that is the result of different configurations for the electrons and holes between the valleys where the fine structure splitting in energy results from different exchange term values for each configuration [290]. Additionally, there have been predictions of an excited biexciton in the literature that at this time remains illusive [345].

Aside from the predictive modeling for binding energies, there is another signature that can determine whether a features is a biexciton: the relationship between the intensity of the exciton peak and the suspected biexciton peak. Following simple kinetic theory laid out in Reference 230,

$$\frac{dn_{\mathrm{X}}}{dt} = \Gamma - \frac{n_{\mathrm{X}}}{\tau_{\mathrm{X}}} + \frac{n_{\mathrm{XX}}}{\tau_{\mathrm{XX}}} - 2\frac{n_{\mathrm{X}}^2}{n^*}\frac{1}{\tau_C} + 2\frac{n_{\mathrm{XX}}}{\tau_C} \tag{2.26a}$$

and

$$\frac{dn_{\mathrm{XX}}}{dt} = -\frac{n_{\mathrm{XX}}}{\tau_{\mathrm{XX}}} + \frac{n_{\mathrm{X}}^2}{n^*}\frac{1}{\tau_C} - \frac{n_{\mathrm{XX}}}{\tau_C} \tag{2.26b}$$

Here, Γ is the continuous-generation rate ($\propto$ the laser pump power), $\mathrm{n_X}$ is the number of excitons, $\mathrm{n_{XX}}$ is the number of biexcitons, τ_{X} is the excitons lifetime, τ_{XX} is the biexciton lifetime, τ_{C} is the interconversion time between excitons and biexcitons (and vice versa) when $\mathrm{n_X} = \mathrm{n_{XX}} = \mathrm{n}^*$ where n^* is the equilibrium constant.

When one solves these equations, the following solution is obtained,

$$n_{\mathrm{X}} \propto \left[\left[1 + \frac{\Gamma}{\Gamma_0}\right]^{1/2} - 1\right] \tag{2.27a}$$

and

$$n_{\mathrm{XX}} \propto \left[\left[1+\frac{\Gamma}{\Gamma_0}\right]^{1/2}-1\right]^2. \tag{2.27b}$$

Here, $\Gamma_0 = (n^* \tau_{\mathrm{XX}}/4\tau_{\mathrm{X}}^2)(1+\tau_{\mathrm{C}}/\tau_{\mathrm{X}})$ and is the characteristic generation rate that determines the separation of the exciton/biexciton-dominant regions [95]. Thus, from this we can predict from this at low generation rates ($\Gamma < \Gamma_0$), the exciton population will grow linearly, while the biexciton population will grow quadratically [135]. We expect this to manifest as,

$$I_{\mathrm{XX}} \propto I_{\mathrm{X}}^{\alpha}. \tag{2.28}$$

Here, I_{XX} and I_X are the PL intensities of the biexciton and excitons states, respectively. As we can see from Equations 2.27a and 2.27b, α = 2 when the system is in equilibrium.

Returning to our experimental system, in the WSe_2 the researcher found for the lower binding energy peak α = 1.94, and for the higher binding energy peak α = 1.82. These are nearly 2 and in reasonably good agreement with the expected power relation between the exciton and biexcitons emission intensities. In other quantum-well type systems where biexcitons have been previously studied, a typical α value falls in the α = 1.2-1.9 range. Researchers have generally attributed these lower values to systems that are varying degrees out of equilibrium [25, 286]. In light of this, researchers felt comfortable taking this as additional confirmation of the biexciton state.

2.3.1.5.2 *Trions* As the name suggests, trions are quantum systems consisting of three charged particles. Positively charge trions consist of two holes and an electron, while

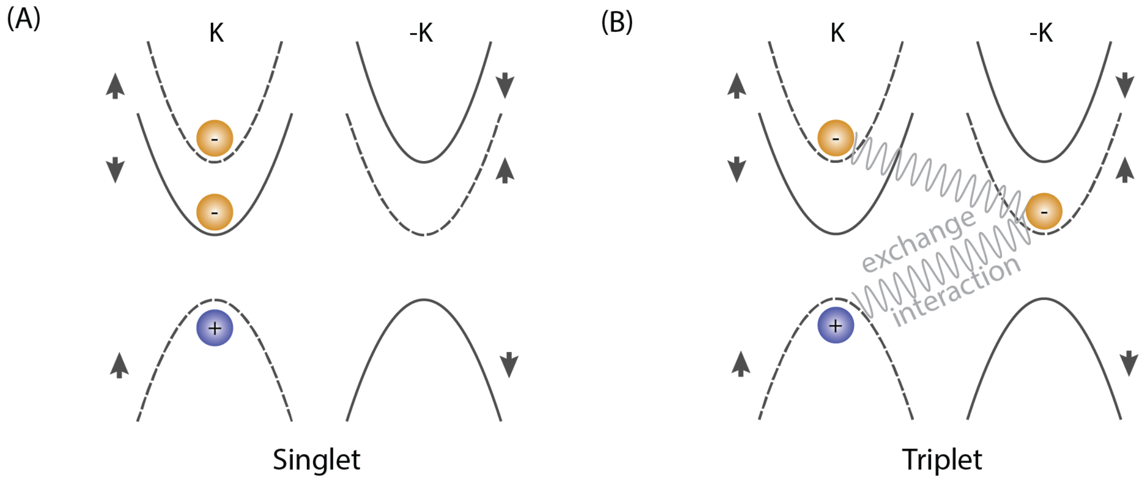

Figure 2.9: Focusing just on K-valley trions (A) shows the intravalley singlet trion and (B) shows the intervalley triplet trion and its associated exchange interaction. It should also be noted the bands are structured in this diagram for WX_2 systems. All trions here are negative and a similar configuration to both (A) and (B) can be produced in the -K valley.

negatively charge trions consist of two electrons and a hole. They were originally predicted and observed in bulk semiconductor systems, but they have also been widely observed in TMD systems [10, 53, 190, 196, 288].

Much like biexcitons, the formation of trions via the reversible process $\mathrm{X}_0 + \mathrm{e}^-(\mathrm{h}^+) \leftrightarrow \mathrm{X}_{-(+)}$ is a function of the electrons (or holes) density in the system. Moving forward, we focus solely on negative trions, but a similar formalism can be used to discuss positive trions. We show this in the following, using a dynamical equilibrium model,

$$n_{\mathrm{background}} = n_{\mathrm{e}} + n_{\mathrm{X}_-}. \tag{2.29}$$

Here, $n_{\mathrm{background}}$ is the initial background charge density controlled by gate voltage. $n_{\mathrm{e}}, n_{\mathrm{X}}, n_{\mathrm{X}_-}$ are the density of free electrons, neutral excitons, and trions and are considered to be steady state variables [257]. Our relationship between these quantities is defined through the reaction rate from above.

Next, we apply the law of mass action onto our trion state:

$$\frac{n_{\mathrm{X}}n_{\mathrm{e}}}{n_{\mathrm{X}_-}} = Ak_{\mathrm{B}}Te^{-\frac{E_{\mathrm{B}}^{\mathrm{T}}}{k_{\mathrm{B}}T}} = \Gamma_{\mathrm{X}_-} \tag{2.30a}$$

and

$$A = \frac{4M_{\mathrm{X}}m_{\mathrm{e}}}{\pi\hbar^2 M_{\mathrm{X}_-}}. \tag{2.30b}$$

Here, k_{B} it the Boltzmann constant, T is the temperature, $E_{\mathrm{B}}^{\mathrm{T}}$ is the trion binding energy, and $M_{\mathrm{X}}/M_{\mathrm{X}_-}$ are the composite exciton and trion masses, respectively, and the right-hand side becomes Γ_{X_-} which is the trion formation coefficient [257, 281].

If we rewrite Eqn. (2.30a) as $n_{\mathrm{X}_-} = \Gamma_{\mathrm{X}_-}n_{\mathrm{X}}n_{\mathrm{e}}$ and substitute Eqn. (2.29) into it, we get a final expression for the trion density as a function of initial background charge in the system,

$$n_{\mathrm{X}_-} = \frac{\Gamma_{\mathrm{X}_-}n_{\mathrm{X}}}{1+\Gamma_{\mathrm{X}_-}n_{\mathrm{X}}}n_{\mathrm{background}}. \tag{2.31}$$

From this, we can see when the exciton density is low in the system ($\Gamma_{\mathrm{X}_-}n_{\mathrm{X}} \ll 1$) then $n_{\mathrm{X}_-} \sim n_{\mathrm{X}}$ and the exciton and trion densities are roughly proportional. However, when the exciton density in the system is high ($\Gamma_{\mathrm{X}_-}n_{\mathrm{X}} \gg 1$), the number of trions in the system $n_{\mathrm{X}_-} \sim n_{\mathrm{background}}$ approaches the background charge concentration [175]. As indicated earlier, this is a reversible process $\mathrm{X}_0 + \mathrm{e}^- \leftrightarrow \mathrm{X}_-$ and population in $\mathrm{X}(\mathrm{X}_-)$ will feed into $\mathrm{X}_-(\mathrm{X})$ as the system evolves in time. In fact, researchers have been able to show this using two-color pump probe spectroscopy [36, 103, 154, 278].

Now that we know how trions are formed, let's look a little more closely at what kinds of trions we can form. Like excitons, trions can exist in both bright and dark states. In order for a trion to be bright, the selection rules mandate one of the electrons must have the same valley and spin index as the hole in the trion [2,279]. This amounts to four total bright ground states – two intervalley and two-intravalley – which are illustrated in Fig. 2.9 [191]. If we examine the spin configurations of the bands of the different bright excitons in Fig. 2.9, we can see in the intravalley trions exist in a *singlet* state (X^s_-), while the intervalley trions exist in a *triplet* state (X^t_-).

In the case of the intervalley trions, there is an intervalley exchange interaction between the e^-/h^+ pair and the extra electrons, which researchers expect to be on the order of about 6 meV in WSe_2 [53,191,338] and reflects the energy preference for aligning spins in the system. This results in a difference in energy between the singlet and triplet exciton states, essentially splitting them and manifesting as trion fine structure. The trion fine structure is well documented in the literature in the WX_2 system [125,172,191,232, 279,305].

Just like bright excitons have dark exciton counterparts, bright trions have dark trion counterparts due to spin forbidden transitions. Dark trion form in a triplet configuration, but with the electron in the same valley as the hole in the opposite spin state. Like in excitons, this suppresses the radiative recombination. An illustration of the difference between a bright and dark triplet trion can be found in Fig. 2.10. The existence of dark trions is well documented in the literature in PL studies of dark excitons [184,350,355]. However, there has been recent interest in the specific study and control of these dark states due to their extremely long lifetimes. Typically, the lifetime of bright excitons is $<$ 1ps, triplet trions have lifetimes of a few ps and singlet trions have lifetimes of $>$

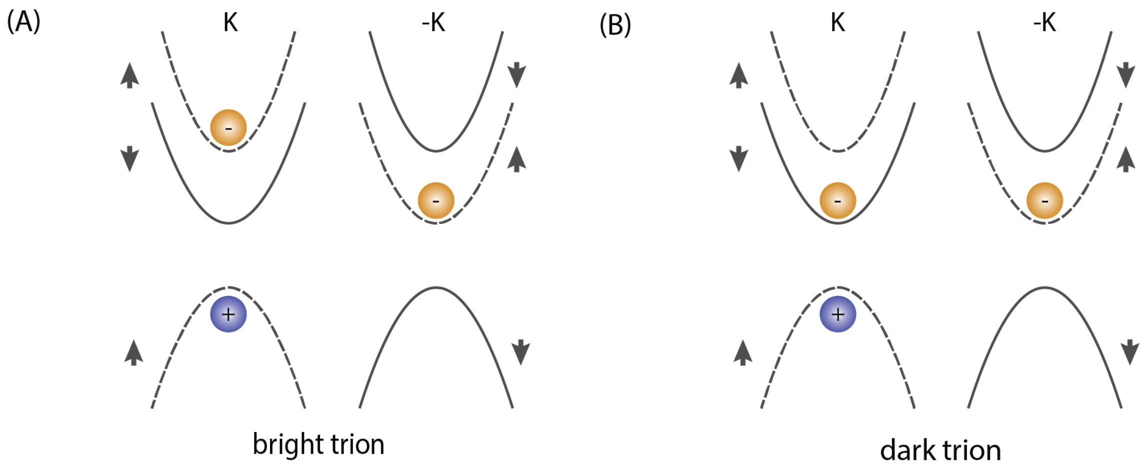

Figure 2.10: (A) the formation of a bright trion in a TMD, denoting the positions in the bands of the carriers. (B) the formation of a dark trion in a TMD, denoting the positions in the bands of the carriers. It should also be noted the bands are structured in this diagram for WX_2 systems.

25ps [279]. Recent work has shown that the lifetime of dark trions is > 1ns, which is an order of magnitude higher than even dark excitons, and because of the charge of the species this lifetime can be controlled by means of electrostatic gating [181]. The tunable nature is extremely exciting for those interested in TMDs for quantum computation, and these findings will open more serious study into manipulating the dark trion state.

2.3.2 Many-Body States

2.3.2.1 Break Down of the Single-Particle Model

As mentioned briefly earlier, all of the excitations we have discussed in this section (bright excitons, dark excitons, etc.) are exciton species that fit within the *single-particle* framework. Because of the finite number of particles in the system, these kind of excitations are much simpler to model mathematically which makes them a convenient tool. However, the realistic use of this type of model is limited to situations in which there are very few free carriers present in the system and these single-particle type species can remain largely isolated from one another.

In real experiments, there are usually many carriers present in the system ($\mathcal{O} \approx 10^{11} - 10^{12}\mathrm{cm}^{-2}$) if we do not artificially hold the system at neutrality by means of electrostatic gating (a technique we will discuss more in Ch. 4). In this *many-body* regime, the properties predicted by the single-particle model begin to diverge from observed physics and a new model is needed to describe the scenario playing out where excitons interact with and are dressed by the Fermi sea of carriers that now exist.

2.3.2.2 Historical Context of Polarons

If we cannot use single-particle physics anymore, what do we replace it with? It turns out this question comes up frequently in condensed matter systems where we are faced with *impurity problems* – that is, what happens when a quantum impurity interacts with a reservoir of bosons or fermions. A very common technique is to introduce the concept of polarons as the many-body quasiparticle resulting from that interaction. In traditional polaron theory, a polaron is an electron or hole (impurity) that is dressed by a cloud of virtual phonons (boson reservoir). As the impurity travels through the lattice, the virtual phonons distort the lattice and other excess charges around the impurity creating a traveling polarization cloud – hence the name polaron.

This concept of the polaron dates back to the early days of quantum theory in the early-to-mid $20\mathrm{th}$ century, with the pioneering work performed by Lev Landau and Solomon Pekar in the 1930s-1940s [156, 159]. Later Holstein and Fröhlich built on this

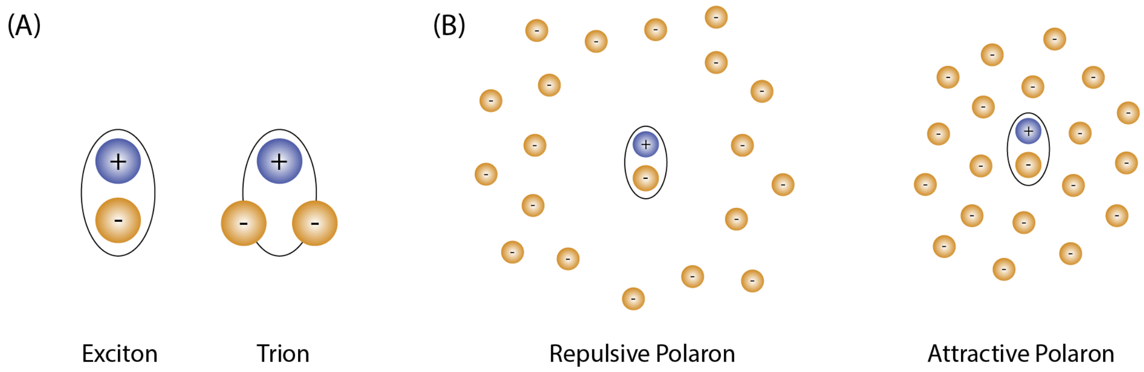

Figure 2.11: (A) Neutral (exciton) and charged (trion) single-particle species and their (B) many-body interpretations, the repulsive and attractive polarons.

to further develop the two regimes of large and small polarons [84, 85, 112, 113]. This idea has become a very useful one to describe many-body induced quasiparticles and today the framework has been extended to include ideas like bipolarons [5, 215, 353], polaron excitons [115, 302], and 2D Fermi-polarons – which are the kind found in TMDs [15, 69, 275]. For the curious reader, Franchini *et al.* have an excellent and recent review on the large variety of polarons currently known [81].

2.3.2.3 2D Fermi Polarons in TMDs

In the presence of excess carriers, we look to replace the concept of excitons and trions with 2D Fermi exciton-polarons. Fermi polarons were widely explored in cold-atom systems in the early 2000s [136, 143]. During all of this work, two species of polaron were identified: the repuslive Fermi polaron and the attractive Fermi polaron. As the name would suggest, the attractive (stable) Fermi polaron interacts attractively with the Fermi sea by pulling in the charges to screen itself, which the repulsive (metastable) Fermi polaron repels the Fermi sea and carves out a neutral environment for itself. See Fig. 2.11 for an illustration of the transition from single-particle to polaron states.

The discovery of trion-like resonances became a catalyst for applying polaron theory in TMDs. As discussed earlier in this chapter, significant work has been done to characterize and model the trion state in TMDs. The largest snag in that effort lies in the interpretation of the observed resonances themselves. The single-particle model for trions is only theoretically-applicable when the Fermi energy in the system $\mathrm{E_F} \ll \mathrm{E_{X_-}}$, the binding energy of the trion. However, experimental results for the trion are limited to the regime in which $\mathrm{E_F} \approx \mathrm{E_{X_-}}$.

To resolve this issue, Efimkin *et. al*, amongst others, suggested that much like in cold-atom systems, the exciton could form a Fermi polaron in the presence of excess charges in the system [68–70]. In TMDs, this would mean that the extension of the exciton state under doping becomes the *repulsive* polaron branch and the state originally thought to be trions are actually *attractive* polaron states. It can be helpful to think of these polarons as *continuum* excitons, where the excited bound electron now lies in the actual conduction band in contrast to the below band states typical of a single-particle like exciton. In this context, we can illustrate the repulsive and attractive polarons in a similar manner to the excitons and trions, which can be seen in Fig. 2.12. The experimental confirmation of these states was performed shortly after their prediction by Sidler and Back *et al.*, who also contributed to the theoretical interpretation [15, 275].

One important question that remains is determining when the single-particle and many-body interpretations are valid. We can think of the carrier concentration as the knob that lets us tune the strength of the many-body state (we will discuss this more in Ch. 4.3.2). Glazov showed that in the extremely low carrier limit, the physical properties predicted by both the trion and polaron interpretations converge [91]. This indicates that

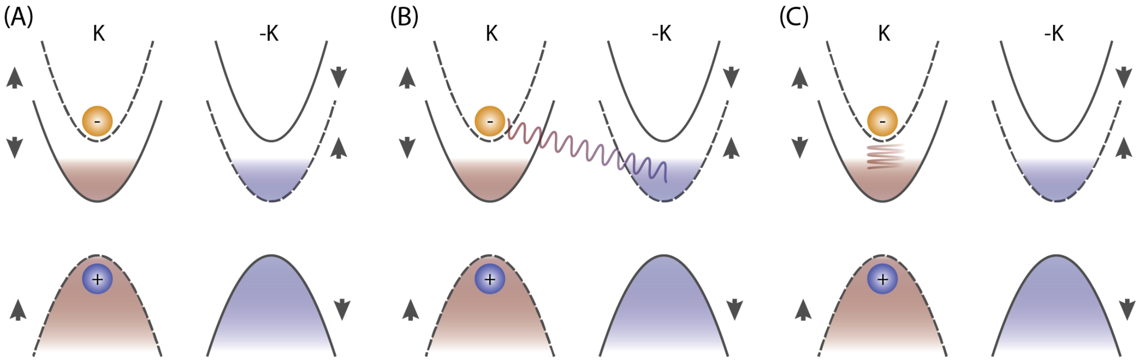

Figure 2.12: (A) Repulsive polaron, (B) intervalley attractive polaron, and (C) intravalley attractive polaron in WSe_2. Figure is adapted with some modification from Ref. [91].

the many-body interaction involved in polaron formation is more of a sliding scale than an on-off switch.

In this thesis, we discuss briefly the influence of many-body interaction our experiments. Our chosen metric to measuring this interaction strength is the g-factor extracted from Zeeman splitting. In many way, the g-factor can act as a barometer for *correlated magnetism* and indeed researchers have found atypically large g-factors [15, 133, 174, 320] in the polaron regime. We will discuss more about interpreting this g-factor metric in Ch. 5. In Ch. 6, our work studying the g-factor of the excited trion-like state is highlighted.

Chapter 3: Device Fabrication Methodology

3.1 Materials Synthesis and Extraction

In order to experimentally probe the properties of TMDs, we must first produce samples or devices from them. Generally speaking, there are several methods for producing the pieces needed to do this. In this work, two methods were used: mechanical exfoliation and chemical vapor deposition (CVD) growth. The details of each method are outlined in the following subsections and serve to help explain this type of fabrication from the very building blocks up. As a rule of thumb, mechanically exfoliated materials tend to have higher mobilities and therefore better transport properties, while CVD grown materials tend to produce fewer optical defects but have lower mobilities.

3.1.1 Mechanical Exfoliation or the "Scotch-Tape Method"

Mechanical exfoliation was the technique originally used to isolate graphene [217]. Since the original method used by Geim and Novosolev utilized everyday Scotch tape, the method has since been colloquially dubbed the "Scotch-tape method." The individual layers of graphene, hexagonal boron nitride (hBN), and TMDs are all held together in the bulk by van der Waals (vdW) bonds. These bonds are extremely weak compared to the intralayer covalent bonds that hold the atoms in the plane of each sheet together, and the shearing force applied mechanically by the tape is enough to cleave the bonds and thin the material down to monolayer thickness when it is repeated several times.

The process for mechanical exfoliation is illustrated in Figure 3.1. First, the tape is brought into contact with the bulk crystal and used to remove a chunk of materials (Figure 3.1 (A)/(B)). Then the tape is repeatedly stuck together and peeled apart to thin the material removed from the bulk and to cover the entirety of the tape (not pictured). After the crystal has been sufficiently thinned through mechanical exfoliation, the tape is applied to a substrate on which to deposit the material (Figure 3.1 (C)). For the work outlined in this thesis, the substrate used was degenerately doped Si, with 285nm of SiO_2 on top. While the Si/SiO_2 can be utilized for electrostatic gating or transport measurements, the SiO_2 thickness turns out to be the key to actually being able to optically identify graphene and other 2D materials. At this thickness, the contrast between monolayer materials and the background SiO_2 is optimal under magnification to the human eye due to thin-film interference effects [26]. Even a 15 nm difference in thickness of the oxide is enough to almost completely obscure the monolayer material on the surface of the sample. Uniform pressure is applied gently to the surface of the tape now in contact with the SiO_2 and heat is applied from the bottom using a hot plate. Both the pressure and elevated temperature help facilitate the fracturing and adhesion of the exfoliated crystal from the tape to the substrate. Finally, the tape is gently and slowly peeled back from the surface of the SiO_2 (Figure 3.1 (D)). Images taken of a piece of exfoliated WSe_2 on SiO_2 and cleaved hBN on Si/SiO_2 can be seen in Figure 3.1 (E)/(F), respectively.

Though the process is simple conceptually, it turns out to be incredibly nuanced to

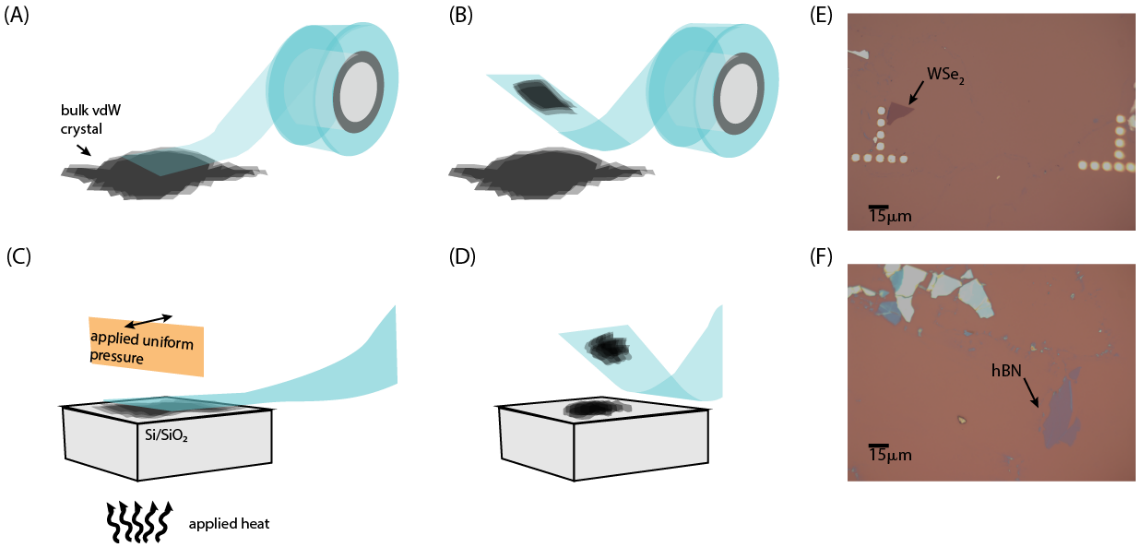

Figure 3.1: Panels (A)-(D) shows the mechanical exfoliation or “Scotch-tape method” for extracting monolayers crystals and panel (E)/(F) shows a microscope image of resulting monolayer WSe_2 and hBN respectively, obtained using mechanical exfoliation. Figure adapted with some modification from Ref. [216].

achieve consistent results from the process in terms of both uniform thickness and sheet size. Each material has its own quirks. For example, it is necessary to plasma clean the surface of the SiO_2 with oxygen for graphene to achieve large sample sizes of monolayer material, but it’s nearly impossible to get monolayer material of any size without extensive plasma cleaning for both hBN and TMDs. The type of adhesive, the pressure applied to the tape, and the temperature at which the Si/SiO_2 substrates are heated turn out to play crucial roles in the success of exfoliation as well.

After exfoliation, monolayer flakes are optically identified under a microscope. As mentioned earlier, the oxide thickness used (285nm) has been experimentally determined to be optimum for identifying monolayer materials [26]. If there was ever a question of if the sample was in fact monolayer, atomic force microscopy (AFM) was used to verify the optical signature.

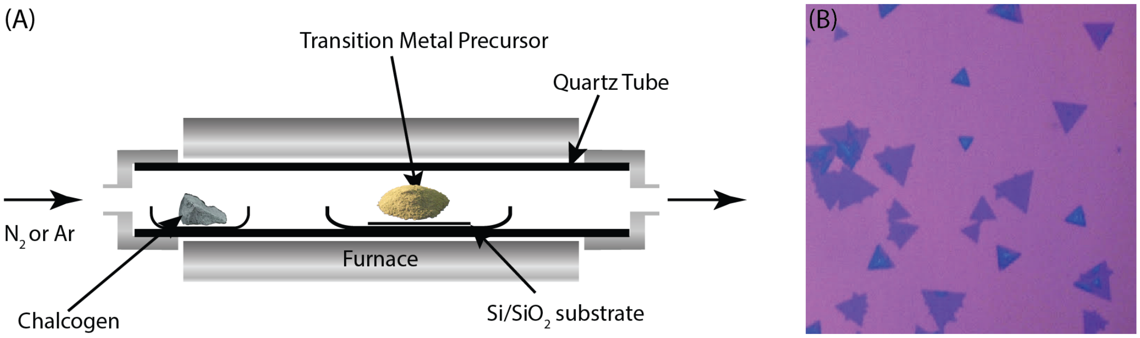

Figure 3.2: (A) Setup of the tube furnace for depositing monolayers of TMDs using the chemical vapor deposition (CVD) process. The examples materials here are raw selenium (Se) for the chalcogen and tungsten trioxide (WO_3) for the transition metal precursor, since our experiments focus on WSe_2. (B) CVD grown WSe_2 monolayers on SiO_2. The natural termination of the monolayer into a triangle is due to the underlying crystal structure and a typical size is $\sim$30-40 μm per side of the triangle.

Generally speaking, these crystals are sourced from various growers, as we do not grow them in house. During the course of this work, we purchased HOPG, natural graphite, hBN, and several kinds of bulk TMDs from HQ+ graphene, natural graphite from Manchester Nanomterials, and bulk TMDs from 2D Semiconductor. Through academic collaboration, we also received hBN from the Watanabe group at the University of Tokyo.

3.1.2 Chemical Vapor Deposition Growth

One of the drawbacks to mechanical exfoliation is that extracted monolayer flakes tend to be small in their lateral dimensions and the yield of even these small pieces is very low. It requires significant time, effort, and skill to produce just one monolayer sheet which makes the process of fabricating devices even more difficult. CVD growth of monolayers is one method that overcomes this issue. In this method, instead of thinning to one atomic unit from a bulk crystal, you grow just the monolayer sheets themselves. This method, though requiring its own set of skills, produces numerous large-area monolayer sheets at a time and does so consistently once a recipe for growth is developed.

Through our collaboration with researchers in Dr. Berry Jonker's group at the Naval Research Laboratory (NRL) in Washington, D.C., we had access to CVD grown TMDs that their group specialized in producing. An illustration of the CVD process for producing TMDs is shown in Figure 3.2(A). Referring to Figure 3.2(A), we see that a chalcogen source (S or Se) is placed upstream in a tube furnace from the metallic source (typically MoO_3 or WO_3 [164, 352]) with the desired substrates placed very close to the metallic source. During this process, an inert gas like N_2 or Ar is flushed through the tube to prevent atmospheric contamination and the furnace is heated in the range of 600-1000 °C to promote reaction between the precursors. In the gas of Se-based TMDs, hydrogen gas is used to help enhance the reactivity of Se since it is reductive by nature. The final result of this deposition is shown in Figure 3.2(B). This is simply a brief overview of the techniques involved, but for a more in-depth look at the growth of TMDs and other 2D materials, please refer to Reference [250] which is a review of CVD techniques coauthored by one of our NRL collaborators. A recipe provided by our NRL collaborators specifically for growing WSe_2 can be found in Ch. 6.3.1.1

3.2 Hexagonal Boron Nitride Encapsulation

Following the optical identification of material on the surface of the Si/SiO_2chips, the next step in fabricating a device is to "encapsulate" the 2D material between two layers of hBN. This process was originally pioneered in graphene by Philip Kim's research group in 2010 [61]. There, Dean *et al.* showed that they could achieve mobilities of

10,000 cm^2/Vs [217]. Though low by today's standards, it was extremely groundbreaking at the time and opened up the possibility of further improvement to 2D samples. In fact, within a year there were theoretical works providing predictions that graphene should be able to achieve mobilities of 1,000,000 cm^2/Vs, provided the sample is clean enough [1, 41]. The allure of achieving these high mobilities was not simply intellectual, but practical: with high mobilities comes richer physics to probe.

To understand why this encapsulation process is so revolutionary, let us consider the 2D system further. By their nature 2D materials are composed almost entirely of exposed surfaces, which means that they are strongly susceptible to environmental disorder. Early graphene devices made simply from graphene mechanically exfoliated on Si/SiO_2 had low mobilities and high disorder due to surface phonons, charge impurities native to the oxide substrate, and strain from lattice mismatch between the crystal and substrate [40, 64, 203]. The first attempt to fix this issue was to fabricate suspended graphene samples where a portion of the SiO_2 was selectively etched [27, 66]. However, these devices were extremely fragile, difficult to fabricate, and had substantial issues with strain. The advance by Dean *et al.* solved most of these problems and allowed more researchers the chance to enter the field as the work became more accessible.

While the improvement seems simple at first glance, significant work has gone into understanding the subtleties that led to improved material properties. To begin with, because graphene and TMDs are atomically thin, they tend to conform to the substrate they are placed on. On SiO_2, this can lead to a surface roughness of $\sim$0.5nm due to the amorphous structure of the SiO_2 [54]. However, results of microprobe studies have found that the roughness on hBN is $<$ 50pm, which will lead to reduced potential traps

[62, 331]. Additionally, since hBN also has a hexagonal lattice structure with similar lattice parameters to both graphene and the TMDs this greatly reduces strain induced from a lattice mismatch between the substrate and the material of interest when compared to traditional SiO_2 substrates.

The technique that evolved from hBN encapsulation can be utilized to stack just about any combination of 2D materials and led to even further developments in the field. The next step came when researchers sandwiched the hBN encapsulated structure with few-layer graphite sheets and used the graphite to electrostatically gate – i.e. control the number of free carriers – in the TMD layer [360]. Research has shown that this technique also effectively eliminated charge inhomogenity in the graphene or TMDs which further enhances the mobility [331]. We utilize this type of electrostatic gating in our devices as well, as it allows us to tune the Fermi level within our sample and probe different regions of charge interaction within the system. From there, 2D materials have become a playground for interesting physics with the addition of using twist angle between the layers to create moiré lattices with many astonishing properties from superconductivity to Mott states [34, 243, 268, 303].

In the next section, we will discuss the different techniques that can be used to perform the kind of stacking described above. There are a significant number of variations in methods for stacking with nearly every research group having their own recipes, so this section is not meant to be all-encompassing. Instead, outlined are the techniques used by this author through her doctoral research. The first several years of work performed for this thesis are nearly all encompassed by different transfer techniques. Since we were building our experiment from scratch, many different attempts were made with

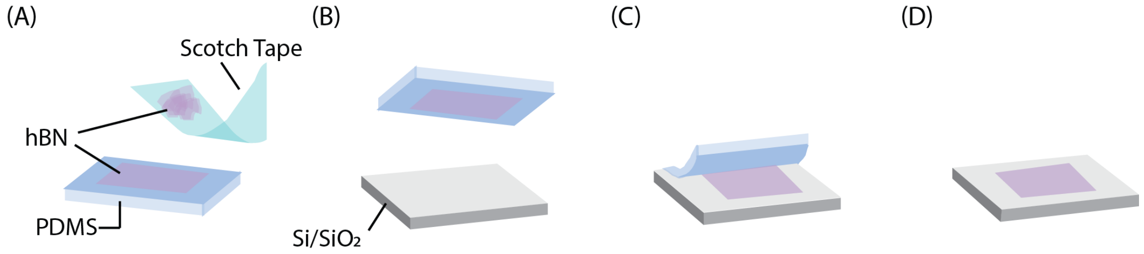

Figure 3.3: Panels (A)-(D) show chronologically the steps for creating one layer of a stack using visoelastic stamping.

different techniques before a successful method was found through expertise from and collaboration with NRL. Note that all techniques discussed below focus only on encapsulating a monolayer sheet with hBN to serve as a standard example between techniques. All techniques could be used to create more complex structures like moiré lattices or electrostatically gated samples.

3.2.1 Dry Encapsulation Techniques

Dry encapsulation techniques, as the name might suggest, refer to all techniques that do not utilize a liquid in the process. Ultimately, the polymer-based techniques with Poly(Bisphenol A carbonate) (PC) and poly(propylene carbonate) (PPC) proved to be the most fruitful in terms of dry techniques. In addition to these methods, we will discuss some earlier methods as they represent significant effort and energy by this author.

3.2.1.1 Visoelastic Stamping

Visoelastic stamping was the first method that was used in an attempt to pickup and ultimately stack 2D materials. The method was based off of work by Castellanos-Gomez *et al.* [37]. In this method, the top hBN and TMD are both directly mechanically

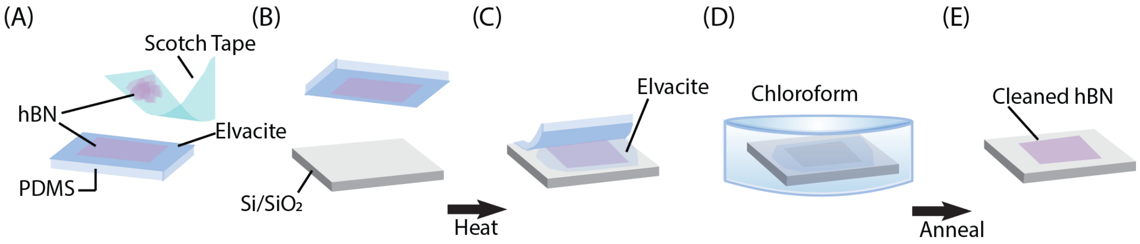

Figure 3.4: Panels (A)-(E) illustrate, in order, the process for producing one layer of an encapsulated stack using the "drop-down" method. The method must be repeated with each layer of the stack.

exfoliated onto a base polydimethylsiloxane (PDMS) stamp that is attached to a transparent glass slide. PDMS itself is also transparent, so it is possible to see straight through both the slide and stamp with a microscope. In our own adaption, to make it easier to keep track of the exfoliated material we pre-patterned the PDMS with embossed alignment marks using soft lithography – a technique commonly used in microfluidics [209, 347]. The TMD is optically aligned with the bottom piece of hBN and gently pressed down onto it and the stamp is slowly peeled back, leaving the TMD on the surface of the bottom hBN. An illustration of this can be seen in Figure 3.3. This process is repeated to place the top hBN. Because the pieces of the stack are dropped down, this is considered a bottom up method for encapsulation.

3.2.1.2 Sacrificial Polymers A.K.A the "Drop-Down" Method

Following the visoelastic stamping method, we attempted a similar method that relied on the release of a sacrificial polymer layer to drop the 2D material onto the surface of the sample. The method was originally pioneered by Zomer *et al.* and relies on an industrial resin known as Elvacite® 2550 [362]. The preparation procedure for this polymer can be found in Appendix A. Similar to the visoelastic stamping method, the 2D material is exfoliated directly onto the stamp that has been pre-embossed with alignment marks using soft lithography. However, this time the PDMS stamp has a thin layer of Elvacite® (Figure 3.4 (A)) spun onto the surface prior to exfoliation. The stamp is then loaded into the encapsulation system and aligned over the Si/SiO_2 (Figure 3.4 (B)). Because Elvacite® has a low glass temperature, it melts around 75-100°C. In order to drop the 2D layers, the Si/SiO_2 substrate is heated to about 85°C and the stamp in then gently touched to the surface and then retracted, leaving behind the 2D material with the Elvacite® melted on top (Figure 3.4 (C)). The Elvacite® is then removed in a bath of chloroform or acetone, leaving behind a clean layer of the 2D material (Figure 3.4 (D)/(E)). Between steps (D) and (E) the sample is annealed to remove residue. This process must be repeated for each piece of the stack, though Figure 3.4 shows only the process for the bottom piece of hBN. Since this method "drops" the sample using the weight of the polymer, this is also a bottom-up encapsulation process.

3.2.1.3 van der Waals Pick-Up with Heat-Expansive Polymers

The final, and most reliable dry-method used for stacking 2D materials is based on heat-expansive polymers. Both PC and PPC based polymers work in this manner and recipes for these polymers can be found in Appendix A. Cleanliness of samples is an ongoing issue in all areas of research. In order to try to expose the "functional" components of a stack (say the graphene or TMD) to as few contaminants as possible, Wang *et al.* pioneered a method that relied on vdW attraction and heat-expansive polymers [314]. This is an incredibly popular method since it reduces the introduction of contaminants

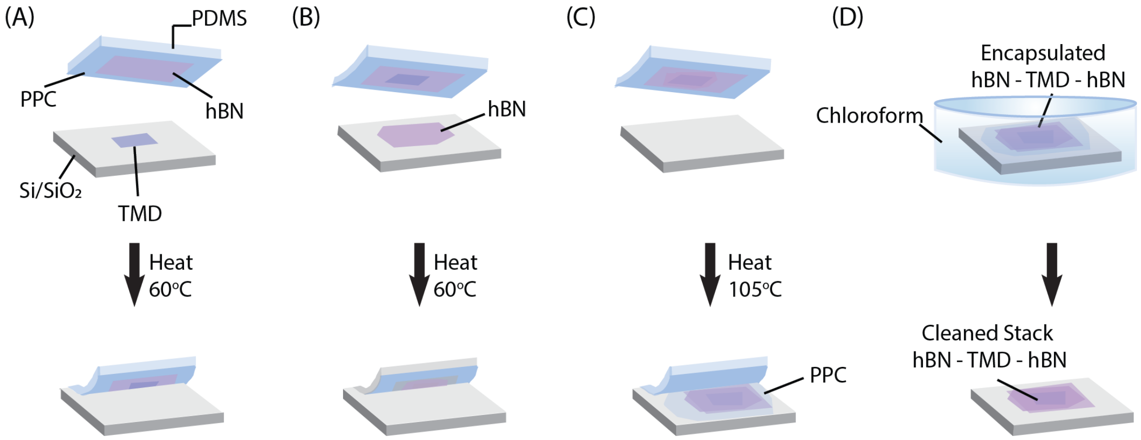

Figure 3.5: Dry pickup method for sequentially picking up 2D materials to form heterostructures with PPC.

between the constituent layers. As a result, a large of number of variations are seen in the literature with PPC as the heat-expansive polymer. This method also works with PC as the polymer as well [363].

Figure 3.5 illustrates how this dry pickup technique works with heating specifications for PPC. A PDMS stamp is adhered to a glass slide and wrapped in clear tape. A thin layer of 6-15% PPC is spin-coated on the surface of the PDMS stamp. The PDMS stamp is brought just barely into contact with the top piece of hBN and then heat is used to slowly expand the PPC polymer to pickup the top layer and then it is cooled to retract it from the surface. The target temperature for this step is 60°C, the heating rate is 2°C/min, and the cooling rate is simply based on radiative cooling after the heater is turned off. The hBN is then used to pickup the TMD via vdWs attraction using the same heating procedure (Figure 3.5 (A)). The bottom piece of hBN is picked up in the same fashion (Figure 3.5 (B)). Finally, the whole stack is dropped down onto a pre-patterned piece of Si/SiO$_2$ with gold alignment marks. This is done by heating the PPC to a higher temperature than to pickup, so that it is heated beyond its elastic limit and drops to the surface (about 105°C,

Figure 3.5 (C)). The PPC is cleaned in a chloroform bath leaving an encapsulate stack on the surface of the Si/SiO$_2$ (Figure 3.5 (D)). The procedure for picking up with PC is largely the same, except the pickup stages are done at 80°C and the final drop is done in the 160-175°C range.

3.2.2 Capillary Action Assisted Encapsulation

A problem that plagued our pursuit of high-quality samples was that CVD grown TMDs are incredibly difficult to remove from the surface they are grown on. Significant efforts were made to try to utilize the vdW method with heat-expansive polymer, but the TMD would always remain stubbornly stuck to the surface it originated on. Researchers had found many years ago with graphene that it's difficult to remove CVD grown material in general, not just for stacking. They could grow large area sheets of graphene, but were unable to remove them from the growth substrate without causing significant damage to the material.

Eventually, scientists determined that they could use a polymer spin-coated onto the surface of the CVD grown material to support it and then float the CVD grown material off after disrupting the bond between the sheet and the substrate [346]. This method became the basis for what is referred to as the "wedging transfer method" for stacking 2D materials [264]. In this method, the transfer relies on different affinities for water of the materials in the system. A thin layer of water is inserted between the hydrophilic substrate and the hydrophobic polymer that is spun onto the 2D material, allowing them to separate. However, the group found that because the material ends up free-floating on the water, it

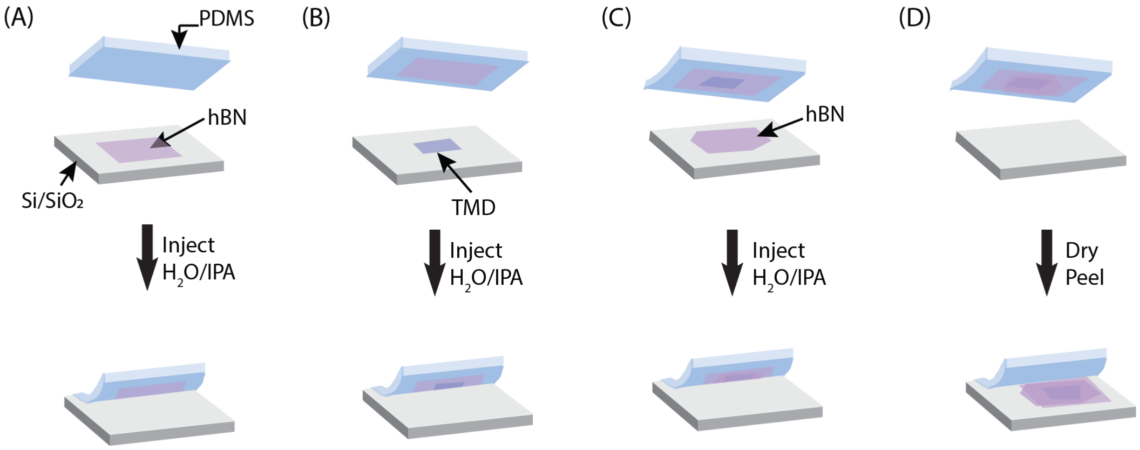

Figure 3.6: Capillary-action assisted pickup of a TMD stack using a combination of liquid injection and dry transfer.

leads to significant wrinkles and water trapped between the layers of the stack [31].

Several years later, another group showed that the same process could be achieved using heated water vapor [192]. This led to fewer wrinkles, but is very tedious to perform. However, the concept of capillary action also inspired one of our group's collaborators at NRL and led to the development of a more user-friendly fast pick-up method that only relies on a very small amount of liquid [101]. Dr. H.-J. Chuang was kind enough to give us a tutorial on his method, the process of which is outlined below.

On this capillary-action assisted pickup method, we start with a bare piece of PDMS. Since the hBN is in direct contact with the PDMS it is important that you use a very clean piece of PDMS. It is recommended that you use homemade PDMS made with Sylgard 184 (182 can also be used, a recipe can be found in Appendix A) instead of purchased, pre-made PDMS. The PDMS is brought gently into contact with the to top piece of hBN and approximately 1dL of a mixture of deionized (DI) water/isopropanol (IPA) is injected between the PDMS and the substrate using a syringe. The PDMS is then retracted with the hBN attached and the sample is gently dried with N_2 (Figure 3.6 (A)). Similar to the vdW method, the process is then repeated to pickup the TMD and the bottom hBN (Figure 3.6 (B)/(C)). Finally, the whole stack is brought into contact with a Si/SiO$_2$ substrate with alignment markers and then gently peeled back without the DI water/IPA, leaving the final stack on the substrate (Figure 3.6 (D)).

3.2.3 Comparison of Encapsulation Methods

We worked with the visoelastic stamping method for a short period of time. It proved to be very difficult in our setup to get TMDs and hBN to detach from the PDMS stamp like Castellanos-Gomez, *et al.* were able to, which may have been influenced by the soft lithography we had perform as it could leave residues on the surface of the PDMS. The yield of larger 2D pieces from exfoliating directly onto PDMS is also very low, which was a problem with the "drop down" method as well.

In terms of cleanliness, there were a variety of issues. One of the main reasons that we abandoned the "drop down" method with Elvacite® was the residue that was left behind. No matter the cleaning process, there always seemed to be white, chalky residue that was left on the surface of the sample. We believe this residue was likely a result of the temperatures needed to melt the Elvacite that cause it to completely break down. Moreover, since the process needed to be repeated for each layer, with the sacrificial polymer melted on top of the 2D material each time, there is a large amount of contamination introduced at each step. Large spots of residue that could not be removed in the solvent bath or through high-temperature annealing remained and caused bubbles/wrinkles at each step.

While the procedure for performing pickup is roughly the same for both PC and PPC, there are differences in their functionality. Because the elastic limits of PPC is lower than that of PC, it tends to come off more cleanly during the chloroform cleaning and not leave as much residue on the sample. The residue is an important factor (which we will discuss further in a later subsection of this chapter) and can greatly influence the quality of the sample. However, PC has a desirable quality that PPC does not: it picks up TMD or graphene/graphite not directly underneath the hBN and leave edges exposed. Making 1D contact is notoriously difficult in graphene and nearly impossible with TMDs due to the barrier potential on these edges. Therefore, especially in TMDs, it can be desirable to leave enough of the functional material to make 2D contact. PPC only allows for pickup of material that is directly underneath of the top layer so it is largely useful for making samples that only require optical measurement. Recipes for both polymers can be found in Appendix A.

Ultimately, the samples used in our experiments were made by our collaborators in Berry Jonker's group at NRL. Though countless samples were produced in-house using the techniques above, they were not showing the same consistent quality as those produced at NRL. Those samples were produced using the capillary-action assisted method. Generally speaking, this is a very clean process since it does not rely on any sort of polymer and there is no heating. However, additional care must be taken to make sure that the PDMS is sufficiently clean and thin, as this can lead to poor pick-up and contamination. A sample specific overview of this process can be found in Ch. 6.3.1.2.

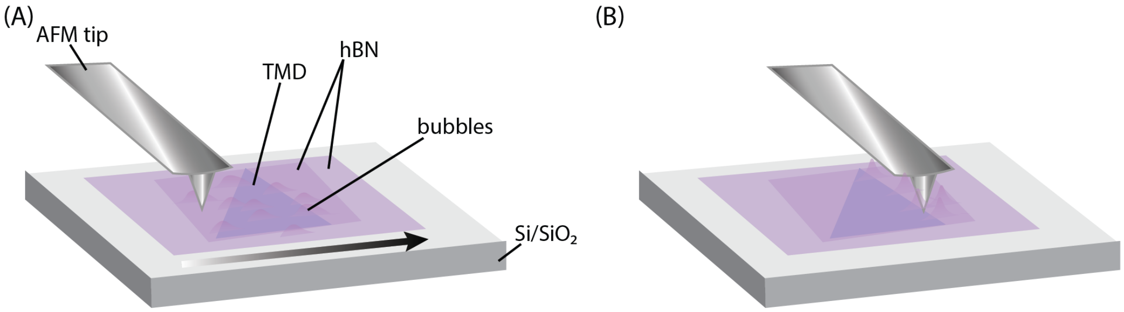

Figure 3.7: Panels (A) and (B) show the nano-squeegee process whereby the bubbles that can appear during encapsulation can be flattened out using the force of the AFM tip. Figure is adapted with some modification from Ref. [255].

3.3 Sample Flattening via Atomic Force Microscopy A.K.A "Nano - Squeegeeing"

As we recall from Section 3.2, the purpose of encapsulating graphene, and later TMDs, was to increase the quality of the sample through reducing charge inhomogeneities, strain, etc. Encapsulating a sample goes a long way to improving sample quality, but it can also introduce new contaminants during the process. Though the vdW pickup methods don't have the active layer in direct contact with the polymer, there is often an extremely thin, uniform layer of contaminants between each layer of the stack and wrinkles and bubbles with additional contaminants can form as well [31, 99, 253]. Some groups will annealing to try remove contaminants through evaporation, but the technique is not well controlled or predictable [8, 329]. Sometimes it can even lead to the destruction of the sample, not an improvement.

Enter the concept of the nano-"squeegee." Through our group's collaboration with scientists at NRL, we became aware of a technique that they pioneered to flatten samples and remove contaminants [255]. An illustration of this method can be seen in Figure

3.7. In essence, the method is very simple: one simply uses an AFM in contact mode to line-by-line push the material out from between the layers using the force of the tip.

There are a few experimental parameters that are important to success. Generally speaking, “soft” AFM tips with a low spring constant are generally used for contact mode scans. Since the tip is deflected from the surface in this mode, springier tips help protect the sample and keep the tip from cracking under the pressure. Rosenberger *et. al* found that it takes about 100 nN of force to flatten a monolayer of a TMD, while flattening an encapsulated stack required more than 1000 nN of force. Since flattening a stack requires a significant amount of force non-traditional, stiffer tips (spring constant (k) of about 40 N/m) proved to be neccessary in order to perform adequate flattening. Additionally, the radius of an AFM tip is nominally 10 nm. In order to ensure the overlap between subsequent passes with the AFM tip, the resolution of the scan needs to be about the same. Otherwise, you will leave space in between each pass and have pocketed lines of residue instead of removing it out of the edges of the sample altogether.

Since the development of this technique by the group at NRL, other researchers have adopted this technique as well. A recent study suggests that the process can introduce charge traps that lead to dominant trion features even at zero bias [114]. They also found that the addition of a few-layer graphite cap (gate) on the surface of the hBN during the squeegee process allows these charge traps to disperse and the dominant trion feature at zero bias disappears. It should be noted that all samples made in our collaboration with NRL featured a graphite gate due to experimental design needs that allow us to control the strength of charged features.

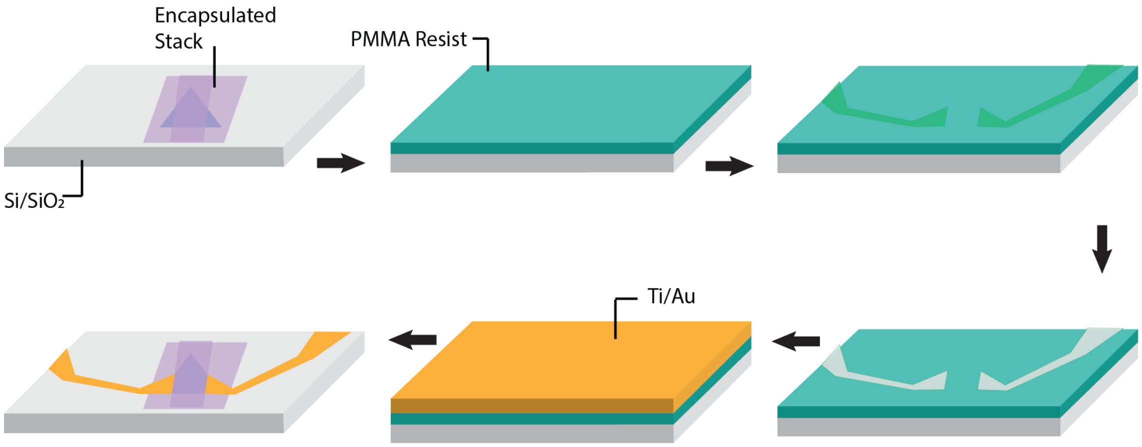

Figure 3.8: EBL process for defining electrical contacts on a sample.

3.4 Lithographic Processing

Once the 2D material has been encapsulated in hBN and/or gated, it is common to perform some sort of lithographic processing like etching or making electrical contact. Much like a snowflake, each stack is unique due to the random nature of the constituent flakes. This makes a more sophisticated technique, electron-beam lithography (EBL), a more practical choice for this process over, say, photolithography since it allows us to tweak each pattern to fit the sample without having to send out for a new mask.

3.4.1 Electron-Beam Lithography

The premise of EBL is similar to photolithography, but due to the fact that electrons have a much smaller wavelength than light, the user is able to achieve much finer control over the features they pattern. Like photolithography, the patterning process hinges on the use of an energy sensitive polymer (in our case, we use polymethyl methacrylate (PMMA) 950A4) that is spin-coated in a uniform layer onto the sample. After the polymer is cured to remove an adequate amount of solvent (per the instructions provided by the manufacturer), the sample is loaded into an EBL machine. These machines operate similarly to a scanning electron microscope (SEM), except they are also outfitted with an electron gun capable of delivering a certain "dose" of current (μC/cm^2) to the sample selectively through use of a finely calibrated stage that can move in x and y. This patterning is controlled through use of a CAD file. The electrons delivered to the polymer break up the bonds, but only where they interact. After the bonds are broken, these areas will preferentially wash away in a chemical referred to as a developer. Resists that work this way leave a positive image of what you have "written" with EBL down to the bare substrate, with the rest of the sample remaining covered in polymer until such time as it is removed with a different solvent; they are aptly named positive resists. It is also possible to purchase a negative resist, where the area written remains after development instead.

Figure 3.8 shows the total EBL process for defining electrical contacts. The example illustrated is for direct contact to a TMD that has the edges exposed after encapsulation. First, you begin with a stack of 2D materials and then spin on a thin coat of PMMA and cure the PMMA per manufacturer instructions. Next, the correct e-beam dose is delivered in the pattern of the contacts, and then developed to remove the exposed PMMA all the way down to the substrate. A thin metallic film – typically either Ti/Au or Cr/Au – is then deposited onto the sample. Post-deposition, the sample is placed in a solvent to "liftoff" the Ti/Au after deposition, leaving behind metal only in the areas that were exposed. This is the basic process for creating all devices. More details and recipe information can be found in Ch. 6.3.1.3.

Chapter 4: Measuring Light-Matter Interaction

4.1 Overview

The goal of this section is to briefly introduce the experimental measurement techniques used within this work.

4.2 Optical Measurement Techniques

Throughout this work, we utilized optical measurements. Though there are merits to performing transport measurements, in our system there are distinct advantages to using optical techniques. TMDs tend to have poor mobility ($\approx$ 100-1000 $\mathrm{cm}^2\mathrm{V}^{-1}\mathrm{s}^{-1}$, in contrast to graphene which has an upward limit of $\approx$ 200,000 $\mathrm{cm}^2\mathrm{V}^{-1}\mathrm{s}^{-1}$ when free-standing), which makes transport difficult. Poor mobility does not prevent light from creating optical excitations though, which circumvents that signal issue in transport. Optical measurements inherently give us the ability to selectively interact with the two valleys by choosing the polarization of the light used for excitation. Comparing the response from the two valleys gives us information about carrier dynamics in state formation, leaving a rich area of physics to explore in this manner. In the following subsections, a we'll provide brief overview of the measurement techniques used in this work as a primer for

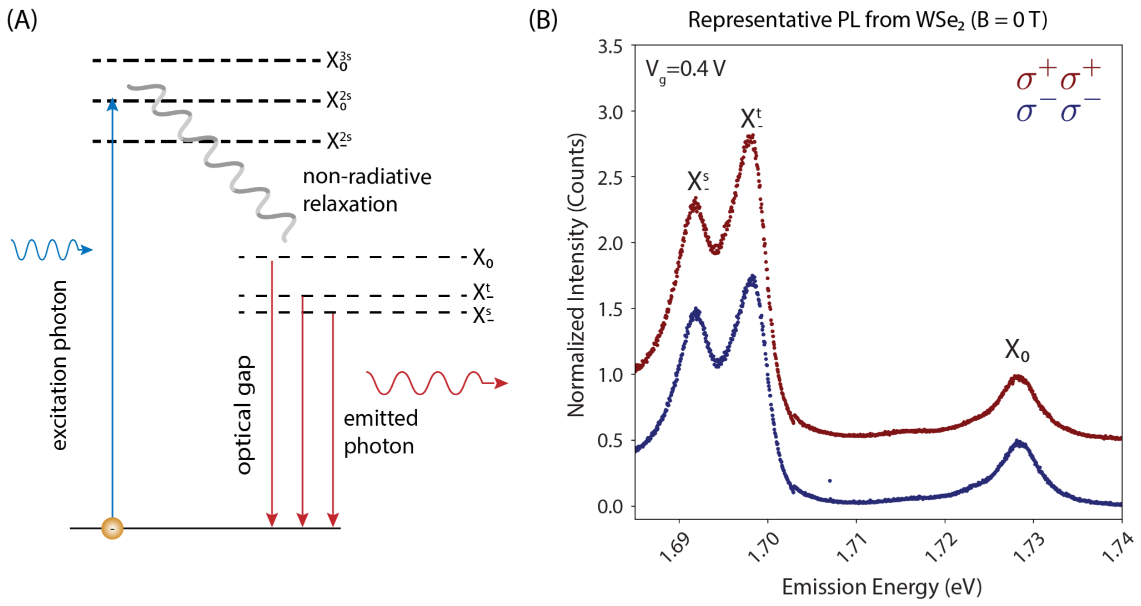

Figure 4.1: Panel (A) shows a diagram representing the energetics of the photoluminescence (PL) process and panel (B) shows a typical PL emission spectra for WSe_2 with labels denoting the different exciton species emission origins.

understanding later experimental results in Ch. 6.

4.2.1 Photoluminescence Measurements

The most common measurement technique we use is photoluminescence (PL). The PL process is outlined in Figure 4.1 (A). A photon is used to excite an electron from the valence band and create a quasiparticle (e.g. exciton or polaron). The electron then has a chance to non-radiatively decay into other, lower energy configurations. Eventually, the electron drops back into the valence band and radiatively recombines with the hole it left behind. These emitted photons can be counted as a function of their energy with a spectrometer and produce a spectrum like that in Figure 4.1 (B). Figure 4.1 (B) is real data from one of our WSe_2 samples under selective excitation and measurements of the ±K valleys. We see here the neutral exciton-like state, X_0, and the singlet and triplet trion-like states, $\mathrm{X}_{-}^{\mathrm{s}}/\mathrm{X}_{-}^{\mathrm{t}}$, which are prominent since we have electrostatically electron doped the system (V_{g} = 0.4 V). A nice feature of this technique is the non-radiative relaxation inherently involved makes it easier to observe exciton species with lower oscillator strengths that can be obscured in techniques like reflectivity.

4.2.2 Photoluminescence Excitation Measurements

As the name would suggest, photoluminescence excitation (PLE) is very similar to PL. Sometimes referred to as resonant PL, the main difference between the techniques is instead of using just one excitation energy (PL), we collect many spectra as a function of a range of excitation energies (PLE). In this scheme, the photon is used to excite an electron from the valence band to a higher energy state. There, it undergoes non-radiative relaxation from an higher energy state (e.g. $\mathrm{X}_0^{2\mathrm{s}}$) to a n=1 state (e.g. X_0, $\mathrm{X}_{-}^{\mathrm{t}}$, or $\mathrm{X}_{-}^{\mathrm{s}}$) and then radiatively recombines with the $n = 1$ emission channels monitored. Fig. 4.2(A) provides an illustration of this process. We can indirectly monitor higher energy states that have a lower radiative oscillator strength, which is what makes this technique particularly useful. Unlike reflectivity, because it involves relaxation it can also give information on decay branching ratio from higher n states.

Since these plots can be less intuitive to read, an illustration of how this works is shown in Figure 4.2 (B). Here, the cooler color indicates low intensity and red indicates the highest intensity of emission. Generally speaking, when the excitation energy is resonant with the optical gap of an exciton species, this state becomes very highly populated. If a non-radiative decay channel exists to a lower, monitored state we can expect that

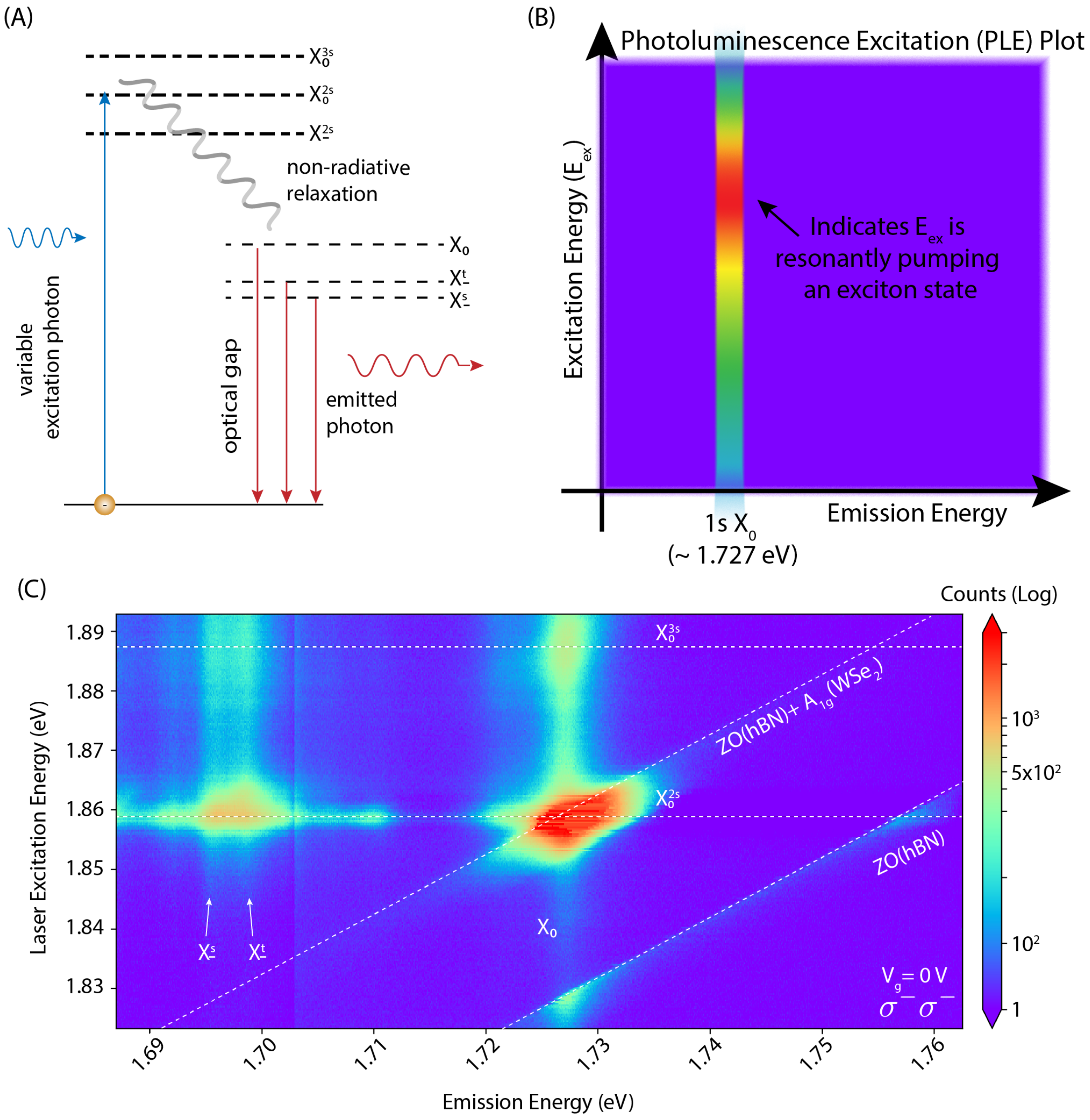

Figure 4.2: Panel (A) shows the diagram representing the energetics of the photoluminescence excitation (PLE) process. It is similar to PL, but the excitation wavelength is varied in this case. Panel (B) shows a diagram of the expected PLE plot, indicating emission to the lowest state from a resonantly excited state, and panel (C) shows a typical PLE emission spectra for WSe_2 in the $2s$ energy region.

the increase in population in the resonantly excited state will lead to an increase in the population of the monitored state. Thus, when we resonantly excite a state, the intensity from the monitored emission state increases dramatically (see the red spot in Figure 4.2 (B)). With an understanding of how this process works in theory, we can see a real example of this process in WSe_2 in Figure 4.2 (C). Here, we are exciting in the $2s$ energy region and monitoring $1s$ states. The resonantly excited states (X_0^{2s},X_0^{3s}), monitored decay channels (X_0, X_-^t, or X_-^s), and Raman modes are all marked. This spectra is related to the work in Ch. 6 and will be discussed in greater detail there. It serves as an excellent illustration of the power of this technique for studying higher n states.

4.3 Experimental "Knobs"

Below is an outline of the experimental "knobs" in the system used in this work. That is, what can we change easily in an experiment to investigate the phenomena of interest and what effect does that "knob" have. Note there are other "knobs", such as temperature dependence and spatial resolution, but they are not used in this body of work.

4.3.1 Light Polarization

This is the simplest parameter in our system. If we recall Ch. 2.2, one of the interesting properties of TMDs is that the populations of the two valleys are preferentially accessed with LCPL and RCPL. This allows us to access the population of one valley at a time and contrast their behavior under other applied conditions. Polarization selective excitation is easily achievable in the lab by passing linearly polarized laser light through a

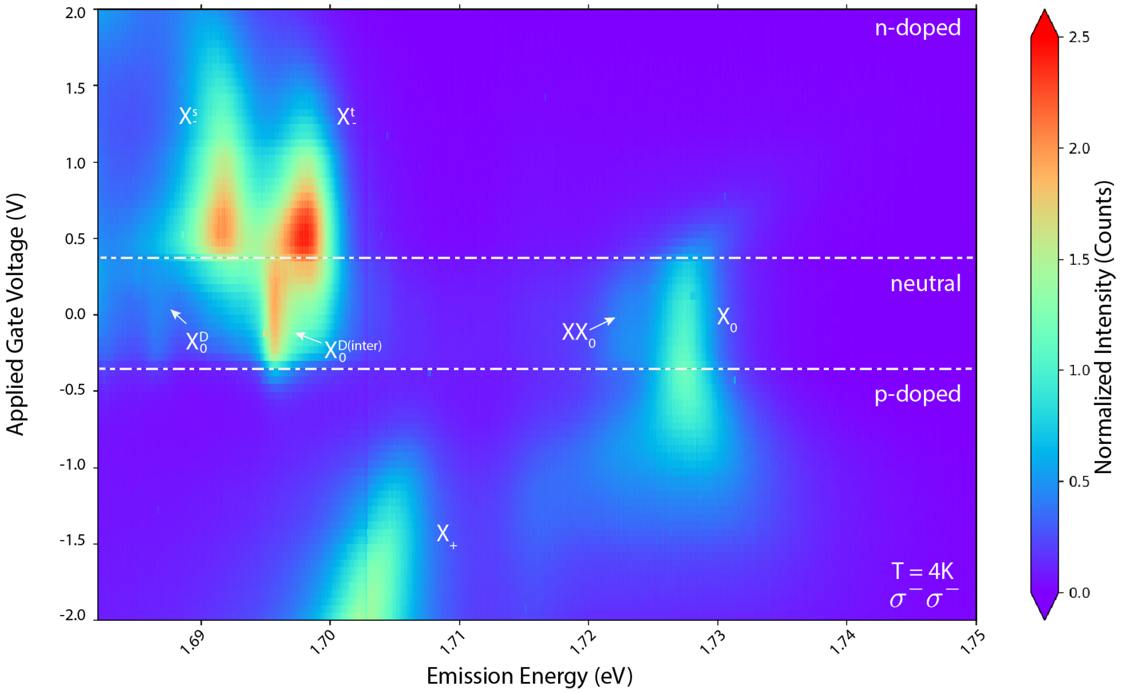

Figure 4.3: PL measurement of the gate response in a representative sample of WSe_2.

quarter-wave plate; theoretically the degree of polarization should be 100%, but typically lab experiments realize ≈20-70%. This, is generally enough to extract valley dependent behavior. .

4.3.2 Electrostatic Gating

Electrostatic gating allows us to tune the Fermi level in our sample and investigate different doping regimes. Note that frequently the term “doping” is used in the semiconductor field to refer to atomic substitution in the lattice to increase the number of donor/acceptor state (depending on the dopant). However, here we will use it to refer to excess electrons and hole introduced through electrostatic gating. In Ch. 2.3 we discussed the formation of both single-particle (trion) and many-body (attractive/repulsive polaron) states that are the result of excess charge in the system. With the use of an electrostatic gate, we can tune the sample to the “neutral” region (intrinsic doping of electrons/holes only) and observe the exciton strongly. Or, we can pull the Fermi level into the conduction (valence) band and introduce excess electrons (holes) into the system and promote the formation of trions/polarons. This type of gating allows us to focus our study on either neutral or charged exciton species by promoting their respective formation by varying the Fermi level.

In order to make sure that the sample is functioning correctly and that this electrostatic gating process is working, one of the first measurements is a PL sweep as a function of the back gate voltage. A representative spectra of what we are looking to see in a high-quality, working WSe_2 sample is shown in Figure 4.3. In this spectra, all the data has been normalized by the $1s$ exciton peak at V_g = 0 V, and the white dashed lines divide the spectra into three regions: neutral, n-doped, and p-doped. We will discuss this type of electrostatic characterization in much greater detail in Ch. 6.

4.3.3 Magnetic Field (Zeeman Effect)

The Zeeman effect, discovered by Pieter Zeeman in the late 1890s, describes the splitting of atomic transitions based on their angular momentum when a magnetic field is applied [343]. When we performs spectroscopy on a material in the presence of no magnetic field, all of the fine structure is degenerate and hidden (Figure 4.4(A)). However, Zeeman found that when a magnetic field is applied, there were more optically bright transitions observed. It would take another couple of decades and the advent of quantum

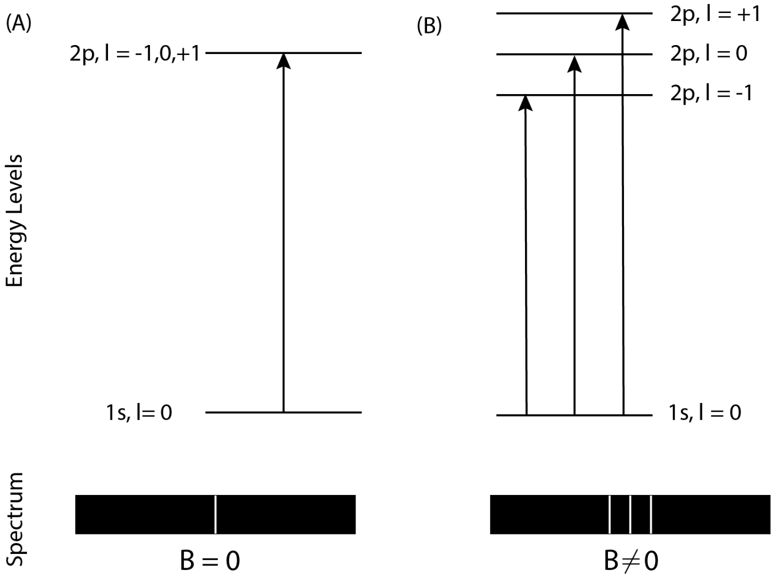

Figure 4.4: Visual representation of the effect of applying a magnetic field and observing the splitting of different angular momentum states (the Zeeman effect).

mechanics to understand the origin of the splitting. This splitting occurs because when electrons move around their nuclei in an atom they generate a magnetic field with a magnetic moment. The magnitude of this magnetic moment is determined by which orbitals the electrons originate from. When an external magnetic field is applied, the field does work on this moment to align it. This work changes the energy of the affected state as a function of the field and the change in energy is directly proportional to how much work it takes to perform the alignment.

Importantly for us, the application of a magnetic field is a friend to those performing spectroscopy. The splitting of states by magnetic field allows one to observe energetically bunched states more easily, and the evolution with the amount of field applied can tell us something of the character of the state itself and even quantify the degree of many-body interaction in the system. In the next chapter, we will dived heavily into the specifics of this and look at a comparison of the effect in 3D with the unusual case of valley dependent

Zeeman splitting in TMDs. The phenomenon is discussed further in Ch. 5.

4.3.4 A Note on Measurement Energies

Many of the "knobs" discussed can result in a change in the emission energy of different excitonic states in TMDs. In the literature, it is common to see the absolute energy of any particular state (ex. exciton, dark exciton, etc.) has a wide variety of reported values. This is simply a function of different sample parameters, like dielectric environment and stress. The most reliable metric is the relative spacing in energy between features. For example, the dark exciton and bright exciton are separated in energy by the spin-splitting in the conduction band, which is a more fundamental quantity. Thus, in our own work, we rely on the relative position of features to help us determine their origin more than the absolute value for the energy of any given signal.

4.4 Measurement Specifications

A full diagram of the dilution unit with the optical setup is provided in Fig. 4.5. There were two different excitation sources used throughout the main manuscript and the supplemental information. For PLE measurements in the main text, a dye laser with 4-(Dicyanomethylene)-2-methyl-6-(4-dimethylaminostyryl)-4H-pyran (DCM) dye and pumped with a 2.33 eV (532 nm) green laser was used to access a dynamic range from 1.92-1.75 eV. The dye laser was also utilized for PL measurements of the $1s$ state, while for PL measurements accessing both the n=2 and ground states a 2.33 eV green diode laser was used. As with the PLE measurements in the main text, all supplemental

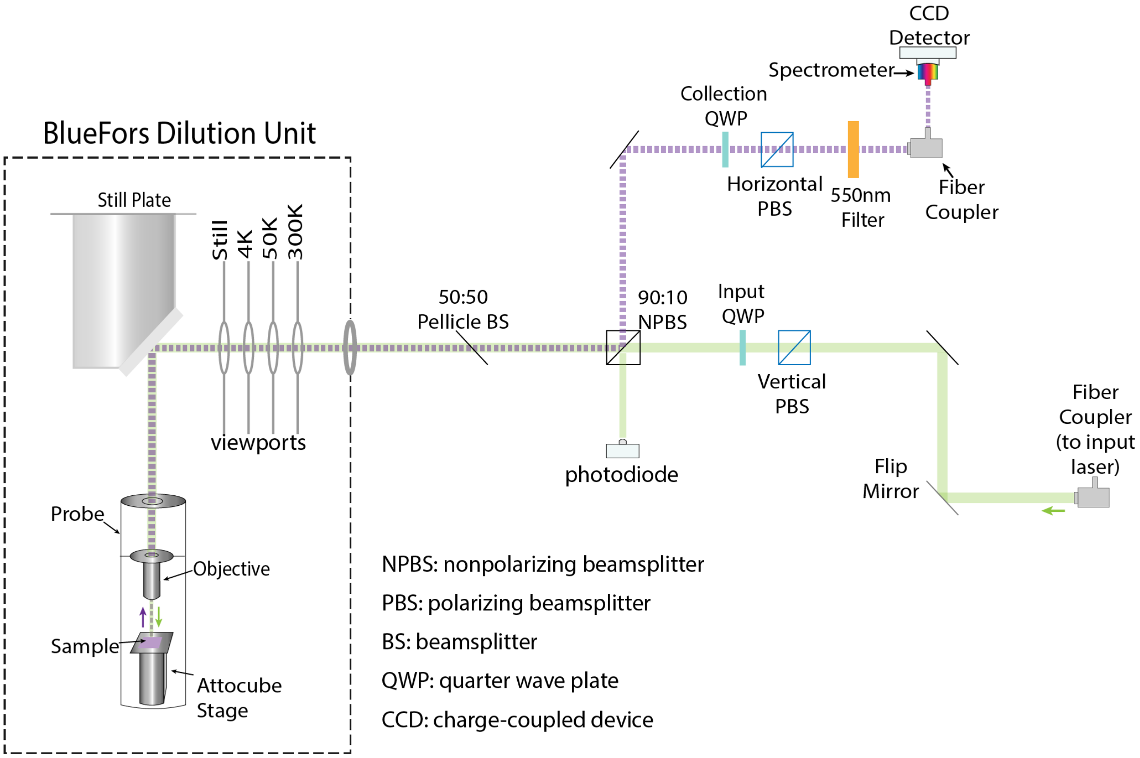

Figure 4.5: Optical diagram depicting the excitation and emission collection scheme used for photoluminescence and photoluminescence excitation measurements. Figure is taken from our own work [266].

measurements were also performed in the confocal configuration and Faraday geometry.

The system is equipped with a 12 T superconducting magnet and the PL/PLE measurements were performed in Faraday geometry. We estimate that with residual heating from the laser and magnet, the ambient temperature of the sample is $<$300 mK.

Chapter 5: Understanding Exciton Dynamics Under Applied Magnetic Field in Transition Metal Dichalcogenides

This chapter serves as a reference for understanding the effect of magnetic field on exciton fine structure in TMDs. We will focus mainly on the Zeeman effect, which is important for understanding the results of Ch. 6, but will also touch on some other high field effects in TMDs. First we will look at the Zeeman effect in the hydrogen atom, since there are many similarities between excitons and the hydrogen atom. Next we will review the single-particle model for predicting g-factor in TMDs. Then we will look at the effects of many-body correlation on the g-factor of polaronic particles. Finally we will briefly touch on some other magnetic field effects that can compete with the Zeeman effect at higher fields and discuss whether we need to consider them in our work.

5.1 The Hydrogen Atom

5.1.1 The (Normal) Zeeman Effect

The Zeeman effect is conceptually simple: energy bands in both atoms and crystals have magnetic moments associated with them that arise from the magnetic field produced by electrons moving around their respective nuclei at high speeds. When an external magnetic field is applied, that field will do work on the atom to try to align its magnetic moment with the field. This work results in an energy shift of the underlying bands as the magnetic field is increased. It follows that this energy shift scales with the magnetic moment since larger magnetic moments will require more work to align with the applied field. As we recall from Ch. 2.3, an exciton is similar in many ways to the hydrogen atom. Thus, understanding the Zeeman effect in hydrogen is an excellent starting point for our discussion.

We begin by constructing the Hamiltonian that describes a single hydrogen atom subject to a perpendicular magnetic field. The magnetic dipole moment for the electron spin and orbital motion are, respectively,

$$\vec{\mu}_{\mathrm{s}} = -\frac{e}{m_{\mathrm{e}}}\vec{S} \tag{5.1a}$$

and

$$\vec{\mu}_{\mathrm{l}} = -\frac{e}{2m_{\mathrm{e}}}\vec{L}. \tag{5.1b}$$

The Zeeman Hamiltonian is then,

$$\begin{aligned}\vec{\mathcal{H}}_{\mathrm{Z}} &= -(\vec{\mu}_{\mathrm{l}} + \vec{\mu}_{\mathrm{s}}) \cdot \vec{B}_{\mathrm{ext}} \\ &= \frac{e}{2m}(\vec{L} + 2\vec{S}) \cdot \vec{B}_{\mathrm{ext}}.\end{aligned} \tag{5.2}$$

Recall that the general Hamiltonian for the hydrogen atom is,

$$\vec{\mathcal{H}}_{\mathrm{H}} = \vec{\mathcal{H}}_{\mathrm{Coulomb}} + \delta\vec{\mathcal{H}}_{\mathrm{fine-structure}}. \tag{5.3}$$

Here, the term fine structure refers to interactions such as spin-orbit coupling and relativistic corrections. The spin-orbit coupling is of particular interest because it arises from the effective internal magnetic field that the electron sees from the nucleus. This implies that we actually have *two* magnetic fields at play: the *internal* magnetic field from spin-orbit interaction and the *external* applied field. How we proceed in our treatment depends on which field is dominant. Here, we will treat the weak-field Zeeman effect where $\mathrm{B}_{\mathrm{ext}} \ll \mathrm{B}_{\mathrm{int}}$, since that is most relevant to the observed Zeeman effect in TMDs. At the end of this section, we will briefly discuss some general high field effects.

Since we assume that we are in the weak-field regime, we can evaluate the Zeeman Hamiltonian using first order perturbation theory. Recall, that under first order perturbation theory the energy correction is given as,

$$E^{(1)} = \left\langle \psi \,\middle|\, \mathcal{H}_{\mathrm{perturb}} \,\middle|\, \psi \right\rangle , \tag{5.4}$$

where $E^{(1)}$ is the first-order energy correction to the eigenstate $|\psi\rangle$ resulting from the perturbation to the system. Assuming that our applied field is along $\hat{z}$, for hydrogen we can rewrite Eqn. (5.4) as,

$$E^{(1)}_{n,l,j,m_{\mathrm{j}}} = \frac{eB}{2m} \left\langle n, l, j, m_{\mathrm{j}} \,\middle|\, L_z + 2S_z \,\middle|\, n, l', j, m'_{\mathrm{j}} \right\rangle . \tag{5.5}$$

Here n is the principle quantum number, l is the azimuthal (angular momentum) quantum number, j is the total angular momentum in the system, and m_{j} is the projection of j along our axis of choices ($\hat{z}$). These are the “good” quantum numbers in our system. Note that

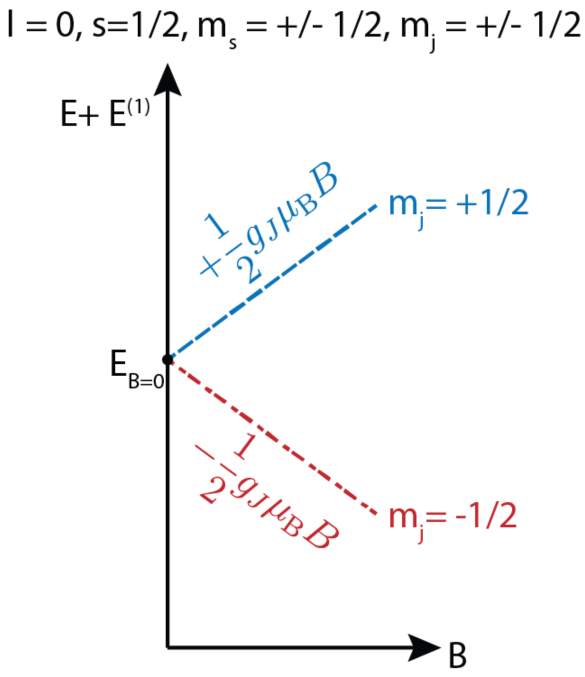

Figure 5.1: Detailed illustration of the Zeeman effect in hydrogen for the ground state.

because of the assumed presence of spin-orbit interaction, the magnetic quantum number m_l and the spin quantum number m_s are not conserved, but their combined total m_j is.

After some algebraic massaging we find the solution,

$$\begin{aligned} E^{(1)}_{\mathrm{n,l,j,m_j}} &= \frac{e\hbar}{2m_{\mathrm{e}}} B g_{\mathrm{J}}(l) m_{\mathrm{J}} \\ &= \mu_{\mathrm{B}} B g_{\mathrm{J}}(l) m_{\mathrm{J}}. \end{aligned} \tag{5.6}$$

Here, $\mu_{\mathrm{B}} = 0.05788$ meV/T is the Bohr magneton and $g_{\mathrm{J}}(l)$ is the Landé g-factor. The Landé g-factor will be discussed in detail later in this chapter, but it essentially represents how much work the magnetic field must do in order to align the magnetic moment of the energy level with the direction of the applied field. Full derivations of the energy correction due to the weak field Zeeman effect in hydrogen and of the Bohr magneton can be found in Appendix B. Figure 5.1 shows a visual representation of the consequences of

Eqn. (5.6) for the ground state of hydrogen. In panel (A) we see the transitions between the $1s$ and $2p$ states. If no field is applied, the three energy levels with different m_l (and hence different m_j) for the $2p$ are degenerate with energy $E = E_{-10}, E_{00}, E_{10}$. If we apply a magnetic field, the Zeeman effect breaks the energetic degeneracy and we can observe three distinct levels each with different m_l, which is shown in panel (B).

5.1.2 Landé g-factor

The Landé g-factor (hereafter referred to just as g-factor) is an important quantity of interest in this chapter, as it can provide a fingerprint for different exciton species and be used as a barometer for many-body interaction. In an atomic system, like the hydrogen atom, the g-factor arises from the internal configuration of the angular momentum and is written as,

$$g_J = 1 + \frac{j(j+1) - l(l+1) + \frac{3}{4}}{2j(j+1)}. \tag{5.7}$$

A full derivation for the g-factor can be found in Appendix B.

5.2 The Zeeman Effect in Transition Metal Dichalcogenides

Now that we have a basic understanding of the Zeeman effect, we need to look at how it manifests in our 2D system. In this section, we will explore the single-particle expectation, g-factor enhancement in the many-body regime, and the high field limit.

5.2.1 Single Particle Model

We begin our discussion of the Zeeman effect in TMDs in the single-particle regime, focusing on the exciton. In contrast to the hydrogen atom, excitons exist in a crystal lattice and the resulting Zeeman splitting is from the magnetic moment contributions from the underlying band structure. Again, we can treat the Zeeman effect as a perturbation in our system and look at the change in energy due to applied field in each valley,

$$\delta E_{\pm\mathrm{K}} = -(\vec{\mu_c} - \vec{\mu_v}) \cdot \vec{B} \tag{5.8}$$

$\mu_{c/v}$ are the magnetic moments of the conduction and valence bands the electron and hole reside in, respectively. In TMDs, the total Zeeman splitting is defined as the difference in splitting between the two valleys (we assume a field along $\hat{z}$):,

$$\Delta E_{\mathrm{Z}} = E_{+\mathrm{K}} - E_{-\mathrm{K}} = -[(\mu_{+\mathrm{K,c}} - \mu_{+\mathrm{K,v}}) - (\mu_{-\mathrm{K,c}} - \mu_{-\mathrm{K,v}})]B_z. \tag{5.9}$$

$\mu_{c/v}$ each have underlying contributions from μ_s and μ_l so it is helpful to evaluate Eqn. 5.9 in this context. A visual representation of the contributions in each valley is shown in Fig. 5.2. To evaluate these components, we will first use an “atomic” perspective that relies on basic spin/orbital band configurations.

Beginning with the spin component μ_s, we see in Fig. 5.2 that for a bright transition in each valley, both the valence and conduction bands have the same spin associated with them. This means that μ_s will shift the energy of each band by the same amount, resulting in $\mu_{s,c} - \mu_{s,v} = 0$ for the bright exciton in each valley.

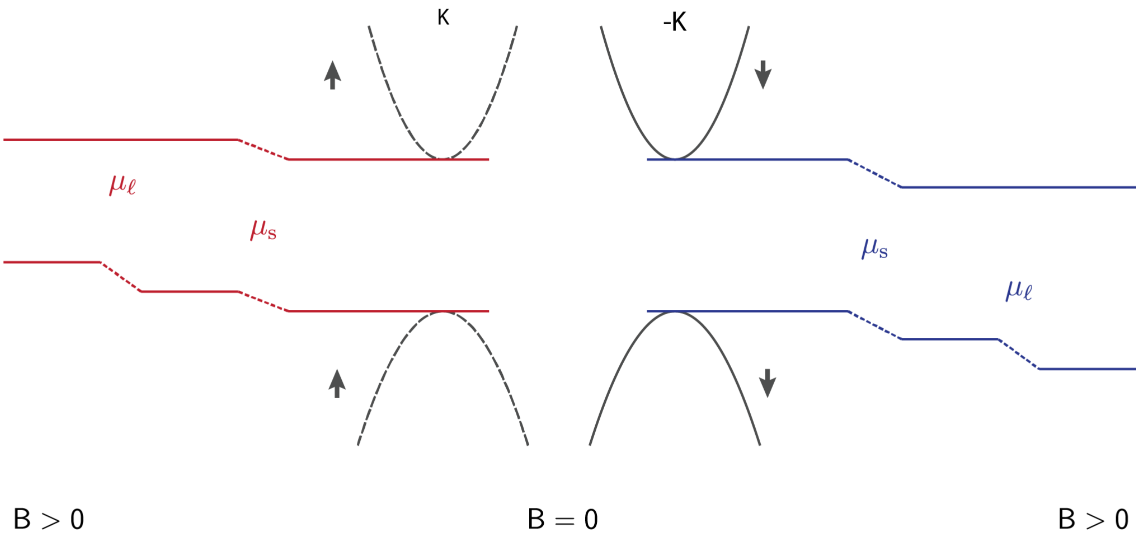

Figure 5.2: Zeeman splitting for excitons in TMDs in the single-particle model. Here, only the bands for the A series bright exciton are shown. Note that if the applied field was negative, we would expect the K-valley to blue shift and the -K-valley to red shift instead.

Next we look at the orbital component μ_l. The value μ_l for the valence and conduction bands can be estimated based on which bonding orbitals contribute to the formation of the band. For WSe_2, Liu *et al.* showed that the K-valley conduction band is made primarily of d_{z^2} orbitals which have $m_l = 0\ \mu_B$, while the valence band is dominated by $d_{xy} + d_{x^2+y^2}$ orbitals, which have $m_l = \pm 2\ \mu_B$ [186]. Using this as an estimate, they find that for the K-valley, m_l = -2 μ_B. K/-K are a time-reversed pair ($\mu_{K,c/v} = -\mu_{-K,c/v}$), which implies that m_l = +2 μ_B in the -K valley. Putting all the contributions together, we get

$$\begin{aligned} \Delta E_Z &= -((\mu_{l,+K,c} - \mu_{l,+K,v}) - (\mu_{l,-K,c} - \mu_{l,-K,v}))B_z \\ &= -((0\ \mu_B - -2\ \mu_B) - (0\ \mu_B - 2\ \mu_B)) \\ &= -4\ \mu_B B_z. \end{aligned} \tag{5.10}$$

Thus, the expected g-factor in the single-particle model for the bright exciton is g=-4.

5.2.1.1 Intercellular Component Correction

Experimentally, many groups observed small deviations from the expected g=-4 value within their work [2, 12, 140, 172, 193, 289, 292] in both $1s$ and higher Rydberg states. It was proposed throughout many of these works that the discrepancy could be attributed to orbital magnetic moment that arises due to the finite Berry curvature in the system [2, 44, 140, 172, 193, 289, 292]. This term is generally called the *intercellular* or *valley* contribution. We can calculate the valley orbital magnetic moment using a multi-band (>2) tight-binding Hamiltonian [186, 289] using the following relation:

$$L_n(k) = i\frac{m}{\hbar}\sum_{j\neq n}\left[\frac{\langle u_{n,k}|\frac{\partial\mathcal{H}}{\partial k_x}|u_{j,k}\rangle - \langle u_{j,k}|\frac{\partial\mathcal{H}}{\partial k_y}|u_{n,k}\rangle}{E_j - E_n} - c.c.\right]. \tag{5.11}$$

This generally leads to ≈10% correction ($\approx 0.4\,\mu_\mathrm{B}$) resulting in a $g \simeq -4.4\,\mu_\mathrm{B}$ estimate for $1s$ excitons, which accounted for the small deviations observed [289].

5.2.1.2 Application of the Single-Particle Model to Other Exciton Species and Break Down of the "Atomic" Picture of Interaction

Due to its apparent success, several groups attempted to increase the accuracy of the additive model by explicitly determining the spin, orbital, and valley contribution. Attempts were made via both experiment [140, 248] or *ab initio* calculations [63, 80, 324, 330] for bright excitons and extend its treatment to other exciton species. These works has been rather successful in predicting g-factor values for neutral exciton species. For example, the predictions for the spin-dark excitons are $|g_{\mathrm{X}_0^\mathrm{D}}| \approx 8 - 10\,\mu_\mathrm{B}$ and momentum-dark excitons would have $|g_{\mathrm{X}_0^{\mathrm{D(inter)}}}| \approx 10 - 13.6\ \mu_{\mathrm{B}}$ [80, 140]. This correlates very well with experimental results which have found that $|g_{\mathrm{X}_0^{\mathrm{D}}}| \approx 9.1 - 9.9\ \mu_{\mathrm{B}}$ [108, 170, 184, 247] and $|g_{\mathrm{X}_0^{\mathrm{D(inter)}}}| \approx 12.1 - 12.6\ \mu_{\mathrm{B}}$ [80, 108, 170], respectively. For charged particles like trions, $|g_{\mathrm{X}_-}| \approx 4\ \mu_{\mathrm{B}}$ is predicted since the excess electron contributes equally to both the initial and final state resulting a similar g to the exciton. A similar correction can be made to account for the intercellular contribution, although the formulation is slightly different (see Ch. 6. This prediction has proven to be fairly accurate at low carrier densities with $|g_{\mathrm{X}_-}| \approx 3.8 - 4.4\ \mu_{\mathrm{B}}$ observed experimentally [140, 170, 184]. We will discuss the influence of many-body interaction at higher carrier densities on g-factor in the next section.

Though this additive method has been rather successful for many exciton species, both the experimental work and *ab initio* calculation revealed something startling: the early success of the "atomic" model – where the majority orbital contributions are used to estimate μ_l – turned out to be correct purely by coincidence. For example, if we were to explicitly sum μ_{s}, μ_{l}, and μ_{v} in the "atomic" picture, we would find that $\mu_{+\mathrm{K,c}} = +3.5\,\mu_{\mathrm{B}}$ and $\mu_{+\mathrm{K,v}} = +5.5\,\mu_{\mathrm{B}}$. However when these contributions were measured experimentally, Robert *et al.* found that $\mu_{+\mathrm{K,c}} = +3.84\ \mu_{\mathrm{B}}$ and $\mu_{+\mathrm{K,v}} = +6.1\ \mu_{\mathrm{B}}$ [248]. This is in excellent agreement with the *ab initio* calculations that find $\mu_{+\mathrm{K,c}} = +3.81 - 3.97\ \mu_{\mathrm{B}}$ and $\mu_{+\mathrm{K,v}} = +5.81 - 5.91\ \mu_{\mathrm{B}}$ [63, 80, 324, 330] and still preserves that prediction of $g_{\mathrm{X}_0} \approx 4.4\ \mu_{\mathrm{B}}$ that is seen experimentally throughout the literature.

5.2.2 Many-Body Regime Enhancement of g-factor

Despite the significant work done to explain the results of valley-dependent Zeeman measurements within the single-particle model, there were still numerous reports of g-factor values that diverged from these expectations. In particular, Mo-based TMDs [15, 94, 118, 133, 282] and charged exciton species [2, 289, 319] reported the most variation with values from $|g| = 1.57 - 18\ \mu_{\rm B}$ reported for bright excitons and trions (polarons). In early TMD work, electrostatic control of the carrier concentration through a top- or back-gate was not a standard technique, and most of the experiments in the literature were performed using either bare monolayer on $\mathrm{SiO_2}$ or a monolayer with simple hBN encapsulation. In those cases, the carrier concentration in the sample was fixed and non-deterministic: the as-grown TMD monolayers can possess an intrinsic hole- or electron-heavy concentration. Other parts of the fabrication process – such as squeegeeing without a graphite contact, or simply resting on bare $\mathrm{SiO_2}$ (see Ch. 3) – can also result in additional, uncontrolled electrostatic doping. In other semiconductor systems, it is well known that the g-factor observed can be manipulated through control of the carrier concentration [73, 238, 244, 270, 271, 274]. Thus it was not a stretch to attribute the range of observed g-factors to variation in the carrier concentration from experiment-to-experiment.

The advent of controlled electrostatic gating in TMDs has allowed researchers to explicitly investigate the relationship between carrier concentration and g-factor. Based on these studies it has become clear that the preference for these systems to minimize their energy by inducing carrier polarization as a result of strong many-body interaction is responsible for the variety of g-factors observed. To fully understand why many-body interaction leads to this observed variation in g-factor, we will first discuss how we might quantify the strength of many-body interaction and then show why this interaction can lead to carrier polarization.

The first step to quantifying many-body interaction is to understand how the number of carriers controls the Fermi level in a system. Throughout this discussion, we will focus on a specific illustration in WSe_2 since this is where we do our own measurements, but it can be similarly applied to other TMDs. We begin by estimating the Fermi level via the following relation,

$$E_{\mathrm{F}} = \frac{n}{\rho(E)} = \frac{n}{m^*/(\pi\hbar^2)}. \tag{5.12}$$

Here, $\rho(E) = m^*/(\pi\hbar^2)$ is the density of available states when the Fermi level is below the upper conduction band and we take the effective mass of the electron m_{e}^* = 0.4 m_{e} [186], and the effective mass of the hole to be m_{h}^* = 0.36 m_{e} [141]. When we pass into the upper conduction band, we go from a degenerate to non-degenerate state and the density of states becomes $\rho(E) = m^*/(2\pi\hbar^2)$. Using these physical parameters, we generate Fig. 5.3(A) and indicate the splitting of the upper and lower conduction band for our system as $\Delta E_{\mathrm{CB}}^{\mathrm{WSe_2}}$ = 38 meV [186]. The density required to make this crossing is indicated with a vertical line marked $n_0 \approx 6.4 \times 10^{12}\ \mathrm{cm}^{-2}$. Note that in all cases, the Fermi energy is measured from the bottom of the lower conduction band at B=0T.

Next, we calculate the Wigner-Seitz radius r_s, which is a dimensionless quantity that is commonly used to gauge the strength of many-body effects in a system [58, 251, 319]. Defined as

$$r_s = \frac{1}{\sqrt{\pi n}} \frac{me^2}{\epsilon\hbar^2}, \tag{5.13}$$

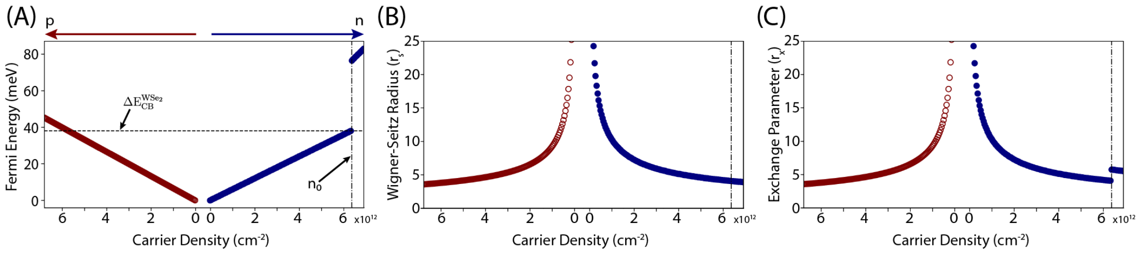

Figure 5.3: Illustration of the relationship between carrier density, Fermi energy, Wigner-Seitz radius, and exchange interaction strength in TMDs. (A) Calculated Fermi energy from carrier dependence with gate voltage. The Fermi energy needed to cross from the lower to upper conduction band is marked, as is the associated density for that transition. (B) Extracted Wigner-Seitz radius for the sample as a function of carrier density. The threshold for crossing into the upper conduction band is marked. (C) The calculated exchange parameter, highlighting the effect of doubling the spin-valley degeneracy upon crossing into the upper conduction band.

the Wigner-Seitz radius can be interpreted as the ratio between average Coulomb potential energy of the carriers and their Fermi energy [58]. It is used to separate carriers into two regimes: (I) $r_s > 1$ (the dilute and strongly interacting regime) and (II) $r_s < 1$ (the dense and weakly interacting regime). Fig. 5.3(B) shows the corresponding Wigner-Seitz radius as a function of carrier density. As we can see, the Wigner-Seitz radius is greater than one even at carrier densities approaching $10^{13}\ \mathrm{cm}^{-2}$, indicating that many-body interaction is strongly favored even in the presence of strong carrier doping.

The exchange parameter, r_x, has been proposed as a related metric to the Wigner-Seitz radius as it characterizes the ratio of the average exchange energy to the average kinetic energy ($\mathrm{E_F}$) at a given carrier density [58]. The exchange parameter is an important quantity because the price that the system has to pay to become fully valley polarized must be less than the exchange energy gained in order to make the polarization to be energetically favorable [15]. Thus when $r_x > 1$, full polarization of the carrier population

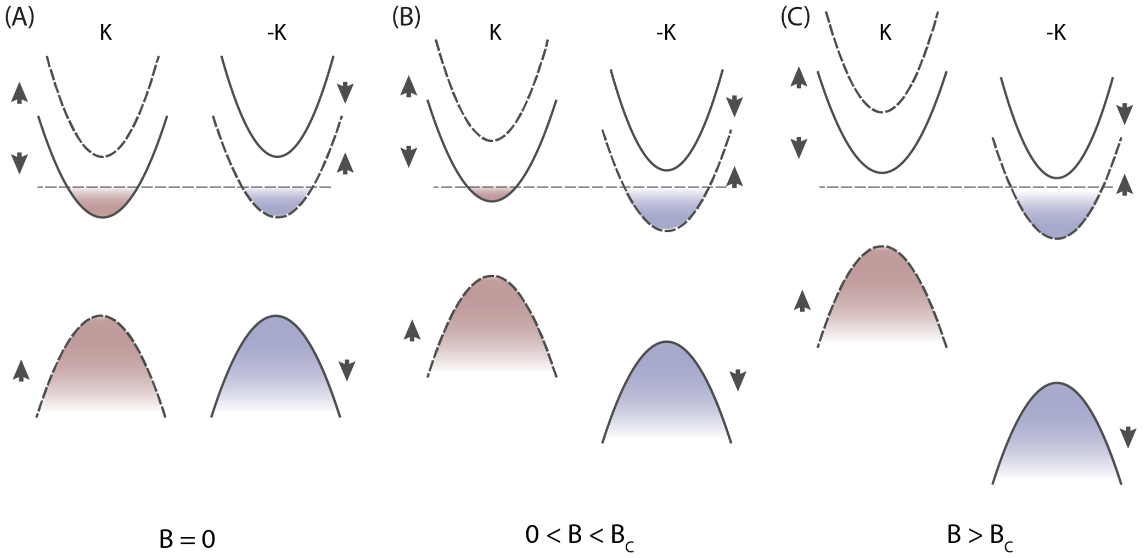

Figure 5.4: Stages of carrier polarization under applied magnetic field (A) B = 0T and there are an equal number of carriers in each valley, (B) 0<B<B$_\mathrm{C}$ and there is a carrier population imbalance between the two valleys, but both valleys have excess carriers, (C) B>B$_\mathrm{C}$ and all of the excess carriers now resides in just one of the two valleys. If we reversed the field, the occupation sequence would flip valleys as |B| increased. In all panels, the dashed horizontal line indicates where the Fermi energy E$_\mathrm{F}$ is in the sample.

is favorable to minimize the energy of the collective ensemble of carriers. We write r_x as

$$r_x = \sqrt{l_\mathrm{s} l_\mathrm{v}} r_s. \tag{5.1}$$

Here, $l_\mathrm{s} l_\mathrm{v}$ characterizes the spin-valley degeneracy. When we cross into the upper conduction band at n_0, we have $l_\mathrm{s} l_\mathrm{v} = 2 \rightarrow l_\mathrm{s} l_\mathrm{v} = 4$, which results in an abrupt change in the exchange parameter. We illustrate where this transition would occur in our model system in Fig. 5.3(C) and see the resulting discontinuity as r_x increases again when we begin to dope into the upper conduction band. We also see that $r_x > 1$ even at extremely high doping, indicating that valley polarization is highly favorable in the system.

To visualize how this interaction induced valley polarization occurs in the system, we recall the picture of polaron formation from Ch. 2.3.2.3. At B = 0 T, Fig. 5.4(A) shows that the population of excess carriers in each valley is the same – as indicated with the horizontal dashed line representing $\mathrm{E_F}$. The spin-polarization is defined as $\eta_s = \frac{N_\uparrow - N_\downarrow}{N_\uparrow + N_\downarrow}$, and we have $\eta_s = 0$ when B = 0 T. Once we turn on a positive field, we know from the previous section that our bands offset with the field. In our previous discussion though, we had no excess carriers to worry about. Here, in 5.4(B), we see that the red(blue) shift of the +K(-K) valley results in a population imbalance and a net spin polarization. If we keep the Fermi level fixed, as we have in Fig. 5.4, increasing the field strength will result in progressively more spin-polarization until we reach the critical field $\mathrm{B_C}$. At this point, we have shifted the bands so much the system is *fully spin polarized,* $\eta_s = +1$ as in Fig. 5.4(C). Intuitively, we can see that $\mathrm{B_C}$ depends on the carrier concentration and the g-factor in the system since the polarization condition requires that $E_\mathrm{Z} > E_\mathrm{F}$. If we reverse the field, the valleys will shift in the opposite direction and at $\mathrm{B_C}$ we will end up with $\eta_s = -1$ instead.

Since it is strongly energetically favorable to fully polarize the excess carriers into one valley, it can be reasoned that an enhanced, carrier density dependent g-factor would be the most efficient way for the system to force the lower energy configuration at a small applied field. Thus, what is observed experimentally is a $g \propto r_s$. Experimentally, the earliest signature of this effect in TMDs was demonstrated by Back *et al.* in 2017 where they showed a strongly enhanced g-factor of $\sim 18\ \mu_\mathrm{B}$ in $\mathrm{MoSe_2}$ when the system was fully valley polarized [15]. Following this discovery, both Wang *et al.* [319] and Lin *et al.* [176] showed independently that they could correlate g-factor strength with the Wigner-Seitz radius in $\mathrm{WSe_2}$ and $\mathrm{MoS_2}$, respectively. More recently, Klein *et al.* performed an incredibly thorough study of all exciton species in $\mathrm{MoS_2}$ and showed that each species exhibited smoothly varying g-factor with carrier concentration that was correlated with the degree of polarization in the system. This implies that all species of excitons display many-body physics [133].

In this scenario described above, instead of seeing a linear Zeeman effect, we would see something that looks much more like a net magnetization curve for a paramagnet where we asymptotically approach full polarization. Thus, the net spin imbalance in this case this give by the,

$$\begin{aligned} S_Z(B) &= -s_z \cdot B_J(x) \\ &= s_z \cdot \left[\frac{2s_z+1}{2s_z} \coth\left(\frac{2s_z+1}{2s_z} x \right) - \frac{1}{2s_z} \coth\left(\frac{1}{2s_z} x \right) \right], \end{aligned} \tag{5.14}$$

where $s_z = 1/2$ and $x = \frac{g\mu_\mathrm{B} s_z B}{k_\mathrm{B} T}$ and the total magnetization is $M \sim (N_\uparrow - N_\downarrow) \cdot S_Z(B)$. x is explicitly the ratio of the Zeeman energy to the thermal energy, but the thermal energy is inherently related to the Fermi energy of the excess carriers, so this quantity can be used to extrapolate the critical field for complete polarization. Within this formulation, the carrier dependent g-factor is

$$g^*(n_{e,h}, B) = g_{\mathrm{X}_0} + g_m(n_{e,h}) \cdot S_z(B), \tag{5.15}$$

where g_{X_0} is the g-factor of the exciton in the intrinsic regime where the linear Zeeman effect dominates and $g_m(n_{e,h})$ is the carrier dependent g-factor that is tuned by the strength of the many-body interaction. In this model, the g-factor is only tuned by the strength of the many-body interaction and degree of magnetization at a given applied field, so it is the same for any exciton species that is present at that carrier concentration [133].

5.2.3 High Field Considerations: Paschen-Back Effect, Diamagnetic Shift, and the Quantum Hall Effect

Besides the Zeeman effect, which is dominant at low fields, there are several other effects that are routinely observed in semiconductors under the application of magnetic field. Here, we discuss the conditions needed to observe the anomalous Zeeman effect (the so-called Paschen-Back effect [227]), diamagnetic shift [207], and the quantum Hall effect (QHE) [155, 308]. We will also discuss whether we would expect those conditions to be met in our experimental work.

The Paschen-Back effect occurs when the applied magnetic field becomes large enough that the "normal" Zeeman splitting would be on the order of the splitting due to spin-orbit coupling in the system. At this point, the energetic splitting due to the external magnetic field becomes dominant and the spin-orbit interaction is treated as the perturbation in the system. Since this results in the reordering of the fine structure in the system, it is treated as a distinct phenomenon from the Zeeman effect and is sometimes also referred to as the "anomalous" Zeeman effect. We can recall from Ch. 2.2.2 that the spin-orbit interaction in the conduction band in our system is on the order of 30 meV. For a typical lab experiment, where we achieve $\sim |10|$ T field at most, this would equate to a g-factor of 3 meV/T$\sim$ 50 μ_B in order for the spin-orbit interaction to be comparable to splitting due to the Zeeman effect. Since g $\approx$ 50 μ_B is outlandish, even with the enhancement due to many-body effects, we can safely rule out the Paschen-Back effect from being relevant in our system.

When a magnetic field is applied, we recall that charged particles will undergo cyclotron motion. We extract a quantity called the *magnetic length* $l_{\mathrm{B}} = \sqrt{\frac{\hbar}{eB}}$ that describes the scale of these cyclotron orbits. When the magnetic field is small-to-intermediate, these orbits are large and span many lattice sites/exciton Bohr radii in a solid, i.e. $\gamma = \left(\frac{a_{\mathrm{B}}}{l_{\mathrm{B}}}\right)^2 \ll 1$. In this limit, the diamagnetic shift – which is an additional, higher-order correction to the Zeeman shift – can be observed. Generally, the diamagnetic shift is only significant in its effect in larger radius excitons and high fields. We can see why this is true in the following,

$$\Delta E_{\mathrm{dia}} = \frac{e^2}{8m_r}\langle r_{\perp}^2\rangle B^2 = \sigma B^2. \tag{5.16}$$

Here, m_r is the reduce mass of the exciton and $\langle r_{\perp}^2\rangle$ is the expected radial component and $r_{rms} = \sqrt{\langle r_{\perp}^2\rangle} = \sqrt{8m_r\sigma}/e$ [207, 292]. In WSe_2, the parabolic bending of the Zeeman splitting resulting from the diamagnetic shift is only strongly observed at B$>$ 10 T for $n = 1, 2$ exciton species, which is beyond our experimental range. Additionally, since it affects both valleys equally, when we take the difference of the energy splitting between the valleys to calculate the Zeeman shift the influence of the diamagnetic shift is removed as well [293].

As the field increases, the magnetic length decreases and can become comparable to the Bohr radius of the material, i.e. $\gamma \geq 1$. When this is true, the QHE occurs and overtakes typical Zeeman splitting/diamagnetic correction. In the quantum Hall regime, carriers are forced into a level scheme similar to that of a quantum harmonic oscillator and which we call Landau levels (LLs). The field regime at which this becomes the dominant phenomenon can be approximated by looking at the relevant length scales in the system.

If we take $l_B \approx \frac{25 \text{ nm}}{\sqrt{B}}$ and $a_\text{B} \approx 1.5$ nm:

$$\frac{25 \text{ nm}}{\sqrt{B}} = 1.5 \text{ nm} \rightarrow \text{B} = \left(\frac{25\text{nm}}{1.5\text{nm}}\right)^2 = 277 \text{ T} \tag{5.15}$$

Based on this comparison, we would expect the QHE to only be relevant in TMDs at extremely high fields (unachievable in a lab). However, the QHE has been observed optically and through transport in several TMD systems [98,166,176,185,231,282,319]. The strong many-body interaction and resulting valley polarization is thought to play a large role in observing this effect at much lower fields than would traditionally be expected and has also allowed researchers to experimentally determine the LL ordering through carrier-dependent measurements [166,176]. However, at fields less than 10 T, the spacing of the LLs is sufficiently small that the Zeeman effect dominates as the observable effect [166]. There have been a couple of reports near $B \sim 10$ T, but only in systems with large numbers of excess carriers $n_e \sim 7 \times 10^{12}$ cm^{-2}. In our system the carrier concentration is more than an order of magnitude smaller (see Ch. 6), so we can safely rule out the QHE as a complicating factor in our g-factor measurements.

Chapter 6: Magneto-Optical Measurements of the Negatively Charged $2s$ Exciton in WSe_2

6.1 Notes

This chapter is largely taken verbatim from our paper "Magneto-Optical Measurements of the Negatively Charged $2s$ Exciton in WSe_2" J.C.Sell, J.R.Vannucci, D. Suarez, B. Cao, D. Session, H.-J. Chuang, K.M. McCreary, M.R. Rosenberger, B.T. Jonker, S. Mittal, M. Hafezi, *arXiv:2202.06415* (2022) [266]. It is currently under review for peer-reviewed publication. Small alterations have been made to fit references from earlier sections to this chapter.

As discussed in Chs. 2 and 5, the trion peaks are sometimes interpreted as polarons depending on the carrier concentration in the system [15, 275]. This remains an active area of research at the time of this thesis, with work showing that polaron and trion interpretations converge in their predictions at low-to-intermediate carrier density [91, 361]. These results highlight the difficulty in drawing a dividing line between the two interpretations, and for simplicity we refer to them as charged states throughout this chapter.

6.2 Manuscript

6.2.1 Abstract

Monolayer transition metal dichalcogenides host a variety of optically excited quasiparticles species that stem from two-dimensional confinement combined with relatively large carrier effective masses and reduced dielectric screening. The magnetic response of these quasiparticles gives information on their spin and valley configurations, nuanced carrier interactions, and insight into the underlying band structure. Recently, there have been several reports of $2s$/$3s$ charged excitons in TMDs, but very little is still known about their response to external magnetic fields. Using photoluminescence excitation spectroscopy, we observe the presence of the $2s$ charged exciton and report for the first time its response to an applied magnetic field. We benchmark this response against the neutral exciton and find that both the $2s$ neutral and charged excitons exhibit similar behavior with g-factors of $\mathrm{g}_{\mathrm{X}_0^{2\mathrm{s}}}$=-5.20$\pm$0.11 μ_B and $\mathrm{g}_{\mathrm{X}_-^{2\mathrm{s}}}$=-4.98$\pm$0.11 μ_B, respectively.

6.2.2 Introduction

Monolayer semiconductor TMDs have attracted significant attention in the last decade due to their unique optical properties. Similar to graphene, but with a three-layer (staggered) honeycomb lattice, TMDs host direct-gap transitions at their ±K valleys and exhibit circular-dichroism due to their finite Berry curvature [197, 198, 327]. The reduced dimensionality of materials in this system, coupled with techniques like hexagonal boron nitride (hBN) encapsulation, lead to enhanced Coulomb interaction and excitons with large binding energies ($E_\mathrm{B} \approx 150 - 500$ meV) [46, 107, 293].

When there is excess charge present in the system during exciton formation, the exciton may lower its energy by capturing an electron or hole and form a bound, charged three-body state referred to as a charged exciton [153, 257]. Charged excitons are a ubiquitous feature of semiconductors, but are difficult to observe in traditional systems – like GaAs/AlGaAs quantum wells – due to their small binding energies (1-2 meV) [79, 129, 285]. In TMDs, however, both singlet and triplet charged species have been discovered with $\mathrm{E_B} \approx 20 - 40$ meV [53, 191, 196, 257, 289]. In the high carrier density regime, these resonances have been alternatively interpreted as many-body polaron states [15, 69, 91, 275].

In analogy to the hydrogen atom, excitons are known to form a Rydberg series of higher energy states [128]. In TMDs, they have been observed through a variety of different optical techniques up to principal quantum number n =11 [44, 46, 94, 292, 293, 317]. However, even in the presence of excess charge, a corresponding series for the charged exciton has remained elusive. Lack of experimental observations of these states has been thought of analogously to the H^- ion, for which there exists no bound excited state [111]. Recently, there have been a series of compelling reports of metastable $2s$/$3s$ charged excitons in TMDs [10, 92, 182, 309] coupled with theoretical work [77, 242, 273, 332] showing their existence is possible.

The difficulty in observing these higher n states is two-fold: (I) the weak radiative decay rate of excitons with higher n makes them increasingly dim in typical PL measurements [105] and (II) even once the state is observed optically, further carrier-density and magnetic field dependent measurements are needed to correctly identify the exciton species [108,

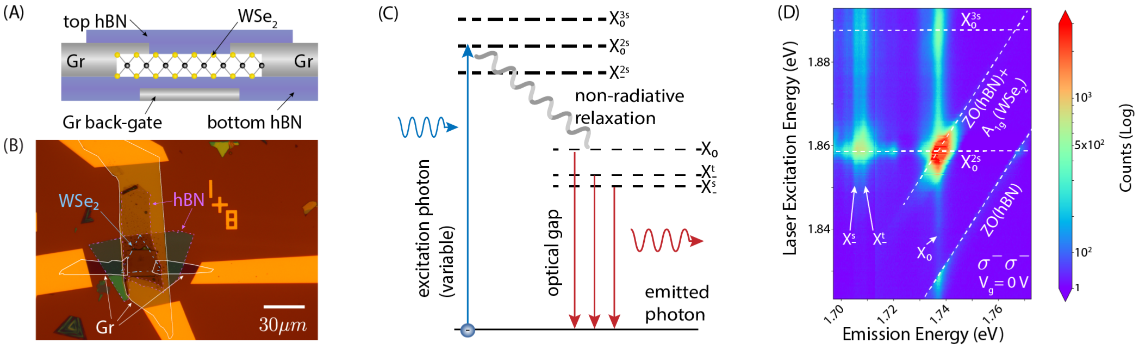

Figure 6.1: (A) Schematic of the hBN encapsulated WSe$_2$ with graphite (Gr) back gate and electrodes. (B) Optical image of device after full fabrication. The compressed area in the center indicates the region of the sample that underwent nanosqueegeeing. (C) Schematic of the PLE process highlighting the higher n states (e.g. $\mathrm{X}_0^{2\mathrm{s}}$) and emission monitored channels (e.g. X_0, $\mathrm{X}_-^{\mathrm{t}}$, or $\mathrm{X}_-^{\mathrm{s}}$). (D) $\sigma^-\sigma^-$ PLE spectra taken at $\mathrm{V_g}$ = 0 V and sample temperature of <300 mK. The monitored emission channels are marked with arrows (X_0, $\mathrm{X}_-^{\mathrm{t}}$, and $\mathrm{X}_-^{\mathrm{s}}$) [16, 181]. Two Raman modes are identified as diagonal dashed lines (ZO(hBN) and ZO(hBN)+A$_{1\mathrm{g}}$(WSe$_2$)), see SM [119, 121]. The resonances of the excited states are marked with horizontal dashed lines ($\mathrm{X}_0^{2\mathrm{s}}$, $\mathrm{X}_0^{3\mathrm{s}}$) [292].

168, 171, 184, 191, 193, 289].

In this work, we confirm the presence of negatively charged 2s-exciton ($\mathrm{X}_-^{2\mathrm{s}}$) in WSe$_2$ via PLE. In PLE, we monitor the emission from the 1s (lowest energy) exciton species while the excitation laser's energy was swept in the energy regime needed to resonantly probe higher n states. This provides a superior signal-to-noise ratio compared to PL. Additionally, we report on the response of $\mathrm{X}_-^{2\mathrm{s}}$ to an applied magnetic field. To the best of our knowledge, these represent the first magneto-optical measurements of a 2s charged exciton in any TMD system. We measure the valley dependent Zeeman splitting for both the 2s neutral ($\mathrm{X}_0^{2\mathrm{s}}$) and charged ($\mathrm{X}_-^{2\mathrm{s}}$) excitons in the carrier density regime in which they coexist. From this, we extract similar g-factors for $\mathrm{X}_0^{2\mathrm{s}}$/$\mathrm{X}_-^{2\mathrm{s}}$, $\mathrm{g}_{\mathrm{X}_0^{2\mathrm{s}}}$=-5.20±0.11 μ_B and $\mathrm{g}_{\mathrm{X}_-^{2\mathrm{s}}}$=-4.98±0.11 μ_B, and discuss the possible physical origins of this result.

In our experiment, a monolayer of CVD grown WSe$_2$ is encapsulated in hBN along with few-layer graphite (Gr) contacts and bottom gate electrode. Encapsulation was performed via the wet capillary action method and interlayer contamination was removed via the nano-squeegee method [255] (see Fig. 6.1(A) for a schematic of the sample and Fig. 6.1(B) for an image of the final device). The full fabrication details are reported in the supplemental material (SM). The joint hBN and Gr encapsulation allows for a high-quality device with electrostatic control over the carriers in the system via the applied gate voltage $\mathrm{V_g}$ [61].

Throughout our work, we utilize PLE to resonantly probe the $2s$ exciton states. In PLE, the energy of the input photons is varied and when their energy resonantly matches a $2s$ exciton state, electrons are excited from the valence band to form these excitons (e.g. $\mathrm{X_0^{2s}}$). There, the $2s$ excitons undergo non-radiative relaxation to a $1s$ state (e.g. the neutral exciton $\mathrm{X_0}$) where they radiatively recombine and emit photons. An illustration of this process is shown in Fig. 6.1(C). For these measurements, the excitation beam is generated using a dye laser with a dynamic excitation range of 1.77-1.99 eV. We use a confocal configuration with circular polarization resolution in both excitation and detection. Throughout the text, we denote the excitation/emission polarization in the format $\sigma^{\mathrm{excitation}}\sigma^{\mathrm{emission}}$. The sample was placed in a dilution refrigerator equipped with a 12 T superconducting magnet in a Faraday geometry. We estimate that with residual heating from the laser and magnet, the ambient temperature of the sample is $<$300 mK.

Fig. 6.1(D) shows a baseline PLE spectrum taken with $\sigma^-\sigma^-$ (-K-valley selective) at $\mathrm{V_g}$ = 0V and B = 0T. We identify the $2s$ and $3s$ neutral Rydberg excitons ($\mathrm{X_0^{2s}}$, $\mathrm{X_0^{3s}}$) by their binding energies [44, 183] and labeled them with white dashed lines at 1.859 eV and 1.887 eV, respectively. The $1s$ neutral ($\mathrm{X_0}$) exciton's emission channel and the triplet

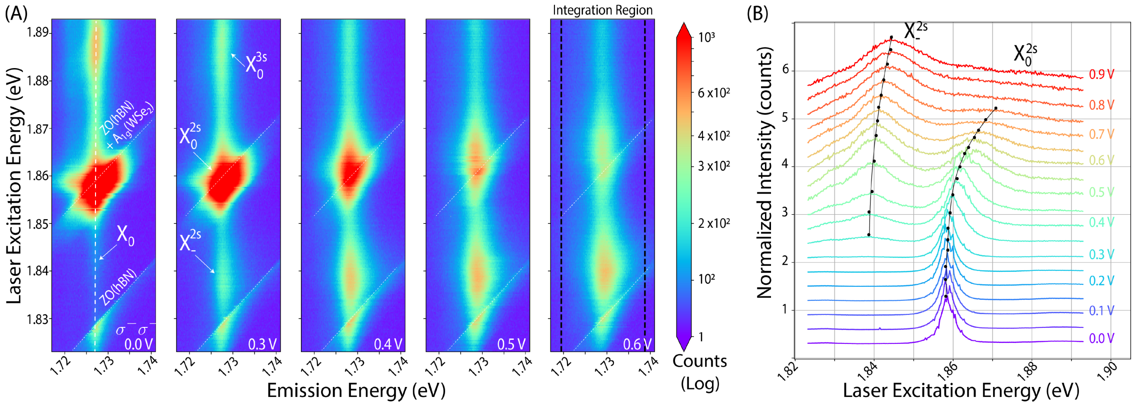

Figure 6.2: (A) PLE data with increasing n_e-doping while monitoring the X_0 recombination channel in the -K-valley ($\sigma^-\sigma^-$). (B) Waterfall plot of vertical cross-sections from V_g = 0 - 0.9 V. The integration region is annotated in panel (A). The counts were summed over the emission width for each excitation energy.

(X^t_-)/singlet (X^s_-) charged excitons' emission channels were identified by their binding energies [16, 173] and PL gate voltage dependence [321] (see SM).

6.2.3 Identification of the Excited Charged State via Gate-Dependent PLE

Next, we tune V_g to n_e-dope the system and look for signs of an emerging charged $2s$ exciton in our PLE spectra. Fig. 6.2 highlights the results of this while monitoring the X_0 emission channel; Fig. 6.2(A) shows the full PLE spectra at selected V_g, while Fig. 6.2(B) is the integrated vertical cross-section of the emission spectrum around the X_0 signal. The integration region used for all gate voltages is denoted in the V_g = 0.6 V panel of Fig. 6.2(A) by the vertical dashed lines. As in Fig. 6.1, we identify the resonance at 1.859 eV as X_0^2s.

At V_g = 0.3 V, a lower energy resonance begins to emerge at 1.838 eV. We label this state as the $2s$ charged exciton X_-^2s and base this identification on two observations:

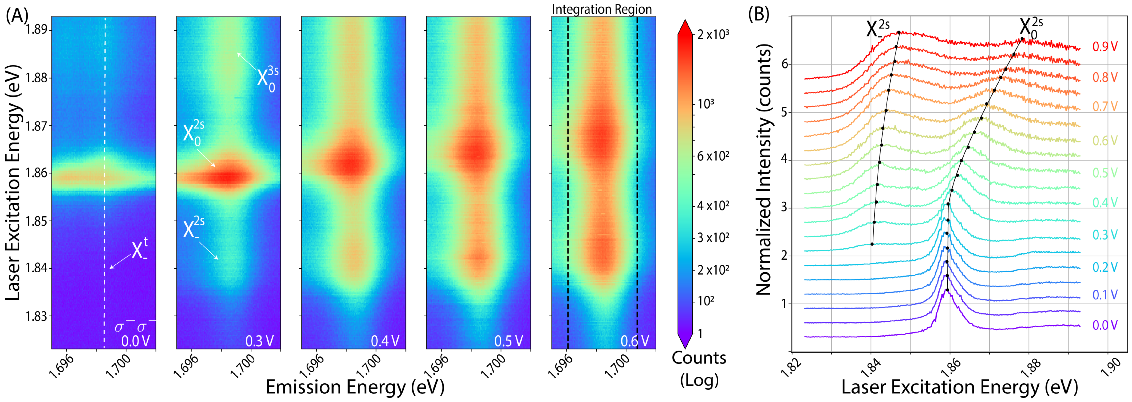

Figure 6.3: (A) PLE data with increasing n_e-doping while monitoring the X_-^t recombination channel ($\sigma^-\sigma^-$). (B) As in Fig. 6.2, the waterfall plot corresponds to vertical cross-sections from V_g = 0 - 0.9 V.

(I) V_g = 0.3 V corresponds to the transition of the sample from charge neutrality to n_e-doped and the emergence of the negatively charged $1s$ excitons X_-^t/X_-^s (see SM for $1s$ PL data). The X_-^{2s} resonance displays a similar onset at V_g = 0.3 V indicating a similar negative charge character. (II) When the X_-^{2s} resonance first appears at V_g = 0.3 V, we find that $\Delta E_{(X_0^{2s}-X_-^{2s})}$ = 21 meV while $\Delta E_{(X_0-X_-^t)}$ = 29 meV and $\Delta E_{(X_0-X_-^s)}$ = 35 meV. This reduction indicates that the $2s$ charged exciton is less tightly bound than its $1s$ state counterpart. This is in accordance with other observations in the literature [**?**,92,182,309] and consistent with the fact that Rydberg states display a reduction in relative binding energy with each increasing n.

Since the $2s$ charged exciton is expected to be a doublet, as observed for the $1s$ charged excitons, the extracted position of X_-^{2s} is an average. X_-^t and X_-^s have a narrow linewidth and a strong intervalley exchange interaction that splits them (≈ 6 meV [53, 338]) which allows us to spectrally resolve them. However, the broadness of the $2s$ states combined with a reduced intervalley exchange energy (theoretically predicted to be ≈ 1 meV [10, 338]), prevents us from resolving the doublet of the $2s$ charged exciton. There

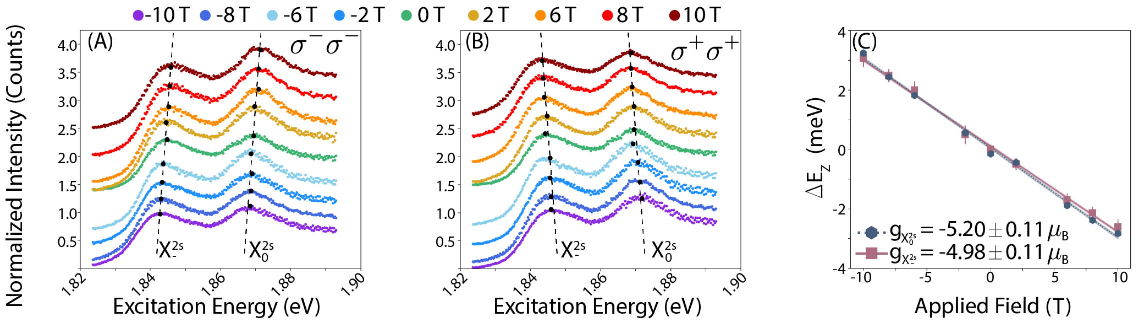

Figure 6.4: Vertical cross-sections from the X_-^t emission channel as a function of field for (A) $(\sigma^-\sigma^-)$ and (B) $(\sigma^+\sigma^+)$ marked with the corresponding peak positions (black dots) for the X_0^{2s} and X_-^{2s} states from fitting with the dashed line serving as a guide to the eye. (C) Extracted g-factors for X_0^{2s} and X_-^{2s} states. The thickness of the fit line in panel (C) corresponds to the error in the fit.

is, however, indication of the two states in the asymmetric lineshape of the X_-^{2s} peak (see SM).

In Fig. 6.2(B), we see the spectral dependence of X_0^{2s} and X_-^{2s} with carrier density. As the n_e-doping increases with increasing gate voltage, the X_0^{2s} resonance broadens, decreases in intensity, and spectrally blueshifts. The broadening and loss of spectral intensity are consistent with more rapid decoherence from interaction with the Fermi sea. The blueshift results from the competing effects of band gap and binding energy renormalization due to decreased $e^- - e^-$ and $e^- - h^+$ interaction from screening by the Fermi sea [47, 251, 309].

In contrast, X_-^{2s} peak grows in intensity and experiences minimal spectral drift with increased carrier density. In the case of a three-body quasiparticle, one expects a redshift that is linearly dependent on the charge concentration in the system resulting from momentum conservation [47, 69, 196]. This competes with the effects of band gap and binding energy renormalization previously discussed for the neutral excitons that favor a blueshift [47], and leads to the minimal spectral drift observed. Both the increase in intensity and small spectral shift are consistent with the behavior of $1s$ and $2s$ charged excitons previously observed [47,251,309].

Since $\mathrm{X}_{-}^{2\mathrm{s}}$ emerges in the n_{e}-doped regime, we expect $\mathrm{X}_{-}^{\mathrm{t}}$ and $\mathrm{X}_{-}^{\mathrm{s}}$ to be the most prominent emission channels for $2s$ exciton species (see SM). To verify this, we monitor the $\mathrm{X}_{-}^{\mathrm{t}}$ emission channel in a similar manner to X_0 and show the results as a function of V_{g} in Fig. 6.3 (the results for $\mathrm{X}_{-}^{\mathrm{s}}$ can be found in the SM). We confirm that the behavior (spectral position, shift with gate, etc.) of $\mathrm{X}_0^{2\mathrm{s}}$ and $\mathrm{X}_{-}^{2\mathrm{s}}$ is independent of the monitored decay channel.

6.2.4 Valley Zeeman Effect in the Excited Charged State

We turn our attention to extracting the behavior of the $\mathrm{X}_0^{2\mathrm{s}}$ and $\mathrm{X}_{-}^{2\mathrm{s}}$ with applied magnetic field. We chose to take the data at $\mathrm{V}_{\mathrm{g}} = 0.6$ V because both the neutral and charged exciton have similar intensity. Integrated vertical cross-sections of the $\mathrm{X}_{-}^{\mathrm{t}}$ emission channel presented in Fig. 6.4 (A)/(B) show the response of the -K($\sigma^{-}\sigma^{-}$) / +K($\sigma^{+}\sigma^{+}$) valleys, respectively, with magnetic field. The extracted peak centers from fitting are marked with black dots. Applying a magnetic field breaks the time-reversal symmetry in the system, and results in a red(blue) shift with positive field for the +K(-K) valley and vice versa with applied negative field [15,289].

Using the definition for the Zeeman splitting in terms of polarization components, $\Delta E_Z = E^{\sigma^{+}\sigma^{+}} - E^{\sigma^{-}\sigma^{-}} = g\mu_{\mathrm{B}}B$, we fit a linear model to our data and extract a g-factor of -5.20±0.11 μ_{B} and -4.98±0.11 μ_{B} for $\mathrm{X}_0^{2\mathrm{s}}$ and $\mathrm{X}_{-}^{2\mathrm{s}}$, respectively. This fit and extracted difference is shown in Fig. 6.4(C). Results that agreed within experimental error were found for both $\mathrm{X}_0^{2\mathrm{s}}$ and $\mathrm{X}_-^{2\mathrm{s}}$ for a similar analysis of the $\mathrm{X}_-^{\mathrm{s}}$ emission channel (see SM).

Frequently, a single-particle model is used to interpret the g-factor for $1s$ excitons. In this model, the contributions to the Zeeman splitting are defined as $\Delta E_{\mathrm{Z}} = -\vec{\mu}\cdot\vec{B}$. The magnetic moment $\vec{\mu}$ is composed of additive terms for the orbital and spin contributions (intracellular components $\mu_{\mathrm{O}}, \mu_{\mathrm{S}}$) along with a correction for the effects of the finite Berry curvature in the system (intercellular component μ_{V}) [80, 140, 168, 193, 338] in each relevant band. Within this interpretation, we expect $g_{\mathrm{X}_0} \approx -4.4\ \mu_{\mathrm{B}}$ and -11 $\mu_{\mathrm{B}} g_{\mathrm{X}_-^{\mathrm{t/s}}} - 4\ \mu_{\mathrm{B}}$ (depending on the method used to calculate μ_{V}, and whether the doublet is resolved [181, 191, 289]).

To serve as a reference point between the literature and our $2s$ results, we also extracted the g-factors for X_0 and $\mathrm{X}_-^{\mathrm{t/s}}$. These values are $\mathrm{g}_{\mathrm{X}_0}$ = -4.22±0.04 μ_{B}, $\mathrm{g}_{\mathrm{X}_-^{\mathrm{t}}}$ = -4.12±0.04 μ_{B}, and $\mathrm{g}_{\mathrm{X}_-^{\mathrm{s}}}$ = -3.86±0.05 μ_{B} in our system at V_{g}=0.6 V. They are consistent with the results from the single particle interpretation, but highlight a distinct increase in our $2s$ g-factors with respect to the corresponding $1s$ states. We discuss two possible contributions to this enhancement.

(I) Enhancement of the g-factor for the $2s$ neutral exciton has been observed in magnetic Rydberg measurements in both intrinsic and electrostatically neutral samples [44, 94, 317]. Since the observation in neutral samples rules out doping effects, the divergence from $g_{\mathrm{X}_0} \approx -4.4\ \mu_{\mathrm{B}}$ has been attributed to enhanced intercellular contributions arising from the increased k-space localization of the wavefunctions with each subsequent n [44]. Extending this technique to charged excitons gives an intercellular component that *decreases* as the Bohr radius *increases*. This is compounded by an increased k-space localization of the charged exciton (see SM). While this model could explain the results for X_0^{2s} it would underestimate the g-factor for X_-^{2s}.

(II) A second possibility is the onset of many-body interaction (polaron picture) between the excitons and the emerging Fermi sea from electrostatic gating. Many-body interactions are expected to be very favorable in WSe_2 which has a Wigner-Seitz radius greater than 1 even at extremely high densities [58,319]. The interaction strength will vary with the Fermi sea's population and the Bohr radius, and induce Fermi sea polarization. Carrier dependent enhancement of the g-factor in TMDs has been documented for many materials/quasiparticles, with the strength of enhancement dictated by the degree of the induced Fermi sea polarization [15, 133, 171, 319].

In the many-body picture, it has been observed that as doping levels are varied there is a convergence of the g-factor between competing quasiparticles (e.g. X_0 and X^-) in regions in which they coexist. In analogy to the Kondo effect, the impurity (exciton) is dressed with either an attractive or repulsive interaction with the Fermi sea. As carrier density increases, the state dressing will become more similar for all exciton species – regardless of the type of interaction – resulting in a convergence of the g-factors [133] for X_0-like and X_--like excitons. Such behavior is not expected to be limited to the $1s$ state excitons and can explain the convergence of our extracted values of g for the X_0^{2s} and X_-^{2s} within experimental error.

6.2.5 Conclusions

Our results serve as the first marker in mapping the behavior of the $2s$ charged state, X_-^{2s}, with magnetic field in TMDs. The stability of the X_-^{2s} state offers a possible medium for studying the cross-over from exciton Rydberg physics to the quantum Hall regime for charged species at high magnetic fields. Recent work by Klein *et al.* used carrier density dependent g-factor measurements to demonstrate tunable many-body physics through all $1s$ exciton species in MoS_2 [133]. Our initial results indicate that it would be possible to produce this type of map for $2s$ species with access to higher magnetic fields and devices with larger dynamic carrier density range. This opens up a unique opportunity to study many-body interactions in higher energy exciton species that is generally limited in traditional semiconductors systems with smaller exciton binding – like GaAs quantum wells.

6.3 Supplemental Material

6.3.1 Fabrication Details

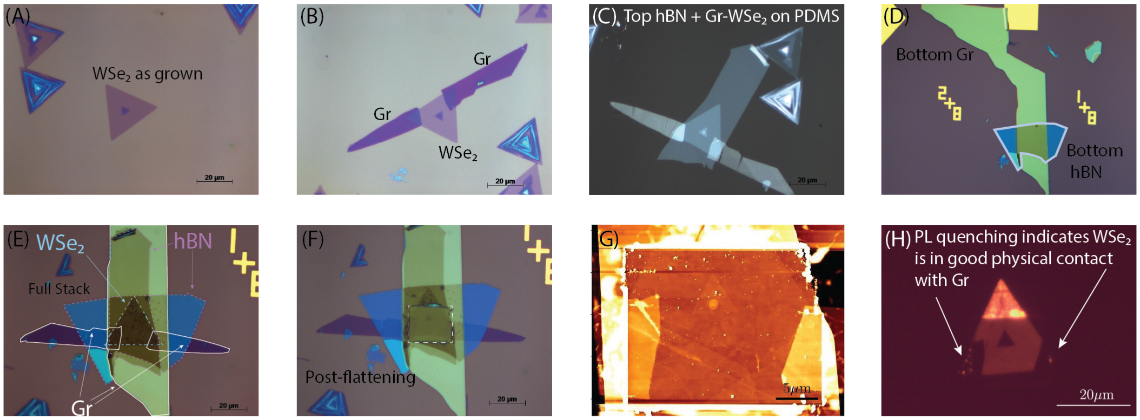

Figure 6.5: More detailed images from the fabrication process showing (A) the as-grown WSe_2, (B)/(C)/(D) graphite leads/gate, (E) full hBN encapsulation, (F) fully encapsulated stack after nano-squeegee process (highlighted with dashed box), (G) an AFM image of the nano-squeegee region highlighting the removal of interlayer impurities from the stacking process, and (H) a PL image of the WSe_2 monolayer and graphite leads, with the quenching of emission at the contact points indicating good physical contact.

6.3.1.1 CVD growth of WSe_2

Chemical vapor deposition (CVD) synthesis of WSe_2 was performed in a two inch quartz tube furnace on SiO_2/Si (275 nm oxide) substrates. Prior to use, all SiO_2/Si substrates were cleaned in acetone, isopropanol (IPA), and Piranha etch (H_2SO_4 + H_2O_2) then thoroughly rinsed in deionized water. At the center of the furnace was positioned a quartz boat containing approximately 1g of WO_3 powder (Alfa Aesar 99.999%). Two SiO_2/Si wafers were positioned face-down, directly above the oxide precursor. A separate quartz boat containing approximately 500 mg selenium powder (Alfa Aesar 99.999%) was placed upstream, outside the furnace-heating zone. The upstream SiO_2/Si wafer contained perylene- 3,4,9,10-tetracarboxylic acid tetrapotassium salt (PTAS) seeding molecules to promote lateral growth, while the downstream substrate was untreated. Pure argon (65 sccm) was used while the furnace ramped to the target temperature. Upon reaching the target temperature of 825 °C, 10 sccm H_2 was added to the Ar flow and maintained throughout the 10 minutes soak and subsequent cooling to room temperature.

6.3.1.2 Heterostructure construction

Mechanical transfer from the deposition substrate and van der Waals heterostructure construction was performed using a wet capillary technique outlined in the experimental methods section of Ref. [255]. The polydimethylsiloxane (PDMS) used in this process was made from a commercially available SYLGARD 184 silicone elastomer kit. To prepare the PDMS mixture, we thoroughly mix Silicone Elastomer and curing agent with a weight ratio of 10:1 followed by a debubbling process under rough vacuum for 30 minutes. This mixture was spin coated on a silicon wafer with a spin rate of 350 rpm for 30 s, then cured at 80 °C for 20 minutes on a hot plate. The resultant PDMS is easily peeled off the silicon wafer for use.

The top and bottom hBN in the heterostructure are 12 nm and 15 nm thick, respectively, as measured by AFM. After the heterostructure was complete, interlayer interfacial contamination was removed via the nano-squeegee method [255]. Fig. 6.5 shows more detailed images from the encapsulation process.

6.3.1.3 Electrical contact fabrication

After the full heterostructure was placed onto the SiO_2/Si substrate, electron beam lithography (EBL) was used to define leads to the graphite contacts and back gate. For this, a bilayer of poly (methyl methacrylate) (PMMA) 950 A4 was spun onto the sample and baked at 185 °C for 5 and 10 minutes, respectively. The patterning was performed on an 100kV system. Post patterning and development, 3 nm Cr/70 nm Au contacts were deposited using thermal evaporation. Excess metal was removed using a standard solvent liftoff procedure in a bath of room temperature acetone for 1 hour.

6.3.2 Optical Configuration

See Ch. 4.4 for optical setup and experimental details regarding light sources and magnetic field configuration.

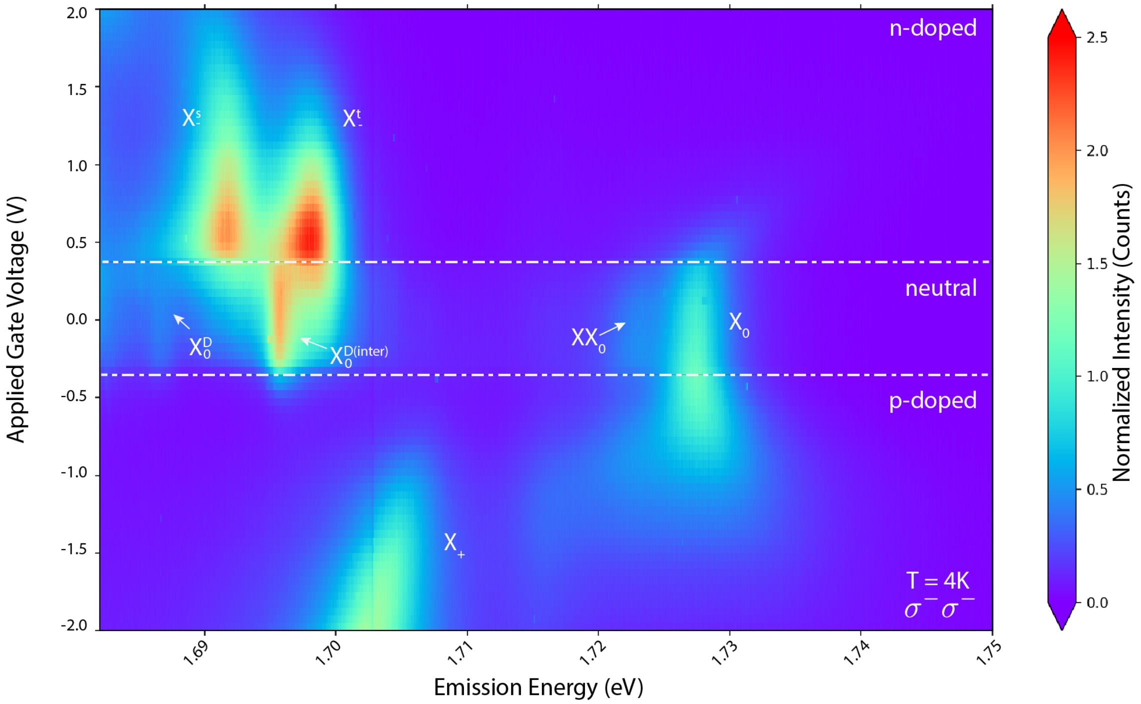

Figure 6.6: PL of the $1s$ exciton species as a function of gate voltage. Here, there are three regions marked based on their charge character: n-doped, neutral, and p-doped. Exciton species are noted. Data collected while the sample was illuminated with an excitation energy of 1.95 eV.

6.3.3 Electrostatic Gate Mapping of the Ground State

As discussed in Ch. 4.3.2, an initial gate map was produced to identify different doping regions. For this measurement, polarization-resolved PL was collected as a function of gate voltage from -2 V to 2 V. The results presented in Fig. 6.6 are from a mapping using $\sigma^-\sigma^-$, but $\sigma^+\sigma^+$ was also collected and found to produce identical results. The spectra is normalized to the $1s$ exciton intensity at $V_g = 0$ V.

In this measurement, we identify three charge regimes: neutral, n-doped, and p-doped. In the neutral regime we identify the $1s$ exciton X_0 [181,289], the neutral biexciton cluster XX_0 [290], the intervalley momentum-dark exciton $X_0^{D(inter)}$ [180], and the intravalley spin-dark exciton $\mathrm{X}_0^{\mathrm{D}}$ [181, 208, 350].

In the charge neutral regime, the Fermi level remains in the band gap and only localized disorder states increase in occupation. These band gap states have little influence on the overall electronic properties of the sample outside of allowing for a small probability that charged exciton states will form through coupling to these localized electrons. In an ideal device, the neutral point in the sample would be just one gate voltage because we have perfect carrier injection efficiency. However, in a real sample we can face issues like Schottky barriers and Fermi level pinning that prevents us from injecting carriers without overcoming a barrier first [354]. This results in a neutral regime with a finite voltage width.

The sample enters the n-doped regime when carriers start to populate the lower conduction bands at $\mathrm{V_g} \approx 0.3$ V. This region is host to the triplet $\mathrm{X}_-^{\mathrm{t}}$ and singlet $\mathrm{X}_-^{\mathrm{s}}$ charged excitons [16, 181, 191]. Their appearance has a significant impact on the exciton emission spectrum from the sample. As the Fermi level crosses the lowest conduction band, both the X_-^{s} and X_-^{t} quickly increase in brightness while the neutral exciton starts to rapidly blue-shift and dim.

On the other side of charge neutrality, the sample enters the p-doped regime at $\mathrm{V_g} \approx -0.3$ V. Here, the dominant excitation is the positively charged exciton X_+ [181].

Exciton species labeled in Fig. 6.6 were identified based on the doping regime and their spacing from the fundamental X_0 excitation at onset gate voltage.

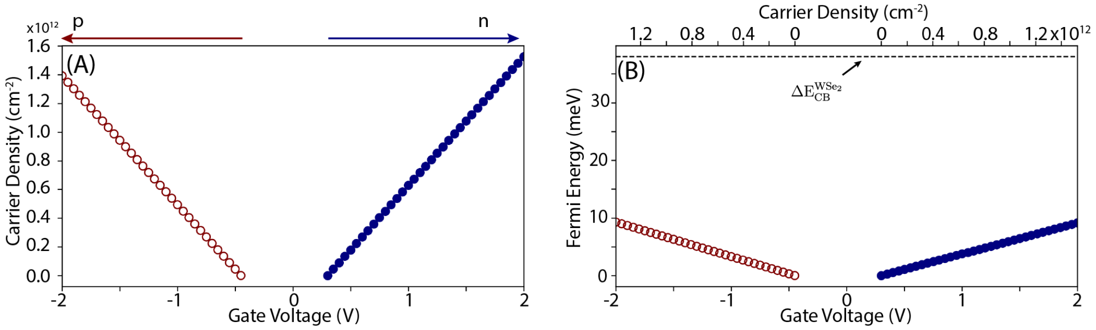

Figure 6.7: (A) Extracted carrier density as a function of applied gate voltage in a capacitive model (B) Calculated Fermi energy from carrier dependence with gate voltage. The energy corresponding to the conduction band spin-splitting is noted.

6.3.4 Extraction of Carrier Concentration

The capacitive model is the simplest model for estimating the carrier density in a sample, and it is usually accurate within 5-10%. Reduction in accuracy is highest near the onset of carrier injection due to nonlinearities that can occur just as carriers overcome the Schottky contact barrier [15]. Generally we reduce the problem to simply the geometric component, but there are technically two components that determine the capacitance of the system [282, 355]:

$$C_{\text{tot}} = (C_{\text{quantum}}^{-1} + C_{\text{geometric}}^{-1})^{-1} \tag{6.1}$$

Where,

$$C_{\text{quantum}} = e^2 \rho(E_{\text{F}}) \tag{6.2}$$

and

$$C_{\text{geometric}} = \frac{\epsilon_0 \epsilon_{\text{hBN}}}{t_{\text{hBN}}} \tag{6.3}$$

We can see that C_{quantum} only plays an important role is the density of states (DOS) $\rho(E_{\text{F}})$ is negligible. In the case that we are in either the conduction or valence band, it is generally assumed that the DOS is sufficiently large enough that C_{quantum} becomes a negligible contributing factor to the overall capacitance and that the geometric contribution is sufficient to accurately extract carrier density information.

In this case, to extract the number of free carriers in the system we can use the relation:

$$\Delta n_{e/h} = \frac{\Delta V C_{\text{geometric}}}{e} = \frac{\Delta V \epsilon_0 \epsilon_{\text{hBN}}}{e t_{\text{hBN}}} \tag{6.4}$$

Here, ΔV is defined as difference between the current gate voltage and the onset or either valence band (VB) or conduction band (CB) filling. ϵ_0 is the permittivity of free space, ϵ_{hBN} is the dielectric constant for hBN, e is the fundamental charge, and t_{hBN} is the thickness of the dieletric spacer. In our case, the dieletric spacer is the hBN between the graphite back gate and our sample, which is estimated to be 15 nm thick. The thickness was measured using AFM and is expected to have a margin of error of approximately 5%. The average dielectric background for the hBN is given as $\epsilon_{\perp} \approx 2.5$ [320]. We estimate the charge neutrality region based on the extension of neutral states in Fig. 6.6, which extends from V_g = -0.3 to 0.3 V. Fig. 6.7(A) shows the results of applying Eqn. 6.4 with our system parameters.

We can use the carrier density to extract an approximate associated Fermi level in the sample. Here, we estimate the Fermi energy based on the carrier density as:

$$E_{\text{F}} = \frac{n_{e/h}}{\rho(E)} = \frac{n_{e/h}}{m^*/(\pi\hbar^2)}, \tag{6.5}$$

with $\rho(E) = m^*/(\pi\hbar^2)$ as the density of available states when the the Fermi level is below the upper conduction band. We take the effective mass of the electron m_e^* = 0.4 m_e [186] and the effective mass of the hole to be m_h^* = 0.36 m_e [141]. $\mathrm{WSe_2}$ transitions from a degenerate to a non-degenerate state as the Fermi level enters the upper conduction band. This results in the density of states becoming $\rho(E) = m^*/(2\pi\hbar^2)$. The Fermi energy is measured from the bottom of the lower conduction band at B = 0 T. Using these physical parameters, we generate 6.7(B) and indicate that the splitting of the upper and lower conduction bands for our system is $\Delta E_\mathrm{CB}^{\mathrm{WSe_2}}$ = 38 meV [186].

We estimate that the carrier concentration in the system is $n_\mathrm{e} \approx$ 2.7×10^{11} cm^{-2} at $\mathrm{V_g}$ = 0.6 V based on the above capacitive model of our device. Based on extracted g-factors, magnetic field range, and carrier concentration we expect the carriers in the system to only be partially valley polarized.

6.3.5 2s Photoluminescence

To collect PL from both the 1s and 2s excitons, we used a green laser ($\mathrm{E_{ex}}$ = 2.33 eV) and hold the sample at $\mathrm{V_g}$ = 0 V. The results of this measurement are shown in Fig. 6.9. We find that $\mathrm{E_{X_0}^{PL}}$ = 1.728 eV and $\mathrm{E_{X_0^{2s}}^{PL}}$ = 1.859 eV. This is comparable to the values extracted from PLE, $\mathrm{E_{X_0}^{PLE}}$ = 1.727 eV and $\mathrm{E_{X_0^{2s}}^{PLE}}$ = 1.859 eV. In either case, we find the $\Delta E_{\mathrm{1s-2s}} \approx$ 132 meV. This is comparable to a spacing of $\Delta E_{\mathrm{1s-2s}} =$ 130 meV found for $\mathrm{WSe_2}$ in the literature [200, 293].

We note that while the excitation energy is high enough to probe the 3s exciton as well, we do not observe this state in our PL measurement. We attribute this to increased

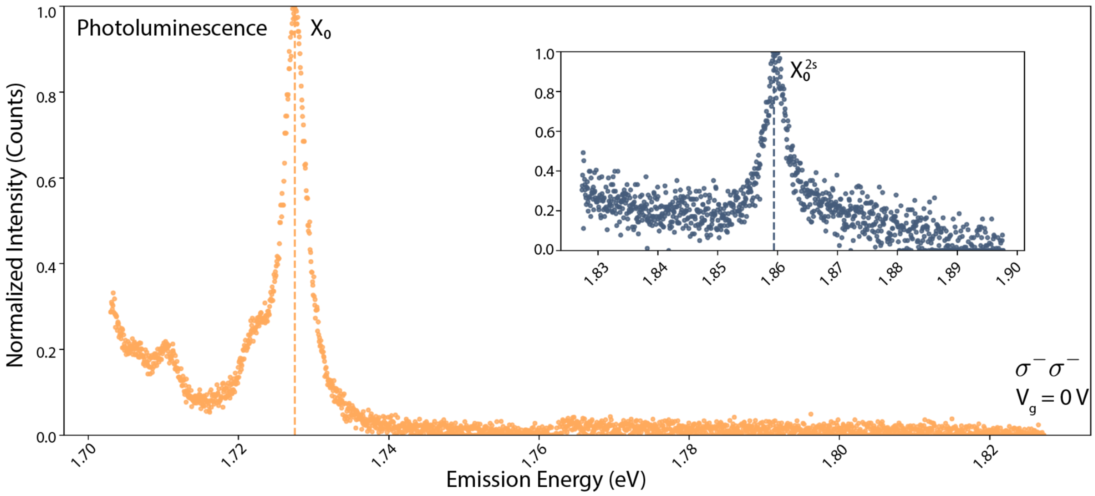

Figure 6.8: Comparison of the PL signal for X_0 and X_0^{2s} for PL measurements with E_{ex} = 2.33 eV. Both spectra are normalized to the emission maximum of their respective exciton lines and the spectral position of each is marked with a dashed line.

noise (evident in Fig. 6.9 around the X_0^{2s} region) and extremely low oscillator strength for the state due to Kasha's rule [43, 127].

In Fig. 1(D) of the main text, we are able to measure a resonance attributed to X_0^{3s} at $E_{X_0^{3s}}^{PLE}$ = 1.884 eV. Its offset of $\Delta E_{2s-3s} \approx 25$ meV is comparable to the $\Delta E_{2s-3s} = 22$ meV measured in previous reports [293].

6.3.6 X_-^{2s} Photoluminescence

To collect PL from both the $1s$ and $2s$ excitons, we used a green laser (E_{ex} = 2.33 eV) and hold the sample at V_g = 0V. The results of this measurement are shown in Fig. 6.9. We find that $E_{X_0}^{PL}$ = 1.728 eV and $E_{X_0^{2s}}^{PL}$ = 1.859 eV. This is comparable to the values extracted from PLE, $E_{X_0}^{PLE}$ = 1.727 eV and $E_{X_0^{2s}}^{PLE}$ = 1.859 eV. In either case, we find the $\Delta E_{1s-2s} \approx 132$ meV. This is comparable to a spacing of $\Delta E_{1s-2s} = 130$ meV found for WSe_2 in the literature [200, 292].

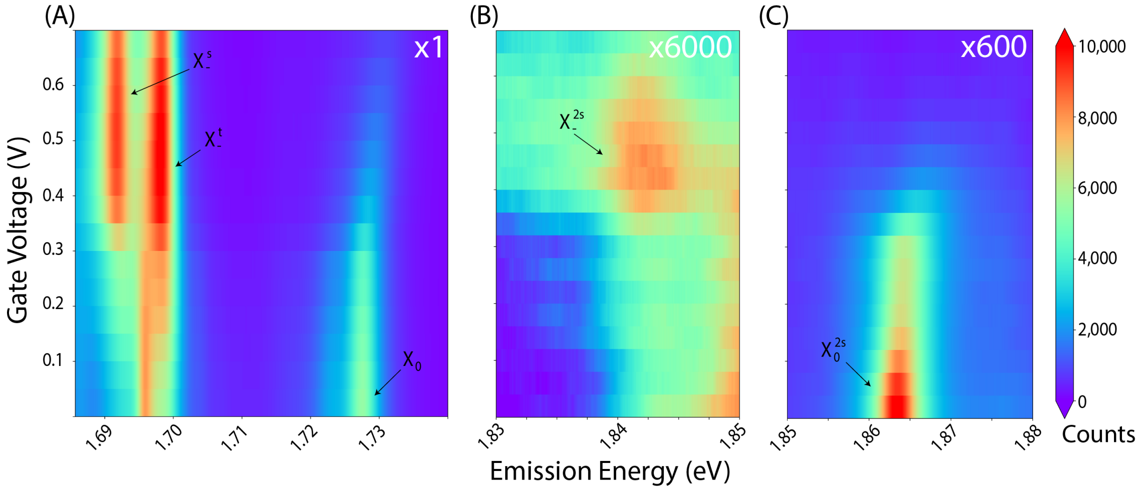

Figure 6.9: Comparison of the PL signal for X_0 and $\mathrm{X}_0^{2\mathrm{s}}$ for PL measurements with E_{ex} = 2.33 eV. Both spectra are normalized to the emission maximum of their respective exciton lines and the spectral position of each is marked with a dashed line.

We note that while the excitation energy is high enough to probe the $3s$ exciton as well, we do not observe this state in our PL measurement. We attribute this to increased noise (evident in Fig. 6.9 around the $\mathrm{X}_0^{2\mathrm{s}}$ region) and increasingly low oscillator strength for the higher n states [105].

In Fig. 1(D) of the main text, we are able to measure a resonance attributed to $\mathrm{X}_0^{3\mathrm{s}}$ at $\mathrm{E}^{\mathrm{PLE}}_{\mathrm{X}_0^{3\mathrm{s}}}$ = 1.884 eV. Its offset of $\Delta E_{2\mathrm{s}-3\mathrm{s}} \approx 25$ meV is comparable to the $\Delta E_{2\mathrm{s}-3\mathrm{s}} = 22$ meV measured in previous reports [292].

6.3.7 $\mathrm{X}_-^{2\mathrm{s}}$ Emission Channel Evolution with Gate

A similar measurement technique to what was outlined in the previous section was used to collect the PL response of the sample as the gate voltage was swept into the n-doped regime. In addition to collecting the PL recombination energies from the $1s$ and $2s$ neutral excitons, we can also see the emergence of the $2s$ charged exciton at $\mathrm{V}_\mathrm{g} \approx +0.3\mathrm{V}$.

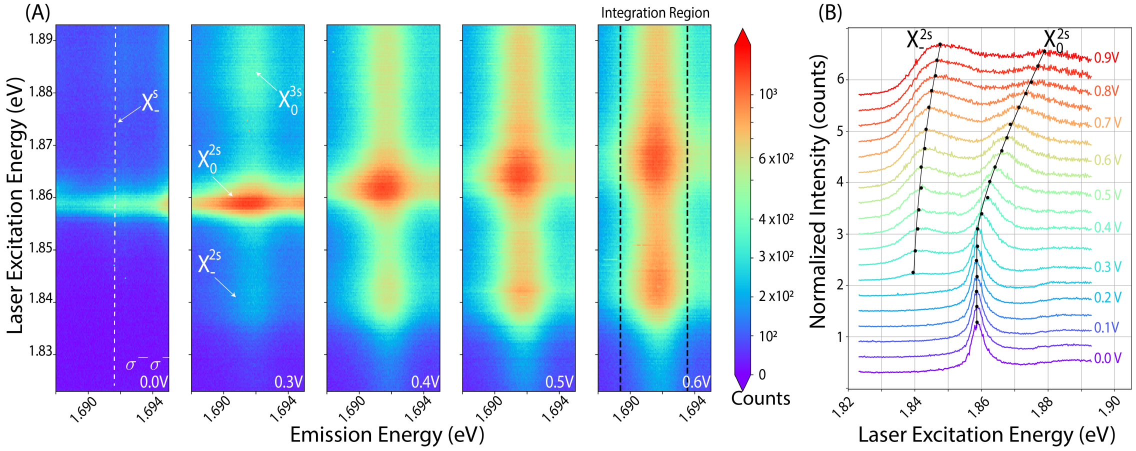

Figure 6.10: Comparison of the PL signal for X_0, X_-^{2s}, and X_0^{2s} for PL measurements with gate dependence. All spectra have been normalized to the same color bar with the scale factor highlighted in the top left of each plot. (A) The 1s exciton species were collected while the sample was illuminated with an excitation energy of 1.95 eV (633 nm). (B/C) The 2s exciton species were collected while the sample was illuminated with an excitation energy of 2.33 eV. The sample was illuminated with linearly polarized light and the collection was polarization resolved for σ^-.

The data presented in Fig. 6.10 shows the emergence of the X_-^{2s} resonance at $E^{PL}_{X_-^{2s}}$ = 1.841 eV. This is in close agreement with our reported value of $E^{PLE}_{X_-^{2s}}$ = 1.838 eV from the PLE.

Although we are able to spectrally resolve the X_0^{2s} and X_-^{2s} through PL in Fig. 6.10 (B/C), the number of counts from the radiative recombination of X_0^{2s} is over two-orders of magnitude smaller than for X_0. The PL contrast is even higher between the X_-^{2s} and $X_-^{t/s}$. Hence, in order to reliably measure the spectral profile of the higher energy excitons, we moved to PLE.

6.3.8 X_-^{2s} Vertical Cross-Section g-factor

In the main text, we analyzed the magneto-optical dependence of the 2s neutral and charged exciton resonances while monitoring the X_-^t emission channel. From their valley

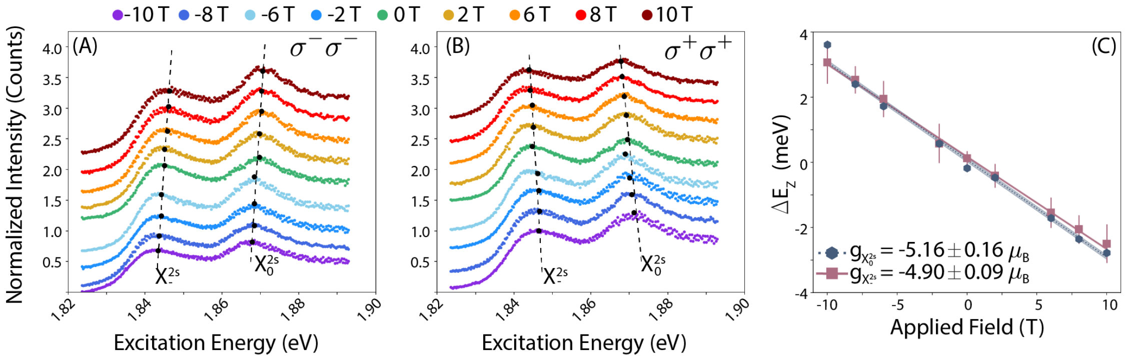

Figure 6.11: Vertical cross-sections in excitation energy as a function of field through the X_-^s emission channel for (A) ($\sigma^-\sigma^-$) and (B) ($\sigma^+\sigma^+$) marked with the corresponding peak positions for the X_0^{2s} and X_-^{2s} excitons from fitting.(C) Extracted g-factor for X_0^{2s} and X_-^{2s}. The shaded regions in panel (C) on the fit line include the error in the extracted slope.

dependent Zeeman splittings, we extracted corresponding g-factors:

$$g^{\text{triplet}}_{X_0^{2s}} = -5.21 \pm 0.11\,\mu_B \quad \text{and} \quad g^{\text{triplet}}_{X_-^{2s}} = -4.98 \pm 0.11\,\mu_B. \tag{6.6}$$

In this notation, the *triplet* superscript denotes the monitored emission channel while the subscript denotes the exciton resonance for each g-factor.

We expect that changing the monitored emission channel would not change the overall results of the extracted g-factors and verify this hypothesis by conducting the same analysis on the X_-^s emission channel. The results of this analysis are shown in Fig. 6.11, which is counterpart to Fig. 4 of the main text. We find that g-factors extracted from the X_-^s emission channel for the excited exciton species are:

$$g^{\text{singlet}}_{X_0^{2s}} = -5.16 \pm 0.16\,\mu_B \quad \text{and} \quad g^{\text{singlet}}_{X_-^{2s}} = -4.90 \pm 0.09\,\mu_B. \tag{6.7}$$

The g-factors extracted from the X_-^s and X_-^t emission channels agree within experimental error. This allows us to make the important conclusion that the results from our PLE

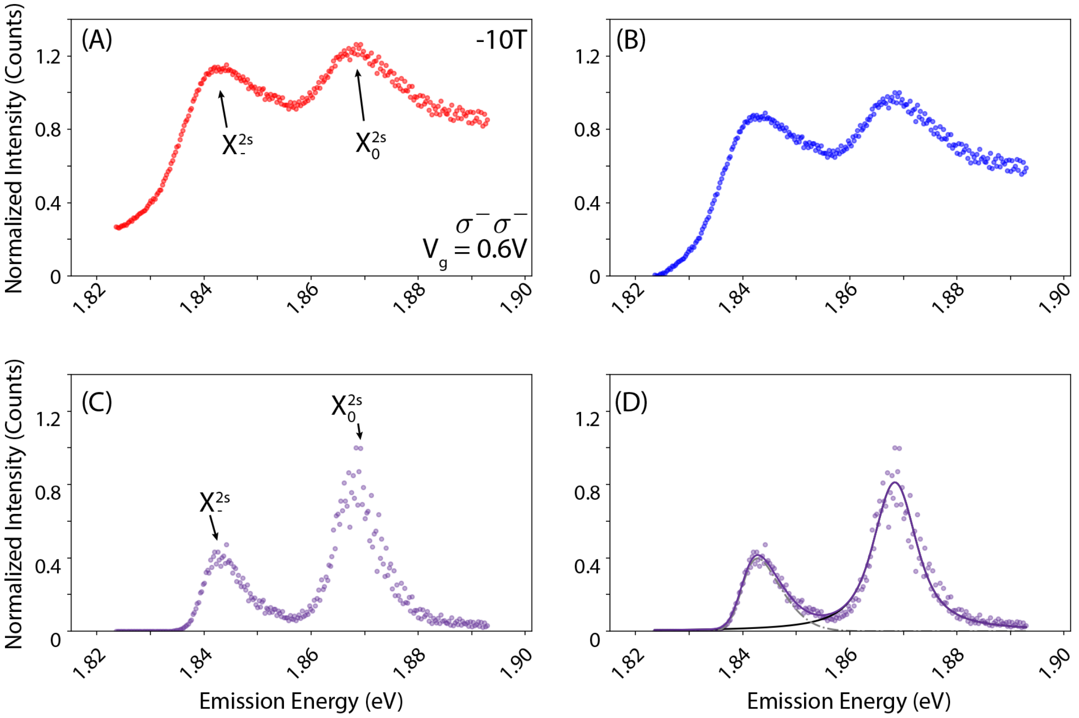

Figure 6.12: (A) Raw Vertical cross-sections of the X^{t}_{-} emission channel at -10T and 0.6V. The data has been normalized to the maxima of the extracted spectra. (B) The same data after the lowest value in the spectra has been subtracted from all points and data has been renormalized to the maxima. (C) Power sharpening of the spectra in panel (B). (D) Peak fitting of the X_0^{2s} and X^{2s}_{-}. The denoted input/output polarizations, magnetic field, and gate voltage in panel (A) are the same for all panels.

measurement are independent of the analyzed emission line.

6.3.9 Fitting Procedure for Extracting g-factor

The Zeeman interaction induced splitting is quite small in TMDs, so it is important to take the utmost care to extract accurate peak center information to produce reliable g-factor measurements. In the literature, common techniques for doing this include using the peak maxima or using a weighted-average fitting scheme [319]. Both techniques work well for reasonably separated peaks. However, if there is overlap between peak envelopes in a multipeak spectra, both can give erroneous results [191]. In our work, to combat this issue, we introduce use of digital signal processing (DSP) techniques to enhance a peak-fitting approach. Specifically we introduce the “power law method” [56, 221, 310].

In this technique, the spectra is sharpened by raising each point in the data to a power greater than 1. The result is that peaks “sharpen” i.e. become narrower and the background/overlap areas between the peaks becomes minimized, effectively giving us a better signal contrast between overlapping peaks. This is namely due to a narrowing of the peaks, so it must be noted that this technique not advisable for extracting information such as full width at half max as a function of a varied parameter. Additionally, it is worth pointing out that while the peaks become narrower the overall shape of the envelope will not change – i.e. if a peak is symmetric this method will preserve that symmetry just as it would preserve asymmetry in a peak that has an asymmetric envelope. Some work has indicated that excessive peak sharpening in this method can reduce asymmetry but it cannot create or destroy that style of line shape; that is dictated by the underlying physics of the system [310]. Crucially though for our purposes, this method preserves the central signal of the peak which is our desired quantity to extract. To walk through the power-law method used in this manuscript, we turn to Fig. 6.12.

Fig. 6.12 (A) contains an example of a raw, vertically integrated cut through the $\mathrm{X}_{-}^{\mathrm{t}}$ emission line with $\sigma^{-}\sigma^{-}$ excitation/collection. Since this technique works best with a minimal background, we first subtract the lowest value of the spectra from the entirety of the signal – Fig. 6.12 (B). Next, we apply a power filter and renormalize the data to the new maxima in Fig. 6.12 (C).

Once the sharpening is performed, the data can be fit with the model of choice. Here, we use a Voigt function to model $\mathrm{X}_{0}^{2\mathrm{s}}$ and an asymmetric Voigt function to model

X_-^{2s}. While the intrinsic lineshape of an exciton is generally assumed to be Lorentzian, there are many sources of potential inhomogeneous broadening (such as lattice defects, exciton-carrier scattering, or temperature induced thermal broadening) that are generally modelled as a Gaussian envelope. Thus, the Voigt lineshape seems to be the best choice since it is a convolution of these two possible sources of signal and it makes no assumptions about the present sources of broadening [3]. Both in the raw and power-sharpened spectra it is clear that the X_-^{2s} state is asymmetric. An asymmetric tail on the lower energy side of a peak is relatively common and is usually indicative of a phonon side band. Higher energy asymmetry is less commonly observed, and generally is attributed to inhomogeneity in the dielectric environment, usually from contamination during the encapsulation process [177, 359]. However, in that case, since optical measurements are local in nature one would expect to see this blue tail on all peaks in a spectra collected at a given location on the sample. Since it is obvious in Fig. 6.12 (C)/(D) that the asymmetry is rather limited to the X_-^{2s} signal, we attribute this asymmetry to the presence of two broad, closely spaced peaks that cannot be spectrally resolved. This picture is consistent with the expected presence of a negatively charged doublet as in the ground state, combined with the reduced intervalley exchange splitting in the excited state discussed in the main text as well as in the literature [10].

The fitting was performed using the LMfit library in python, which includes Voigt and asymmetric (skewed) Voigt models as built-in functions [213]. The library builds on the Levenberg–Marquardt algorithm – sometimes also referred to as a damped least-squares optimization approach – for optimizing the fit of a input function to the data provided [165,202]. The repeated fitting during the optimization process by the algorithm

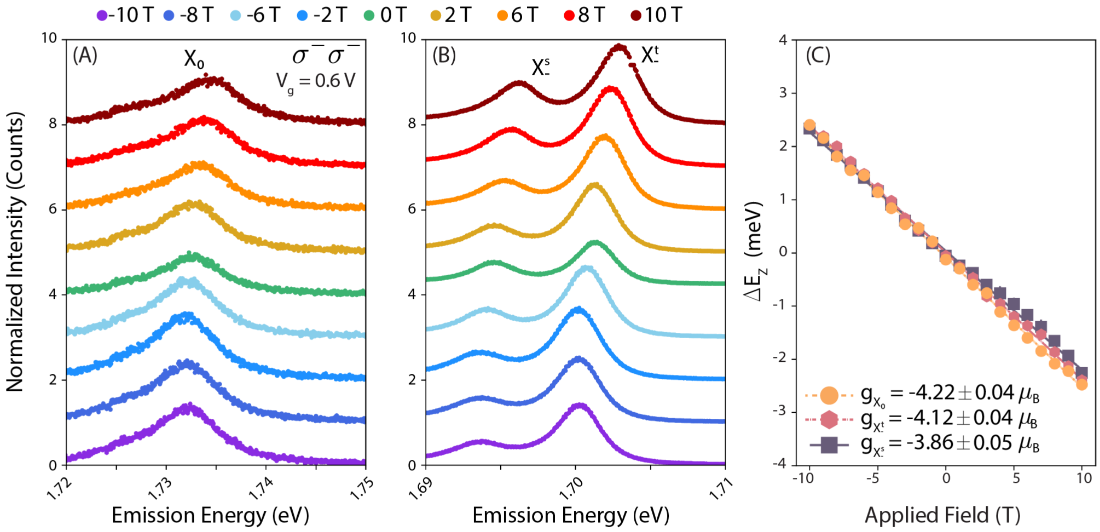

Figure 6.13: $1s$ PL spectra at V_g=0.6V for the (A) X_0, (B) X^t_-/X^s_-. (C) Extracted g-factors from fitting PL as a function of field for X_0, X^t_-, and X^s_-. For all measurements E_{ex}=1.92 eV

allows a standard error to be extracted for all input parameters. Error bars used in the main and supplementary texts for extracted points correspond to the standard error of that point. An example of the resulting fit using this method is shown in Fig. 6.12 (D).

6.3.10 Ground State PL and g-factor

The vast majority of g-factor measurements reported for TMDs in the literature are for $1s$ states with a limited number of results for X_0 Rydberg states. For the purpose of comparison to both the literature and between differing n states, we measured the g-factor of X_0, X^t_-, and X^s_- in our system at V_g = 0.6 V. This is same carrier environment as our main text measurements of the $2s$.

The supplemental measurements of these states were performed using PL with E_{ex} = 1.92 eV. The extracted plots for X_0 and X^s_-/X^t_- are shown in Fig. 6.13(A) and (B), respectively. We note that the relative intensity of X^t_-, and X^s_- changes from -10 T to 10

T indicating that there is a degree of valley polarization that is induced by the Zeeman splitting. However, as neither state is fully suppressed, the system is never fully valley polarized.

To extract the peak centers, we use a similar peak-fitting technique as described in 6.3.9, but with the exception of using symmetric Voigt functions to fit each relevant peak. Using this method we find that ground state g-factors of these states are all $\approx -4\mu_{\mathrm{B}}$:

$$g_{\mathrm{X_0}} = -4.22{\pm}0.04\mu_{\mathrm{B}}, \quad \mathrm{g}_{\mathrm{X^t_-}} = -4.12{\pm}0.04\mu_{\mathrm{B}}, \quad \text{and} \quad \mathrm{g}_{\mathrm{X^s_-}} = -3.86{\pm}0.05\mu_{\mathrm{B}}. \tag{6.8}$$

These results are plotted in Fig. 6.13(C). Our findings are consistent with the relevant literature on WSe_2 [171,289].

6.3.11 Estimating the Intercellular Contribution to g for Charged Excitons in Single-Particle Formalism

It is common practice in the literature to use the orbital magnetic moment (OMM) to calculate the intercellular contribution to g for excitons arising from the Berry curvature [44,63,80,289]. Charged excitons also experience a contribution from the Berry curvature that is induced by the exchange gap near the ±K points [338]. The resulting OMM is written as,

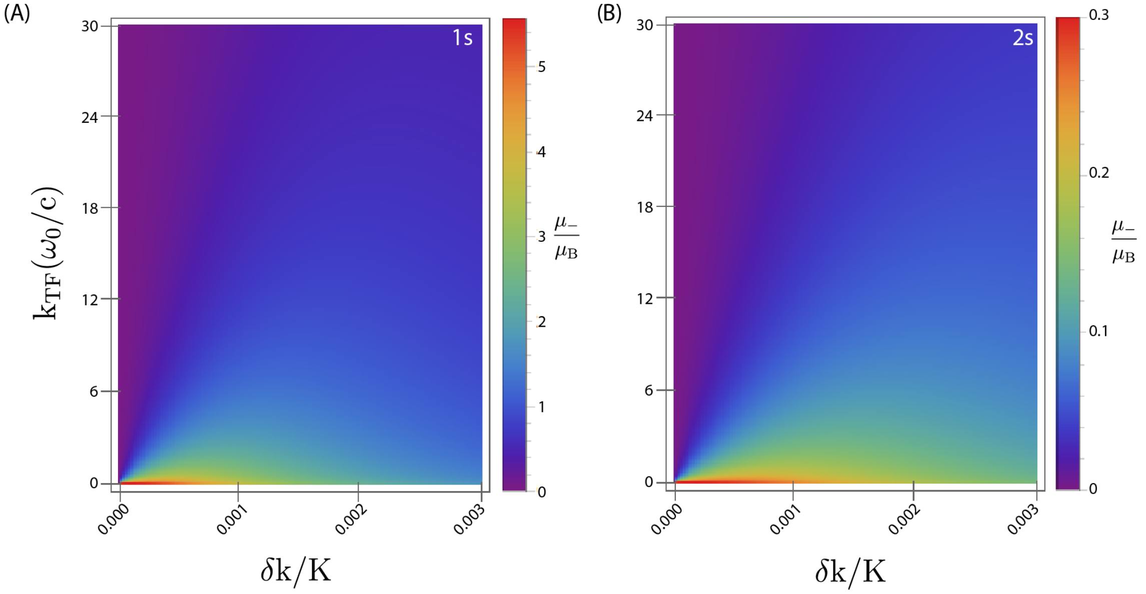

Figure 6.14: Valley orbital magnetic moment for a charged exciton as a function of the center of mass k from the valley center K for different carrier concentrations (expressed in $\mathrm{k_{TF}}$) for (A) $1s$ charged exciton and (B) $2s$ charged exciton. Note the difference in scale for the resulting magnetic moment in each panel.

$$\begin{aligned} L_n(k) &= \frac{m}{\hbar} E_\mathrm{g}(k)\Omega_{\mathrm{X}_-}(k) \\ &= \underbrace{\delta_\mathrm{ex}\left(1+\frac{4J^2k^4}{K^2\delta_\mathrm{ex}^2(k+k_\mathrm{TF})^2}\right)^{1/2}}_{E_\mathrm{g}(k)} \underbrace{\frac{2J^2}{K^2\delta_\mathrm{ex}^2}\frac{k^2(k+2k_\mathrm{TF})}{(k+k_\mathrm{TF})^3}\left(1+\frac{4J^2k^4}{K^2\delta_\mathrm{ex}^2(k+k_\mathrm{TF})^2}\right)^{-3/2}}_{\Omega_{\mathrm{X}_-}(k)}. \end{aligned} \tag{6.9}$$

Thus, the charged exciton valley magnetic moment resulting from this exchange interaction is written as,

$$\mu_{\mathrm{X}_-}(k) = \frac{e}{2m}L(k) = \frac{eJ^2}{\hbar K^2\delta_\mathrm{ex}}\frac{k^2(k+2k_\mathrm{TF})}{(k+k_\mathrm{TF})^3}\left(1+\frac{4J^2k^4}{K^2\delta_\mathrm{ex}^2(k+k_\mathrm{TF})^2}\right)^{-1}. \tag{6.10}$$

Here, J is the e$^-$/h$^+$ exchange coupling strength, k_{TF} is the Thomas-Fermi wavevector for the carrier screening, δ_{ex} is the exchange-induced gap discussed previously, and K is the position of the valleys in k-space [338].

Fig. 6.14 shows the results of evaluating Eqn. 6.10 to extract the magnetic moment as a function of the center of mass (COM) momentum k with respect to its distance from the valley center K and Thomas-Fermi wave vector. The Thomas-Fermi wave vector is used as a proxy in the system the carrier concentration present with 10 $\omega_0/c \simeq 10^{11}\mathrm{cm}^{-2}$ [289,338]. Panel (A) shows the results for a $1s$ charged exciton while panel (B) shows the results for a $2s$ charged exciton. Though the plots look very similar, note the difference in scale for μ_{X_-}: the resulting valley OMM for the $2s$ charged exciton is much smaller than for the $1s$ charged exciton. This difference largely results from an increase in the Bohr radius, while both J and δ_{ex} decrease.

6.3.12 Raman Phonon Lines in X_0 PLE Emission Response

Previous experiments exploring the $\mathrm{X}_0^{2\mathrm{s}}$- $\mathrm{X}_0^{3\mathrm{s}}$ energy regime via PLE have demonstrated two prominent Raman modes resulting from electron-phonon coupling between WSe_2 and hBN that become bright when their emission energies match X_0 [49, 121, 267]; both are labeled in Fig. 1(D) and 2(A) of the main text. The first is an optical phonon, ZO(hBN), that is silent in pure hBN and becomes prominent only when in close proximity to WSe_2 [49, 121, 267]. The second is a combined mode of ZO(hBN) and an out-of-plane optical vibrational mode in WSe_2, $\mathrm{A}_{1\mathrm{g}}(\mathrm{WSe}_2)$ [121]. We measure the spectral displacement of these two phonon line to be 31.1 meV, which is in good agreement with prior reports [123].

Since the ZO(hBN) + $\mathrm{A_{1g}}$($\mathrm{WSe_2}$) phonon has the same energy as the gap between $\mathrm{X_0^{2s}}$ and $\mathrm{X_0}$, when the laser is tuned to the energy of $\mathrm{X_0^{2s}}$, the Raman signal overlaps the $\mathrm{X_0^{2s}}$ resonance and becomes orders of magnitude brighter than any other signal from the sample. This degeneracy can be broken through gating as the $\mathrm{X_0^{2s}}$ resonance blue-shifts with increasing carrier density and the Raman modes are unaffected. Fig. 2(A) depicts this shift, showing the spectral isolation of $\mathrm{X_0^{2s}}$ from the ZO(hBN)+$\mathrm{A_{1g}}$($\mathrm{WSe_2}$).

Chapter 7: Fundamentals of Optical Orbital Angular Momentum

As we discussed in the introduction, the second set of work detailed in this thesis is a theoretical study looking at the effects of twisted light on the spectrum in 2D semiconductors (including TMDs). An overview on twisted light, or light that carries additional orbital angular momentum (OAM), is given here as a primer for understanding Ch. 8. First we discuss the history of twisted light, and then take a detailed look at the types of momentum present in light.

7.1 Optical Orbital Angular Momentum

In the late 1980s, Coulett *et al.* discovered vortex solutions to the optical Bloch equations and proposed the concept of optical vortices or "twisted light" [52]. However, it was not until a few years later that it became clear that the twisted phase of these light beams was associated with non-zero OAM. In 1992, Allen *et al.* published a landmark paper in which they proposed that Laguerre-Gaussian (LG) laser modes had well defined OAM due to their intrinsic azimuthal phase dependence $e^{i\ell\phi}$ [7]. This phase dependence results in tunable quantized momentum given as $\ell\hbar$ per photon, where ℓ is the azimuthal mode index. Scientists had known for a long time that multipole transitions could produce radiation that possessed additional angular momentum beyond spin [57]. However, study of these “forbidden” transitions remained difficult experimentally, and the left the origins of this additional angular momentum as a topic of debate through the 1990s. He *et al.* verified Allen’s proposal in 1995 [106].

The work by Allen *et al.*, which now has more than 5,000 citations, spawned an entirely new field in the study of light-matter interaction. Research utilizing OAM spans the fields of microscopy [245], large-scale telecommunications [167, 269, 333], and astronomy [296, 298] amongst many others. Some excellent review on the topic can be found in Refs. [17, 82, 222, 223, 225, 272].

7.2 Types of Angular Momentum in Light

7.2.1 Linear Momentum

The concept of radiation pressure significantly predates our modern understanding of electromagnetism that derives from Maxwell’s equations. Nearly 200 years before Maxwell’s work, Kepler utilized the concept to explain why the tails of comets always point away from the sun [222]. Radiation pressure stems from the linear momentum of light. In 1884, while exploring Maxwell’s work, Poynting found that the directional energy flux of the electromagnetic field is,

$$\vec{S} = \frac{1}{\mu_0}\vec{E} \times \vec{B}. \tag{7.1}$$

Here $\vec{S}$ is the Poynting vector, $\vec{E}$ is the electric field vector, $\vec{B}$ is the magnetic field vector and μ_0 is the vacuum permeability [236].

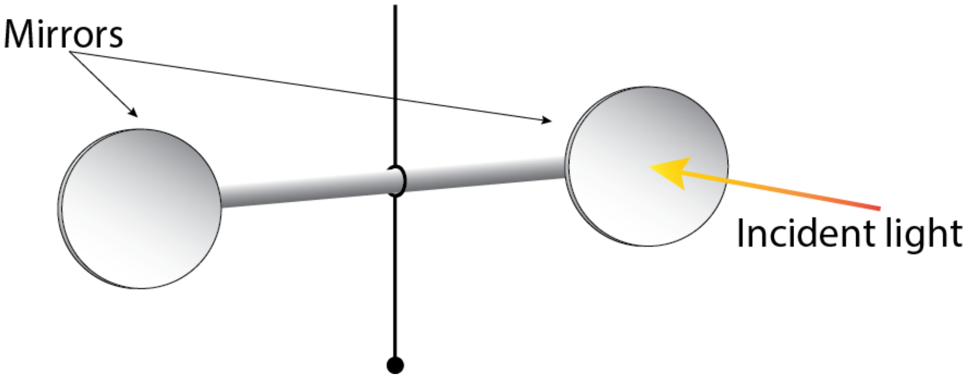

Figure 7.1: Illustration of the Nichols radiometer.

From this, one can find that the linear momentum of the electromagnetic field is,

$$\vec{p} = \frac{\vec{S}}{c^2}, \tag{7.2}$$

where c is the speed of light. The radiation pressure exerted by that field is,

$$p_{\text{rad}} = \begin{cases} \frac{\langle S \rangle}{c}, & \text{for a perfect absorber} \\ \frac{2\langle S \rangle}{c}, & \text{for a prefect reflector} \end{cases} \tag{7.3}$$

Here, $\langle S \rangle = I$, the intensity of the incident light.

In 1901, Nichols and Hull devised an experiment to measure radiation pressure using two silvered mirrors forming a torsion balance hanging from a fiber; a simple illustration of this is shown in Fig. 7.1. In the real experiment, the torsion pendulum was inside a bell jar where the ambient pressure could be controlled. They were able to show that the mirror did indeed deflect under illumination and that the deflection depended on the intensityof the light as expected from Eqn. 7.3 [214].

Adapting this work to the concept of wave-particle duality, in 1905 Einstein showed

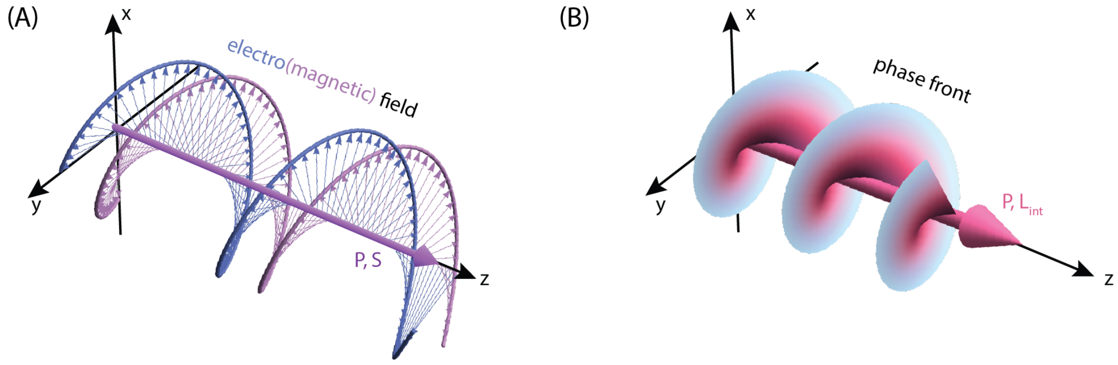

Figure 7.2: (A) Spin angular momentum with illustration of the electromagetic field of circularly polarized light at some instant, t, along with the direction of spin angular momentum (S). (B) Intrinsic OAM arising in a vortex beam with illustration of the phase front at some instant, t, along with the direction of momentum (L_{int}). In both panels P is the direction of propagation.

that photoelectric effect (and blackbody radiation) could be explained if the linear momentum of a single was given by,

$$\vec{p} = \hbar\vec{k}, \tag{7.4}$$

where is the wave number associated with the wavelength of the photon [71]. Today, the relationship for linear momentum is directly utilized by those working the field of atomic and molecular optical physics for trapping and cooling schemes [222].

7.3 Angular Momentum

In addition to linear momentum, light also possesses angular momentum. Here, we will discuss spin angular momentum (SAM), which is associated with the polarization of the light beam and OAM, which is associated with the phase evolution of the light.

7.3.1 Spin Angular Momentum

Beyond his work with linear momentum, Poynting made an important contribution to our understanding of angular momentum in light in 1909 when he inferred that CPL should carry angular momentum [237]. Making an analogy to a rotating cylinder, in this work Poynting reasoned that CPL should posses non-zero angular momentum in the same direction as it propagated. To test this, he suggested that CPL should exert a torque on a wave plate as it passes through. Poynting's theory was experimentally verified by Beth in 1935 [21, 22].

Today, we generally referred to this kind of angular momentum as SAM, due to its quantum mechanical origins. Photons are spin-1 particles and RCPL and LCPL are the manifestations of the two eigenstates of the spin operator. In this formalism, we find that SAM for a single photon is given by,

$$S_z = \sigma_z \hbar. \tag{7.5}$$

Here, $\sigma_z = \pm 1$ and corresponds to the handedness of the light. Linearly polarized light, which is equal parts LCPL and RCPL that are in phase, has no spin angular momentum. In his classical theory, Poynting found that the ratio of the angular to linear momentum with respect to the axis of the beam was $\lambda/2\pi$; the photon picture yields the same result. An illustration of SAM can be found in Fig. 7.2(A).

7.3.2 Orbital Angular Momentum

Finally we come to intrinsic orbital angular momentum (IOAM) or OAM, the type of angular momentum that is more relevant to this work. As mentioned in the introduction, OAM is intrinsically linked to vortex beams. Vortex beams have a helical phases structure with an azimuthal (ϕ) angular dependence – $\mathrm{e}^{i\ell\phi}$ – which causes them to carry OAM that is independent of the polarization of the light [7]. An illustration of the twisted phase of a beam with OAM is shown in Fig. 7.2(B).

We can use a ray optics picture to understand how this phase dependence results in OAM. The phase rotation is correlated with twisting of the Poynting vector itself, which results in rays that are skewed at some angle β at every point on the wavefront [224]. If we pick a point along the phase front at fixed radius r, we can think of the beam like a phase ramp with constant gradient in the azimuthal direction. At point r this means that the base of the phase ramp has a length of $2\pi r$ and a height of $\ell\lambda$. This allows us to calculate the skew of a ray at any point along the phase front,

$$\begin{aligned} \beta &= \frac{\ell\lambda}{2\pi r} \\ &= \frac{\ell}{kr} \end{aligned} \tag{7.6}$$

in terms of both the wavelength and the wavevector $k = \frac{2\pi}{\lambda}$. Each of these rays carriers linear momentum, so the OAM carrier by the beam is given by,

$$\begin{aligned} |\vec{L}| &= |\vec{r} \times \vec{P}| \\ &= |r\hbar k \sin(\beta)| \\ &= \ell\hbar. \end{aligned} \tag{7.7}$$

Unlike SAM, the quantized values of ℓ are not limited to ± 1 and can take on any integer value [162]. In fact, researchers have been able to generate beams up to $\ell = 10,000\hbar$ in the lab [78].

The phase rotation results in a singularity at the center beam which causes a "donut"-like beam spatial profile where the intensity at the center of the beam is zero. As an illustration for what this looks like we turn to LG modes which take the from,

$$LG_{\ell p}(r, z, \phi) = \sqrt{\frac{2p!}{\pi(p + |\ell|)!}} \frac{1}{w} \left(\frac{r\sqrt{2}}{w}\right)^{|\ell|} L_p^{|\ell|}\left(\frac{2r^2}{w^2}\right) e^{\frac{-r^2}{w^2}} e^{\frac{ikr^2}{2R}} e^{-i(2p+|\ell|+1)\Psi} e^{-i\ell\phi}. \tag{7.8}$$

Here, p is the radial mode index, $L_p^{|\ell|}$(x) is a Laguerre polynomial. w, R, and Ψ have an implicit z-dependence and take the form,

$$w(z) = w_0\sqrt{1 + (z/z_R)^2)} \tag{7.9a}$$

$$R(z) = z(1 + (z_R/z)^2) \tag{7.9b}$$

$$\Psi(z) = arctan(z/z_R) \tag{7.9c}$$

$$z_R = \frac{1}{2}kw_0^2, \tag{7.9d}$$

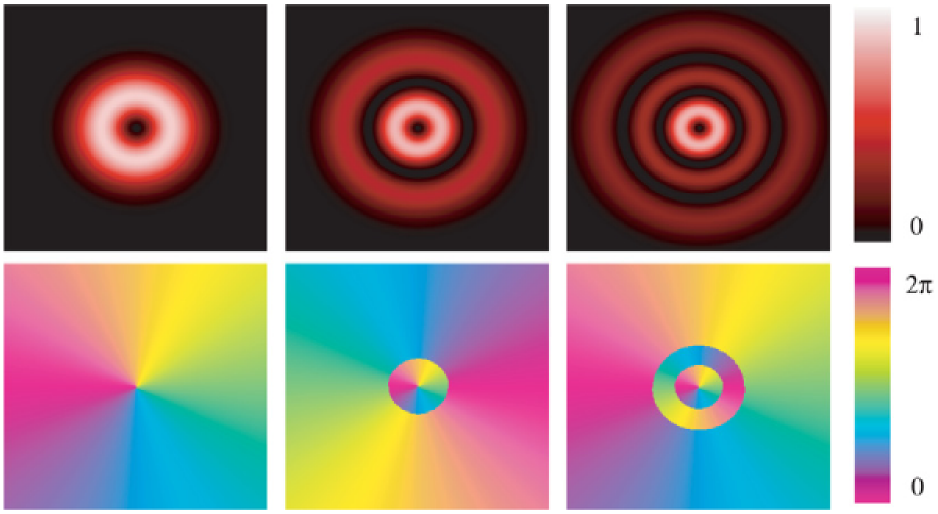

Figure 7.3: Intensity (top panels) and phase (bottom panels) of LG modes with different ℓ. The intensity if normalized to the maximum. From left-to-right the modes are: LG_{01}, LG_{11}, and LG_{21}. The figure is from Ref. [335].

$w(z)$ is the laser spot size (defined by the radius for which the intensity of the Gaussian beam is 1/e^2 its central value), $R(z)$ is the radius of curvature of the wavefront, $\Psi(z)$ is the Gouy phase, z_R is the Rayleigh range, and w_0 is the waist radius of the beam [13, 318]. These definitions are the same as those found for a traditional Gaussian beam. In the event that $\ell = 0$, we get light with no azimuthal phase dependence and therefore no OAM. However, for light with $\ell \neq 0$, the phase dependence produces OAM and the beam profile consists of p + 1 concentric rings [13, 225]. An illustration of the spatial profile and corresponding phase distribution for different LG modes can be found in Figure 7.3.

Though we do not discuss it further here, the curious reader can refer to Ref. [335] for a nice overview on different labs methods for generating beams with OAM, since LG beams are by no means the only option.

Chapter 8: Two-dimensional excitons from twisted light and the fate of the photon's orbital angular momentum

8.1 Notes

This chapter is largely taken verbatim from our paper "Two-dimensional excitons from twisted light and the fate of the photon's orbital angular momentum" T. Graß, U. Bhattacharya, J.C. Sell, and M. Hafezi, *arXiv:2201.13058* (2022) [96]. It is currently under review for peer-reviewed publication. Small alterations have been made to fit references from earlier sections to this chapter. It should be noted that in comparison to the other sections of this thesis these results apply not only to TMDs, but also other 2D semiconductor systems.

8.2 Manuscript

8.2.1 Abstract

As the bound state of two oppositely charged particles, excitons emerge from optically excited semiconductors as the electronic analogue of a hydrogen atom. In the two-dimensional (2D) case, realized either in quantum well systems or truly 2D materials such as transition metal dichalcogenides, the relative motion of an exciton is described by

two quantum numbers: the principal quantum number n, and a quantum number j for the angular momentum along the perpendicular axis. Conservation of angular momentum demands that only the $j = 0$ states of the excitons are optically active in a system illuminated by plane waves. Here we consider the case for spatially structured light sources, specifically for twisted light beams with non-zero orbital angular momentum per photon. Under the so-called dipole approximation where the spatial variations of the light source occur on length scales much larger than the size of the semiconductor's unit cell, we show that the photon (linear and/or angular) momentum is coupled to the center-of-mass (linear and/or angular) momentum of the exciton. As a result, our study shows explicitly that the additional orbital angular momentum imparted by spatially structured light sources cannot be used modify the 2D exciton spectrum by facilitating dipole forbidden transition as it does in atomic systems.

8.2.2 Introduction

Excitons are the bound states formed by an electron-hole pair in a semiconductor crystal [105, 260], and as such, they are close analogues of the hydrogen atom. Excitons manifest themselves as optical absorption or emission lines within the band gap of the material. In the theoretical treatment of exciton formation, light-matter interaction is most often described within the dipole approximation. This approximation disregards the spatial structure of the light field, which is justified by the tiny length scale on which the de Broglie waves vary, as compared to the wavelength of the light [51].

The dipole approximation gives rise to optical selection rules related to the conservation of angular momentum during an optical transition. Within the dipole approximation, light may carry only one quantum of angular momentum per photon, realized through the circular polarization of the light; therefore, optical transitions can change angular momentum quantum numbers of the matter only by one unit. In atoms, this rule selects the s-to-p or p-to-d transitions; in semiconductors, this affects the orbitals of the bands in an analogous way. As a consequence of the dipole approximation, excitons created from such a dipole transition do not carry angular momentum; that is, the respective quantum number j is zero. Moreover, as established by the Elliott formula [72], the transition amplitude quickly decays with the principal quantum n (as $(n+1/2)^{-3}$ in 2D), such that the exciton spectrum is strongly dominated by transitions into the $1s$ state, i.e. the state corresponding to the hydrogenic ground state. A common technique to allow optical access to the p exciton series in semiconductors is nonlinear, two-photon spectroscopy [20, 311].

It is clear that effects beyond the dipole approximation can modify the exciton spectrum. In particular, the dipole approximation disregards the possible spatial structure of the light beam, which in the case of twisted light results in a well-defined orbital angular moment (OAM) per photon [7, 301, 335]. The photon OAM essentially adds another tunable degree of freedom for tailoring light-matter interaction. It has been proposed to use this new degree of freedom for generating a topological band structure by breaking time-reversal symmetry [23], for pumping electrons in a magnetic field through the Landau level [32, 88, 97], or for producing topological defects such as vortices or skyrmions [50, 86, 87, 130]. A striking demonstration of how the optical spectrum can be modified by photon OAM has been achieved in an experiment with trapped ions [263], showing a dipole-forbidden atomic s-to-d transition in the presence of a twisted light field that is the result of additive interaction between SAM and OAM. Given the analogy between an exciton and a hydrogen atom, it might be expected that twisted light can generate transitions into dipole-forbidden excitonic levels in a similar manner. This indeed has theoretically been suggested for the case of Rydberg excitons [138]. On the other hand, there have also been experiments with atomic and polaritonic condensates in which twisted light has led to the formation of vortices [9, 148]. This indeed would suggest that the orbital angular momentum of the photon is absorbed by the center-of-mass (COM) degree of freedom of the exciton, rather than by the relative motion of electron and hole. Also, in the strong drive limit and absence of Coulomb binding, OAM of light can lead to Floquet vortex creation, but it is an open question how strong drive and exciton formation compete with each other.

To better understand the fate of the photonic OAM in excitonic transitions, the present paper studies the case of a single exciton in a two-band semiconductor model in 2D in the presence of a twisted light source. We extend theoretical studies of band-to-band transitions in semiconductors or graphene with twisted light, presented in Refs. [75, 239, 240], to the case where Coulomb interactions give rise to exciton formation. Our analysis demonstrates that, under the assumption that the spatial variation of the light occurs on a length scale much larger than the size of the unit cell of the semiconductor crystal, transitions into excitonic levels $j \neq 0$ remain completely forbidden even in the presence of twisted light. Instead, the structure of the light field selects the COM degree of freedom of the excitons. Since it is the relative motion that essentially determines the energy of an exciton, it follows that the twist of the light source does not modify the excitonic spectrum. In this context, we also note that small shifts of the spectrum are possible if the COM dispersion of the exciton is taken into account. This indeed has been observed in a recent experiment with excitons in a Dirac material, which found a blueshift of the exciton lines for sufficiently large values of photon OAM [277].

Our paper is organized in the following way: In Sec. II, we develop the general analytical formalism to describe exciton transitions in structured light beam. In Sec. III, we specifically address the case of a Bessel beam. To evaluate this case, we make use of the rotational symmetry of the beam which makes an explicit numerical treatment feasible. With this we are able to show, for a finite system size, that the s states are optically bright, in quantitative good agreement with the 2D Elliot formula, independent from the choice of the photon OAM. Our numerical calculation also confirms that the COM momentum of the exciton is peaked at the linear momentum of the photon.

8.2.3 General Analytical Model

8.2.4 Light-matter coupling

We consider a 2D semiconductor with Bloch bands λ and wave vector $\mathbf{k}$, described by Bloch functions $\varphi_{\lambda,\mathbf{k}}(\mathbf{r}) = \frac{1}{\sqrt{S}} e^{i\mathbf{k}\cdot\mathbf{r}} u_{\lambda,\mathbf{k}}(\mathbf{r})$, where $u_{\lambda,\mathbf{k}}(\mathbf{r}+\mathbf{R_i}) = u_{\lambda,\mathbf{k}}(\mathbf{r})$ with $\mathbf{R}_i$ a lattice vector. In this basis, the crystal Hamiltonian reads $H_0 = \sum_{\lambda,\mathbf{k}} \epsilon_{\lambda,\mathbf{k}} c^\dagger_{\lambda,\mathbf{k}} c_{\lambda,\mathbf{k}}$, with $c_{\lambda,\mathbf{k}}$ ($c^\dagger_{\lambda,\mathbf{k}}$) being the annihilation (creation) operators, and $\epsilon_{\lambda,\mathbf{k}}$ the dispersion. We assume a light field given by a vector potential $\mathbf{A}(\mathbf{r}) = A(\mathbf{r}) \cdot \mathbf{e}$ in the Coulomb gauge, such that the light-matter Hamiltonian is given by:

$$H_{\mathrm{LM}} = \sum_{\lambda',\lambda} \sum_{\mathbf{k}',\mathbf{k}} \frac{ie\hbar}{M} \langle \lambda', \mathbf{k}' | \mathbf{A}(\mathbf{r}) \cdot \nabla_{\mathbf{r}} | \lambda, \mathbf{k} \rangle c^{\dagger}_{\lambda',\mathbf{k}'} c_{\lambda,\mathbf{k}}. \tag{8.1}$$

We are only interested in the matrix element

$$h^{\lambda',\lambda}_{\mathbf{k}',\mathbf{k}} = \langle \lambda', \mathbf{k}' | \mathbf{A}(\mathbf{r}) \cdot \nabla_{\mathbf{r}} | \lambda, \mathbf{k} \rangle = \int d^2 r \varphi^{*}_{\lambda',\mathbf{k}'}(\mathbf{r}) A(\mathbf{r}) \mathbf{e} \cdot \nabla_{\mathbf{r}} \varphi_{\lambda,\mathbf{k}}(\mathbf{r}), \tag{8.2}$$

with $\lambda = \mathrm{c}$ and $\lambda' = \mathrm{v}$, i.e. transitions amplitudes between conduction and valence band. Taking into account the orthonormality of the bands, the derivative operator has to act onto the lattice-periodic function $u_{\lambda,\mathbf{k}}$ to yield non-zero contributions. Explicitly, we have

$$h^{\mathrm{v,c}}_{\mathbf{k}',\mathbf{k}} = \frac{1}{S} \int d^2 r A(\mathbf{r}) e^{i(\mathbf{k}-\mathbf{k}')\cdot\mathbf{r}} u^{*}_{\mathrm{v},\mathbf{k}'}(\mathbf{r}) \mathbf{e} \cdot \nabla_{\mathbf{r}} u_{\mathrm{c},\mathbf{k}}(\mathbf{r}). \tag{8.3}$$

Here, S is the size of the system.

At this stage, we make the approximation **(A1)**: the vector potential and the exponential do not vary within a unit cell. By keeping variations beyond the scale of a unit cell, this approximation is less restrictive than the dipole approximation which would fully ignore the spatial structure of the light. Yet without considering a particular choice of vector potential, the spatial variations of the beam is generally limited by a length scale on the order of the wavelength of the light. The same length scale also determines the variation of the exponential $e^{i(\mathbf{k}-\mathbf{k}')\cdot\mathbf{r}}$, since it will turn out *a posteriori* that $\mathbf{k} - \mathbf{k}'$ is determined through the photon momentum. Since the optical wavelength is usually several orders of magnitude larger than the size of unit cell, the approximation is totally valid in the usual cases, but might not hold in some special cases, e.g. of Moiré lattices with enlarged unit cells [6, 122, 268, 303]. Applying (**A1**) to Eq. (8.3), we write:

$$\begin{aligned} h^{\mathrm{v,c}}_{\mathbf{k}',\mathbf{k}} &= \frac{1}{N_{\text{sites}}} \sum_{\mathbf{R}_i} A(\mathbf{R}_i) e^{i(\mathbf{k}-\mathbf{k}')\cdot\mathbf{R}_i} \\ &\times \frac{1}{S_{\text{cell}}} \mathbf{e} \cdot \left[\int_{\text{cell}} d^2 r u^*_{\mathrm{v},\mathbf{k}'}(\mathbf{r}) \nabla_{\mathbf{r}} u_{\mathrm{c},\mathbf{k}}(\mathbf{r}) \right] \\ &\equiv A_\kappa \times \mathbf{e} \cdot \mathbf{p}^{\mathrm{vc}}_{\mathbf{k}',\mathbf{k}}, \end{aligned} \tag{8.4}$$

where $\kappa = \mathbf{k} - \mathbf{k}'$ and $A_\kappa = \frac{1}{N_{\text{sites}}} \sum_{\mathbf{R}_i} A(\mathbf{R}_i) e^{i\kappa\cdot\mathbf{R}_i}$ the Fourier transform of the vector potential. The dipole moment between the $\mathbf{k}'$ state in the valence band and the $\mathbf{k}$ state in the conduction band is denoted by $\mathbf{p}^{\mathrm{vc}}_{\mathbf{k}',\mathbf{k}}$.

We proceed by making a second approximation **(A2)**: the dipole moment depends only weakly on the wave vectors $\mathbf{k}$ and $\mathbf{k}'$. Indeed, the most radical implementation of this approximation in which the dipole moment is set to a constant $\mathbf{p}^{\mathrm{vc}}_0$ is commonly used in the literature, cf. Ref. [105]. To be less restrictive, we argue that $\mathbf{p}^{\mathrm{vc}}_{\mathbf{k}',\mathbf{k}}$ may depend on $\mathbf{k}+\mathbf{k}'$ (which can take relatively large values), whereas the dependence on $\mathbf{k}-\mathbf{k}'$ (which remains small since it is equivalent to the photon momentum) is neglible. To this end we introduce the quantity $\mathbf{K} = \frac{1}{2}(\mathbf{k}+\mathbf{k}')$ and assume a linear (or linearized) dependence on $\mathbf{K}$:

$$\mathbf{p}^{\mathrm{vc}}_{\mathbf{K}} = \mathbf{p}^{\mathrm{vc}}_0 + (\alpha \cdot \mathbf{K})\mathbf{p}^{\mathrm{vc}}_1. \tag{8.4}$$

For notational convenience, we write $\mathbf{e} \cdot \mathbf{p}^{\mathrm{vc}}_{\mathbf{K}} = p^{\mathrm{vc}}_{\mathbf{K}} = p^{\mathrm{vc}}_0 + (\alpha \cdot \mathbf{K}) p^{\mathrm{vc}}_1$. The light-matter matrix element is finally written as:

$$h^{\mathrm{v,c}}_{\mathbf{k}',\mathbf{k}} = h^{\mathrm{vc}}_{\kappa,\mathbf{K}} = A_\kappa p^{\mathrm{vc}}_{\mathbf{K}}. \tag{8.5}$$

This expression makes it immediately clear that the wave vector κ is exclusively selected by properties of the light field, whereas the wave vector $\mathbf{K}$ is exclusively determined by material properties. In the following, we will find that, in the case of exciton transitions, κ ($\mathbf{K}$) is related to the COM (relative) momentum of the exciton.

8.2.5 Exciton transitions

We are now interested in the transition amplitude for exciton formation $\mathcal{T}_X \equiv \langle X|H_{\mathrm{LM}}|\mathrm{vac}\rangle$. Here, $|X\rangle$ denotes an excitonic state, which in 2D is characterized through four quantum numbers for relative and COM motion. We choose $|X\rangle = |\mathbf{k}_{\mathrm{com}}, n, j\rangle$, i.e. we describe the excitonic state by its linear COM momentum $\mathbf{k}_{\mathrm{com}}$, and its hydrogenic quantum numbers n and j, representing the relative degrees of freedom. The vacuum state $|\mathrm{vac}\rangle$ corresponds to a filled valence band and an empty conduction band.

The excitonic wave function can be written as

$$\langle \mathbf{R}, \mathbf{r}|X\rangle \equiv \Phi^{\mathbf{k}_{\mathrm{com}}}_{n,j}(\mathbf{R}, \mathbf{r}) \equiv \Phi^{(\mathrm{com})}_{\mathbf{k}_{\mathrm{com}}}(\mathbf{R}) \times \Phi^{(\mathrm{rel})}_{n,j}(\mathbf{r}), \tag{8.6}$$

where $\mathbf{r} = \mathbf{r}_{\mathrm{e}} - \mathbf{r}_h$ are relative coordinates of an electron-hole pair, and $\mathbf{R} = \frac{1}{2}(\mathbf{r}_{\mathrm{e}} + \mathbf{r}_{\mathrm{h}})$ are the COM coordinates. The relative motion of electron and hole is described by the solutions to the 2D hydrogen atom, which are given by [105]

$$\Phi^{(\text{rel})}_{n,j}(\mathbf{r}) = \tilde{\mathcal{N}}_{n,j} f_{nj}(r) e^{ij\phi_r} = \tilde{\mathcal{N}}_{n,j} \rho^{|j|} e^{-\frac{|\rho|}{2}} L^{2|j|}_{n-|j|}(\rho) e^{ij\phi_r}, \tag{8.7}$$

where $\rho = r\rho_n$, with the inverse length scale given by $\rho_n = \frac{2}{(n+1/2)a_0}$. The material-specific length scale $a_0 = \hbar^2\epsilon/(e^2 M)$ is the effective Bohr radius depending on effective mass M and dielectric constant ϵ. The normalization of the relative wave function is given by

$$\tilde{\mathcal{N}}_{n,j} = \sqrt{\frac{(n-|j|)!}{(n+|j|)!}\left(\frac{\rho_n}{2}\right)^2 \frac{1}{\pi}\frac{1}{n+1/2}}. \tag{8.8}$$

For the COM part, we simply assume plane waves, $\Phi^{(\text{com})}_{\mathbf{k}_{\text{com}}}(\mathbf{R}) = e^{i\mathbf{k}_{\text{com}}\cdot\mathbf{R}}$.

Without making use of the explicit solution for the excitonic wave functions, we write for the transition amplitude:

$$\begin{aligned} \mathcal{T}_X = \int d^2\mathbf{R} \int d^2\mathbf{r} \sum_{\kappa,\mathbf{K}} \langle X|\mathbf{R},\mathbf{r}\rangle\langle \mathbf{R},\mathbf{r}|\kappa,\mathbf{K}\rangle \\ \times \langle \kappa,\mathbf{K}|H_{\text{LM}}|\text{vac}\rangle. \end{aligned} \tag{8.9}$$

The last term corresponds to the band-to-band transition amplitude evaluated above,

$$\begin{aligned} \langle \kappa,\mathbf{K}|H_{\text{LM}}|\text{vac}\rangle &= \langle \mathbf{K}-\frac{\kappa}{2}|H_{\text{LM}}|\mathbf{K}+\frac{\kappa}{2}\rangle \\ &= h^{\text{v,c}}_{\mathbf{K}-\frac{\kappa}{2},\mathbf{K}+\frac{\kappa}{2}} = A_\kappa p^{\text{vc}}_{\mathbf{K}}, \end{aligned} \tag{8.10}$$

which is Fourier transformed to spatial coordinates by the second term,

$$\langle \mathbf{R}, \mathbf{r} | \kappa, \mathbf{K} \rangle = \frac{1}{S^2} e^{i(\mathbf{K}+\frac{\kappa}{2})\cdot\mathbf{r}_\mathrm{e} - i(\mathbf{K}-\frac{\kappa}{2})\cdot\mathbf{r}_\mathrm{h}} = \frac{1}{S^2} e^{i(\mathbf{K}\cdot\mathbf{r} + i\kappa\cdot\mathbf{R})}. \tag{8.11}$$

This expression explicitly shows that the wave vector κ ($\mathbf{K}$) is conjugate to the COM (relative) variable.

Plugging all expressions into Eq. (8.9), the $\mathbf{R}$ integral is immediately evaluated into a Kronecker-Delta $\delta_{\kappa,\mathbf{k}_\mathrm{com}}$, so photon momentum κ and COM momentum $\mathbf{k}_\mathrm{com}$ must match. We obtain:

$$\begin{aligned} \mathcal{T}_X = & \frac{(2\pi)^2 \tilde{\mathcal{N}}_{nj}}{S^2} A_{\mathbf{k}_\mathrm{com}} \int d^2\mathbf{r} f_{nj}(r) e^{ij\phi_r} \\ & \times \sum_{\mathbf{K}} e^{i\mathbf{K}\cdot\mathbf{r}} (p_0^\mathrm{vc} + \alpha \cdot \mathbf{K} p_1^\mathrm{vc}). \end{aligned} \tag{8.12}$$

The $\mathbf{K}$-sum is a Fourier transform into the relative variable $\mathbf{r}$, and we can write $\sum_{\mathbf{K}} e^{i\mathbf{K}\cdot\mathbf{r}}(p_0^\mathrm{vc} + \alpha \cdot \mathbf{K} p_1^\mathrm{vc}) = (2\pi)^2 [p_0^\mathrm{vc} \delta(\mathbf{r}) - i p_1^\mathrm{vc} \alpha \cdot \nabla_r \delta(\mathbf{r})]$. From this expression it can immediately be seen that a constant dipole moment leads to non-zero transition amplitudes only if the relative exciton wavefunction $f_{nj}(r)$ is non-zero at $r = 0$. This is the case only for s-excitons. The linear dependence of the dipole momentum on $\mathbf{K}$, expressed by the second term, gives rise to non-vanishing transition amplitudes if the first derivative of $f_{nj}(r)$ is non-zero at $r = 0$.

This second term enables the formation of excitons in higher momentum states than the s series. However, we emphasize that this term is independent from the light source, and with respect to the relative degrees of freedom (n, j), we get the same transitions, no matter what the spatial structure of the light might be (as long as approximation (**A1**) holds). Our analysis shows that the Elliott formula is unchanged by spatial structure of light beyond the scale of the unit cell.

Our result agrees with a recent experiment in 2D transition metal dichalcogenides (TMDs) where twisted light has been used to reveal light-like exciton dispersion [277]. Using non-resonant Laguerre-Gaussian beams, they observed a blue shift of the exciton energy that increased with ℓ; this indicates that the OAM was transferred preferentially to the COM of the exciton during its creation. However, we stress that our results apply much more generally since no particular 2D semiconductor or spatial light profile was specified during the analysis. This implies that the dispersion of all 2D excitons could be probed in a similar manner, presenting an alternative method to the traditional angle-resolved photoluminescence measurements [148].

8.2.6 Example: Excitons from twisted light

Thus far, we have been very general in our treatment with respect to the profile of the optical excitation. In the following, we are going to treat the specific case of a Bessel beam and, besides the analytical treatment along the lines presented in the previous sections, we will also present the result of numerical evaluations. With this choice of the vector potential, our system exhibits a cylindrical symmetry, since the light field has an azimuthal phase dependence $\exp(i\ell\phi)$, where ℓ defines the OAM per photon (in units $\hbar$). To match this symmetry, we consider a cylindrical sample, noting that the sample geometry becomes irrelevant in the thermodynamic limit. Accordingly, we adopt our

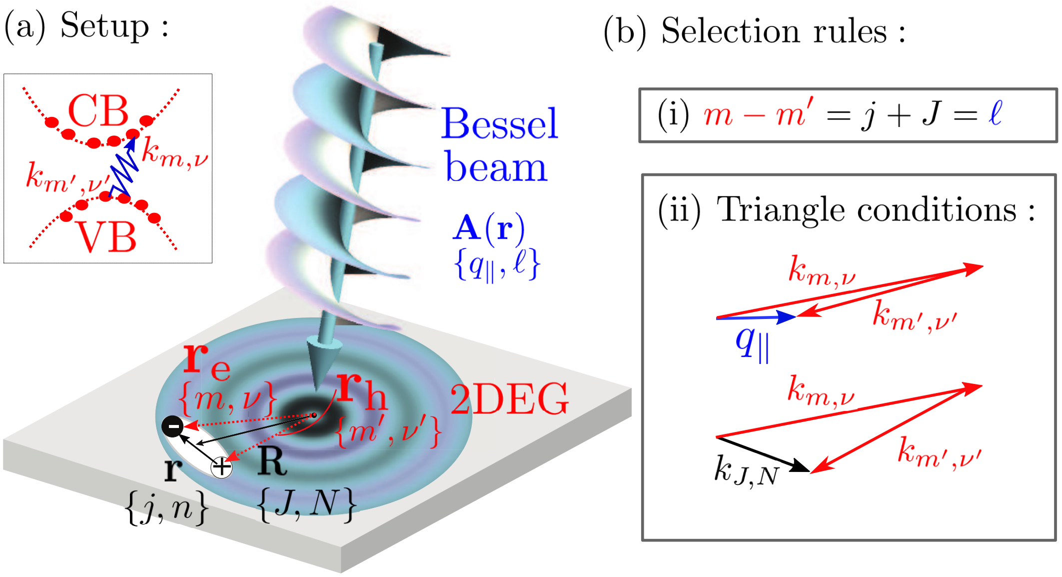

Figure 8.1: (a) A Bessel light beam $\mathbf{A}$ with photon momentum/angular momentum $(q_\parallel, \ell)$ creates an electron-hole pair in a 2D electron gas (2DEG). The electron [hole] is characterized by quantum numbers (m, ν) [(m', ν')] for angular momentum/ momentum. The pair can form a bound state, and the degrees of freedom of such an exciton are the center-of-mass motion, characterized by angular momentum/ momentum quantum numbers (J, N), and the relative motion, characterized by quantum numbers (j, n) for angular momentum and energy. (b) The selection rules for optical transitions and exciton formation reflect (i) conservation of angular momentum, and (ii) conservation of linear momentum, reflected by the illustrated triangle conditions.

theoretical description to this symmetry, and express the light-matter coupling in terms of a cylindrical wave functions, see also Refs. [75, 240]. We illustrate this case in Fig. 8.1, where we also sketch the resulting selection rules in terms of the good quantum numbers for the cylindrical symmetry.

8.2.7 Band-to-band transitions in cylindrical basis

Instead of plane waves with linear momentum quantum number, the electronic basis in a cylindrical sample is best described by wave functions $\varphi_{m,\nu}(\mathbf{r}) = \mathcal{N}_{m,\nu} J_m(k_{m,\nu} r) \exp(im\phi)$, which solve the Schrödinger equation for free electrons with cylindrical boundary conditions.

Here, $J_m(x)$ denotes the mth Bessel function, and the momenta $k_{m,\nu}$ must be chosen such that the wave function vanishes at the system boundary (i.e. for $|\mathbf{r}| = R_0$). Therefore, we have $k_{m,\nu} = x_{m,\nu}/R_0$, with $x_{m,\nu}$ the νth zero of the mth Bessel function. The normalization is given by $\mathcal{N}_{m,\nu} = (R_0\sqrt{\pi}|J_{|m-1|}(x_{m,\nu})|)^{-1}$. As in the previous section, the crystal lattice is taken into account by multiplying the wave functions $\varphi_{m,\nu}$ with lattice-periodic Bloch functions $u_\lambda(\mathbf{r})$ for the bands λ. For simplicity, the Bloch functions are assumed to be independent from the quantum numbers m and ν. With this, the electronic basis is given

$$\varphi_{\lambda;m,\nu}(\mathbf{r}) = \mathcal{N}_{m,\nu} J_m(k_{m,\nu} r) \exp(im\phi) u_\lambda(\mathbf{r}). \tag{8.13}$$

In this basis, the light-matter transition amplitudes in the Coulomb gauge (within the weak field limit) are given by

$$h^{\mathrm{v,c}}_{m,\nu;m',\nu'} = \frac{-i\hbar e}{SM} \int d\mathbf{r} \bar{\varphi}_{+,m',\nu'}(\mathbf{r}) \left[\mathbf{A}(\mathbf{r}) \cdot \nabla_{\mathbf{r}}\right] \varphi_{-,m,\nu}(\mathbf{r}), \tag{8.14}$$

with $\bar{\varphi}$ denoting the complex conjugate of φ.

Before we proceed, let us first fix the vector potential. We consider a vector potential which in the sample plane reads $\mathbf{A}(\mathbf{R}) = A_0 a(R) e^{i\ell\phi} \mathrm{e}_\sigma$, where e_σ is the polarization in the plane. For a circularly polarized Bessel beam with OAM ℓ, we have $a(R) = J_\ell(q_{\|} R)$, with $q_{\|}$ the in-plane photon momentum. Note that a vertical contribution to the vector potential, needed to fulfill Maxwell's equation, is neglected here since it is not relevant for light-matter interaction with a two-dimensional medium. However, it is important to keep in mind that the frequency ω of the photon depends also on the perpendicular momentum component q_z, $\omega = \frac{c}{\hbar}\sqrt{q_\parallel^2 + q_z^2}$.

Invoking the approximations (**A1**) and (**A2**), both $\mathbf{A}(\mathbf{r})$ and $J_m(k_{m,\nu}r)\exp(im\phi)$ can be considered constant on the scale of the lattice constant a. Thus, the evaluation of $h^{\mathrm{v,c}}_{m,\nu;m',\nu'}$ can be split into an integral $\mathcal{I}$ restricted to the unit cell and a sum over units cells $\mathcal{S}_{m,\nu;m',\nu'}$, that is, we can write $h^{\mathrm{v,c}}_{m,\nu;m',\nu'} = \frac{-i\hbar}{SM}\mathcal{S}_{m,\nu;m',\nu'} \times \mathcal{I}$. As before, the sum over the whole system takes into account the variation of the light field, occurring on larger scales, whereas the unit cell integral determines the material's dipole moment taken to be a constant.

Explicitly, the two contributions are given by

$$\mathcal{I} = e\int_{\mathrm{c}} \mathrm{d}\mathbf{r}\bar{u}_+(\mathbf{r})(\mathbf{e}_\sigma \cdot \nabla_{\mathbf{r}})u_-(\mathbf{r}), \tag{8.15}$$

and

$$\begin{aligned}\mathcal{S}_{m,\nu;m',\nu'} =& \mathcal{N}_{m,\nu}\mathcal{N}_{m',\nu'}A_0\sum_i J_m(k_{m,\nu}R_i)J_{m'}(k_{m',\nu'}R_i)\\ &\times J_\ell(q_\parallel R_i)\exp[i(m-m'+\ell)\phi_i],\end{aligned} \tag{8.16}$$

where (R_i, ϕ_i) denote the lattice vectors. In analogy to Eq. (8.4), we can read off the results of the cell integral $\mathcal{I}$ as the interband dipole moment $p_{\mathrm{vc}} \equiv \mathbf{e}_\sigma \cdot \mathbf{d} = \mathcal{I}$, which depends only on the material. Since we take it to be constant here, it will enter the transition amplitudes only as a prefactor. To evaluate $\mathcal{S}_{m,\nu;m',\nu'}$, we replace the summation over cells by an integral. With this, we immediately arrive at a first selection rule from the angular part of the integral:

$$\mathcal{S}_{m,\nu;m',\nu'} \propto \delta_{\ell+m-m'}. \tag{8.17}$$

The radial integral in $\mathcal{S}_{m,\nu;m',\nu'}$ is over a product of three Bessel functions, $\mathcal{S}_{m,\nu;m',\nu'} \propto \int_0^{R_0} dr\ r J_m(k_{m,\nu}r) J'_m(k_{m',\nu'}r) J_\ell(q_\parallel r)$. Its analytic solution (in the limit $R_0 \to \infty$) has been derived in Ref. [117], and can also be found in the Supplemental Material (SM). Here, we only consider that, from this solution, the integral takes non-zero values only if a triangle condition is fulfilled: The three scalars $k_{m,\nu}$, $k_{m',\nu'}$, and $q_\parallel$ must be such that they can form a triangle (including the limit in which the triangle is squeezed to a line). Therefore, this condition yields a second selection rule: the change of electron momentum upon a band-to-band transition is bounded by the in-plane momentum of the photon.

8.2.8 Exciton transitions

The amplitudes $h^{\mathrm{v,c}}_{m,\nu;m',\nu'}$ quantify the band-to-band transition which generates an electron-hole pair characterized by $m - m' = \ell$ and $|k_{m,\nu} - k_{m',\nu'}| \le q_\parallel$. Next, we have to ask which excitonic states can be formed from these pairs. In accordance with the presumed cylindrical symmetry of the system, we now also describe the excitonic states in terms of cylindrical-symmetric quantum numbers, $|X\rangle = |N, J, n, j\rangle$, where n, j account for the state of relative motion (as before), and N, J for the COM degrees of freedom (instead of $\mathbf{k}_{\mathrm{com}}$ used in the previous section). Again, the excitonic wave function is a product of the relative ($\mathbf{r}$) and COM ($\mathbf{R}$) contributions: $\langle \mathbf{R}, \mathbf{r}|X\rangle \equiv \Phi^{J,N}_{n,j}(\mathbf{R}, \mathbf{r}) \equiv \Phi^{(\mathrm{com})}_{N,J}(\mathbf{R}) \times \Phi^{(\mathrm{rel})}_{n,j}(\mathbf{r})$. The relative part is unchanged, given by Eq. (8.7). Since the COM of the exciton is subject to the same boundary conditions as electron and hole individually, its wave function is given by:

$$\Phi^{(\mathrm{com})}_{J,N}(\mathbf{R}) = \mathcal{N}_{J,N} J_J(k_{J,N} R) \exp(iJ\phi_{\mathrm{com}}), \tag{8.18}$$

where the quantum number J denotes the angular momentum of the COM, and both J and N together define the total COM momentum $Q_{\mathrm{com}} = x_{J,N}/R_0$.

Projecting the excitonic wave function onto the rotationally symmetric basis for electron and hole wave functions is equivalent to a Hankel transform. This projection yields a quantity $\mathcal{B}^{n,j;J,N}_{m,\nu;m',\nu'}$:

$$\begin{aligned}\mathcal{B}^{n,j;J,N}_{m,\nu;m',\nu'} =& \mathcal{N}_{m,\nu}\mathcal{N}_{m',\nu'} \int \mathrm{d}\mathbf{r}_{\mathrm{e}} \int \mathrm{d}\mathbf{r}_{\mathrm{h}} \bar{\Phi}^{J,N}_{n,j}(\mathbf{R},\mathbf{r}) \\ & \times J_m(k_{m,\nu} r_{\mathrm{e}}) J_{m'}(k_{m',\nu'} r_{\mathrm{h}}) \exp[i(m\phi_{\mathrm{e}} - m'\phi_{\mathrm{h}})].\end{aligned} \tag{8.19}$$

An explicit analytic expression which solves this integral is provided in the SM. As before for $\mathcal{S}_{m,\nu;m',\nu'}$, we also encounter a triangle condition in the evaluation of $\mathcal{B}^{n,j;J,N}_{m,\nu;m',\nu'}$: it is non-zero, only if the lengths $k_{m,\nu}$, $k_{m',\nu'}$, and $k_{J,N}$ form a triangle, i.e. $|k_{m,\nu} - k_{m',\nu'}| \leq k_{J,N}$. More importantly, as shown in the SM, one of the integrals in Eq. (8.19) yields a Kronecker-δ:

$$\mathcal{B}^{n,j;J,N}_{m,\nu;m'\nu'} \sim \delta_{j+J,m-m'}. \tag{8.20}$$

Together with the selection rule for band-to-band transitions, Eq. (8.17), Eq. (8.20) reflects conservation of angular momentum.

We are now in the position to calculate the exciton transition amplitude $\mathcal{T}_{n,j}^{J,N} \equiv \langle X_{n,l}^{J,N}|H_{\rm LM}|{\rm vac}\rangle$:

$$\mathcal{T}_{n,j}^{J,N} = \sum_{m,\nu;m',\nu'} h^{\rm v,c}_{m,\nu;m',\nu'} \mathcal{B}^{n,j;J,N}_{m,\nu;m'\nu'}. \tag{8.21}$$

These sums should go over all occupied (empty) levels m', ν' (m, ν), but a more practical limitation of these sums is due to the fact that $\mathcal{B}^{n,j;J,N}_{m,\nu;m'\nu'} \approx 0$ when either $k_{m,\nu}$ or $k_{m',\nu'}$ become much larger than the inverse of the Bohr radius, a_0^{-1}.

8.2.9 Numerical evaluation

The last observation allows us to introduce a cutoff momentum $k_{\rm cut} \gg a_0^{-1}$ at which the sums can be truncated. With this, the numerical evaluation of Eq. (8.21) become feasible. For concreteness, by comparison of $\mathcal{T}_{n,j}^{J,N}$ obtained from different cutoff momenta $k_{\rm cut}$, we estimate that the relative error remains below 0.1 for $k_{\rm cut}a_0 \geq 3.75$. In the numerical evaluation of $\mathcal{T}_{n,j}^{J,N}$ presented below, we have included 47,100 Bessel functions. With that, $k_{\rm cut}a_0 > 3.75$ for system sizes up to $R_0/a_0 = 12,500$. We note that $k_{\rm cut}$ also restricts the sums in m and ν in the following way: $|m| < \pi k_{\rm cut} R$ and/or $\nu < k_{\rm cut} R$.

The numerical evaluation confirms the analytical result from Sec. II that the Elliott formula remains unchanged by the spatial structure of the light source. To this end, we obtained the height of the spectral lines, $\tilde{\mathcal{T}}_{n,j}$, by summing the contributions from all COM

	1s	2s	3s
OAM 0	0.998	0.037	0.0079
OAM 1	0.995	0.037	0.0079
2D Elliott	0.9993	0.037	0.0080

Table 8.1: Relative transition strength, $|\tilde{\mathcal{T}}_{n,j}|^2$, for a system of size $R_0 = 10^4 a_0$ in a Bessel beam with OAM $\ell = 0$ and $\ell = 1$ and in-plane photon momentum $q_\parallel = 10^{-3} a_0^{-1}$. For comparison, we also provide the results from 2D Elliott formula for an infinite system in a Gaussian beam.

momentum modes at a given n and j:

$$\tilde{\mathcal{T}}_{n,j} = \frac{1}{\mathcal{N}_{\mathcal{T}}} \sum_{N,J} \mathcal{T}_{n,j}^{J,N}. \tag{8.22}$$

To make this quantity independent from the intensity of the light, we normalize by $\mathcal{N}_{\mathcal{T}} = \sqrt{\sum_{n,j,N} \left|\mathcal{T}_{n,j}^{J,N}\right|^2}$. The results are shown in Table 8.1 for a system of size $R_0 = 10^4 a_0$ in a Bessel beam with OAM $\ell = 0$ and $\ell = 1$ and in-plane photon momentum $q_\parallel = 10^{-3} a_0^{-1}$. For comparison, we also provide the results from the 2D Elliott formula for an infinite system. All values agree very well with each other.

We note that the numerical evaluation also yields small but finite values for transitions into p-states. However, in contrast to the values for the transitions into s-states, these values show a strong and non-monotonic dependence on the system size and/or photon momentum. This suggests that, in accordance with our general arguments presented in Sec. II, the finite transition amplitudes into p-states are numerical artifacts, and the only bright transitions occur into the s states.

Our numerical evaluation also confirms that the COM momentum of the exciton is determined by the linear in-plane momentum of the photon. To this end, we focus on the $1s$ transition and evaluate the transition strengths $\mathcal{T}_{0,0}^{\ell,N}$ into the different COM modes

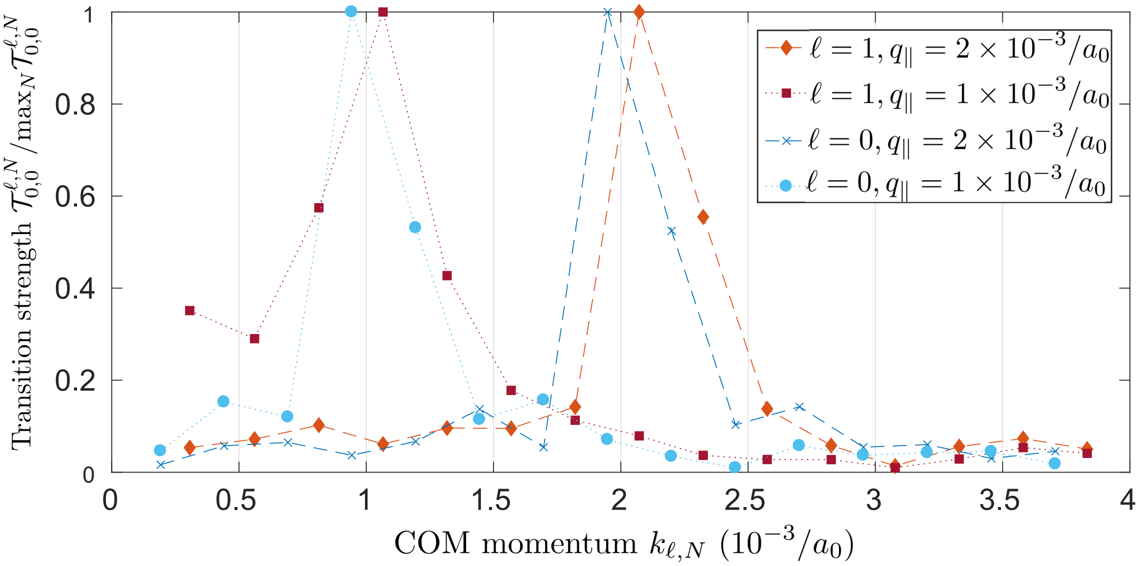

Figure 8.2: For the $1s$ transition, we plot the transition strength $\mathcal{T}_{0,0}^{\ell,N}$ into the different COM modes $k_{\ell,N}$, normalized by the peak value $\max_N(\mathcal{T}_{0,0}^{\ell,N})$, for illumination with $\ell = 0$ and $\ell = 1$ Bessel beams. The peak is obtained for the best match between COM momentum $k_{\ell,N}$ and in-plane photon momentum, $q_{\|} = 10^{-3}a_0^{-1}$.

$k_{\ell,N}$. The results, normalized by the peak value $\max_N(\mathcal{T}_{0,0}^{\ell,N})$, are shown in Fig. 8.2 for different values of photon OAM ℓ and photon momentum. The transition strength is clearly peaked for the COM momenta which match with the momentum of the photon, but barely depends on the OAM.

Let us finally discuss the different length scales which appear in the calculation, that is, the effective Bohr radius a_0, the sample size R_0, and the inverse of the photon momentum $q_{\|}^{-1}$. In the calculation, we have taken the effective Bohr radius a_0 as the unit of length. With typical values of the dielectric constant being much greater than 1 (e.g. ≈ 13 in GaAs [294] and 7 in semiconducting TMDs [161]), and the effective mass being much smaller than the electron mass (e.g. 0.067 and 0.39 electron masses for the conduction band in GaAs [35] and model TMDs [141], respectively), the effective Bohr radius can significantly exceed the Bohr radius of the hydrogen atom (≈ 0.05nm).

Typical values range between 0.1 to 1 nm. Taking the numerical constraints into account (i.e. truncation errors), our study examines sample sizes R_0 on the order of 10^4 effective Bohr radii which corresponds to sample sizes on the order of 1-10 microns. Importantly, this size is significantly larger than the optical vortex. Regarding the in-plane photon momentum $q_{\|}$, an upper limit is given by the inverse of the wavelength, $2\pi/\lambda_0$, assuming vertical incidence on the sample. The wave length λ_0 is determined by the band gap of the material. As an estimate for this limit, we obtain $100\mathrm{nm}^{-1}$. Thus, our choice of $q_{\|} = 10^{-3}a_0^{-1}$ corresponds to the upper limit if $a_0 = 0.1$ nm, while this choice remains below that limit if a_0 is larger.

8.2.10 Summary and Conclusions

We have shown that the vector potential selects the COM quantum numbers (absolute value of COM momentum + COM angular momentum), but has no effect on the transition amplitudes into states with different relative quantum numbers n and j. This implies that Elliott's formula is unchanged by the structure in the light field. The approximation which gives rise to these conclusion is the separation of length scales: unit cell vs. wavelength. This assumption implies that $A(x)$ and e^{iqx} are constant on the the level of a unit cell, and for the dipole moment, $p^{\mathrm{vc}}_{\mathbf{k},\mathbf{k}+\mathbf{q}} \approx p^{\mathrm{vc}}_{\mathbf{k},\mathbf{k}}$. We have confirmed our general analytical result by performing numerical evaluations for the concrete case of Bessel beams in a circularly symmetric sample. Qualitatively, we have shown that, for a transition to be optically bright, the sum of both relative and COM angular momenta, $j + J$, must be equal to the OAM value ℓ of the light. Quantitatively, we have evaluated that the transition amplitudes are given by the Elliott formula.

While our results rule out twisted light for the generation of dark excitons, the predicted transfer of OAM to the COM degree of freedom can be useful from the perspective of quantum simulation, and especially from the point of view of artificial gauge fields. In Ref. [126], it has been shown that artificial flux is generated in a photonic system when OAM light is injected into a waveguide lattice. Excitons in tunable lattices have recently be shown to form strongly correlated many-body phases, such as Mott insulating phases [152] or checkerboard phases [151]. If, in the future, twisted light provided excitonic lattices with artificial magnetic fluxes, this could give rise to chiral Mott insulators [65] or extended supersolid regimes [295].

8.3 Supplemental Material

8.3.1 Band-to-band transition matrix for a Bessel beam

The band wave functions are expressed in terms of Bessel functions $J_m(k_{m,\nu}r)$, and the spatial profile of the light is given by a Bessel beam $J_\ell(q_{\|}r)$. Thus, the matrix elements for band-to-band transitions are proportional to the integral over a product of three Bessel functions:

$$\mathcal{S}_{m,\nu;m',\nu'} \propto \int_0^{R_0} dr\, r J_m(k_{m,\nu}r) J'_m(k_{m',\nu'}r) J_\ell(q_{\|}r). \tag{8.23}$$

To evaluate this integral, we take the limit $R_0 \to \infty$, and follow the procedure as described in Ref. [117]; that is, we perform a plane-wave expansion of the Bessel functions. With this, the integral is found to take the following value:

$$\mathcal{J} \equiv \int_0^\infty dr\; r J_m(k_{m,\nu} r) J'_m(k_{m',\nu'} r) J_\ell(q_\| r)$$
$$= \begin{cases} \frac{1}{2\pi A_\triangle} \cos\left(m\alpha_2 - m'\alpha_1\right), & \text{if } k_{m,\nu}, k_{m',\nu'}, q_\| \text{can form a triangle ,} \\ 0 & \text{otherwise.} \end{cases} \tag{8.24}$$

If a triangle with lengths $k_{m,\nu}, k_{m',\nu'}$, and $q_\|$ can be formed, the quantity $A_\triangle$ denotes the area of this triangle, and α_1 and α_2 are exterior angles of this triangle. Defining $\kappa \equiv (k_1 + k_2 + k_3)/2$, we have

$$A_\triangle = \sqrt{\kappa(\kappa - k_1)(\kappa - k_2)(\kappa - k_3)}. \tag{8.25}$$

The angles are given by:

$$\alpha_1 = \arccos\left(\frac{k_1^2 - k_2^2 - k_3^2}{2k_2k_3}\right), \tag{8.26}$$
$$\alpha_2 = \arccos\left(\frac{k_2^2 - k_3^2 - k_1^2}{2k_1k_3}\right). \tag{8.27}$$

8.3.2 Hankel transform of the exciton

In a circularly-symmetric system, the electronic bands are conveniently given by Bessel functions. Decomposing the excitonic wave function in terms of these single-particle states is equivalent to a Hankel transform of the exciton. Let the relative motion of electron and hole of the exciton be described by a principal quantum number n, and an angular momentum quantum number j, and the center-of-mass (COM)motion be described by quantum numbers J for angular momentum and momentum and N for momentum/energy. The overlap of such exciton with an electron in a state described by quantum numbers m, ν, and a hole described by m', ν' reads:

$$\begin{aligned}\mathcal{B}^{n,j;J,N}_{m,\nu;m',\nu'} = \mathcal{N}_{m,\nu}\mathcal{N}_{m',\nu'} \int \mathrm{d}\mathbf{r}_\mathrm{e} \int \mathrm{d}\mathbf{r}_\mathrm{h} \bar{\Phi}^{(\mathrm{com})}_{J,N}(\mathbf{R})\bar{\Phi}^{(\mathrm{rel})}_{n,j}(\mathbf{r}) \\ \times J_m(k_{m,\nu}r_\mathrm{e})J_{m'}(k_{m',\nu'}r_\mathrm{h}) \exp\left[i(m\phi_\mathrm{e} - m'\phi_\mathrm{h})\right].\end{aligned} \tag{8.28}$$

Here, $\mathbf{R} = (\mathbf{r}_\mathrm{e} + \mathbf{r}_\mathrm{h})/2$ describes the COM motion, and $\mathbf{r} = \mathbf{r}_\mathrm{e} - \mathbf{r}_\mathrm{h}$ describes the relative motion, and $\mathbf{r}_\mathrm{e,h}$ are expressed in polar coordinates $(r_\mathrm{e,h}, \phi_\mathrm{e,h})$. As a first step to evaluate $\mathcal{B}$, we will expand the Bessel functions (including the one contained in the definition of $\bar{\Phi}^{(\mathrm{com})}_{J,N}$, see main text) in terms of plane waves. To this end, we note that

$$e^{iz\cos(\theta)} = \sum_{n=-\infty}^{n=\infty} i^n e^{in\theta} J_n(z). \tag{8.29}$$

Therefore,

$$e^{i\vec{k}\cdot\vec{r}_e} = e^{ikr_e\cos(\phi_e - \phi_k)} = \sum_{n=-\infty}^{n=\infty} i^n e^{in\phi_e} e^{-in\phi_k} J_n(kr_e). \tag{8.30}$$

Integrating both sides over $\int_0^{2\pi} d\phi_k \, e^{im\phi_k}$ gives

$$J_m(kr_e)e^{im\phi_e} = \frac{1}{2\pi}(-i)^m \int_0^{2\pi} e^{i\vec{k}\cdot\vec{r}_e} e^{im\phi_k} d\phi_k. \tag{8.31}$$

Applying this expansion, below we associate $\mathbf{k} \equiv (k, \phi_k)$ with electron momentum, and $\mathbf{k}' \equiv (k', \phi_{k'})$ with hole momentum, where k and k' are introduced as short-hand notations for $k_{m,\nu}$ and $k_{m;,\nu'}$. Similarly, the center-of-mass momentum will be associated with a vector $\mathbf{Q} = Q, \phi_Q$. With this, and re-expressing electron and hole coordinates in terms of relative and center-of-mass coordinates, we get

$$\begin{aligned} \mathcal{B}^{n,j;J,N}_{m,\nu;m',\nu'} &= \tilde{\mathcal{N}}_{n,j}\mathcal{N}_{J,N}\mathcal{N}_{m,\nu}\mathcal{N}_{m',\nu'}\frac{-i^{m-m'+J}}{(2\pi)^3} \\ &\times \int_0^{2\pi} \mathrm{d}\phi_k \int_0^{2\pi} \mathrm{d}\phi_{k'} \int_0^{2\pi} \mathrm{d}\phi_Q \int \mathrm{d}\mathbf{r} \int \mathrm{d}\mathbf{R} e^{i\mathbf{R}\cdot(\mathbf{k}-\mathbf{k}'-\mathbf{Q})} \\ &\times e^{i\mathbf{r}\cdot(\mathbf{k}+\mathbf{k}')/2} e^{im\phi_k} e^{-im'\phi_{k'}} e^{-iJ\phi_Q} \rho^{|j|} e^{-\frac{|\rho|}{2}} L^{2|j|}_{n-|j|}(\rho) e^{-ij\phi_{\mathrm{rel}}}, \end{aligned} \tag{8.32}$$

where $\rho \equiv r\rho_n$ with $\rho_n \equiv 2r/[a_0(n+\frac{1}{2})]$. The integration in $\mathbf{R}$ yields a δ-function, which imposes a triangle condition for the momenta:

$$\int \mathrm{d}\mathbf{R} e^{i\mathbf{R}\cdot(\mathbf{k}-\mathbf{k}'-\mathbf{Q})} = (2\pi)^2 \delta^{(2)}(\mathbf{k}-\mathbf{k}'-\mathbf{Q}). \tag{8.33}$$

Let us next carry out the angular part of the integral in $\mathbf{r}$.:

$$\int \mathrm{d}\phi_{\mathrm{rel}} e^{-ij\phi_{\mathrm{rel}}} e^{irq\cos(\phi_{\mathrm{rel}}-\phi_q)} = 2\pi i^j e^{-ij\phi_q} J_j(qr). \tag{8.34}$$

Here, as a short-hand notation, we have introduced $\mathbf{q} = (q, \phi_q) \equiv \frac{\mathbf{k}+\mathbf{k}'}{2}$. For the radial part of the relative position integral we write:

$$\begin{aligned} f(q,n,j) &\equiv \int \mathrm{d}\rho\rho^{j+1} e^{-\frac{\rho}{2}} L_{n-j}^{2j}(\rho) J_j\left(\frac{q}{\rho_n}\rho\right) \\ &= \sum_{s=0}^{n-j} \frac{\sqrt{2}(-1)^s(\frac{q}{\rho_n})^j}{\left(\frac{2q^2}{\rho_n^2}+\frac{1}{2}\right)^{j+s+\frac{3}{2}}} \frac{\Gamma(n+j+1)\Gamma(2j+s+2)}{\Gamma(s+1)\Gamma(j+1)\Gamma(n-j-s+1)\Gamma(2j+s+1)} \\ &\times \ {}_2F_1\left(\frac{-s}{2}, \frac{-1-s}{2}, 1+j, -\frac{4q^2}{\rho_n^2}\right), \end{aligned} \tag{8.35}$$

with ${}_2F_1$ being the hypergeometric function Note that here we have changed the integration variable from r to ρ, which yields a factor $1/\rho_n^2$. For the analytic solution of the integral, we have taken the integration boundary to be at infinity.

Putting all together, we arrive at the following intermediate result:

$$\begin{aligned} \mathcal{B}_{m,\nu;m',\nu'}^{n,j;J,N} &= \tilde{\mathcal{N}}_{n,j}\mathcal{N}_{J,N}\mathcal{N}_{m,\nu}\mathcal{N}_{m',\nu'}\frac{i^{m-m'+J+j}}{\rho_n^2} f(q,n,j)\times \\ &\times \int_0^{2\pi}\mathrm{d}\phi_k \int_0^{2\pi}\mathrm{d}\phi_{k'} \int_0^{2\pi}\mathrm{d}\phi_Q \delta^{(2)}(\mathbf{k}-\mathbf{k}'-\mathbf{Q}) e^{i(m\phi_k - m'\phi_{k'} - j\phi_q - J\phi_Q)}. \end{aligned} \tag{8.36}$$

Let us for a moment assume ϕ_Q to be fixed. Then, in the remaining two integrals, ϕ_k and $\phi_{k'}$ will be fixed such that the triangle condition expressed by the δ-function is met. To proceed, we write the delta function $\delta^{(2)}\left(\vec{k}-\vec{k}'-\vec{Q}\right)$ explicitly in terms of ϕ_k, $\phi_{k'}$, and

ϕ_Q:

$$\begin{aligned}\delta^{(2)}\left(\vec{k}-\vec{k}'-\vec{Q}\right) &= \delta\left(k\cos\phi_k - k'\cos\phi_{k'} - Q\cos\phi_Q\right) \\ &\quad\times \delta\left(k\sin\phi_k - k'\sin\phi_{k'} - Q\sin\phi_Q\right).\end{aligned} \tag{8.37}$$

To perform the integral over these δ functions, we first note the identity

$$\int d\phi g(\phi)\delta(h(\phi)) = \sum_w \frac{g(\phi^w)}{\left|\frac{\mathrm{d}h(\phi)}{\phi}\right|}\Bigg|_{\phi=\phi^w}, \tag{8.38}$$

where $\phi = \phi^w$ denote the solutions to $h(\phi) = 0$. We define $h_1(\phi_k) = k\cos\phi_k - k'\cos\phi_{k'} - Q\cos\phi_Q$ and $h_2(\phi_{k'}) = k\sin\phi_k - k'\sin\phi_{k'} - Q\sin\phi_Q$. The zeros of h_1 and h_2 are given by

$$\cos\phi_k = \frac{k'\cos\phi_{k'} + Q\cos\phi_Q}{k}, \tag{8.39}$$

$$\sin\phi_{k'} = \frac{k\sin\phi_k - Q\sin\phi_Q}{k'}. \tag{8.40}$$

If there is a triangle with lengths given by k, k', and Q, the angles ϕ_k and $\phi_{k'}$ of such triangle solve these equations. Note that a second solution can then be obtained from a mirror transformation of the triangle, but since the solutions are equivalent, considering only one of them is sufficient. On the other hand, if such triangle does not exist, the equations (8.39) have no solution, and the integral is zero. Explicitly, the solutions can be written as

$$\begin{aligned}\phi_k &= \tilde{\phi}_k + \phi_Q \text{ with } \tilde{\phi}_k = \arccos\left(\frac{k^2+Q^2-k'^2}{2kQ}\right), && (8.41)\\ \phi_{k'} &= \tilde{\phi}_{k'} + \phi_Q \text{ with } \tilde{\phi}_{k'} = \arccos\left(\frac{k^2-Q^2-k'^2}{2k'Q}\right). && (8.42)\end{aligned}$$

The angle ϕ_q in Eq. (8.36) is given by:

$$\begin{aligned}\phi_q &= \tan^{-1}\left(\frac{q_y}{q_x}\right)\\ &= \tan^{-1}\left(\frac{k_y+k'_y}{k_x+k'_x}\right)\\ &= \tan^{-1}\left(\frac{k\sin(\tilde{\phi}_k-\phi_Q)+k'\sin(\tilde{\phi}_{k'}-\phi_Q)}{k\cos(\tilde{\phi}_k-\phi_Q)+k'\cos(\tilde{\phi}_{k'}-\phi_Q)}\right) \qquad (8.43)\\ &= \tan^{-1}\left(\frac{k\sin(\tilde{\phi}_k)+k'\sin(\tilde{\phi}_{k'})}{k\cos(\tilde{\phi}_k)+k'\cos(\tilde{\phi}_{k'})}\right)+\phi_Q\\ &\equiv \tilde{\phi}_q+\phi_Q.\end{aligned}$$

We can also express q in terms of k, k', $\tilde{\phi}_k$, and $\tilde{\phi}_{k'}$:

$$q = \frac{1}{2}\sqrt{k^2+k'^2+kk'\cos(\tilde{\phi}_k-\tilde{\phi}_{k'})}. \qquad (8.44)$$

The term $\left|\frac{\mathrm{d}h_1(\phi_k)}{\mathrm{d}\phi_k}\right|^{-1} \times \left|\frac{\mathrm{d}h_2(\phi_{k'})}{\mathrm{d}\phi_{k'}}\right|^{-1}$, evaluated at $\phi_k = \tilde{\phi}_k+\phi_Q$ and $\phi_{k'} = \tilde{\phi}_{k'}+\phi_Q$, which we get according to Eq. (8.38) from the two integrals in ϕ_k and $\phi_{k'}$, is given by:

$$|h'_1(\tilde{\phi}_k+\phi_Q)|^{-1}|h'_2(\tilde{\phi}_k+\phi_Q)|^{-1} = \frac{1}{kk'|\sin(\tilde{\phi}_k-\tilde{\phi}_{k'})|}. \qquad (8.45)$$

Putting all together, we arrive at

$$\begin{aligned}\mathcal{B}^{n,j;J,N}_{m,\nu;m',\nu'} &= \tilde{\mathcal{N}}_{n,j}\mathcal{N}_{J,N}\mathcal{N}_{m,\nu}\mathcal{N}_{m',\nu'}\frac{i^{m-m'+J+j}}{\rho_n^2}f(q,n,j)\frac{1}{kk'|\sin(\tilde{\phi}_k-\tilde{\phi}_{k'})|} \\ &\quad\times e^{i(m\tilde{\phi}_k-m'\tilde{\phi}_{k'}-j\tilde{\phi}_q)}\int_0^{2\pi}\mathrm{d}\phi_Q e^{i(m-m'-j-J)\phi_Q}.\end{aligned} \tag{8.46}$$

From this, we finally obtain the selection rule $\delta_{m-m',j+J}$ which expresses the conservation of angular momentum. Recalling that $k=k_{m,\nu}$, $k'=k_{m',\nu'}$, $Q=k_{J,N}$, we write as the final result

$$\begin{aligned}\mathcal{B}^{n,j;J,N}_{m,\nu;m',\nu'} &= \delta_{m-m',j+J}\tilde{\mathcal{N}}_{n,j}\mathcal{N}_{J,N}\mathcal{N}_{m,\nu}\mathcal{N}_{m',\nu'}\frac{2\pi}{\rho_n^2}f(q,n,j) \\ &\quad\times\frac{1}{k_{m,\nu}k_{m',\nu'}|\sin(\tilde{\phi}_k-\tilde{\phi}_{k'})|}e^{i(m\tilde{\phi}_k-m'\tilde{\phi}_{k'}-j\tilde{\phi}_q)}.\end{aligned} \tag{8.47}$$

The angles ϕ_k, $\phi_{k'}$, $\tilde{\phi}_q$ are defined in Eqs. (8.41) and (8.43). The value of q is given by Eq. (8.44).

Chapter 9: Conclusions and Future Avenues of Work

As we discussed in Ch. 1, the fields of photonics/optoelectronics are in need of new optically controllable materials that operate efficiently in the visible regime to help overcome the computational issues that we face today. From a practical perspective, three things need to be achieved in order for a material to becomes useful: (I) the system needs to be well characterized, meaning that all particle interactions are documented, (II) selective control of optical states, and (III) reliable control mechanisms. The study of higher energy exciton species in this thesis addresses a mixture of points (I) and (II).

We have demonstrated the first magnetic field measurements of the novel charged $2s$ exciton and utilized the valley Zeeman effect to extract an anomalously large g-factor. Recent reports in the literature show that $1s$ exciton species in TMDs exist along a sliding scale of carrier density induced many-body states. Our measurements place the first marker in mapping this interaction for $2s$ charged excitons, and indicate that the behavior observed for $1s$ exciton species likely continues into the $2s$ regime. From a fundamental physics perspective, this opens up a unique opportunity to study many-body interactions in higher energy exciton species. This would be energetically very difficult in traditional semiconductors systems with smaller exciton binding energies – like GaAs quantum wells – showcasing another area in which TMDs outperform their industry standard counterparts.

From an applications perspective, many-body interaction effects could be particularly useful for controlling excitons selectively. When a system is fully valley-polarized – a possible result of many-body interaction that we discussed in Ch. 5 – it can induce complete, preferential quenching of an exciton species which depends on the direction of the applied magnetic field ($\pm\hat{z}$). Having a larger family of documented exciton species over an an increased energy range allows for more options when engineering optical devices, making the $2s$ species a valuable addition.

In the later part of the thesis, we showed that twisted light does not modify the exciton spectrum in 2D semiconductors (including TMDs). This work was initially motivated by the idea that we could utilize twisted light to brighten dipole-forbidden transitions in TMDs (and other semiconductor systems), which would have been an novel, selective optical technique. However, this work yielded the interesting result that the momentum is instead transferred to the COM which has its own uses. As discussed in the Ch. 8, this could be used to provide excitonic lattices with artificial magnetic flux to aid in the production of chiral Mott insulators [65].

Another particularly interesting implication is that twisted light could be used as an alternative for performing in-plane momentum resolved PL – a technique that is particularly useful for studying band dispersion – but can be tricky to achieve. Our theoretical results, coupled with some early experimental results by another group indicate that the transfer of OAM to the COM can be used to reconstruct the dispersion of exciton bands [277]. Application of light with increasing ℓ pushes the electron to higher energies/momentum within the band and creating another way to measure the dispersion through PL.

Appendix A: Fabrication Recipes

A.1 Polymers

- Elvacite

  1. Per online instructions, the polymer should prepared in a 20% concentration by weight solution. The 80% volume of methyl isobutyl ketone (MIBK) should be agitated by the magnetic stirrer prior to and during the inclusion on the powdered Elvacite 2550 to reduce clumping.
  2. Agitate the polymer for 4 hours.
  3. Every hour after the first 4 hours, a seed sampling test should perform. This is done by spreading a small dot of the mixture on a glass slide and evaporating the solvent to see if seeds remain. Repeat until no seeds are left during the seed test.
  4. Spin at 750 rpm for 1 minute, bake at 120 °C for 10 minutes to cure.

- Polycarbonate (PC) - 15% Solution by Weight

  1. Carefully measure and pour 15g of PC and 57mL of chloroform into an amber bottle and replace the lid.

2. Place the sealed bottle into a sonicator filled with just enough water that the bottle isn't floating and let sonicate for about 6 hours. Note: There will still be a solid in the middle of the sample, but as long as it has formed a ball in the middle that's okay.
3. Spin at 750 rpm for 1 minute, bake at 100 °C for 5 minutes to cure.

- Polypropolene Carbonate (PPC) - 15% Solution by Weight

    1. Carefully measure and pour 15g of PPC and 57mL of chloroform into an amber bottle and replace the lid.
    2. Place the sealed bottle into a sonicator filled with just enough water that the bottle isn't floating and let sonicate for about 6 hours. It should completely dissolved.
    3. Spin at 750 rpm for 1 minute, bake at 70 °C for 4 minutes to cure.

Appendix B: Expanded Derivations for Magnetic Field Effects

B.1 The Weak-Field Zeeman Effect

Beginning by restating Eqn. 5.9

$$E^{(1)}_{\mathrm{n,l,j,m_j}} = \frac{eB}{2m} \left\langle n, l, j, m_{\mathrm{j}} \middle| \hat{L}_z + 2\hat{S}_z \middle| n, l', j, m'_{\mathrm{j}} \right\rangle . \tag{B.1}$$

To start, we can look to see if Eqn. B.1 commutes with any of the operators in the system to try to reduce our task at hand. We start with the commutation relation,

$$[L^2, \hat{L}_z + 2\hat{S}_z] = 0. \tag{B.2}$$

Recalling our elementary quantum mechanics, we know this to be true because L^2 commutes with any L operator and L and S are compatible observables. This implies that $\delta_{l,l'}$ is true, which allows us to reduce to,

$$E^{(1)}_{\mathrm{n,l,j,m_j}} = \frac{eB}{2m} \left\langle n, l, j, m_{\mathrm{j}} \middle| \hat{L}_z + 2\hat{S}_z \middle| n, l, j, m'_{\mathrm{j}} \right\rangle . \tag{B.3}$$

Similarly,

$$[\hat{J}_z, \hat{L}_z + 2\hat{S}_z] = [\hat{L}_z + \hat{S}_z, \hat{L}_z + 2\hat{S}_z] = 0. \tag{B.4}$$

Which implies that $\delta_{m_j,m_j'}$ is true, and that

$$E^{(1)}_{\mathrm{n,l,j,m_j}} = \frac{eB}{2m}\left\langle n,l,j,m_{\mathrm{j}} \middle| \hat{L}_z + 2\hat{S}_z \middle| n,l,j,m_{\mathrm{j}} \right\rangle. \tag{B.5}$$

This allows us to use non-degenerate perturbation theory and tells us that the matrix for our Zeeman Hamiltonian is perfectly diagonal. Now the task at hand is to solve for the energy correction. We begin by noting that if we apply the definition of $\hat{J}_z$ we can turn $\hat{L}_z + 2\hat{S}_z = \hat{J}_z + \hat{S}_z$, and we get,

$$\begin{aligned} E^{(1)}_{\mathrm{n,l,j,m_j}} &= \frac{eB}{2m}\left\langle n,l,j,m_{\mathrm{j}} \middle| \hat{J}_z + \hat{S}_z \middle| n,l,j,m_{\mathrm{j}} \right\rangle \\ &= \frac{eB}{2m}\Big[\underbrace{\left\langle n,l,j,m_{\mathrm{j}} \middle| \hat{J}_z \middle| n,l,j,m_{\mathrm{j}} \right\rangle}_{\mathrm{I}} + \underbrace{\left\langle n,l,j,m_{\mathrm{j}} \middle| \hat{S}_z \middle| n,l,j,m_{\mathrm{j}} \right\rangle}_{\mathrm{II}}\Big] \\ &= \frac{eB}{2m}\Big[\underbrace{\hbar m_j}_{\mathrm{I}} + \underbrace{\left\langle n,l,j,m_{\mathrm{j}} \middle| \hat{S}_z \middle| n,l,j,m_{\mathrm{j}} \right\rangle}_{\mathrm{II}}\Big]. \end{aligned} \tag{B.6}$$

The result of term I in Eqn. B.6 is a simple consequence of the $\hat{J}_z$ operator, but term II is a little trickier; we will now focus just on this to get our full result.

To begin with, we start with the statement that $\vec{S}$ is a vector operator under $\vec{J}$,

$$[\hat{J}_i, \hat{S}_j] = i\hbar\epsilon_{ijk}\hat{S}_k. \tag{B.7}$$

In quantum mechanics, vector operators have an unusual property that is,

$$[J^2[J^2,\vec{S}]] \propto (\vec{S}\cdot\vec{J})\vec{J} - \frac{1}{2}(J^2\vec{S} + \vec{S}J^2). \tag{B.8}$$

Supposed we take,

$$\left\langle jm_j \left| \frac{1}{\alpha}[J^2[J^2,\vec{S}]] \right| jm_j \right\rangle = \left\langle jm_j \left| (\vec{S}\cdot\vec{J})\vec{J} - \frac{1}{2}(J^2\vec{S}+\vec{S}J^2) \right| jm_j \right\rangle, \tag{B.9}$$

where $|jm_j\rangle$ is some generic eigenstate of $\vec{J}$. Since there will always be a J^2 term near both the bra and ket in the expectation value on the left-hand side, we can see that the terms they produce will cancel and we'll be left with,

$$\begin{aligned} 0 &= \left\langle jm_j \left| (\vec{S}\cdot\vec{J})\vec{J} \right| jm_j \right\rangle + \left\langle jm_j \left| -\frac{1}{2}(J^2\vec{S}+\vec{S}J^2) \right| jm_j \right\rangle \\ &= \left\langle jm_j \left| (\vec{S}\cdot\vec{J})\vec{J} \right| jm_j \right\rangle - \hbar^2 j(j+1)\left\langle jm_j \left| \vec{S} \right| jm_j \right\rangle. \end{aligned} \tag{B.10}$$

This implies that,

$$\langle\vec{S}\rangle_j = \frac{\langle(\vec{S}\cdot\vec{J})\vec{J}\rangle_j}{\langle\vec{J}^2\rangle_j}, \tag{B.11}$$

which is a projection formula, and we can use this result to finish computing Eqn. B.6.

Applying this formula to

$$\begin{aligned} \mathrm{II} &= \frac{eB}{2m}\left[\left\langle n,l,j,m_{\mathrm{j}} \left| \hat{S}_z \right| n,l,j,m_{\mathrm{j}} \right\rangle\right] \\ &= \frac{eB}{2m}\frac{\hbar m_j}{\hbar^2 j(j+1)}\left[\left\langle n,l,j,m_{\mathrm{j}} \left| \vec{S}\cdot\vec{J} \right| n,l,j,m_{\mathrm{j}} \right\rangle\right], \end{aligned} \tag{B.12}$$

we can use the fact that $\vec{J}=\vec{L}+\vec{S} \rightarrow \vec{S}\cdot\vec{J} = \frac{1}{2}(J^2+S^2+L^2)$ and assume a spin =1/2 system,

$$\begin{aligned}\mathrm{II} &= \frac{eB}{2m}\frac{\hbar m_j}{\hbar^2 j(j+1)}\frac{1}{2}\left[\left\langle n,l,j,m_{\mathrm{j}}\,\middle|\,J^2+S^2+L^2\,\middle|\,n,l,j,m_{\mathrm{j}}\right\rangle\right] \\ &= \frac{eB}{2m}\frac{\hbar m_j}{\hbar^2 j(j+1)}\frac{\hbar^2}{2}(j(j+1)+\underbrace{s(s+1)}_{=3/4}+l(l+1)).\end{aligned} \tag{B.13}$$

Plugging into Eqn. (B.6) and reducing, we find that

$$E^{(1)}_{\mathrm{n,l,j,m_j}} = \frac{eB}{2m}\left[\hbar m_j\underbrace{\left(1+\frac{j(j+1)-l(l+1)+\frac{3}{4}}{2j(j+1)}\right)}_{g_J(l)}\right]. \tag{B.14}$$

$g_J(l)$ is the Landé g-factor which takes into account all of the contributions to the angular momentum of the multiplet. It was first derived in 1921 by Alred Landé in 1921 [160]. We can further reduce and find that,

$$E^{(1)}_{\mathrm{n,l,j,m_j}} = \mu_{\mathrm{B}} B g_J(l) m_j. \tag{B.15}$$

Here, μ_{B} is the Bohr magneton, which is derived in the next section. Overall, we can take away that the magnetic field will split the energy linearly.

B.2 The Bohr Magneton

The magnetic dipole moment is the amount of torque caused by an external field on the dipole on a magnetic object and the *Bohr magneton* μ_{B} is the magnetic dipole moment of the hydrogen atom. Since most of our understanding of quantum mechanics begins with a fundamental understanding of the hydrogen atom, μ_{B} is generally considered the

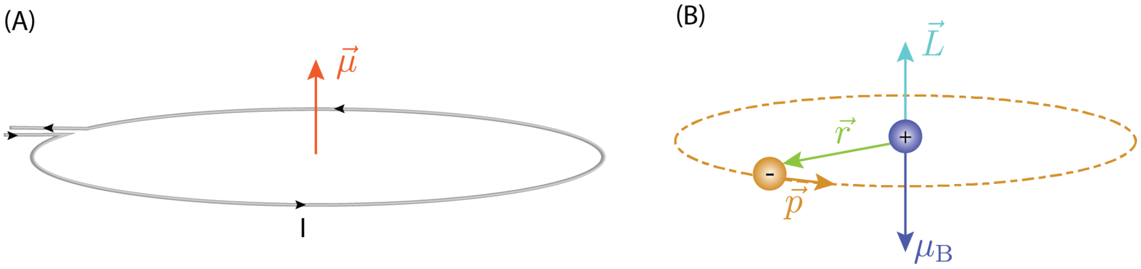

Figure B.1: (A) Current carrying loop with magnetic moment $\vec{\mu}$ and (B) the Bohr magneton (μ_B) arising from the Bohr model of the hydrogen atom.

natural unit of the magnetic dipole moment. Where does this unit come from though? As the name might suggest, μ_B arises when we envision the hydrogen atom in the Bohr picture (Figure B.1(B)). The single electron orbiting around the proton core of the hydrogen atom is very similar to a current carrying loop (Figure B.1(A)), since current is fundamentally moving electrons (or holes in a semiconductor).

Recall from elementary physics class that the magnetic moment (derived through the torque on a current carrying loop) is,

$$\vec{\mu} = I\vec{A}. \tag{B.16}$$

Where $\vec{\mu}$ is the magnetic moment, I is the current in the loop, and $\vec{A}$ is the area vector of the loop. Extending this to the Bohr picture, the current in that system is

$$I = -\frac{e}{\tau}. \tag{B.17}$$

Where -e is the single electron charge, and τ is the time that it takes to orbit the nucleus. If we assume that the electron travels in uniform circular motion around the nucleus, we can define the orbital period as,

$$\tau = \frac{2\pi r}{v}. \tag{B.18}$$

Here, r is the radius of the orbit and v is the velocity the electron. The assumption that the electron is experiencing uniform circular motion also allows us to define the area vector in the system and rewrite Eqn. (B.16) as,

$$\vec{\mu} = I\vec{A} = -\frac{e}{\frac{2\pi r}{v}}\pi r^2 = \frac{evr}{2}. \tag{B.19}$$

Recall, again from elementary physics, that the orbital angular momentum $\vec{L}$ is defined as,

$$\vec{L} = \vec{r} \times \vec{p} \tag{B.20}$$

Here, $\vec{p}$ is the linear momentum. Since $\vec{r}$ and $\vec{p}$ as always at a right-angle from one another in uniform circular motion, we can show that the magnitude of the orbital angular momentum as,

$$L = |\vec{L}| = |\vec{r} \times \vec{p}| = rp\sin(\theta) = rmv. \tag{B.21}$$

Substituting this result into Eqn. (B.19) and applying the full vector form,

$$\vec{\mu} = -\left(\frac{e}{2m_{\mathrm{e}}}\right)\vec{L}. \tag{B.22}$$

If we consider a field applied along $\hat{z}$, the momentum eigenstates are all multiples of $\hbar$, so we can take this to be the fundamental unit of momentum in this system, which gives

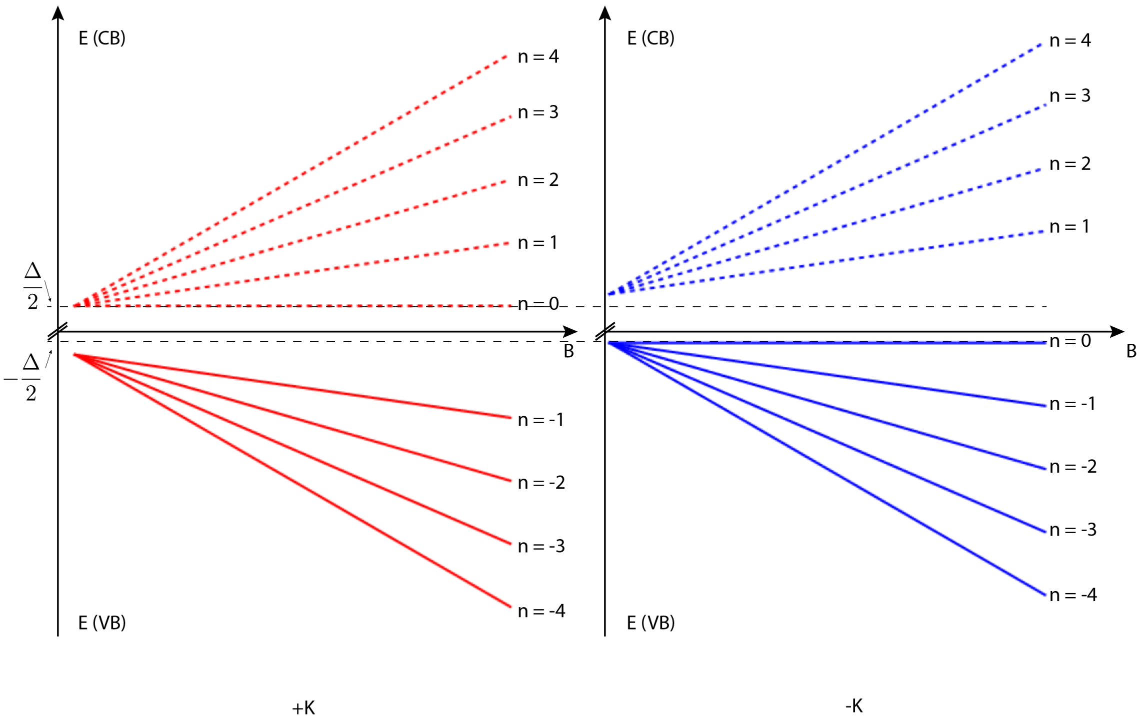

Figure B.2: Valley-resolved LLs in TMDs resulting from a real magnetic field. Note that the energy axis is split so as to showcase both the valence and conduction bands at the same time.

us the true definition of the Bohr magneton:

$$\mu_{\mathrm{B}} = -\frac{e\hbar}{2m_{\mathrm{e}}}. \tag{B.23}$$

B.3 Modified Landau Level Spectrum in TMDs

We start with the 2-band, basic $k \cdot p$ Hamiltonitan for TMDs [327]:

$$\hat{\mathcal{H}}_0 = v_{\mathrm{F}}(\tau p_x \hat{\sigma}_x + p_y \hat{\sigma}_y) + \frac{\Delta}{2}\hat{\sigma}_z. \tag{B.24}$$

Here, v_{F} is the Fermi velcoty, $\tau = \pm 1$ is the valley index in the $\pm$K valley, p_x/p_y are the momentum in the respective directions, Δ is the optical gap, and $\hat{\sigma}_i$ are the Pauli spin matrices.

We want to study the application of magnetic field, so we want to replace the momentum with a gauge-invariant form (i.e. use minimal substitution)

$$\vec{p} \to \vec{\Pi} = \vec{p} + e\vec{A}(\vec{r}). \tag{B.25}$$

Here, $\vec{A}(\vec{r})$ is the vector potential describing the magnetic field. We can use this substitution in Eqn. B.24 to obtain

$$\hat{\mathcal{H}}_B = \begin{bmatrix} \frac{\Delta}{2} & v_{\mathrm{F}}(\tau\Pi_x - i\Pi_y) \\ v_{\mathrm{F}}(\tau\Pi_x + i\Pi_y) & -\frac{\Delta}{2} \end{bmatrix}. \tag{B.26}$$

Since, in many way the QHE is similar to the quantum harmonic oscillator, is serves to take advantage of this and write the gauge invariant momentum operators in terms of the classic ladder operators,

$$\hat{a} = \frac{1}{\sqrt{2}}\left(\frac{x}{x_0} - i\frac{p}{p_0}\right) \tag{B.27a}$$

and

$$\hat{a}^{\dagger} = \frac{1}{\sqrt{2}}\left(\frac{x}{x_0} + i\frac{p}{p_0}\right). \tag{B.27b}$$

Here, x and p are the position and momentum, $x_0 = \sqrt{\frac{\hbar}{m\omega}}$, and $p_0 = \sqrt{\hbar m\omega}$. Working through some algebra, it can be shown that

$$\Pi_x = \frac{\hbar}{\sqrt{2}l_B}(\hat{a}^{\dagger} + \hat{a}) \tag{B.28a}$$

and

$$\Pi_y = \frac{\hbar}{i\sqrt{2}l_B}(\hat{a}^\dagger - \hat{a}). \tag{B.28b}$$

Here, $l_b = \sqrt{\frac{\hbar}{eB}}$ is the magnetic length associated with the cylcotron motion of carriers in the system. Substituting this into Eqn. B.26 and making the substitution that $\frac{\omega}{2} = \frac{v_\mathrm{F}}{\sqrt{2}*l_B}$ we get,

$$\hat{\mathcal{H}}_B = \begin{bmatrix} \frac{\Delta}{2} & \frac{1}{2}\omega\hbar(\hat{a}(1+\tau) + (\tau-1)\hat{a}^\dagger) \\ \frac{1}{2}\omega\hbar(\hat{a}(\tau-1) + (1+\tau)\hat{a}^\dagger) & -\frac{\Delta}{2} \end{bmatrix}. \tag{B.29}$$

We now want to solve for the new eigenvalues in the system with the applied field, so we take $|\hat{\mathcal{H}}_B - \epsilon_n \nVdash| = 0$ and solve for ϵ_n. This gives us,

$$\epsilon_n = \pm\frac{1}{2}\sqrt{\Delta^2 + a^2(-1+\tau^2)\omega^2\hbar^2 + 2a(1+\tau^2)\omega^2\hbar^2 a^\dagger + (-1+\tau^2)\omega^2\hbar^2 a^{\dagger 2}}. \tag{B.30}$$

We want to simplify things, and also know what the behavior is in both of the valleys, so we can substitute $\tau = 1$ to get the +K-valley behavior

$$\epsilon_n^{\tau=+1} = \pm\frac{1}{2}\sqrt{\Delta^2 + 4\omega^2\hbar^2 a a^\dagger} = \pm\frac{1}{2}\sqrt{\Delta^2 + 4\omega^2\hbar^2 n}, \tag{B.31}$$

and for $\tau = -1$ to get the -K-valley behavior

$$\epsilon_n^{\tau=-1} = \pm\frac{1}{2}\sqrt{\Delta^2 + 4\omega^2\hbar^2 a a^\dagger} = \pm\frac{1}{2}\sqrt{\Delta^2 + 4\omega^2\hbar^2 n}. \tag{B.32}$$

If we take the cyclotron frequency to be $\omega_c = \frac{e\hbar B}{m}$ and do a first order expansion in both valleys we get,

$$\epsilon_n \approx \pm\frac{\Delta}{2} \pm \hbar\omega_c n. \tag{B.33}$$

A peculiarity in TMDs arising from inequivalent Berry curvature at each valley ($\Omega_{+K} = -\Omega_{-K}$) is that the n index labeling for the Landau levels is different in each valley given by +K$_c$ = n = 0,1,2,3... and -K$_c$ = n = 1,2,3... while +K$_v$ =-K$_c$ and -K$_v$ =+K$_c$ [254, 320]. An illustration can be found in Fig. B.3.

Appendix C: Elionix Standard Operating Procedure

Between the end of the first and second year of my doctoral study I was heavily involved with the commissioning of the Elionix GS-100 system on campus. During that time, it was my job to train and clear new users and as part of that work I wrote a detailed standard operating procedure as a reference for users. That reference is still in use, and has assisted dozens of users during their training and work. It details the standard operating procedure for many common tasks that users perform. The rest of this section holds a copy of the procedure.

Elionix Loading Procedure

1. Check that the sample holder is at the exchange position before beginning

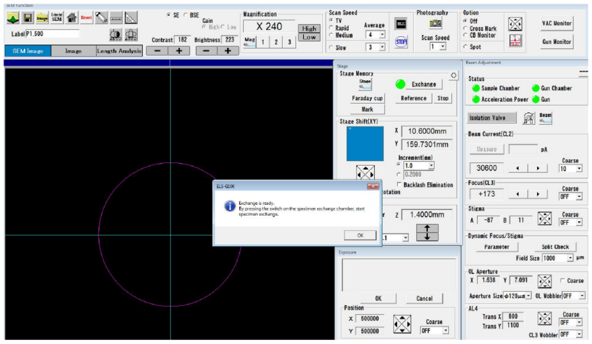
ELS-G100

Exchange is ready.
By pressing the switch on the specimen exchange chamber, start specimen exchange.

2. Vent the load-lock

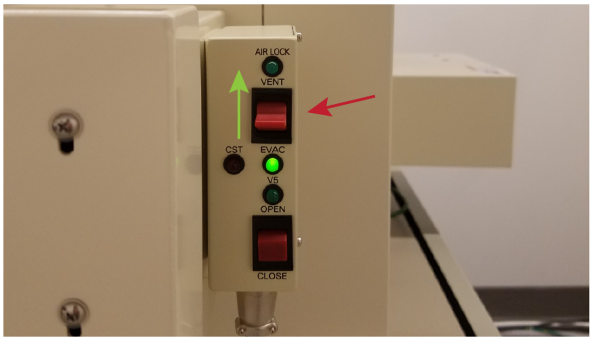

3. Unlock the load-lock

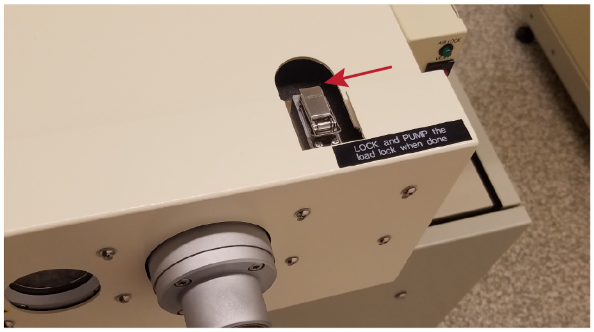

4. Gently open the load-lock and secure the sample(s) with appropriate clips (arrows mark the clips)

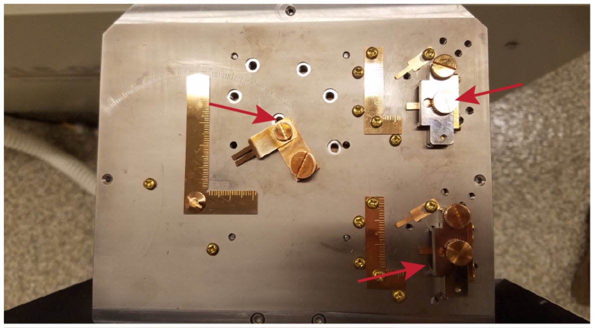

5. Gently close and lock the load-lock, then flip the evacuation switch (flashing = pumping)

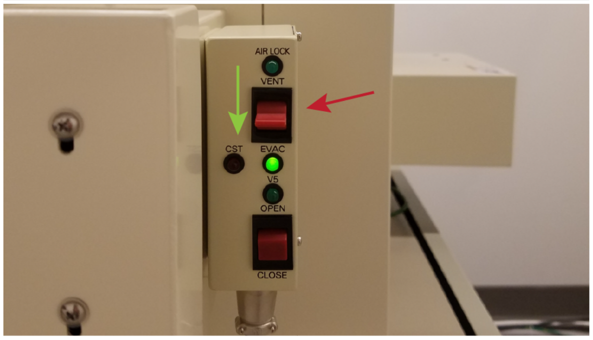

6. Flip the open switch when the light stops flashing. You have about 20s to do this, otherwise you'll need to re-pump the load-lock

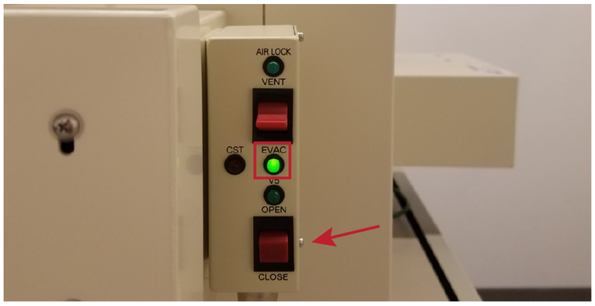

7. Unlock the transfer rod and gently push the stage into the sample chamber

8. Unscrew the sample transfer rod and pull it back gently

9. Pull the transfer rod gently back in and check to make sure that the stage is unattached through the port on the top of the load-lock

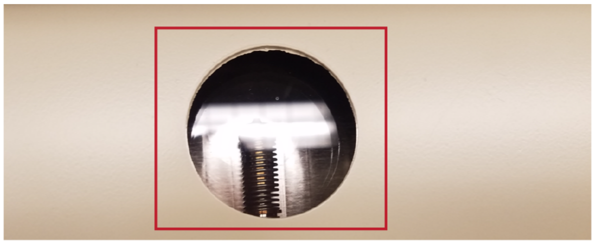

10. Push the sample transfer rod all the way in gently and then pull it back out all the way (this step ensures that the stage is at the correct position)

11. Lock the sample transfer rod once it is fully out of the load-lock

12. Close the gate valve between the sample chamber and the load-lock

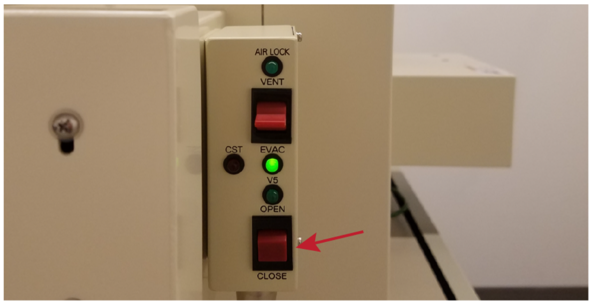

Elionix Unloading Procedure

1. Close the isolation valve. This isolates the electron gun from the sample chamber

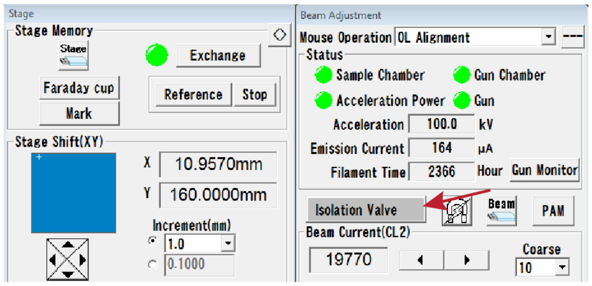

X 10.9570mm
Y 160.0000mm
Increment(mm) ● 1.0 ○ 0.1000
Mouse Operation OL Alignment
Acceleration 100.0 kV
Emission Current 164 µA
Filament Time 2366 Hour
Beam Current(CL2) 19770
Coarse 10

2. Press the "Exchange" button in the SEM software and then wait for the stage to move to that position

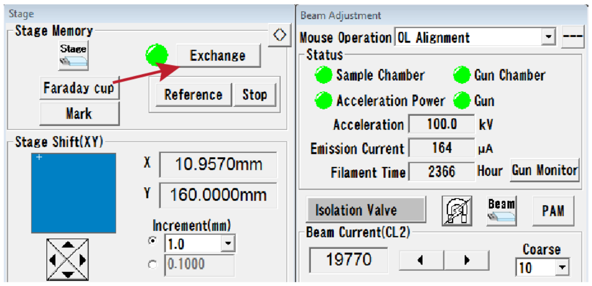

X 10.9570mm
Y 160.0000mm
Increment(mm) ● 1.0 ○ 0.1000
Mouse Operation OL Alignment
Acceleration 100.0 kV
Emission Current 164 µA
Filament Time 2366 Hour
Beam Current(CL2) 19770
Coarse 10

3. Flip the evacuation switch on the load-lock (flashing = pumping)

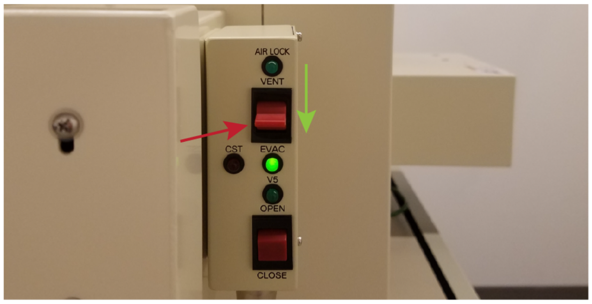

4. Flip the open switch when the light stops flashing (you have about 20s to do this, otherwise you'll need to re-pump the load-lock)

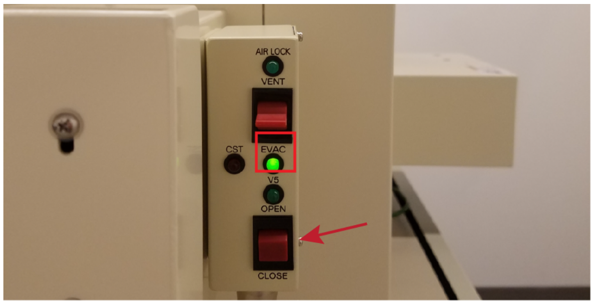

5. Unlock the transfer rod and gently push the transfer rod all the way in

6. Fully screw the transfer rod into the sample stage until the handle rachets over, then loosen by 1/2 turn

7. Gently pull the transfer rod all the way out, then lock the rod

8. Close the gate valve between the load-lock and the inner chamber

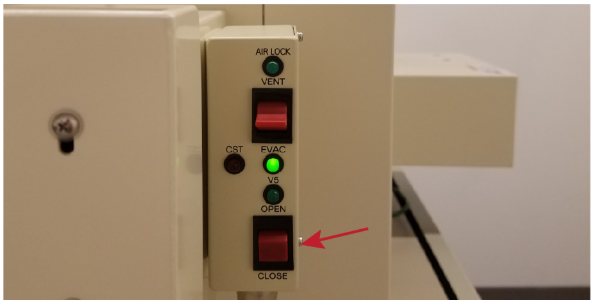

9. Flip the vent button to vent the load-lock, unlock the load-lock, and unload your sample from the sample stage

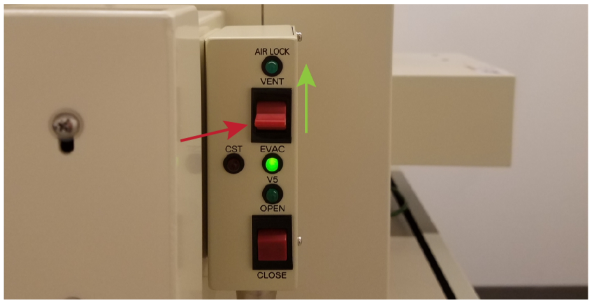

10. After unloading is complete, close the door to the load-lock and evacuate the chamber again

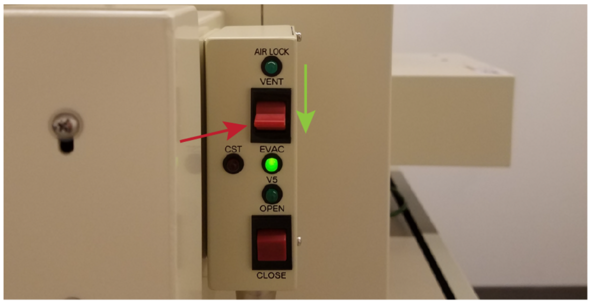

Writing a Pattern

Overview:
1. Import and format files
2. Setup schedule file and alignment
3. Place design
4. Expose

1. Press "Select Field Size/Dot"

2. Select a writefield size and the number of dots per field (technically the system optimized for 500um, but all of them work well)

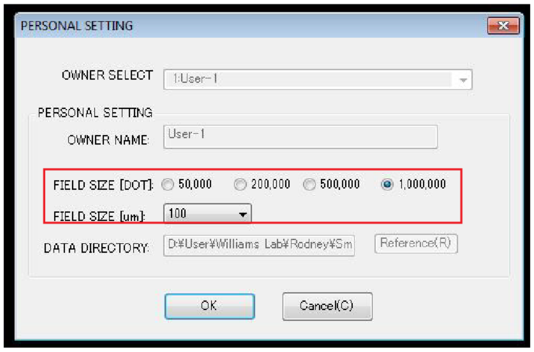
PERSONAL SETTING

OWNER SELECT: 1:User-1

PERSONAL SETTING

OWNER NAME: User-1

FIELD SIZE [DOT]: ○ 50,000 ○ 200,000 ○ 500,000 ● 1,000,000

FIELD SIZE [um]: 100

DATA DIRECTORY: D:¥User¥Williams Lab¥Rodney¥Sm

3. Select either GDS or DXF

4. Select "Ref.(R)" and then select your file. Note that this system will only import AutoCAD 2010 .dxf files

5. Select layers of interest by double-clicking on them or using the "Select all" button

6. Click "Conversion(D)"

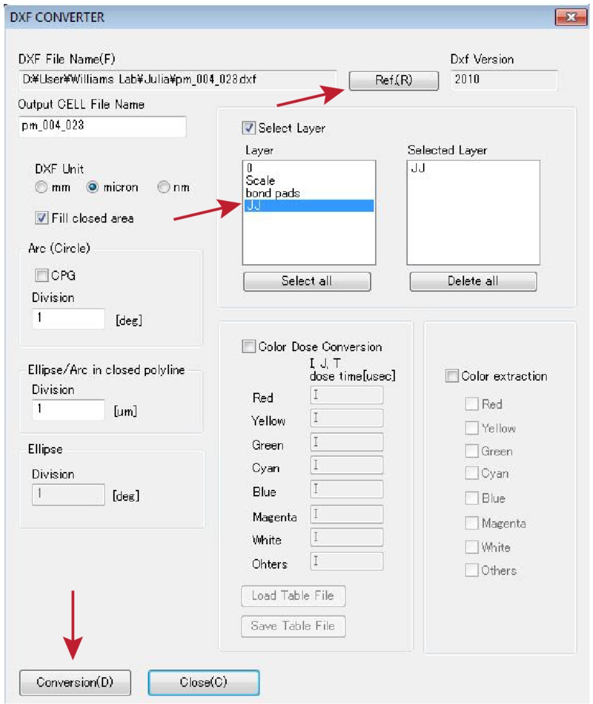
DXF CONVERTER

DXF File Name(F): D:¥User¥Williams Lab¥Julia¥pm_004_023.dxf

Dxf Version: 2010

Output CELL File Name: pm_004_023

DXF Unit: ○ mm ● micron ○ nm

☑ Fill closed area

Arc (Circle): ☐ CPG

Division: 1 [deg]

Ellipse/Arc in closed polyline

Division: 1 [um]

Ellipse

Division: 1 [deg]

☑ Select Layer

Layer:
0
Scale
bond pads
JJ

Selected Layer:
JJ

☐ Color Dose Conversion

I, J, T dose time[usec]

☐ Color extraction

7. Press "Select CELL file." During the conversion process in the last step, a .cell file with the same name as your .dxf was generated. Select this file and choose your coordinate origin. Press OK

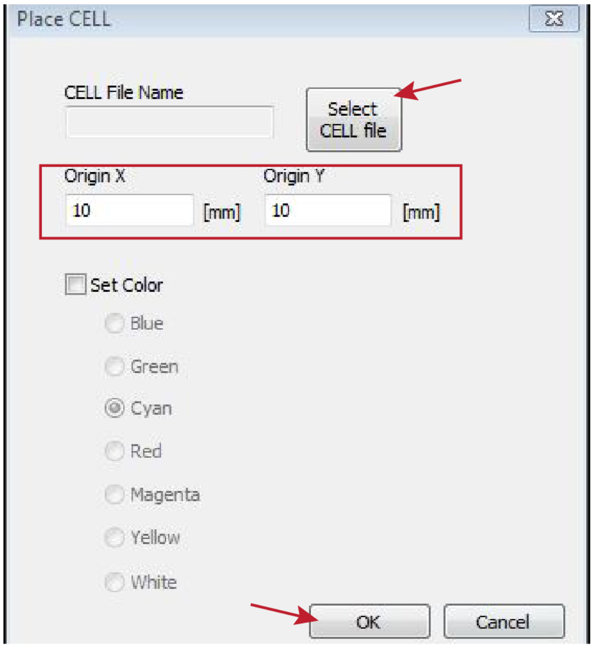
Place CELL

CELL File Name:

Origin X: 10 [mm]

Origin Y: 10 [mm]

☐ Set Color

○ Blue
○ Green
● Cyan
○ Red
○ Magenta
○ Yellow
○ White

Placing a Writefield

Any elements that you want to write needs to be in a "writefield." The writefield tells the lithography system where to expose your sample to the electron beam. After importing your design using the instructions above, use one of the following options to place writefields on your design.

Option 1

1. Select the automatic writefield button. This places writefields of the previously specified size across the pattern at the discretion of the software

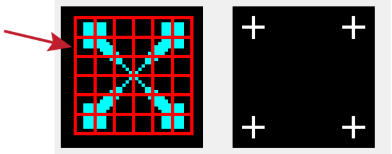

2. Give the field matrix a name and choose the writing order. Press OK

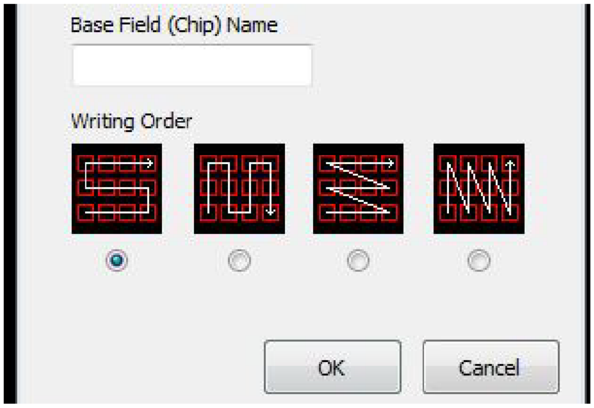

Base Field (Chip) Name

Writing Order

● ○ ○ ○

Option 2

1. Select the single writefield button

2. Define a name for your writefield. It should start with a letter, not a number

3. Define coordinates for the writefield. The coordinates correspond to the center of the writefield

4. Hit OK

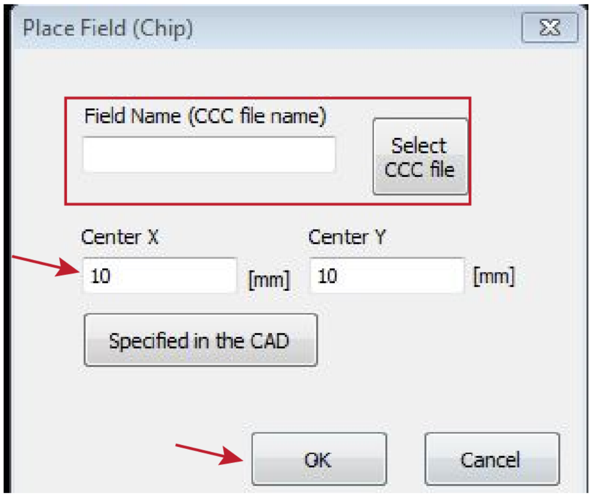

Place Field (Chip)

Field Name (CCC file name)

Center X 10 [mm]

Center Y 10 [mm]

Option 3

1. Select he single writefield button

2. Define a name for your writefield. It should start with a letter, not a number

3. Define coordinates for the writefield using the "Specified in CAD" button. After clicking this button, click on your CAD file where you want to place the writefield. The point where you click will be the center of the writefield

4. Hit OK

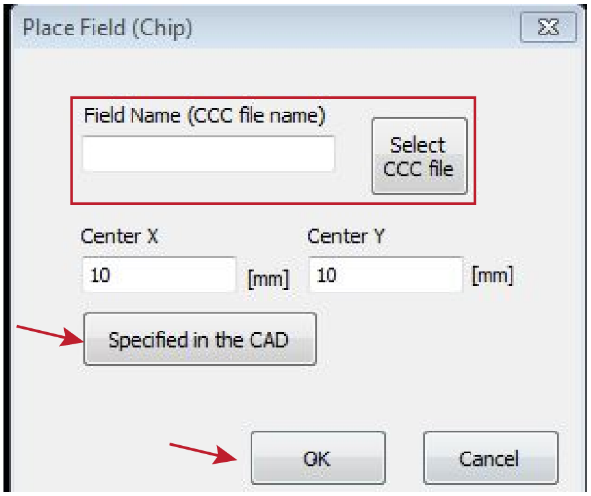
Place Field (Chip)

Field Name (CCC file name):

Center X: 10 [mm]

Center Y: 10 [mm]

<u>Option 4</u>

1. Follow Option 2 or Option 3 to define a single writefield

2. Click the matrix writefield button, then select the writefield you want to build the matrix off from

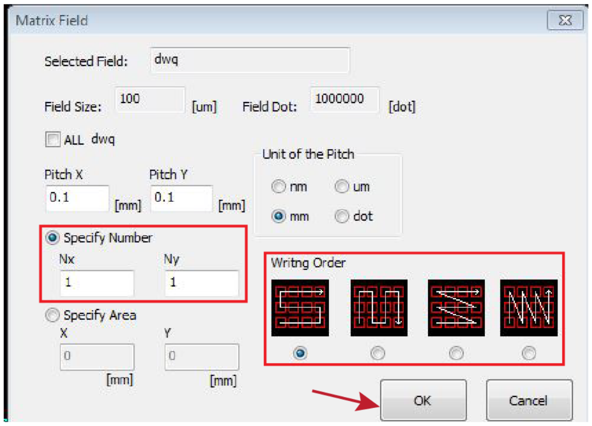
Matrix Field

Selected Field: dwq

Field Size: 100 [um] Field Dot: 1000000 [dot]

☐ ALL dwq

Pitch X: 0.1 [mm] Pitch Y: 0.1 [mm]

Unit of the Pitch: ○ nm ○ um ● mm ○ dot

● Specify Number Nx: 1 Ny: 1

○ Specify Area X: 0 [mm] Y: 0 [mm]

Writng Order: ● ○ ○ ○

3. Define the dimensions of the writefield matrix

4. Select the writing order and hit OK

Deleting a Writefield

1. Select single writefield deletion (L) or lasso deletion button (R)

2. Select writefield(s) of interest, then hit OK when prompted about deletion

Calculating and Assigning Dose

All writefields need a dose time, and writing feed/scan pitch associated with them. This tells the lithography system how many electrons to deliver to a given region (the dose) and how far is should move in x and y in between delivering that dose

1. Select "Dose Calculator"

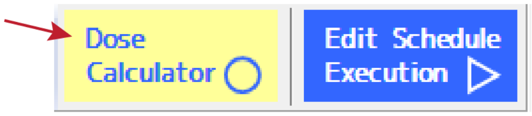

2. Adjust the Dot Number and Field Size to match the parameters you selected at the beginning of the write

3. Enter the desired Dose Area

4. Enter the Beam Current you are writing with

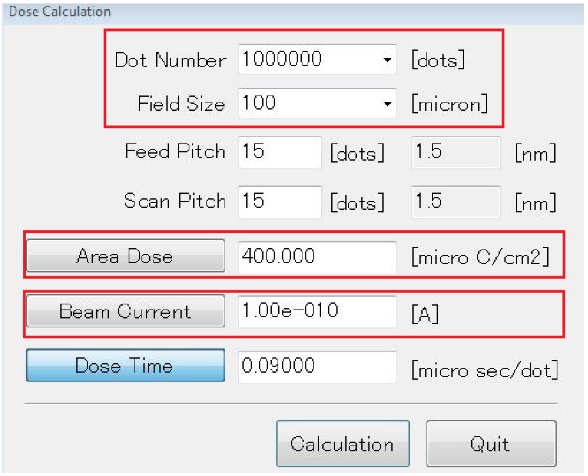

Dose Calculation

Dot Number 1000000 [dots]

Field Size 100 [micron]

Feed Pitch 15 [dots] 1.5 [nm]

Scan Pitch 15 [dots] 1.5 [nm]

Area Dose 400.000 [micro C/cm2]

Beam Current 1.00e-010 [A]

Dose Time 0.09000 [micro sec/dot]

5. Adjust the Feed Pitch/Scan Pitch and hit "Calculation" until the dose time isn't red (i.e. not too short for machine capabilities)

6. Copy the Dose Time

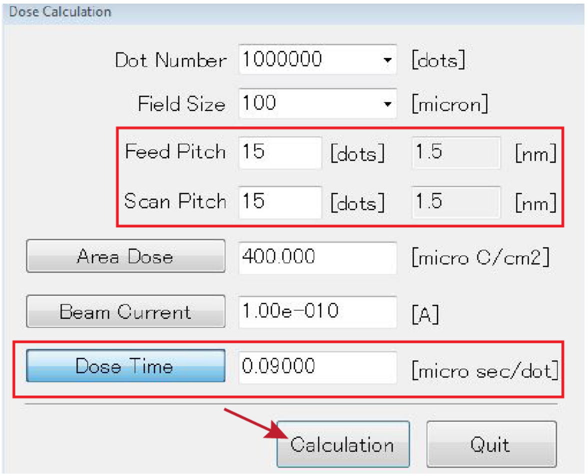

Dose Calculation

Dot Number 1000000 [dots]

Field Size 100 [micron]

Feed Pitch 15 [dots] 1.5 [nm]

Scan Pitch 15 [dots] 1.5 [nm]

Area Dose 400.000 [micro C/cm2]

Beam Current 1.00e-010 [A]

Dose Time 0.09000 [micro sec/dot]

7. Select the Dose Pallet

8. In the line corresponding to the color of your layer, input the Feed and Scan pitch values from the last step. Paste the Dose Time in and click "Apply" before closing the window

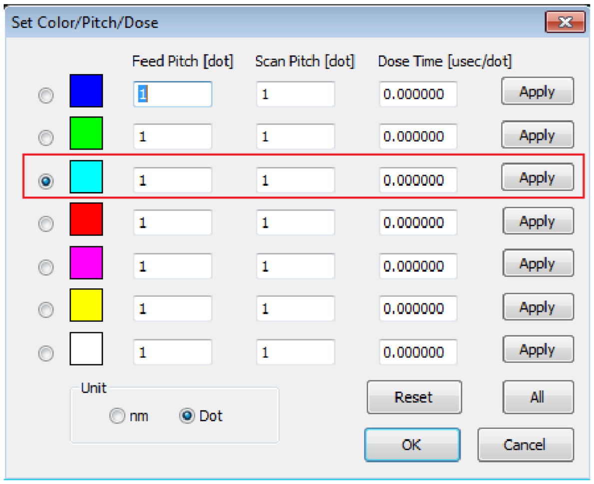
Set Color/Pitch/Dose

		Feed Pitch [dot]	Scan Pitch [dot]	Dose Time [usec/dot]	
○	🟦	1	1	0.000000	Apply
○	🟩	1	1	0.000000	Apply
●	🟦	1	1	0.000000	Apply
○	🟥	1	1	0.000000	Apply
○	🟪	1	1	0.000000	Apply
○	🟨	1	1	0.000000	Apply
○	⬜	1	1	0.000000	Apply

Unit ○ nm ● Dot

9. Your file is now complete. Hit the Save.CON button and save your file

Building in an Alignment Procedure

Having an alignment step during your write ensures that you pattern ends up where you expect it to be. This procedure helps you correct for small rotations of the sample that could result in misalignment of the write with the desired area

1. Click the alignment mark button

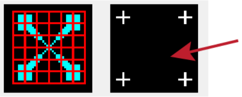

2. Choose 2 or 4 point alignment

3. Enter the position to which you want to align during the write. Hit OK

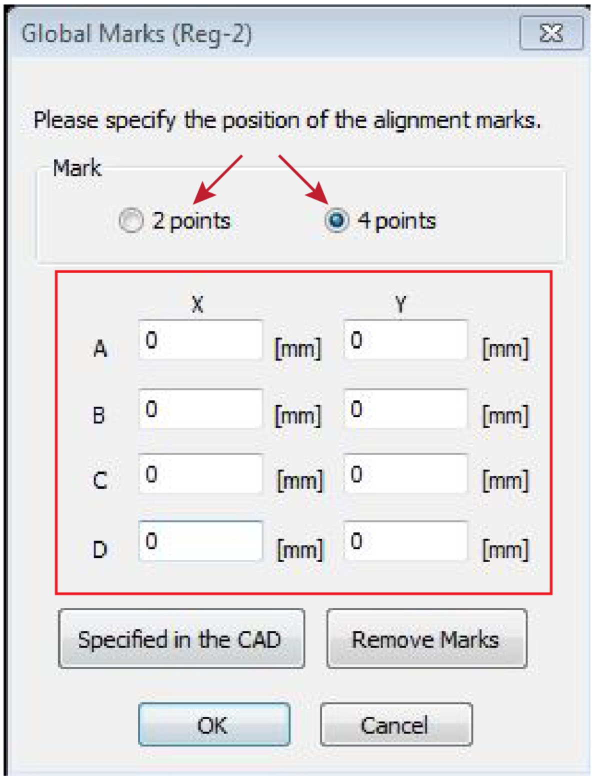
Global Marks (Reg-2)

Please specify the position of the alignment marks.

Mark ○ 2 points ● 4 points

	X		Y	
A	0	[mm]	0	[mm]
B	0	[mm]	0	[mm]
C	0	[mm]	0	[mm]
D	0	[mm]	0	[mm]

4. Press Save.CON and save your alignment layer

Creating a Schedule File

A schedule file runs the alignment procedure, tells the lithgraphy system what order to write your .CON files in, and lets you change the beam current in the middle of the write

1. Once you have made all of your .CON files for the write, select "Edit Schedule Execution"

2. Import each .CON file in the order you would like to write them. Alignment comes before any writing is done.

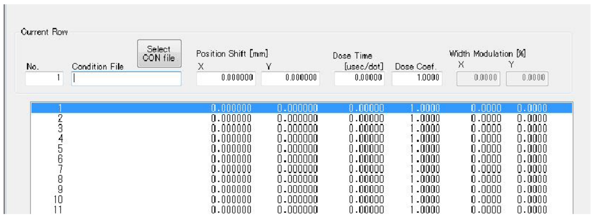

No.	Condition File	Position Shift [mm] X	Position Shift [mm] Y	Dose Time [usec/dot]	Dose Coef.	Width Modulation [%] X	Width Modulation [%] Y
1		0.000000	0.000000	0.00000	1.0000	0.0000	0.0000

1	0.000000	0.000000	0.00000	1.0000	0.0000	0.0000
2	0.000000	0.000000	0.00000	1.0000	0.0000	0.0000
3	0.000000	0.000000	0.00000	1.0000	0.0000	0.0000
4	0.000000	0.000000	0.00000	1.0000	0.0000	0.0000
5	0.000000	0.000000	0.00000	1.0000	0.0000	0.0000
6	0.000000	0.000000	0.00000	1.0000	0.0000	0.0000
7	0.000000	0.000000	0.00000	1.0000	0.0000	0.0000
8	0.000000	0.000000	0.00000	1.0000	0.0000	0.0000
9	0.000000	0.000000	0.00000	1.0000	0.0000	0.0000
10	0.000000	0.000000	0.00000	1.0000	0.0000	0.0000
11	0.000000	0.000000	0.00000	1.0000	0.0000	0.0000

3. Check the dosage of the different .CON files to verify they are correct

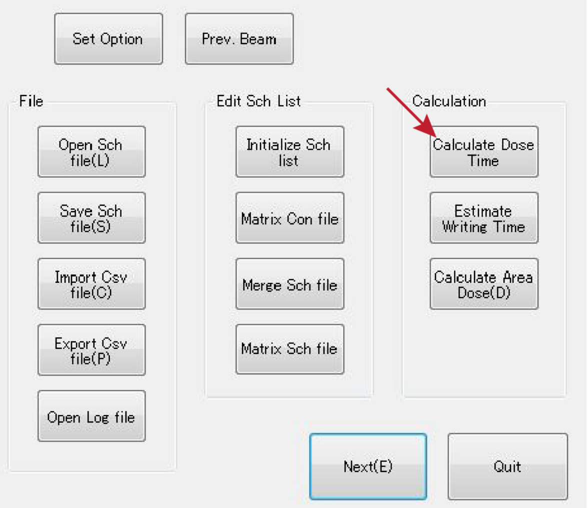

4. To do this, enter the current that will be used to write features and click "Calculation(C)" to verify the dose of each .CON file

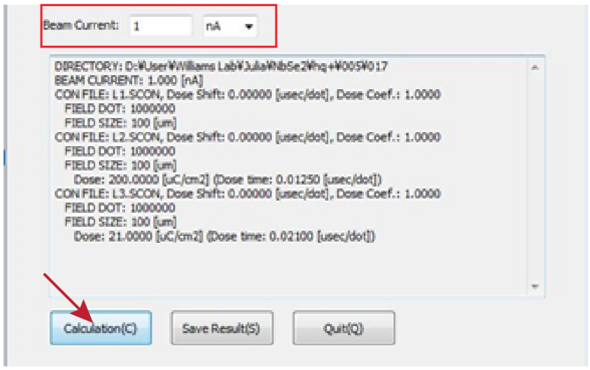

Beam Current: 1 nA

```
DIRECTORY: D:¥User¥Williams Lab¥Julia¥NbSe2¥hq+¥005¥017
BEAM CURRENT: 1.000 [nA]
CON FILE: L1.SCON, Dose Shift: 0.00000 [usec/dot], Dose Coef.: 1.0000
  FIELD DOT: 1000000
  FIELD SIZE: 100 [um]
CON FILE: L2.SCON, Dose Shift: 0.00000 [usec/dot], Dose Coef.: 1.0000
  FIELD DOT: 1000000
  FIELD SIZE: 100 [um]
    Dose: 200.0000 [uC/cm2] (Dose time: 0.01250 [usec/dot])
CON FILE: L3.SCON, Dose Shift: 0.00000 [usec/dot], Dose Coef.: 1.0000
  FIELD DOT: 1000000
  FIELD SIZE: 100 [um]
    Dose: 21.0000 [uC/cm2] (Dose time: 0.02100 [usec/dot])
```

5. Back on the menu from step 3. click “Estimate Write Time.” It is extremely uncommon for even a large write to take than an hour. Use this as a metric to judge if something seems off in one of the previous steps

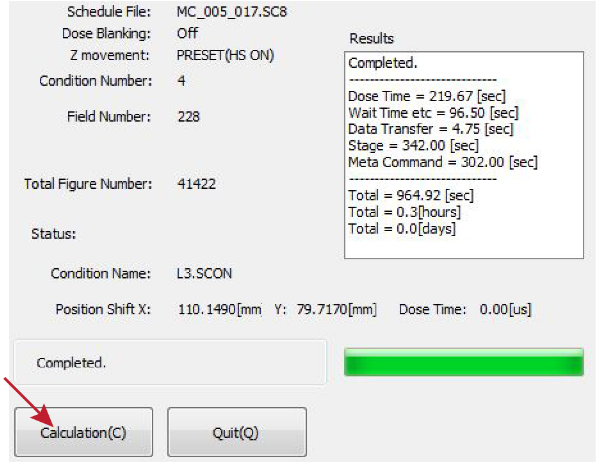

Schedule File: MC_005_017.SC8
Dose Blanking: Off
Z movement: PRESET(HS ON)
Condition Number: 4
Field Number: 228
Total Figure Number: 41422
Status:
Condition Name: L3.SCON
Position Shift X: 110.1490[mm Y: 79.7170[mm] Dose Time: 0.00[us]

Results

```
Completed.
------------------------------
Dose Time = 219.67 [sec]
Wait Time etc = 96.50 [sec]
Data Transfer = 4.75 [sec]
Stage = 342.00 [sec]
Meta Command = 302.00 [sec]
------------------------------
Total = 964.92 [sec]
Total = 0.3[hours]
Total = 0.0[days]
```

Completed.

6. Save your schedule file

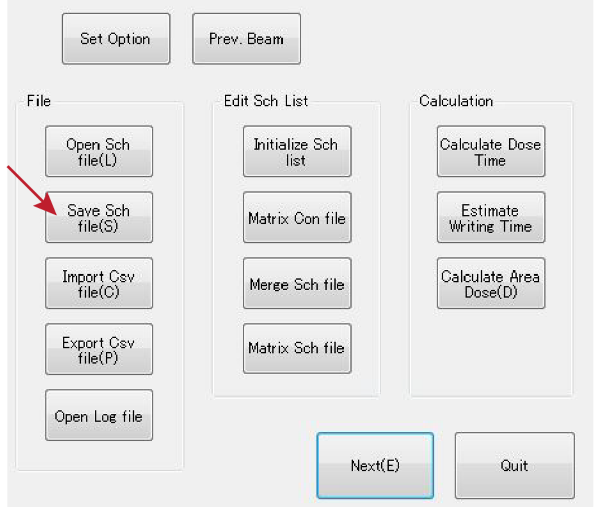

Adjusting Alignment in the Schedule File

1. Using the schedule file you just created, you need to turn on the alignment procedure. Click the “Set Option” to open the menu to engage this feature

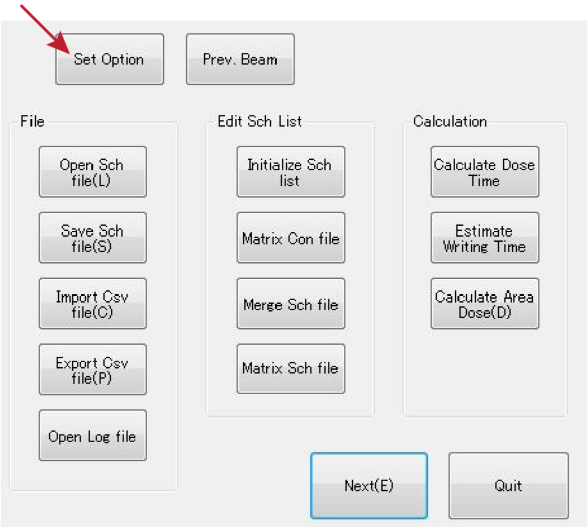

3. Turn on “Global Mark (Reg-2)”, then click “Search Settings & View Profile”

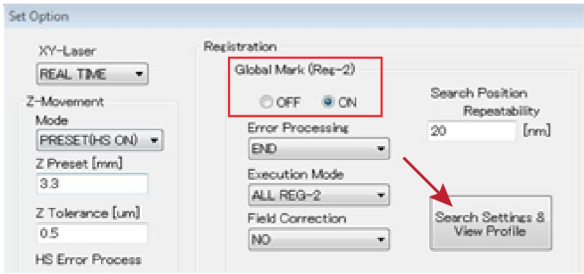

Set Option

XY-Laser: REAL TIME
Z-Movement Mode: PRESET(HS ON)
Z Preset [mm]: 3.3
Z Tolerance [um]: 0.5
HS Error Process

Registration
Global Mark (Reg-2): ○ OFF ● ON
Error Processing: END
Execution Mode: ALL REG-2
Field Correction: NO
Search Position Repeatability: 20 [nm]

4. Change “Control Type” to “Manual”

5. Hit Okay

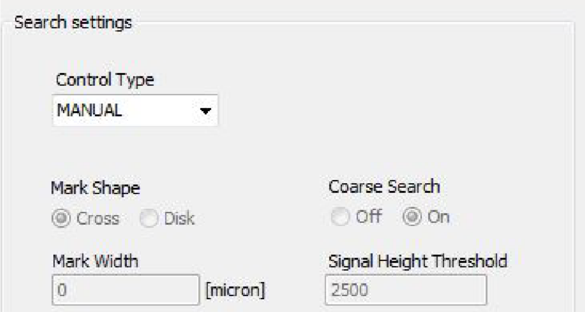

Search settings

Control Type: MANUAL
Mark Shape: ● Cross ○ Disk
Coarse Search: ○ Off ● On
Mark Width: 0 [micron]
Signal Height Threshold: 2500

Inserting a Meta Command

Meta commands allow you to change the writing current between .Con files. This is very useful to optimize both the accuracy and speed of your write by writing delicate features at low current and large features at high current

1. Right click on the .CON file in your schedule file you want to insert the command after

2. Click “Insert Meta Command”

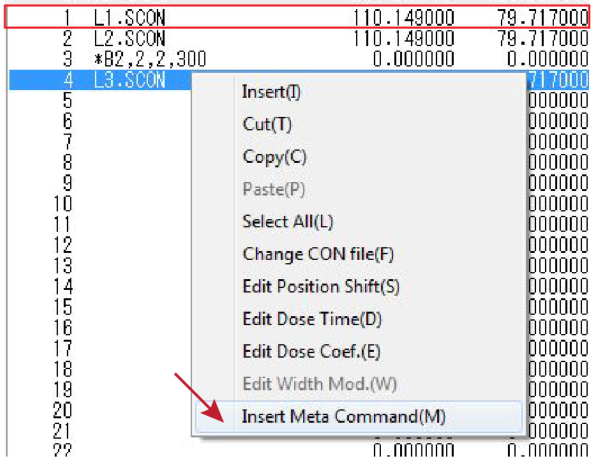

```
 1  L1.SCON          110.149000    79.717000
 2  L2.SCON          110.149000    79.717000
 3  *B2,2,2,300        0.000000     0.000000
 4  L3.SCON
```

3. Select the program corresponding to the current you want to change to

4. Assign a wait time for the current change. This is how long the machine waits for the beam to settle after the current is changed to minimize drift

5. Click insert

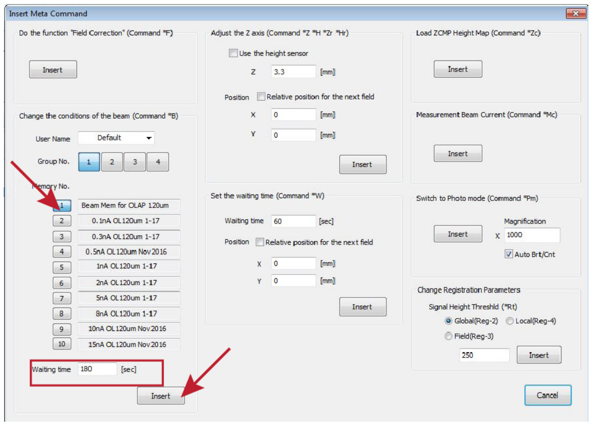

Insert Meta Command

Do the function "Field Correction" (Command *F)

Change the conditions of the beam (Command *B)
User Name: Default
Group No.: 1 2 3 4
Memory No.

1	Beam Mem for OLAP 120um
2	0.1nA OL120um 1-17
3	0.3nA OL120um 1-17
4	0.5nA OL120um Nov2016
5	1nA OL120um 1-17
6	2nA OL120um 1-17
7	5nA OL120um 1-17
8	8nA OL120um 1-17
9	10nA OL120um Nov2016
10	15nA OL120um Nov2016

Waiting time: 180 [sec]

Adjust the Z axis (Command *Z *H *Zr *Hr)
☐ Use the height sensor
Z: 3.3 [mm]
Position ☐ Relative position for the next field
X: 0 [mm]
Y: 0 [mm]

Set the waiting time (Command *W)
Waiting time: 60 [sec]
Position ☐ Relative position for the next field
X: 0 [mm]
Y: 0 [mm]

Load ZCMP Height Map (Command *Zc)

Measurement Beam Current (Command *Mc)

Switch to Photo mode (Command *Pm)
Magnification: x 1000
☑ Auto Brt/Cnt

Change Registration Parameters
Signal Height Threshld (*Rt)
● Global(Reg-2) ○ Local(Reg-4)
○ Field(Reg-3)
250

Building a Dose Test

A dose test lets you write the same pattern repeatedly with different electron doses in a systematic way. This is a calibration procedure used to make sure that you final devices have clean, sharp edges and that no contacts are shorted

1. Open a schedule file that has already been built. It is better if this file doesn't have the alignment step yet, otherwise the following steps will result in repetitive alignment. It is better to add alignment after step 7.

2. Select "Matrix Sch file"

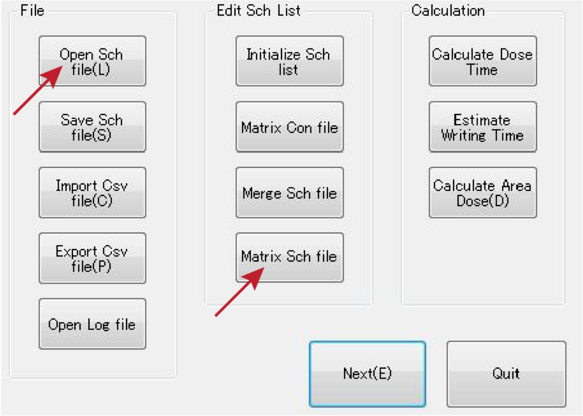

3. Select your schedule file

4. Set spacing between elements in the dose test

5. Assign your dose increment for each portion of the dose test. Only use one of the options to increase the dose

6. Set the size of the array

7. Select the order for writing the pattern. For ease of discerning dose when looking at the test, the third from the left is the best option

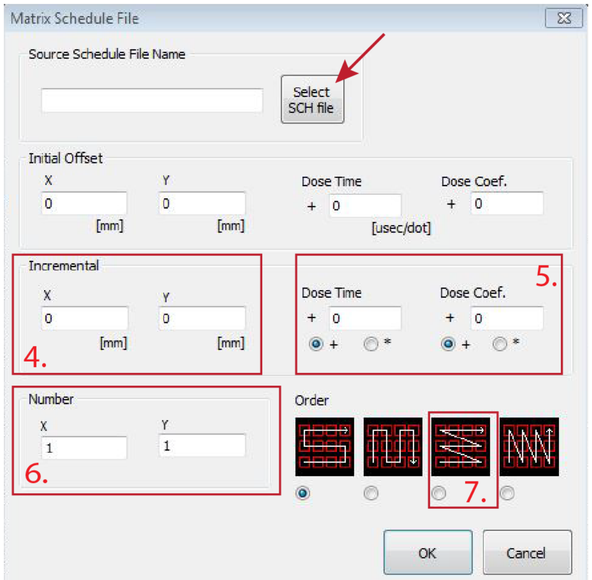
Matrix Schedule File

Source Schedule File Name

Initial Offset
X 0 [mm]
Y 0 [mm]
Dose Time + 0 [usec/dot]
Dose Coef. + 0

Incremental
X 0 [mm]
Y 0 [mm]

Dose Time + 0 ● + ○ *
Dose Coef. + 0 ● + ○ *

Number
X 1
Y 1

Order

Writing the Pattern

Placing the Pattern

1. Once the schedule file is complete, hit next

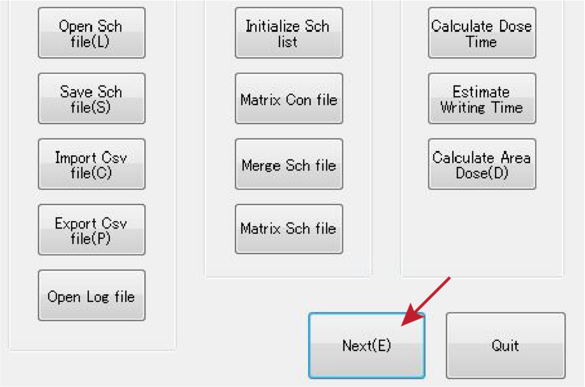

2. Press “Display Sample Holder”

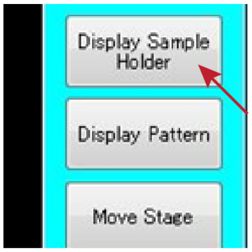

3. From the dropdown menu, select the “MultiPiece MS01960” carrier and enter the size of your sample

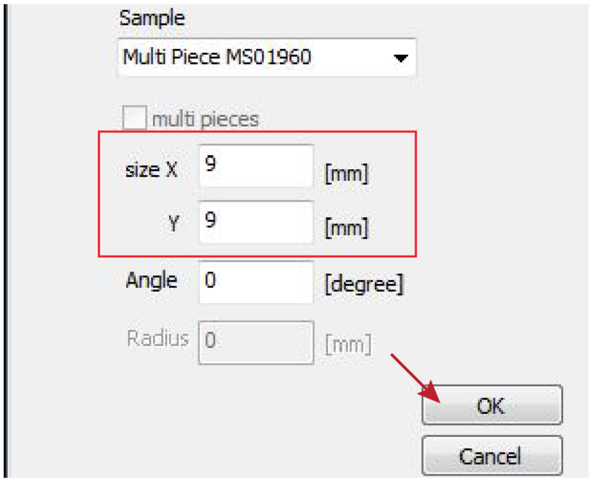
Sample: Multi Piece MS01960

☐ multi pieces

size X 9 [mm]

Y 9 [mm]

Angle 0 [degree]

Radius 0 [mm]

4. Click “Move Stage”

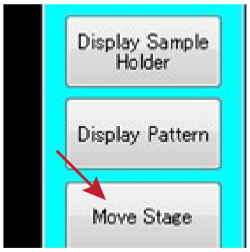

5. Click where you like to move the stage to (position of your chip). When asked to automatically adjust the height sensor - say “No”

6. After the stage has moved to the position of interest unblank the beam. Drive to the position you want to define as the origin of your sample

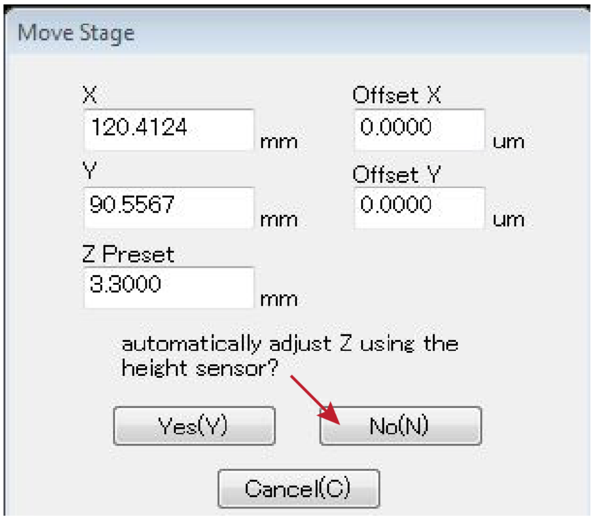
Move Stage

X 120.4124 mm

Y 90.5567 mm

Z Preset 3.3000 mm

Offset X 0.0000 um

Offset Y 0.0000 um

automatically adjust Z using the height sensor?

7. Once at the origin, click “Move Pattern”

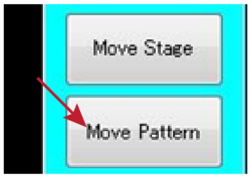

8. Click "Read Stage Position" to move your pattern to the origin spot. Next, click "OK"

9. Save your schedule file again when prompted

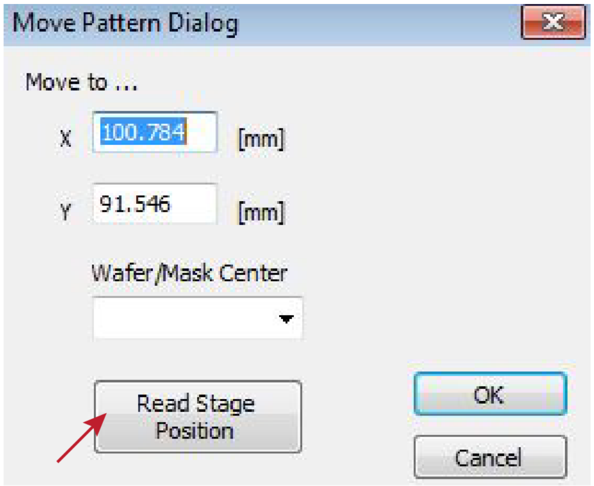

X 100.784 [mm]

Y 91.546 [mm]

Measuring Sample Inclination

Usually your sample isn't perfectly flat on the back and this can negatively impact your write if not accounted for. Measuring the sample allows the lithography system to correct for this issue by asjusting the gun height based on an inclination map

3 Point Method

1. Move to the position where you you would like to measure the sample inclination. Usually it is the origin and close to it

2. Click "Measure Sample Inclination"

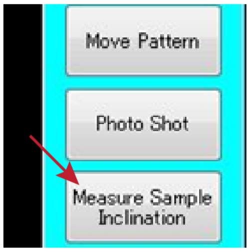

3. Define the distance over which you want to measure the height differential. You do not want to drive off the sample, so make sure you define this so that you stay on your chip.

4. Press "Start"

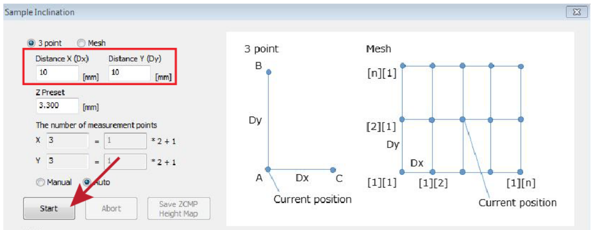

● 3 point ○ Mesh

Distance X (Dx) 10 [mm] Distance Y (Dy) 10 [mm]

Z Preset 3.300 [mm]

The number of measurement points

X 3 = 1 * 2 + 1

Y 3 = 1 * 2 + 1

○ Manual ● Auto

Height Maps

1. Move to the position from which you would like to measure sample height on the sample

2. Click "Measure Sample Inclination"

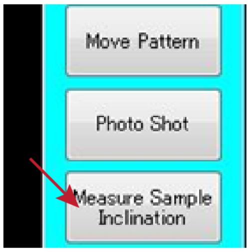

3. Select “Mesh”. Define the distance over which you want to measure the heigh differential. You do not want to drive off the sample, so make sure you define this so that you stay on your chip

4. Select the number of points in the X and Y directions you want to form the mesh

5. Press “start”

6. “Save ZOMP Height Map” when finished

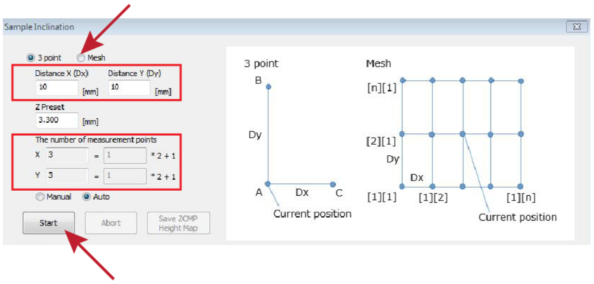
Sample Inclination

● 3 point ○ Mesh

Distance X (Dx) 10 [mm]
Distance Y (Dy) 10 [mm]

Z Preset 3.300 [mm]

The number of measurement points
X 3 = 1 *2 + 1
Y 3 = 1 *2 + 1

○ Manual ● Auto

Exposure

1. After placing the pattern and measuring the sample inclination, press next

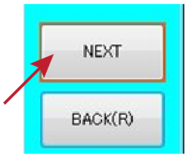

2. Recalculate the write time just as a final check to make sure there are no errors

3. Run Field Corrections to make sure there are no beam distortions

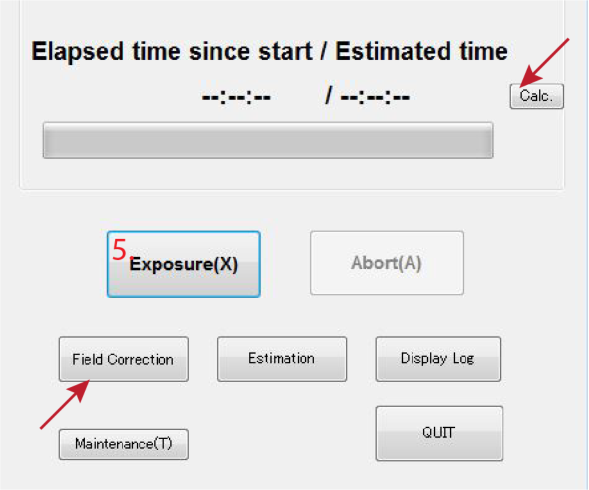
Elapsed time since start / Estimated time

--:--:-- / --:--:--

4. Press “Start,” and wait for the field corrections to finish. Exit the window.

5. Press “Exposure”

6. For files with alignment, the software will walk you through the alignment process

7. Alignment should be done at the same magnification for each step

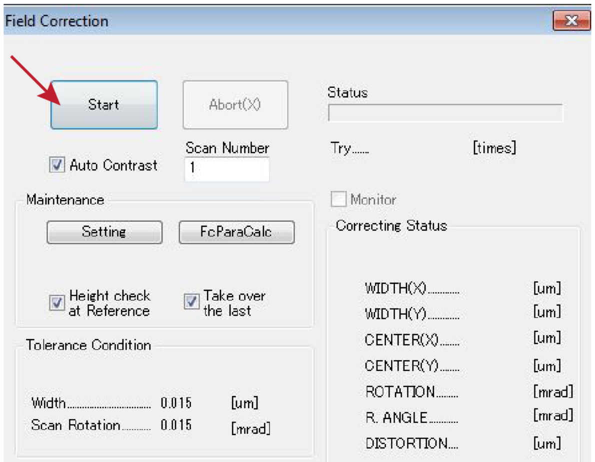
Field Correction

Scan Number 1

☑ Auto Contrast

☐ Monitor

☑ Height check at Reference

☑ Take over the last

Tolerance Condition

Width 0.015 [um]

Scan Rotation 0.015 [mrad]

Bibliography

[1] S. Adam, E.H. Hwang, V.M. Galitski, and S. Das Sarma. A self-consistent theory for graphene transport. *Proceedings of the National Academy of Sciences*, 104:18392, 2007.

[2] G. Aivazian, Z. Gong, A.M. Jones, R.-L. Chu, J. Yan, D.G. Mandrus, C. Zhang, D. Cobden, W. Yao, and X. Xu. Magnetic control of valley pseudospin in monolayer WSe_2. *Nature Physics*, 11:148–152, 2015.

[3] O.A. Ajayi, J.V. Ardelean, G.D. Shepard, J. Wang, A. Antony, T. Taniguchi, K. Watanabe, T.F. Heinz, S. Strauf, X.-Y. Zhu, and J.C. Hone. Approaching the Intrinsic Photoluminescence Linewidth in Transition Metal Dichalcogenide Monolayers. *2D Materials*, 4:031011, 2017.

[4] A.R. Akhmerov and C.W.J. Beenakker. Detection of valley polarization in graphene by a superconducting contact. *Physical Review Letters*, 98:157003, 2007.

[5] A.S. Alexandrov and N.F. Mott. Polarons and Bipolarons. *World Scientific*, 1996.

[6] Evgeny M. Alexeev, David A. Ruiz-Tijerina, Mark Danovich, Matthew J. Hamer, Daniel J. Terry, Pramoda K. Nayak, Seongjoon Ahn, Sangyeon Pak, Juwon Lee, Jung Inn Sohn, Maciej R. Molas, Maciej Koperski, Kenji Watanabe, Takashi Taniguchi, Kostya S. Novoselov, Roman V. Gorbachev, Hyeon Suk Shin, Vladimir I. Fal'ko, and Alexander I. Tartakovskii. Resonantly hybridized excitons in moiré superlattices in van der waals heterostructures. *Nature*, 567(7746):81–86, Mar 2019.

[7] L. Allen, M.W. Beijersbergen, R.J.C. Spreeuw, and J.P. Woerdman. Orbital angular momentum of light and the transformation of Laguerre-Gaussian laser modes. *Physical Review A*, 45:8185, 1992.

[8] M. Amani, D.-H. Lien, D. Kiriya, J. Xiao, A. Azcatl, J. Noh, S.R. Madhvapathy, R. Addou, K.C. Santosh, M. Dubey, K. Cho, R.M. Wallace, S.-C. Lee, J.-H. He, J.W. Ager III, X. Zhang, E. Yablonovich, and A. Javey. Near-unity photoluminescence qunatum yield in MoS_2. *Science*, 350:1065–1068, 2015.

[9] M. F. Andersen, C. Ryu, Pierre Cladé, Vasant Natarajan, A. Vaziri, K. Helmerson, and W. D. Phillips. Quantized Rotation of Atoms from Photons with Orbital Angular Momentum. *Phys. Rev. Lett.*, 97:170406, Oct 2006.

[10] A. Arora, T. Deilmann, T. Reichenauer, J. Kern, S. Michaelis de Vasconcellos, M. Rohlfing, and R. Bratschitsch. Excited-state trions in monolayer WS_2. *Physical Review Letter*, 123:167401, 2019.

[11] A. Arora, M. Koperski, K. Nogajewski, J. Marcus, C. Faugeras, and M. Potemski. Excitonic resonances in thin films of WSe_2: from monolayer to bulk material. *Nanoscale*, 7:10421–10429, 2015.

[12] A. Arora, R. Schmidt, R. Schneider, M.R. Molas, I. Breslavetz, M. Potemski, and Bratschitsch. Valley Zeeman Splitting and Valley Polarization of Neutral and Charged Excitons in Monolayer $MoTe_2$ at High Magnetic Fields. *Nano Letters*, 16:3624–3629, 2016.

[13] J. Artl. *Applications of Laguerre-Gaussian beams and Bessel beams to both nonlinear optics and atom optics*. PhD thesis, University of St. Andrews, 1999.

[14] O.B. Aslan, M. Deng, and T.F. Heinz. Strain tuning of excitons in monolayer WSe_2. *Physical Review B*, 98:115308, 2018.

[15] P. Back, M. Sidler, O. Cotlet, A. Srivastava, M. Kroner, and A. Imamoğlu. Giant Paramagnetism-Induced Valley Polarization of Electrons in Charge-Tunable Monolayer $MoSe_2$. *Physical Review Letters*, 118:237404, 2017.

[16] M. Barbone, A.R.P. Montblanch, D.M. Kara, C. Palacios-Berraquero, A.R. Cadore, D. De Fazio, B. Pingault, E. Mostaani, H. Li, B. Chen, K. Watanabe, T. Taniguchi, S. Tongay, G. Wang, A.C. Ferrari, and M. Atature. Charge-Tunable biexciton complexes in monolayer WSe_2. *Nature Communications*, 9:1–6, 2018.

[17] S.M. Barnett, M. Babiker, and M.J. Padgett. Optical orbital angular momentum. *Philosophical Transactions of the Royal Society A: Mathematical, Physical and Engineering Sciences*, 375, 2017.

[18] T.C. Berkelbach, M.S. Hybertsen, and D.R. Reichman. Theory of neutral and charged excitons in monolayer transition metal dichalcogenides. *Physical Review B*, 88:045318, 2013.

[19] T.C. Berkelbach, M.S. Hybertsen, and D.R. Reichman. Bright and dark singlet excitons via linear and two-photon spectroscopy in monolayer transition metal dichalcogenides. *Physical Review B*, 92:085413, 2015.

[20] Timothy C. Berkelbach, Mark S. Hybertsen, and David R. Reichman. Bright and dark singlet excitons via linear and two-photon spectroscopy in monolayer transition-metal dichalcogenides. *Phys. Rev. B*, 92:085413, Aug 2015.

[21] R.A. Beth. Direct detection of the angular momentum of light. *Physical Review*, 48:471, 1935.

[22] R.A. Beth. Mechanical detection and measurement of the angular momentum of light. *Physical Review*, 50:115–125, 1936.

[23] Utso Bhattacharya, Swati Chaudhary, Tobias Grass, Allan S. Johnson, Simon Wall, and Maciej Lewenstein. Fermionic chern insulator from twisted light with linear polarization, 2021.

[24] J. Binder, J. Howarth, F. Withers, M.R. Molas, T. Taniguchi, K. Watanabe, C. Faugeras, A. Wysmolek, M. Danovich, V.I. Fal'ko, A.K. Geim, K.A. Novoselov, M. Potemksi, and A. Kozikov. Upconverted electroluminescence via Auger scattering of interlayer excitons in van der Waals heterostructures. *Nature Communications*, 10:2335, 2019.

[25] D. Birkedal, J. Singh, V.G. Lyssenko, J. Erland, and J.M. Hvam. Binding of quasi-two-dimensional biexcitons. *Physical Review Letters*, 76:672–675, 1996.

[26] P. Blake and E.W. Hill. Making graphene visible. *Applied Physics Letters*, 91:063124, 2007.

[27] K. Bolotin, K.J. Sikes, Z. Jiang, M. Klima, G. Fudenberg, J. Hone, P Kim, and H.L. Stormer. Ultrahigh electron mobility in suspended graphene. *Solid State Communications*, 146:351–355, 2008.

[28] K.I. Bolotin, F. Ghahari, M.D. Shulma, H.L. Stormer, and P. Kim. Observation of the fractional quantum Hall effect in graphene. *Nature*, 462:196–199, 2009.

[29] H. Bragança, R. Vasconcelos, J. Fu, R.P. D'Azevedo, D.R. da Costa, A.L.A. Fonseca, and F. Qu. Magnetic brightening, large valley Zeeman splitting, and dynamics of long-lived A and B dark excitonic states in monolayer WS_2. *Physical Review B*, 100:115306, 2019.

[30] S. Brem, A. Ekman, D. Christiansen, F. Katsch, M. Selig, C. Robert, X. Marie, B. Urbaszek, A. Knorr, and E. Malic. Phonon-Assisted Photoluminescence from Indirect Excitons in Monolayers of Transition-Metal Dichalcogenides. *Nano Letters*, 4:2849–2856, 2020.

[31] V.E. Calado, G.F. Schneider, A.M.M.G. Theulings, C. Dekker, and L.M.K. Vandersypen. Formation and control of wrinkles in graphene by the wedging transfer method. *Applied Physics Letters*, 101:103116, 2012.

[32] Bin Cao, Tobias Grass, Glenn Solomon, and Mohammad Hafezi. Optical flux pump in the quantum hall regime. *Phys. Rev. B*, 103:L241301, Jun 2021.

[33] T. Cao, W. Wang, H. Ye, C. Zhu, J. Shi, Q. Niu, P. Tan, E. Wang, B. Liu, and J. Feng. Valley-selective circular dichroism in monolayer molybdenum disulpide. *Nature Communications*, 2012.

[34] Y. Cao, V. Fatemi, S. Fang, K. Watanabe, T. Taniguchi, E. Kaxiras, R.C. Ashoori, and P. Jarillo-Herrero. Unconventional superconductivity in magic-angle graphene superlattices. *Nature*, 556:43–50, 2018.

[35] M. Cardona. Electron Effective Masses of InAs and GaAs as a Function of Temperature and Doping. *Physical Review*, 121:752, 1961.

[36] J.J. Carmiggelt, M. Borst, and T. van der Sar. Exciton-to-trion conversion as a control mechanism for valley polarization in room-temperature monolayer WS_2. *Scientific Reports*, 10:17389, 2020.

[37] A. Castellanos-Gomez, M. Buscema, R. Moelnaar, V. Singh, L. Janssen, H.S.J. van der Zant, and G.A. Steele. Deterministic transfer of two-dimensional materials by all-dry viscoelastic stamping. *2D Materials*, 1, 2014.

[38] G. Catarina, N.M.R. Peres, and J. Fernández-Rossier. Magneto-optical Kerr effect in spin split two-dimensional massive Dirac materials. *2D Materials*, 7:025011, 2020.

[39] C. Chakraborty, L. Kinnischtzke, K.M. Goodfellow, R. Beams, and A.N. Vamivakas. Voltage-controlled quantum light from an atomically thin semiconductor. *Nature Nanotechnology*, 10:507–511, 2015.

[40] M.C. Chang and Q. Niu. Berry phase, hyperorbits, and the Hofstadter spectrum: Semiclassical dynamics in magnetic Bloch bands. *Physical Review B*, 53:7010–7023, 1996.

[41] J.H. Chen, C. Jang, S. Xiao, M. Ishigami, and M.S. Fuhrer. Intrinsic and extrinsic performance limits of graphene devices on SiO_2. *Nature Nanotechnology*, 3:206, 2008.

[42] K. Chen, R. Ghoch, X. Meng, A. Roy, J.-S. Kim, F. He, S.C. Mason, X. Xu, J.-F. Lin, D. Akinwande, S.K. Banjeree, and Y. Wang. Experimental evidence of exciton capture by mid-gap defects in CVD grown monolayer $MoSe_2$. *npj 2D Materials and Applications*, 1, 2017.

[43] S.-Y. Chen, T. Goldstein, J. Tong, T. Taniguchi, K. Watanabe, and J. Yan. Superior Valley Polarization and Coherence of 2s Excitons in Monolayer WSe_2. *Physical Review Letters*, 120:046402, 2018.

[44] S.-Y. Chen, Z. Lu, T. Goldstein, J. Tong, A. Chaves, J. Kunstmann, T. Cavalcante, L.S.R. in Woźniak, G. Seifert, D.R. Reichman, T. Taniguchi, K. Watanabe, D. Smirnov, and J. Yan. Luminescent Emission of Excited Rydberg Excitons from Monolayer WSe_2. *Nano Letters*, 19:2464–2471, 2019.

[45] X. Chen, Y. Xie, Y. Sheng, H. Tang, Z. Wang, Y. Wang, Y. Wang, F. Liao, J. Ma, X. Guo, L. Tong, H. Liu, H. Liu, T. Wu, J. Cao, S. Bu, H. Shen, F. Bai, D. Huang, J. Deng, A. Riaud, Z. Xu, C. Wu, S. Xing, Y. Lu, S. Ma, Z. Sun, Z. Xue, Z. Di,

X. Gong, D.W. Zhang, P. Zhou, J. Wan, and W. Bao. Wafer-scale functional circuits based on two dimensional semiconductors with fabrication optimized by machine learning. *Nature Communications*, 12:5953, 2021.

[46] A. Chernikov, T.C. Berkelbach, H.M. Hill, A. Rigosi, Y. Li, O.B. Aslan, D.R. Reichman, M.S. Hybertsen, and T.F. Heinz. Exciton binding energy and nonhydrogenic Rydberg series in monolayer WS_2. *Physical Review Letters*, 113:076802, 2014.

[47] A. Chernikov, A.M. van der Zande, A.F. Hill, H.M. anf Rigosi, A. Velauthapillai, J. Hone, and T.F. Heinz. Electrical Tuning of Exciton Binding Energies in Monolayer WS_2. *Physical Review Letters*, 115:126802, 2015.

[48] T. Chervy, S. Azzini, E. Lorchat, S. Wang, Y. Gorodetski, J.A. Hutchinson, S. Cerciaud, T.W. Ebbesen, and C. Genet. Room Temperature Chiral Coupling of Valley Excitons with Spin-Momentum Locked Surface Plasmons. *ACS Photonics*, 5:1281–1287, 2018.

[49] C.M. Chow, H. Yu, A.M. Jones, J. Yan, D.G. Mandrus, T. Taniguchi, K. Watanabe, W. Yao, and X. Xu. Unusual exciton–phonon interactions at van der Waals engineered interfaces. *Nano letters*, 17(2):1194–1199, 2017.

[50] Ze-Pei Cian, Tobias Grass, Abolhassan Vaezi, Zhao Liu, and Mohammad Hafezi. Engineering quantum Hall phases in a synthetic bilayer graphene system. *Phys. Rev. B*, 102:085430, Aug 2020.

[51] Claude Cohen-Tannoudji, Jacques Dupont-Roc, and Gilbert Grynberg. John Wiley & Sons, Ltd, Weinheim, 1998.

[52] P. Coullet, G. Gil, and F. Rocca. Optical vortices. *Optics Communications*, 73:403–408, 1989.

[53] E. Courtade, M. Semina, M. Manca, M.M. Glazov, C. Robert, F. Cadiz, G. Wang, T. Taniguchi, K. Watanabe, M. Pierre, W. Escoffier, E.L. Ivchenko, P. Renucci, X. Marie, T. Amand, and B. Urbaszek. Charged excitons in monolayer WSe_2: experiment and theory. *Physical Review B*, 96:085302, 2017.

[54] W. Cullen, M. Yamamoto, K.M. Burson, C. Chen, J.H. nd Jang, L. Li, M.S. Fuhrer, and E.D. Williams. High-fidelity conformation of graphene so SiO_2 topograhic features. *Physical Review Letters*, 105:215504, 2010.

[55] Sun D., Y. Rao, G.A. Reider, G. Chen, Y. You, L. Brézin, A.R. Harutyunyan, and T.F. Heinz. Observation of rapid exciton-exciton annihilation in monolayer molybdenum disulfide. *Nano Letters*, 14:5625, 2014.

[56] P.K. Dagupta, Y. Chen, C.A. Serrno, G. Guiochon, H. Liu, J.N. Fairchild, and R.A. Shalliker. Black Box Linearization for Greater Linear Dynamic Range: The Effect of Power Transforms on the Representation of Data. *Analytical Chemistry*, 82:10143–10150, 2010.

[57] C.G. Darwin. Notes on the theory of radiation. *Proceedings of the Royal Society A*, 136:36, 1932.

[58] S. Das Sarma, E.H. Hwang, and Q. Li. Valley dependent many-body effects in 2D semiconductors. *Physical Review B*, 80:121303, 2009.

[59] M.W. Davidson. Numerical aperture and resolution. *Optical Micrscopy Primer*.

[60] C.R. Dean, L. Wang, P. Maher, C. Forsythe, F. Chahari, Y. Gao, J. Katoch, M. Ishigami, P. Moon, M. Koshino, T. Taniguchi, K. Watanabe, K.L. Shepard, J. Hone, and P. Kim. Hofstadter's butterfly and the fractal quantum Hall effect in moiré superlattices. *Nature*, 497:598–602, 2013.

[61] C.R. Dean, A.F Young, I. Meric, C. Lee, L. Wang, S. Sorgenfrei, K. Watanabe, T. Taniguchi, P. Kim, K.L. Shepard, and J. Hone. Boron nitride substrates for high-quality graphene electronics. *Nature Nanotechnology*, 5:722–726, 2010.

[62] R. Decker, Y. Wang, V.W. Brar, W. Regan, H.Z. Tasi, Q. Wu, W. Gannett, A. Zettl, and M.F. Crommie. Local electronic properties of graphene on a BN substrate via scanning tunneling microscopy. *Nano Letters*, 11:2291–2295, 2011.

[63] T. Deilmann, P. Krüger, and M. Rohlfing. *Ab Initio* Studies of Exciton g Factors: Monolayer Transition Metal Dichalcogenides in Magnetic Fields. *Physical Review Letters*, 124:226402.

[64] A. Deshpande, W. Bao, F. Miao, C.N. Lau, and B.J. LeRoy. Spatially resolved spectroscopy of monolayer graphene on SiO_2. *Physical Review B*, 79:205411, 2009.

[65] Arya Dhar, Maheswar Maji, Tapan Mishra, R. V. Pai, Subroto Mukerjee, and Arun Paramekanti. Bose-hubbard model in a strong effective magnetic field: Emergence of a chiral mott insulator ground state. *Phys. Rev. A*, 85:041602, Apr 2012.

[66] X. Du, I. Skachko, A. Barker, and E.Y. Andrei. Approaching ballistic transport in suspended graphene. *Nature Nanotechnology*, 3:491–495, 2008.

[67] J.P. Echeverry, B. Urbaszek, T. Amand, X. Marie, and I.C. Gerber. Splitting between bright and dark excitons in transition metal dichalcogenides. *Physical Review B*, 93:121107, 2016.

[68] D.K. Efimkin, E.K. Laird, J. Levinsen, M.M. Parish, and A.H. MacDonald. Electron-exciton interactions in the exciton-polaron problem. *Physical Review B*, 103:075417, 2021.

[69] D.K. Efimkin and A.H. MacDonald. Many-body theory of trion absorption features in two-dimensional semiconductors. *Physical Review B*, 95:035417, 2017.

[70] D.K. Efimkin and A.H. MacDonald. Exciton-polarons in doped semiconductors in a strong magnetic field. *Physical Review B*, 97:235432, 2018.

[71] A. Einstein. Über einen die erzeugung un verwandlung des lichtes betreffenden heuristichen gesichtpunkt. *Annalen der Physik*, 17:132–148, 1905.

[72] R. J. Elliott. Intensity of Optical Absorption by Excitons. *Phys. Rev.*, 108:1384–1389, Dec 1957.

[73] F.F. Fang and P.J. Stiles. Effects of a Tilted Magnetic Field on a Two-Dimensional Electron Gas. *Physical Review*, 174:823, 1968.

[74] H. Fang, C. Battaglia, C. Carraro, S. Mensak, B. Ozdol, J.S. Kang, H.A. Betchel, S.B. Desai, F. Kronast, A.A. Unal, G. Conti, C. Conlon, G.K. Palsson, M.C. Martin, A.M. Minor, C.S. Fadley, E. Yablonovitch, R. Maboudian, and A. Javey. Strong interlayer coupling in van der Waals heterostructures built from single-layer chalcogenides. *Proc Natl Acad Sci USA*, 111:6198–6202, 2014.

[75] M. B. Farías, G. F. Quinteiro, and P. I. Tamborenea. Photoexcitation of graphene with twisted light. *Eur. Phys. J. B*, (10):432, 2013.

[76] M. Feierabend, S. Brem, A. Ekman, and E. Malic. Brightening of spin- and momentum-dark excitons in transition metal dichalcogenides. *2D Materials*, 8:015013, 2020.

[77] C. Fey, P. Schmelcher, A. Imamoğlu, and R. Schmidt. Theory of exciton-electron scattering in atomically thin semiconductors. *Physical Review B*, 101:195417, 2020.

[78] R. Fickler, G. Campbell, B. Buchler, P.K. Lam, and A. Zeilinger. Quantum entanglement of angular momentum states with quantum numbers up to 10,010. *PNAS*, 113:13642–13647, 2016.

[79] G. Finkelstein, H. Shtrikman, and I. Bar-Joseph. Negatively and positively charged excitons in GaAs/$\mathrm{Al_xGa_{1-x}As}$ quantum wells. *Physical Review B*, 53:R1709, 1996.

[80] J. Förste, N.V. Tepliakov, S.Y. Kruchinin, J. Lindau, V. Funk, M. Förg, K. Watanabe, T. Taniguchi, A.S. Baimuratov, and A. Högele. Exciton g-factors in monolayer and bilayer $\mathrm{WSe_2}$ from experiment and theory. *Nature Communications*, 11:4539, 2020.

[81] C. Franchini, M. Reticcioloi, M. Setvin, and U. Diebold. Polarons in Materials. *Nature Review Materials*, 6:560–586, 2021.

[82] S. Franke-Arnold and N. Radwell. Light served with a twist. *Optics & Photonics News*, page 29, 2017.

[83] R. Frindt. Single crystal of $\mathrm{MoS_2}$ several molecular layers thick. *Journal of Applied Physics*, 37:1928, 1966.

[84] H. Fröhlich. Electrons in lattice fields. *Adv. Phys*, 3:325, 1954.

[85] H. Fröhlich, H. Pelzer, and S. Zienau. Properties of slow electrons in polar materials. *Phil. Mag*, 41:314, 1950.

[86] Hiroyuki Fujita and Masahiro Sato. Encoding orbital angular momentum of light in magnets. *Phys. Rev. B*, 96:060407, Aug 2017.

[87] Hiroyuki Fujita and Masahiro Sato. Ultrafast generation of skyrmionic defects with vortex beams: Printing laser profiles on magnets. *Phys. Rev. B*, 95:054421, Feb 2017.

[88] Hiroyuki Fujita, Yasuhiro Tada, and Masahiro Sato. Accessing electromagnetic properties of matter with cylindrical vector beams. *New J. Phys.*, 21(7):073010, jul 2019.

[89] A.K. Geim and I.V. Grigorieva. Van der Waals heterostructures. *Nature*, 499:419–425, 2013.

[90] E. Gibney. 2D or not 2D. *Nature*, 522:274–276, 2015.

[91] M. Glazov. Optical properties of charged excitons in two-dimensional semiconductors. *The Journal of Chemical Physics*, 153:034703, 2020.

[92] T. Goldstein, Y.-C. Wu, S.-Y. Chen, T. Taniguchi, K. Watanabe, K. Varga, and J. Yan. Ground and excited state exciton polarons in monolayer $MoSe_2$. *The Journal of Chemical Physics*, 153:071101, 2020.

[93] P. Gong, H. Yu, Y. Wang, and W. Yao. Optical selection rules for excitonic Rydberg series in the massive Dirac cones of hexagonal two-dimensional materials. *Physical Review B*, 95:125420, 2017.

[94] M. Goryca, J. Li, A.V. Stier, T. Taniguchi, K. Watanabe, E. Courtade, S. Shree, C. Robert, B. Urbaszek, X. Marie, and S.A Crooker. Revealing exciton masses and dielectric properties of monolayer semiconductors with high magnetic fields. *Nature Communications*, 10:4172, 2019.

[95] P.L. Gourley and J.P. Wolfe. Thermodynamics of exciton molecules in silicon. *Physical Review B*, 20:3319, 1979.

[96] T. Graß, U. Bhattacharya, J.C. Sell, and M. Hafezi. Two-dimensional excitons from twisted light and the fate of the photon's orbital angular momentum, 2022.

[97] Tobias Graß, Michael Gullans, Przemyslaw Bienias, Guanyu Zhu, Areg Ghazaryan, Pouyan Ghaemi, and Mohammad Hafezi. Optical control over bulk excitations in fractional quantum Hall systems. *Phys. Rev. B*, 98:155124, Oct 2018.

[98] M.V. Gustafsson, M. Yankowitz, C. Forsythe, D. Rhodes, K. Watanabe, T. Taniguchi, J. Hone, X. Zhu, and C.R. Dean. Ambipolar Landau levels and strong band-selective carrier interactions in monolayer WSe_2. *Nature Materials*, 17:411, 2018.

[99] S.J. Haigh, A. Gholinia, R. Jalil, S. Romani, L. Britnell, D.C. Elias, K.S. Novoselov, L.A. Ponomarenko, A.K. Geim, and R. Gorbachev. Cross-sectional imaging of individual layers and buried interfaces of graphene-based heterostructures and superlattices. *Nature Materials*, 11:764–767, 2012.

[100] B. Han, C. Robert, E. Courtade, M. Manca, S. Shree, T. Amand, P. Renucci, T. Taniguchi, K. Watanabe, X. Marie, L.E. Golub, M.M. Glazov, and B. Urbaszek. Exciton States in Monolayer $MoSe_2$ and $MoTe_2$ Probed by Upconversion Spectroscopy. *Physical Review X*, 8:031073, 2018.

[101] A.T. Hanbicki, H.-J. Chuang, M.R. Rosenberger, C.S. Hellberg, S.V. Sivaram, K.M. McCreary, I.I. Mazin, and B.T. Jonker. Double Indirect Interlayer Exciton in a $MoSe_2$/WSe_2 van der Waals Heterostructure. *ACS Nano*, 12:4719–4726, 2018.

[102] A.T. Hanbicki, C. Kioseoglou, M. Currie, C.S. Hellberg, K.M. McCreary, A.L. Friedman, and B.T Jonker. Anomalous Temperature-Dependent Spin-Valley Polarization in Monolayer WS_2. *Science Reports*, 6:18885, 2016.

[103] K. Hao, L. Xu, P. Nagler, A. Singh, K. Tran, C.K. Dass, C. Schüller, T. Korn, X. Li, and G. Moody. Coherent and Incoherent Coupling Dynamics between Neutral and Charged Excitons in Monolayer $MoSe_2$. *Nano Letters*, 2016.

[104] K. Hao, L. Xu, J.F. Specht, P. Nagler, K. TRan, A. Singh, C.K. Dass, C. Schuüller, T. Korn, M. Richter, A. Knorr, X. Li, and G. Moody. Neutral and charged intervalley biexcitons in monolayer $MoS2_2$. *Nature Communications*, 8:15552, 2017.

[105] Hartmut Haug and Stephan W. Koch. *Quantum Theory of the Optical and Electronic Properties of Semiconductors*. World Scientific, 4th ed. edition, 2004.

[106] H. He, M.E.J. Friese, N.R. Heckenberg, and H. Rubinsztein-Dunlop. Direct Observation of Transfer of Angular Momentum to Absorptive Particles from a Laser Beam with a Phase Singularity. *Physical Review Letters*, 75:826, 1995.

[107] K. He, N. Kumar, L. Zhao, Z. Wang, K.F. Mak, H. Zhao, and J. Shan. Tightly bound excitons in monolayer WSe_2. *Physical Review Letters*, 113:026903, 2014.

[108] M. He, P. Rivera, D. Van Tuan, N.P. Wilson, M. Yang, T. Taniguchi, K. Watanabe, J. Yan, D.G. Mandrus, H. Yu, H. Dery, W. Yao, and X. Xu. Valley phonons and exciton complexes in a monolayer semiconductor. *Nature Communications*, 11:618, 2020.

[109] Y.-M. He, G. Clark, J.R. Schaibley, Y. He, M.-C. Chen, Y.-J. Wei, X. Ding, Q. Zhang, W. Yao, X. Xu, C.-Y. Lu, and J.-W. Pan. Single quantum emitters in monolayer semiconductors. *Nature Nanotechnology*, 10:497–502, 2015.

[110] T. Heindel, A. Thoma, I. Schwartz, E.R. Schmidgall, L. Gantz, D. Cogan, M. Straub, P. Schnauber, M. Gschrey, J. Schulze, A. Strittmatter, S. Rodt, D. Gershoni, and S. Reitzenstein. Accessing the dark exciton spin in deterministic quantum-dot microlenses. *APL Photonics*, 2:121303, 2017.

[111] R.N. Hill. Proof that the H Ion Has Only One Bound State. *Physical Review Letters*, 38:643.

[112] T. Holstein. Studies of polaron motion: Part I. The molecular-crystal model. *Annals of Physics*, 8:325–342, 1959.

[113] T. Holstein. Studies of polaron motion: Part II. The "small" polaron. *Annals of Physics*, 8:343–389, 1959.

[114] T. Hotta, A. Ueda, S. Haniguchi, M. Okada, T. Shimizu, T. Kubo, K. ueno, T. Taniguchi, K. Watanabe, and R. Kitaura. Enhanced Exciton–Exciton Collisions in an Ultraflat Monolayer $MoSe_2$ Prepared through Deterministic Flattening. *ACS Nano*, 15:1370–1377, 2021.

[115] H.-C. Hsu and W.-F. Hsieh. Excitonic polaron and phonon assisted photoluminescence of ZnO nanowires. *Solid State Communications*, 131:371–375, 2004.

[116] B. Hunt, J. D. Sanchez-Yamagishi, A. F. Young, M. Yankowitz, B. J. LeRoy, K. Watanabe, T. Taniguchi, P. Moon, M. Koshino, P. Jarillo-Herrero, and R. C. Ashoori. Massive Dirac fermions and Hofstadter butterfly in a van der Waals heterostructure. *Science*, 340:1427–1430, 2013.

[117] A. D. Jackson and L. C. Maximon. Integrals of Products of Bessel Functions. *SIAM J. Math. Anal.*, 3(3):446, 1972.

[118] J. Jadczak, J. Kutrowska, Girzycka, M. Bieniek, T. Kazimierczyk, P. Kossacki, J.J. Schindler, J. Debus, K. Watanabe, T. Taniguchi, C.H. Ho, A. Wójs, P. Hawrylak, and L. Bryja. Probing negatively charged and neutral excitons in MoS_2/hBN and hBN/MoS_2/hBN van der Waals heterostructures. *Nanotechnology*, 32:145717, 2021.

[119] J. Jadczak, J. Kutrowska-Girzycka, J.J. Schindler, J. Debus, K. Watanabe, T. Taniguchi, C.-H. Ho, and L. Bryja. Investigations of Electron-Electron and Interlayer Electron-Phonon Coupling in van der Waals hBN/WSe_2/hBN Heterostructures by Photoluminescence Excitation Experiments. *Materials*, 14:399, 2021.

[120] C. Jiang, W. Xu, A. Rasmita, Z. Huang, K. Li, Q. Xiong, and W-B Gao. Microsecond dark-exciton valley polarization memory in two-dimensional heterostructures. *Nature Communications*, 9, 2018.

[121] C. Jin, J. Kim, J. Suh, Z. Shi, B. Chen, X. Fan, M. Kam, K. Watanabe, T. Taniguchi, S. Tongay, A. Zettl, J. Wu, and F. Wang. Interlayer electron-phonon coupling in WSe_2/hBN heterostructures. *Nature Physics*, 13:127–131, 2017.

[122] Chenhao Jin, Emma C. Regan, Aiming Yan, M. Iqbal Bakti Utama, Danqing Wang, Sihan Zhao, Ying Qin, Sijie Yang, Zhiren Zheng, Shenyang Shi, Kenji Watanabe,

Takashi Taniguchi, Sefaattin Tongay, Alex Zettl, and Feng Wang. Observation of moiré excitons in wse2/ws2 heterostructure superlattices. *Nature*, 567(7746):76–80, Mar 2019.

[123] Z. Jin, X. Li, J.T. Mullen, and K.W. Kim. Intrinsic transport properties of electrons and holes in monolayer transition-metal dichalcogenides. *Physical Review B*, 90(4):045422, 2014.

[124] P. Joensen, R. Frindt, and S.R. Morrison. Single-layer MoS_2. *Materials Research Bulletin*, 21:457, 1986.

[125] A.M. Jones, H. Yu, J.R. Schaibley, J. Yan, D.G. Mandrus, T. Taniguchi, K. Watanabe, H. Dery, W. Yao, and X. Xu. Excitonic luminescence upconversion in two-dimensional semiconductor. *Nature Physics*, 12, 2016.

[126] Christina Jörg, Gerard Queraltó, Mark Kremer, Gerard Pelegrí, Julian Schulz, Alexander Szameit, Georg von Freymann, Jordi Mompart, and Verònica Ahufinger. Artificial gauge field switching using orbital angular momentum modes in optical waveguides. *Light Sci. Appl.*, 9(1):150, Aug 2020.

[127] M. Kasha. Characterization of Electronic Transitions in Complex Molecules. *Discussions of the Faraday Society*, 9:14–19, 1950.

[128] T. Kazimierczuk, D. Frölich, S. Scheel, H. Stolz, and M. Bayer. Giant Rydberg excitons in the copper oxide Cu_2O. *Nature*, 514:343–347, 2014.

[129] K. Kheng, R.T. Cox, M.Y. d'Abigné, F. Bassani, K. Saminadayar, and S. Tatarenko. Observation of negatively charged excitons X in semiconductor quantum wells. *Physical Review Letters*, 71:1752, 1993.

[130] Hwanmun Kim, Hossein Dehghani, Iman Ahmadabadi, Ivar Martin, and Mohammad Hafezi. Floquet vortex states induced by light carrying the orbital angular momentum, 2021.

[131] J. Kim, C. Jin, B. Chen, H. Cai, T. Zhao, P. Lee, S. Kahn, K. Watanabe, T. Taniguchi, S. Tongay, M.F. Crommie, and F. Wang. Observation of Ultralong Valley Lifetime in WSe_2/MoS_2 Heterostructures. *Scientific Advances*, 3:e1700518, 2017.

[132] C. Kittel. *Introduction to Solid State Physics*. Wiley, 7th edition, 1995.

[133] J. Klein, A. H otger, M. Florian, A. Steinhoff, A. Delhomme, T. Taniguchi, K. Watanabe, F. Jahnke, A.W. Holleitner, M. Potemski, C. Faugeraus, J.J. Finley, and A.V. Stier. Controlling exciton many-body states by the electric-field effect in monolayer MoS_2. *Physical Review Research*, 3:L022009, 2021.

[134] D.A. Kleinman. Binding energy of biexcitons and bound excitons in quantum wells. *Physical Review B*, 28:871, 1983.

[135] C. Klingshirn. *Semiconductor Optics*. Springer, Berlin Heidelberg New York, 2 edition, 1995.

[136] C. Kohstall, M. Zaccanti, M. Jag, A. Trenkwalder, P. Massignan, G.M. Bruun, F. Schreck, and R. Grimm. Metastability and coherence of repulsive polarons in a strongly interacting Fermi mixture. *Nature*, 486:615–618, 2012.

[137] A.V. Kolobov and J. Tominaga. *Two-Dimensional Transition Metal Dichalcogenides*. Springer International Publishing, 2016.

[138] Annika Melissa Konzelmann, Sjard Ole Krüger, and Harald Giessen. Interaction of orbital angular momentum light with rydberg excitons: Modifying dipole selection rules. *Phys. Rev. B*, 100:115308, Sep 2019.

[139] M. Koperski, N.A. Arora, V. Cherkez, P. Mallet, J.-Y. Veuillen, J. Marcus, P. Kossacki, and M. Potemski. Single photon emitters in exfoliated WSe_2 structures. *Nature Nanotechnology*, 10:503–506, 2015.

[140] M. Koperski, M.R. Molas, A. Arora, K. Nogajewski, M. Bartos, J. Wyzula, D. Vaclavkova, P. Kossacki, and M. Potemski. Orbital, spin and valley contributions to Zeeman splitting of excitonic resonances in $MoSe_2$, WSe_2 and WS_2 Monolayers. *2D Materials*, 6:015001, 2018.

[141] A. Kormányos, G. Burkard, M. Gmitra, J. Fabian, V. Zólyomi, N.D. Drummond, and V. Fal'ko. $\mathbf{k}\cdot\mathbf{p}$ theory for two-dimensional transitional metal dichalcogenide semiconductors. *2D Materials*, 2:022001, 2015.

[142] A. Kormányos, V. Zólyomi, N.D. Drummond, and G. Burkard. Spin-orbit coupling, quantum dots, and qubits in monolayer transition metal dichalcogenides. *Physical Review X*, 4:011034, 2014.

[143] M. Koschorreck, D. Pertot, E. Vogt, B. Frölich, M. Feld, and M. Köhl. Attractive and repulsive Fermi polarons in two dimensions. *Nature*, 486:619–622, 2012.

[144] K. Kośmider, J.W. González, and J. Fernández-Rossier. Large spin splitting in the conduction band of transition metal dichalcogenide monolayers. *Physical Review B*, 88:245436, 2013.

[145] A. Kuc and T. Heine. The electronic structure calculations of two-dimensional transition-metal dichalcogenides in the presence of external electric and magnetic fields. *Chemical Society Reviews*, 44:2603, 2015.

[146] A. Kuc, N. Zibouche, and T. Heine. Influence of quantum confinement on the electronic structure of the transition metal sulfide TS_2. *Physical Review B*, 89:245213, 2011.

[147] N. Kumar, Q. Cui, F. Ceballos, D. He, Y. Wang, and Z. Zhao. Exciton-exciton annihilation in $MoSe_2$ monolayers. *Physical Review B*, 89:125427, 2014.

[148] Min-Sik Kwon, Byoung Yong Oh, Su-Hyun Gong, Je-Hyung Kim, Hang Kyu Kang, Sooseok Kang, Jin Dong Song, Hyoungsoon Choi, and Yong-Hoon Cho. Direct Transfer of Light's Orbital Angular Momentum onto a Nonresonantly Excited Polariton Superfluid. *Phys. Rev. Lett.*, 122:045302, Jan 2019.

[149] I. Kylänpää and H.P. Komsa. Binding energies of exciton complexes in transition metal diclacogenides monolayers and effect of dielectric environment. *Physical Review B*, 92:1–6, 2015.

[150] D. Lagarde, L. Bouet, X. Marie, C.R. Zhu, B.L. Liu, T. Amand, P.H. Tan, and B. Urbaszek. Carrier and Polarization Dynamics in Monolayer MoS_2. *Physical Review Letters*, 112:47401, 2014.

[151] C. Lagoin, U. Bhattacharya, T. Grass, R. Chhajlany, T. Salamon, K. Baldwin, L. Pfeiffer, M. Lewenstein, M. Holzmann, and F. Dubin. Checkerboard solid of dipolar excitons in a two-dimensional lattice, 2022.

[152] Camille Lagoin, Stephan Suffit, Kirk Baldwin, Loren Pfeiffer, and François Dubin. Mott insulator of strongly interacting two-dimensional semiconductor excitons. *Nat. Phys.*, Dec 2021.

[153] M.A. Lampert. Mobile and Immobile Effective-Mass-Particle Complexes in Nonmetallic Solids. *Physical Review Letters*, 1:450, 1958.

[154] W. Lan, J. Wang, M. Xin, Y. Huang, C. Gu, and B. Liu. Trion-to-exciton upconversion dynamics in monolayer WSe_2. *Applied Physics Letters*, 117:083109, 2020.

[155] L. Landau. Diamagnetismus der Metalle [Diamagnetism of Metals]. *Zeitschrift für Physik*, 64:629–637, 1930.

[156] L.D. Landau. On the motion of electrons in a crystal lattice. *Phys. Z. Sowjetunion*, 3:664, 1933.

[157] L.D. Landau. Zur Theorie der phasenumwandlungen II. *Phys. Z. Sowjetunion*, 11:26–35, 1937.

[158] L.D. Landau and E.M. Lifshitz. *Statistical Physics, Part I*. Pergamon, Oxford, 1980.

[159] L.D. Landau and S.I. Pekar. Effective mass of a polaron. *Zh. Eksp. Teor. Fiz.*, 18:419, 1948.

[160] A Landé. Über den anomalen Zeemaneffekt (Teil I). *Zeitschrift für Physik*, 5:231–241, 1921.

[161] A. Laturia, M.L. Van de Put, and W.G. Vandenberghe. Dielectric properties of hexagonal boron nitride and transition metal dichalcogenides: from monolayer to bulk. *NPJ 2D Mater. Appl*, 2:6, 2018.

[162] M.P.J. Lavery. *Measurement of Light's Orbital Angular Momentum*. PhD thesis, University of Glasglow, 2013.

[163] J. Lee, K.F. Mak, and J. Shan. Electrical control of the valley Hall effect in bilayer MoS_2 transistors. *Nature Nanotechnology*, 11:421–425, 2016.

[164] Y.-H. Lee, L. Yu, H. Wang, W. Fang, X. Ling, and Y. Shi. Synthesis and transfer of single-layer transition metal disulfides on diverse surfaces. *Nano Letters*, 13:1852–1857.

[165] K. Levenberg. A method for the solution of certain non-linear problems in least squares. *Quarterly of Applied Mathematics*, 2:164–168, 1944.

[166] J. Li, M. Goryca, N.P. Wilson, A.V. Stier, X. Xu, and S.A. Crooker. Spontaneous Valley Polarization of Interacting Carriers in a Monolayer Semiconductor. *Physical Review Letters*, 125:147602, 2020.

[167] L. Li, R. Zhang, Z. Zhao, G. Xie, P. Liao, K. Pang, H. Song, C. Liu, Y. Ren, G. LaBriolle, P. Jian, D. Starodubov, B. Lynn, R. Bock, M. Tur, and A.E. Willner. High-Capacity Free-Space Optical Communications Between a Ground Transmitter and a Ground Receiver via a UAV Using Multiplexing of Multiple Orbital-Angular-Momentum Beams. *Scientific Report*, 7:17427, 2017.

[168] Y. Li, J. Ludwig, T. Low, A. Chernikov, X. Cui, G. Arefe, Y.D. Kim, A.M. van der Zande, A. Rigosi, H.M. Hill, S.H. Kim, J. Hone, Z. Li, D. Smirnov, and T.F. Heinz. Valley splitting and polarization by the Zeeman effect in monolayer $MoSe_2$. *Physical Review Letters*, 113:266804, 2014.

[169] Z. Li, J. F orste, Watanabem K., T. Taniguchi, B. Urbaszek, A.S. Baimuratov, I.C. Gerber, A. H ogele, and I. Bilgin. Stacking-dependent exciton multiplicity in WSe_2 bilayers. *arXiv preprint*, page 2112.08994v1, 2021.

[170] Z. Li, T. Wang, C. Jin, Z. Lu, Z. Lian, Y. Meng, M. Blei, M. Gao, T. Taniguchi, K. Watanabe, T. Ren, T. Cao, S. Tongay, D. Smirnov, L. Zhang, and S.-F. Shi. Momentum-Dark Intervalley Exciton in Monolayer Tungsten Diselenide Brightened via Chiral Phonon. *ACS Nano*, 13:14107–14113, 2019.

[171] Z. Li, T. Wang, C. Jin, Z. Lu, Z. Lian, Y. Meng, M. Blei, S. Gao, T. Taniguchi, K. Watanabe, T. Ren, S. Tongay, L. Yang, D. Smirnov, T. Cao, and S.-F. Shi. Emerging photoluminescence from the dark-exciton phonon replica in monolayer WSe_2. *Nature Communications*, 10:2469, 2019.

[172] Z. Li, T. Wang, Z. Lu, C. Jin, Y. Chen, Y. Meng, Z. Lian, T. Taniguchi, K. Watanabe, S. Zhang, D. Smirnov, and S.-F. Shi. Revealing the biexciton and trion-exciton complexes in BN encapsulated WSe_2. *Nature Communications*, 9:3719, 2018.

[173] Z. Li, T. Wang, Z. Lu, M. Khatoniar, Z. Lian, Y. Meng, M. Blei, T. Taniguchi, K. Watanabe, S.A. McGill, S. Tongay, V.M. Menon, D. Smirnov, and S.-F. Shi. Direct Observation of Gate-Tunable Dark Trions in Monolayer WSe_2. *Nano Letters*, 19:6886–6893, 2019.

[174] Z. Li, T. Wang, S. Miao, Y. Li, Z. Lu, C. Jin, Z. Lian, Y. Meng, M. Blei, T. Taniguchi, K. Watanabe, S. Tongay, W. Yao, D. Smirnov, C. Zhang, and S.-F. Shi. Phonon-exciton Interactions in WSe_2 under a quantizing magnetic field. *Nature Communications*, 11:1–7, 2020.

[175] D.-H. Lien, S.Z. Uddin, M. Yeh, M. Amani, H. Kim, E. Ager II, J.W. anf Yablonovitch, and A. Javey. Electrical suppression of all nonradiative recombination pathways in monolayer semiconductors. *Science*, 364:468–471, 2019.

[176] J. Lin, T. Han, B. Piot, Z. Wu, S. Xu, G. Long, L. An, P. Cheung, P.-P. Zheng, P. Plochocka, X. Dai, D.K. Maude, Zhang F., and N. Wang. Determining Interaction Enhanced Valley Susceptibility in Spin-Valley-Locked MoS_2. *Nano Letters*, 19:1736–1742, 2019.

[177] Y. Lin, X. Ling, L. Yu, S. Huang, A.L. Hsu, Y.-H. Lee, J. Kong, M.S. Dresselhaus, and T. Palacios. Dielectric screening of excitons and trions in single-layer MoS_2. *Nano Letters*, 14:5569–5576, 2014.

[178] E. Lindary, D. Yadav, D. Vella, I.A. Verzhbitskiy, K. Watanabe, T. Taniguchi, F. Pauly, M. Trushin, and G. Eda. Harnessing Exciton-Exciton Annihilation in Two-Dimensional Semiconductors. *Nano Letters*, 20:1647–1653, 2020.

[179] J. Lindau, M. Selig, A. Neumanm, L. Colombier, J. Förste, V. funk, M. Förg, J. Kim, G. Berghäuser, T. Taniguchi, K. Watanabe, F. Wang, E. Malic, and Högele. The role of momentum-dark excitons in the elementary optical response of bilayer WSe_2. *Nature Communications*, 9, 2018.

[180] E. Liu, J. van Baren, C.-T. Liang, T. Taniguchi, K. Watanabe, N.M. Gabor, Y.-C. Chang, and C.H. Lui. Multipath Optical Recombination of Intervalley Dark Excitons and Trions in Monolayer WSe_2. *Physical Review Letters*, 124:196802, 2020.

[181] E. Liu, J. van Baren, Z. Lu, M.M. Altaiary, T. Taniguchi, D. Smirnov, and C.-H. Lui. Gate tunable dark trions in Monolayer WSe_2. *Physical Review Letters*, 123, 2019.

[182] E. Liu, J. van Baren, Z. Lu, T. Taniguchi, K. Watanabe, D. Smirnov, Y.-C. Chang, and C.H. Lui. Exciton-polaron Rydberg states in monolayer $MoSe_2$ and WSe_2. *Nature Communications*, 12:6131, 2021.

[183] E. Liu, J. van Baren, T. Taniguchi, K. Watanabe, Y-C Chang, and C.H. Lui. Magnetophotoluminescence of exciton Rydberg states in monolayer WSe_2. *Physical Review B*, 99:205420, 2019.

[184] E. Liu, J. van Baren, T. Taniguchi, K. Watanabe, Y.-C. Chang, and C.H. Lui. Valley-selective chiral phonon replica of dark excitons and trions in monolayer WSe_2. *Physical Review Letters*, 1:032007, 2019.

[185] E. Liu, J. van Baren, T. Taniguchi, K. Watanabe, Y.-C. Chang, and C.H. Lui. Landau-Quantized Excitonic Absorption and Luminescence on Monolayer Valley Semiconductors. *Physical Review Letters*, 124:097401, 2020.

[186] G-B Liu, W-Y Shan, Y. Yao, W. Yao, and D. Xiao. Three-band tight-binding model for monolayers of group-VIB transition metal dichalcogenides. *Physical Review B*, 88:085433, 2013.

[187] S. Liu, A. Granados del Águila, X. Liu, Y. Zhu, Y. Han, A. Chaturvedi, P. Gong, H. Yu, H. Zhang, W. Yao, and Q. Xiong. Room-Temperature Valley Polarization in Atomically Thin Semiconductors via Chalcogenide Alloying. *ACS Nano*, 14:9873–9883, 2020.

[188] O. Lopez-Sanchez, D. Lembke, M. Kayci, A. Radenovic, and A. Kis. Ultrasensitive photodetectors based on monolayer MoS_2. *Nature Nanotechnology*, 8:497–501, 2013.

[189] E. Lorchat, S. Azzini, T. Chervy, T. Taniguchi, K. Watanabe, T.W. Ebbesen, C. Genet, and S. Berciaud. Room-Temperature Valley Polarization and Coherence in Transition Metal Dichalcogenide–Graphene van der Waals Heterostructures. *ACS Photonics*, 5:5047–5054, 2018.

[190] C. Lui, A.J. Frenzel, D.V. Pilon, Y.H. Lee, X. Ling, G.M. Akselrod, J. Kong, and N. Gedik. Trion-induced negative photoconductivity in monolayer MoS_2. *Physical Review Letters*, 113:166801, 2014.

[191] T.P. Lyons, S. Dufferwiel, M. Brooks, F. Withers, T. Taniguchi, K. Watanabe, K.S. Novosolev, G. Burkard, and A.I. Tartakovskii. The valley Zeeman effect in inter- and intra-valley trions in monolayer WSe_2. *Nature Communications*, 10:1–8, 2019.

[192] X. Ma, Q. Liu, D. Xu, Y. Zhu, S. Kim, Y. Cui, L. Zhong, and M. Liu. Capillary-force-assisted clean-stamp transfer of two-dimensional materials. *Nano Letters*, 17:6961–6967, 2017.

[193] D. MacNeill, C. Keikes, K.F. Mak, Z. Anderson, A. Kormányos, V. Zólyomi, J. Park, and D.C. Ralph. Breaking of Valley Degeneracy by Magnetic Field in Monolayer $MoSe_2$. *Physical Review Letters*, 2014:037401, 2015.

[194] J. Madéo, M.K.L. Man, C. Sahoo, M. Campbell, V. Pareek, E.L. Wong, N.S. Al-Mahboob, A. Chan, A. Karmakar, B.M.K. Mariserla, X. Li, T.F. Heinz, T. Cao, and K.M. Dani. Directly visualizing the momentum-forbidden dark excitons and their dynamics in atomically thin semiconductors. *Science*, 370:1199–1204, 2020.

[195] K.F. Mak, K. He, J. Shan, and T.F Heinz. Control of valley polarization in monolayer MoS_2 by optical helicity. *Nature Nanotechnology*, 7:494–498, 2012.

[196] K.F. Mak, L. He, C. Lee, G.H. Hone, T.F. Heinz, and J. Shan. Tightly bound trions in monolayer MoS_2. *Nature Materials*, 12:207–11, 2013.

[197] K.F. Mak, C. Lee, J. Hone, J. Shan, and T.F. Heinz. Atomically thin MoS_2: A new direct-gap semiconductor. *Physical Review Letters*, 105:136805, 2010.

[198] K.F. Mak, K.L. McGill, J. Park, and P.L. McEuen. The valley Hall effect in MoS_2 transistors. *Science*, 344:1489, 2014.

[199] K.F. Mak and J. Shan. Photonics and optoelectronics of 2D semiconductor transition metal dichalcogenides. *Nature Photonics*, 10:216–226, 2016.

[200] M. Manca, M.M. Glazov, C. Robert, F. Cadiz, T. Taniguchi, K. Watanabe, E. Courtade, T. Amand, P. Renucci, X. Marie, G. Wang, and B. Urbaszek. Enabling valley selective exciton scattering in monolayer WSe_2 through upconversion. *Nature Communications*, 8:14927, 2017.

[201] S. Manzeli, D. Ovchinnikov, D. Pasuqier, O.V. Yazyev, and A. Kis. 2D transition metal dichalcogenides. *Nature Review Materials*, 2:17033, 2017.

[202] D. Marquardt. An Algorithm for Least-Squares Estimation of Nonlinear Parameters. *SIAM Journal of Applied Mathematis*, 11:431–441, 1963.

[203] J. Martin, G. Akerman, N. anf Ulbricht, T. Lohmann, J.H. Smet, K. von Klitzing, and A. Yacoby. Observation of electron-hole puddles in graphene using a scanning single-electron transistor. *Nature Physics*, 4:144–148, 2008.

[204] M.Z. Mayers, T.C. Berkelbach, M.S. Hybertsen, and D.R. Reichman. Binding energies and spatial structures of small carrier complexes in monolayer transition metal dichalcogenides via diffusion Monte Carlo. *Physical Review B*, 92:1–5, 2015.

[205] K. McCreary, M. Currie, A.T. Hanbicki, H.-J. Chuang, and B.T. Jonker. Understanding Variations in Circularly Polarized Photoluminescence in Monolayer Transition Metal Dichalocogenides. *ACS Nano*, 11:7988–7994, 2017.

[206] K.M. McCreary, M. Phillips, H.-J. Chuang, D. Wickramaratne, M. Rosenberger, C.S. Hellberg, and B.T. Jonker. Stacking-dependent optical properties in bilayer WSe_2. *Nanoscale*, 2022.

[207] N. Miura. *Physics of semiconductors in high magnetic fields*. Oxford University Press, 2008.

[208] M.R. Molas, C. Faugeras, A.O. Slobodeniuk, K. Nogajewski, M. Bartos, D.M. Basko, and M. Potemski. Brightening of dark excitons in monolayers of semiconducting transition metal dichalcogenides. *2D Materials*, 4:021003, 2017.

[209] F.T.C. Moreira, J.R.L. Guerreiro, L. Brandão, and M.G.F Sales. *Biomimetic Technologies: Principles and Applications*. Woodhead Publishing, 2015.

[210] S.A. Moskalenko. Towards to theory of Mott excitons in alkali halides crystals. *Optical Spectroscopy*, 5:147–155, 1958.

[211] S. Mouri, Y. Miyauchi, M. Toh, W. Zhao, G. Eda, and L. Matsuda. Nonlinear photoluminescence in atomically thin layered WSe_2 arising from diffusion-assisted exciton-exciton annihilation. *Physical Review B*, 90:155449, 2014.

[212] P. Nagler, M.V. Ballottin, A.A. Mitioglu, F. Mooshammer, N. Paradio, C. Strunk, R. Huber, A. Chernikov, P.C.M. Christianen, C. Schüller, and T. Korn. Giant magnetic splitting inducing near-unity valley polarization in van der Waals heterostructures. *Nature Communications*, 8:1551, 2017.

[213] M. Newville, T. Stensitzki, D. B. Allen, and A. Ingargiola. LMFIT: Non-Linear Least-Square Minimization and Curve-Fitting for Python. 2014.

[214] E.F. Nichols and G.F Hull. A Preliminary Communication on the Pressure of Heat and Light Radiation. *Physical Review (Series I)*, 5:307, 1901.

[215] T. Nishio, J. Ahmad, and H. Uwe. Spectroscopic observation of bipolaronic point defects in $Ba_{1x}K_xBiO_3$. *Physical Review Letters*, 95:176403, 2005.

[216] K.S. Novoselov and A.H. Castro Neto. Two-dimensional crystals-based heterostructures: materials with tailored properties. *Physica Scripta*, 2012.

[217] K.S. Novoselov, A.K. Geim, S.V. Morozov, D. Jiang, Y. Zhang, S.V. Dubonos, I.V. Griorieva, and A.A. Firsov. Electric field effect in atomically thin carbon films. *Science*, 306:666–669, 2004.

[218] K.S. Novoselov, D. Jiang, F. Schedin, T.J. Booth, V.V. Khotkevich, S.V. Morozov, and A.K. Geim. Two-dimension atomic crystals. *Proceedings of the National Academy of Sciences*, 102:10451–10453, 2005.

[219] K.S. Novosolev, A.K. Geim, S.V. Morozov, D. Jiang, M.I. Katsnelson, I.V. Grigorieva, S.V. Dubonos, and A.A. Firsov. Two-dimensional gas of massless Dirac fermion in graphene. *Nature*, 438:197–200, 2005.

[220] K.S. Novosolev, Z. Jiang, Y. Zhang, S.V. Morozov, H.L. Stormer, U. Zeitler, J.C. Maan, G.S. Boebinger, and P. Kim. Room temperature quantum Hall effect in graphene. *Science*, 315:1379, 2007.

[221] T.C. O'Haver. *A Pragmatic Introduction to Signal Processing*. July 2021 edition.

[222] M. Padgett, J. Courtial, and L. Allen. Light's orbital angular momentum. *Physics Today*, 57:35–40, 2004.

[223] M.J. Padgett. Structured light concepts and theory, light twist OAM. `https://www.youtube.com/watch?v=V06Cs7Cuk7c`, 2017.

[224] M.J. Padgett and L. Allen. The Poynting vector in Laguerre-Gaussian laser modes. *Optics Communications*, 121:36–40, 1995.

[225] Padgett-M. Orbital angular momentum 25 years on. *Optics Express*, 25:11265, 2017.

[226] I. Paradisanos, S. Germanis, N.T. Pelekanos, C. Fotakis, E. Kymakis, G. Kioseoglou, and E. Stratakis. Room temperature observation of biexcitons in exfoliated WS_2 monolayers. *Applied Physics Letters*, 110:193102, 2017.

[227] F. Paschen and E. Back. Liniengruppen magnetisch vervollst andigt [Line groups magnetically completed]. *Physica*, 1:261–272, 1921.

[228] R.E. Peierls. Quelques proprietes typiques des corpses solides. *Ann. I. H. Poincare*, 5:177–222, 1935.

[229] G-H Peng, P-Y Lo, W-H Li, Y-C Huang, Y-H Chen, C-H Lee, C-K Yang, and S-J Cheng. Distinctive Signatures of Spin- and Momentum- Forbidden Dark Exciton States in Photoluminescence of Strained WSe_2 Monolayers under Thermalization. *Nano Letters*, 19:2299–2312, 2019.

[230] R. Phillips, D. Lovering, G. Denton, and G. Smith. Biexciton creation and recombination in a GaAs quantum well. *Physical Review B*, 45:4308–4311, 1992.

[231] R. Pisoni, A. Kormányos, M. Brooks, Z. Lei, P. Back, H. Eich, M. andand Overweg, Y. Lee, P. Rickhaus, K. Watanabe, T. Taniguchi, A. Imamoğlu, G. Burkard, T. Ihn, and K. Ensslin. Interactions and Magnetotransport through Spin-Valley Coupled Landau Levels in Monolayer MoS_2. *Physical Review Letters*, 121:247701, 2018.

[232] G. Plechinger, P. Nagler, A. Arora, R. Schmidt, A. Chernikov, A. Granados del Águila, P.C.M. Christianen, R. Bratschitsch, C. Schüller, and T. Korn. Trion fine structure and coupled spin-valley dynamics in monolayer tungsten disulfide. *Nature Communications*, 7, 2016.

[233] G. Plechinger, P. Nagler, J. Kraus, N. Paradiso, C. Strunk, C. Schüller, and T. Korn. Identification of excitons, trions and biexcitons in single-layer WS_2. *Physica Status Solidi - Rapid Research Letters*, 9:457–461, 2015.

[234] L. A. Ponomarenko, R. V. Gorbachev, G. L. Yu, D. C. Elias, R. Jalil, A. A. Patel, A. Mishchenko, A. S. Mayorov, C. R. Woods, J. R. Wallbank, M. Mucha-Kruczynski, B. A. Piot, M. Potemski, I. V. Grigorieva, K. S. Novoselov, F. Guinea, V. I. Fal'ko, and A. K. Geim. Cloning of Dirac fermions in graphene superlattices. *Nature*, 497:594–597, 2013.

[235] A. Pospischil, M.M. Furchi, and T. Mueller. Solar-energy conversion and light emission in an atomic monolayer p-n junction. *Nature Nanotechnology*, 9:257–261, 2014.

[236] J.H. Poynting. On the transfer of energy in the electromagnetic field. *Philosophical transactions of the Royal Society of London*, 175:343–361, 1884.

[237] J.H. Poynting. The wave motion of a revolving shaft, and a suggestion as to the angular momentum in a beam of circularly polarized light. *Proc. R. Soc. Lond., A Contain. Pap. Math. Phys. Character*, 82:560–567, 1909.

[238] V.M. Pudalov, M.E. Gershenson, H. Kojima, N. Butch, E.M. Dizhur, G. Brunthaler, A. Prinz, and G. Bauer. Low-Density Spin Susceptibility and Effective Mass of Mobile Electrons in Si Inversion Layers. *Physical Review Letters*, 88:196404, 2002.

[239] G. F. Quinteiro and P. I. Tamborenea. Theory of the optical absorption of light carrying orbital angular momentum by semiconductors. *EPL*, 85(4):47001, feb 2009.

[240] G. F. Quinteiro and P. I. Tamborenea. Twisted-light-induced optical transitions in semiconductors: Free-carrier quantum kinetics. *Phys. Rev. B*, 82:125207, Sep 2010.

[241] B. Radisavljevic, A. Radenovic, J. Brivio, V. Giacometti, and A. Kis. Single-layer MoS_2 transistors. *Nature Nanotechnology*, 6:147–150, 2011.

[242] A.R.P. Rau. The negative ion of hydrogen. *Journal of Astrophysics and Astronomy*, 17:113–145, 1996.

[243] E.C. Regan, D. Wang, C. Jin, M.I.B. Utama, B. Gao, X. Wei, S. Zhao, W. Zhao, Z. Zhang, K. Yumigeta, M. Blei, J.D. Carlström, K. Watanabe, T. Taniguchi, S. Tongay, M. Crommie, A. Zettl, and F. Wang. Mott and generalized Wigner crystal states in WSe2/WS2 moiré superlattices. *Nature*, 579:359–363, 2020.

[244] V.T. Renard, B.A. Piot, X. Waintal, G. Fleury, D. Cooper, Y. Niida, D. Tregurtha, A. Fujiwara, Y. Hirayama, and K. Takashina. Valley polarization assisted spin polarization in two dimensions. *Nature Communications*, 6:7230, 2015.

[245] M. Ritsch-Marte. Orbital angular momentum light in microscopy. *Philosophical Transactions of the Royal Society A*, 375, 2017.

[246] P. Rivera, J.R. Schaibley, A.M. Jones, J.S. Ross, S. Wu, P. Aivazian, G. anf Klement, K. Seyler, G. Clark, N.J. Chimire, J. Yan, D.G. Mandrus, W. Yao, and X. Xu. Observation of long-lived interlayer excitons in monolayer $MoSe_2$-WSe_2 heterostructures. *Nature Communications*, 6, 2015.

[247] C. Robert, T. Amand, F. Cadiz, D. Largarde, E. Courtade, M. Manca, T. Tainiguchi, K. Watanabe, B. Urbaszek, and X. Marie. Fine structure and lifetime of dark excitons in transition metal dichalcogenide monolayers. *Physical Review B*, 96:155423, 2017.

[248] C. Robert, H. Dery, L. Ren, D. Van Tuan, E. Courtade, M. Yang, B. Urbaszek, D. Largarde, K. Watanabe, T. Taniguchi, T. Amand, and X. Marie. Measurement of Conduction and Valence Bands g-factors in a Transition Metal Dichalcogenide Monolayer. *Physical Review Letters*, 126:067403, 2021.

[249] C. Robert, B. Han, P. Kapuscinski, A. Delhomme, C. Faugeras, T. Amand, M.R. Molas, M. Bartos, K. Watanabe, T. Taniguchi, B. Urbasek, M. Potemski, and X. Maire. Measurement of the spin-forbidden dark excitons in MoS_2 and $MoSe_2$ monolayers. *Nature Communications*, 11:4037, 2020.

[250] Z.R. Robinson, S.W. Schmucker, K.M. McCreary, and E.D. Cobas. *Handbook of Crystal Growth: Thin Films and Epitaxy: Second Edition*. 2014.

[251] J.G. Roch, N. Leisgang, G. Froelicher, P. Makk, K. Watanabe, T. Taniguchi, C. Schönenberger, and R.J. Warburton. Quantum-Confined Stark Effect in a MoS_2 Monolayer van der Waals Heterostructure. *Nano Letters*, 18:1070–1074, 2018.

[252] R. Roldán, A. Castellanos-Gomez, E. Cappelluti, and F. Guinea. Strain engineering in semiconducting two-dimensional crystals. *Journal of Physics Condensed Matter*, 27:313201, 2015.

[253] A.P. Rooney, A. Kozikov, A.N. Rudenko, E. Prestat, M.J. Hamer, F. Withers, Y. Cao, K.S. Katsnelson, M.L. Gorbachev, and S.J. Haigh. Observing imperfection in atomic interfaces for van der Waals heterostructures. *Nano Letters*, 17:5222–5228, 2017.

[254] F. Rose, M. Goerbig, and F. Piéchon. Spin-and valley-dependent magneto-optical properties of MoS_2. *Physical Review B*, 88:125438, 2013.

[255] M.R. Rosenberger, H.-J. Chuang, K.M. McCreary, A.T. Hanbicki, S.V. Sivaram, and B.T. Jonker. Nano-"Squeegee" for the Creation of Clean 2D Material Interfaces. *ACS Applied Materials and Interfaces*, 10:10379–10387, 2018.

[256] J.S. Ross, P. Klement, A.M. Jones, N.J. Ghimire, J. Yan, D.G. Mandrus, T. Taniguchi, K. Watanabe, K. Kitamuer, W. Yao, D.H. Cobden, and X. Xu. Electrically tunable excitonic light-emitting diodes based on monolayer WSe_2 p–n junctions. *Nature Nanotechnology*, 9:268–272, 2104.

[257] J.S. Ross, S. Wu, H. Yu, N.J. Ghimire, A.M. Jones, G. Aivazian, J. Yan, D.G. Mandrus, D. Xiao, W. Yao, and X. Xu. Electrical control of neutral and charge excitons a monolayer semiconductor. *Nature Communications*, 4, 2013.

[258] A. Rycerz, J. Tworzydlo, and C.W.J. Beenakker. Valley filter and valley valve in graphene. *Nature Physics*, 3:172–175, 2007.

[259] G. Sallen, L. Bouet, X. Marie, G. Wang, C.R. Zhu, W.P. Han, Y. Lu, P.H. Tan, T. Amand, B.L. Liu, and B. Urbaszek. Optical Emission Polarization in MoS_2 Monolayers through Selective Valley Excitation. *Physical Review B*, 86:81301, 2012.

[260] W. Schäfer and M. Wegener. Springer, Berlin, 1st edition, 2002.

[261] J.R. Schaibley, H. Yu, G. Clark, P. Rivera, J.S. Ross, K.L. Seyler, W. Yao, and X. Xu. Valleytronics in 2D materials. *Nature Reviews Materials*, 1:16055, 2016.

[262] D. Schmidt, B. Berger, M. Kahlet, M. Bayer, C. Schneider, S. Höfling, E.S. Sedov, A.V. Kavokin, and M. Abmann. Tracking dark excitons with exciton polaritons in semiconductor microcavities. *Physical Review Letters*, 122:047403, 2019.

[263] Christian T. Schmiegelow, Jonas Schulz, Henning Kaufmann, Thomas Ruster, Ulrich G. Poschinger, and Ferdinand Schmidt-Kaler. Transfer of optical orbital angular momentum to a bound electron. *Nat. Commun.*, 7(1):12998, 2016.

[264] G.F. Schneider, V.E. Calado, H. Zandbergen, L.M.K. Vandersypen, and C. Dekker. Wedging transfer of nanostructures. *Nano Letters*, 10:1912–1916, 2010.

[265] A. Sebastian, R. Pendurthi, T.H. Choudhury, J.M. Redwing, and S. Das. Benchmarking monolayer MoS_2 and WS_2 field-effect transistors. *Nature Communications*, 12:693, 2021.

[266] J.C. Sell, J.R. Vannucci, D.G. Suárez-Forero, B. Cao, D.W. Session, H-.J. Chuang, K.M. McCreary, M.R. Rosenberger, B.T. Jonker, S. Mittal, and M. Hafezi. Magneto-Optical Measurements of the Negatively Charged $2s$ Exciton in WSe_2, 2022.

[267] J. Serrano, A. Bosak, R. Arenal, M. Krisch, K. Watanabe, T. Taniguchi, H. Kanda, A. Rubio, and L. Wirtz. Vibrational properties of hexagonal boron nitride: inelastic X-ray scattering and *ab initio* calculations. *Physical Review Letters*, 98(9):095503, 2007.

[268] K.L. Seyler, P. Rivera, H. Yu, N.P. Wilson, E.L. Ray, D.G. Mandurs, J. Yan, W. Yao, and X. Xu. Signatures of moiré-trapped valley excitons in $MoSe_2$/WSe_2 heterobilayers. *Nature*, 567:66–70, 2019.

[269] G.H. Shao, S.-C. Yan, W. Luo, G.-W. Lu, and Y.-Q. Lu. Orbital angular momentum (OAM) conversion and multicasting using N-core supermode fiber. *Scientific Reports*, 7:1062, 2017.

[270] A.A. Shashkin, S.V. Kravchenko, V.T. Dolgopolov, and T.M. Klapwijk. Indication of the Ferromagnetic Instability in a Dilute Two-Dimensional Electron System. *Physical Review Letters*, 87:086801, 2001.

[271] A.A. Shashkin, S.V. Kravchenko, V.T. Dolgopolov, and T.M. Klapwijk. Sharp increase of the effective mass near the critical density in a metallic two-dimensional electron system. *Physical Review B*, 66:073303, 2002.

[272] Y. Shen, X. Wang, Z. Xie, C. Min, X. Fu, Q. Liu, M. Gong, and X. Yuan. Optical vortices 30 years on: OAM manipulation from topological charge to multiple singularities. *Light: Science & Applications*, 8, 2019.

[273] S.-Y. Shiau, M. Combescot, and Y.-C. Chang. Trion ground state, excited states,and absorption spectrum using electron-exciton basis. *Physical Review B*, 86:115210, 2012.

[274] Y.P. Shkolnikov, K. Vakili, E.P. De Poortere, and M. Shayegan. Dependence of Spin Susceptibility of a Two-Dimensional Electron System on the Valley Degree of Freedom. *Physical Review Letters*, 92:246804, 2004.

[275] M. Sidler, P. Back, O. Cotlet, A. Srivastava, T. Fink, M. kroner, E. Demler, and A. Imamoğlu. Fermi polaron-polaritons in charge-tunable atomically thin semiconductors. *Nature Physics*, pages 255–261, 2017.

[276] E.J. Sie, A.J. Frenzel, Y.-H. Le, J. Kong, and N. Gedik. Intervalley biexcitons and many-body effects in monolayer MoS_2. *Physical Review B*, 92:125417, 2015.

[277] Kristan Bryan Simbulan, Teng-De Huang, Guan-Hao Peng, Feng Li, Oscar Javier Gomez Sanchez, Jen-Dong Lin, Junjie Qi, Shun-Jen Cheng, Ting-Hua Lu, and Yann-Wen Lan. Selective Photoexcitation of Finite-Momentum Excitons in Monolayer MoS_2 by Twisted Light. *ACS Nano*, 15, 2021.

[278] A. Singh, G. Moody, K. Tran, M.E. Scott, V. Overbeck, G. Berghäuser, J. Schiabley, E.J. Seifert, D. Pelskot, N.M. Gabor, J. Yan, D.G. Mandrus, M. Richter, E. Malic, X. Xu, and X. Li. Trion formation dynamics in monolayer transition metal dichalcogenides. *Physical Review B*, 93:041401, 2016.

[279] A. Singh, K. Tran, M. Kolarczik, J. Seifert, Y. Wang, K. Hao, D. Pleskot, N.M. Gabor, S. Helmrich, N. Owschimikow, U. Woggon, and X. Li. Long-lived valley polarization of intravalley trions in monolayer WSe_2. *Physical Review Letters*, 117:257402, 2016.

[280] J. Singh, D. Birkedal, V.G. Lyssenko, and J.M. Hvam. Binding energy of two-dimensional biexcitons. *Physical Review B*, 53:15909, 1996.

[281] J. Siviniant, D. Scalbert, A.V. Kavokin, D. Coquillat, and J.-P. Lascaray. Chemical equilibrium between excitons, electrons, and negatively charged excitons in semiconductor quantum wells. *Physical Review B*, 59, 1999.

[282] T. Smoleński, O. Cotlet, A. Popert, P. Back, Y. Shimazaki, P. Knüppel, N. Dietler, T. Taniguchi, K. Watanabe, M. Kroner, and A. Imamoğlu. Interaction-Induced Shubnikov–de Haas Oscillations in Optical Conductivity of Monolayer $MoSe_2$. *Physical Review Letters*, 123:097403, 2019.

[283] T. Smolénski, P.E. Dolgriev, C. Kuhlenkamp, A. Popert, Y. Shimazaki, P. Back, X. Lu, M. Kroner, K. Watanabe, T. Taniguchi, I. Esterkis, E. Demler, and A. Imamoğlu. Signatures of Wigner crystal of electrons in a monolayer semiconductor. *Nature*, 595:53–57, 2021.

[284] M.S. Sokolikova, P.C. Sherrell, P. Palcynski, V.L. Bemmer, and C. Mattevi. Direct solution-phase synthesis of 1T' WSe_2 nanosheets. *Nature Communications*, 10:712, 2019.

[285] V.V. Solovyev and I.V. Kukushkin. Measurement of binding energy of negatively charged excitons in GaAs/$Al_{0.3}Ga_{0.7}As$ quantum wells. *Physical Review B*, 79:233306, 2009.

[286] R. Spiegel, G. BAcher, A. Forchel, B. Jobst, D. Hommel, and Landwehr. Polarization-dependent formation of biexcitons in (Zn,Cd)Se/ZnSe quantum wells. *Physical Review B*, 55:9866, 1997.

[287] A. Splendianni, L. Sun, Y. Zhang, T. Li, J. Kim, C.Y. Chim, G. Galli, and F. Wang. Emerging photoluminescence in monolayer MoS_2. *Nano Letters*, 10:1271–1275, 2010.

[288] A. Srivastava, M. Sidler, A.V. Allain, D.S. Lembke, A. Kis, and A. Imamoğlu. Optically active quantum dots in monolayer WSe_2. *Nature Nanotechnology*, 10:491–496, 2015.

[289] A. Srivastava, M. Sidler, A.V. Allain, D.S. Lembke, A. Kis, and A. Imamoğlu. Valley Zeeman effect in elementary optical excitations of monolayer WSe_2. *Nature Physics*, 11:141–147, 2015.

[290] A. Steinhoff, M. Florian, A. Singh, K. Tran, M. Kolarczik, S. Helmrich, A.W. Achtstein, U. Woggon, N. Owschimikow, F. Jahnke, and X. Li. Biexciton fine structure in monolayer transition metal dichalcogenides. *Nature Physics*, 14:1199–1204, 2018.

[291] C.E. Stevens, J. Paul, T. Cox, P.K. Sahoo, H.R. Gutiérrez, V. Turkowski, D. Semenov, S.A. McGill, M.D. Kapetanaski, I.E. Perakis, D.J. Hilton, and D. Karaiskaj. Biexcitons in monolayer transition metal dichalcogenides tuned by magnetic field. *Nature Communications*, 9:3720, 2018.

[292] A.V. Stier, K. McCreary, B.T. Jonker, J. Kono, and S.A. Crooker. Exciton diamagnetic shifts and valley Zeeman effects in monolayer WS_2 and MoS_2 to 65T. *Nature Communications*, 7:10643, 2016.

[293] A.V. Stier, N.P. Wilson, K.A. Velizhanin, J. Kono, X. Xu, and S.A. Crooker. Magneto-Optics of Exciton Rydberg States in a Monolayer Semiconductor. *Physical Review Letters*, 120:057405, 2018.

[294] I. Strazalkowski, S. Joshi, and C.R. Crowell. Dielectric constant and its temperature dependence for GaAs, CdTe, and ZnSe. *Appl. Phys. Lett.*, 28(6):350, 1976.

[295] K. Suthar, Hrushikesh Sable, Rukmani Bai, Soumik Bandyopadhyay, Sukla Pal, and D. Angom. Supersolid phase of the extended bose-hubbard model with an artificial gauge field. *Phys. Rev. A*, 102:013320, Jul 2020.

[296] G.A. Swartzlander, E.L. Ford, R.S. Abdul-Malik, L.M. Close, M.A. Peters, D.M. Palacios, and D.W. Wilson. Astronomical demonstration of an optical vortex coronagraph. *Optics Express*, 16:10200, 2008.

[297] M. Szyniszewski, E. Mostaani, N.D. Drummond, and V.I. Fal'Ko. Binding energies of trions and biexcitons in two-dimensional semicondcutors from diffusion quantum Monte Carlo calculations. *Physical Review B*, 95:1–5, 2017.

[298] F. Tamburini, B. Thidé, G. Molina-Terriza, and G. Anzolin. Twisting of light around rotating black holes. *Nature Physics*, 7:195–197, 2011.

[299] Y. Tang, K.F. Mak, and J. Shan. Long valley lifetime of dark excitons in single-layer WSe_2. *Nature Communications*, 10:4047, 2019.

[300] P. Tonndorf, R. Schmidt, R. Schnieder, J. Kern, M. Buscema, G.A. Stelle, A. Castellanos-Gomez, H.S.J. van der Zant, S.M. de Vasconcellos, and R. Bratschitsch. Single-photon emission from localized excitons in an atomically thin semiconductor. *Optica*, 2:347–352, 2015.

[301] J.P. Torres and L. Torner. *Twisted Photons: Applications of Light with Orbital Angular Momentum*. Wiley, 2011.

[302] Y. Toyozawa. Interband effect of lattice vibrations in the exciton absorption spectra. *Journal of Physics and Chemistry of Solids*, 25:59–71, 1964.

[303] K. Tran, G. Moody, F. Wu, X. Lu, J. Choi, K. Kim, A. Rai, D.A. Sanchez, J. Quan, A. Singh, J. Embley, A. Zepada, M. Campbell, T. Autry, T. Taniguchi, K. Watanabe, N. Lu, S.K. Banerjee, K.L. Silverman, S. Kim, E. Tutuc, L. Yang, A.H. MacDonald, and X. Li. Evidence for moiré excitons in van der Waals heterostructures. *Nature*, 567:71–75, 2019.

[304] Y. Uchiyama, A. Kutana, K. Watanabe, T. Taniguchi, K. Kojima, T. Endo, Y. Miyata, H. Shinohara, and R. Kitaura. Momentum-forbidden dark excitons in hBN-encapsulated monolayer MoS_2. *npj 2D Materials and Applications*, 3, 2019.

[305] D. Vaclavkova, J. Wyzula, K. Nogajewski, M. Bartos, A.O. Slobodeniuk, C. Faugeras, M. Potemski, and M.R. Molas. Singlet and triplet trions in WS_2 monlayer encapsulated in hexagonal boron nitride. *Nanotechnology*, 29, 2018.

[306] M. Van der Donck, M. Zarenia, and F.M. Peeters. Excitons, trions, and biexcitons in transition-metal-dichalcogenides: magnetic-field dependence. *Physical Review B*, 97:195208, 2018.

[307] S.A. Vitale, D. Nezich, J.O. Varghese, P. Kim, N. Gedik, P. Jarillo-Herrero, D. Xiao, and M. Rothschild. Valleytronics: Opportunities, challenges, and paths forward. *Small*, 14:1801483, 2018.

[308] K. von Klitzig, G. Dorda, and M. Pepper. New Method for High-Accuracy Determination of the Fine-Structure Constant Based on Quantized Hall Resistance. *Physical Review Letters*, 45:494, 1980.

[309] K. Wagner, E. Wietek, J.D. Ziegler, M.A. Semina, T. Taniguchi, K. Watanabe, J. Zipfel, M.M. Glazov, and A. Chernikov. Autoionization and Dressing of Excited Excitons by Free Carriers in Monolayer WSe_2. *Physical Review Letters*, 125:267401, 2020.

[310] M.F. Wahab, F. Gritti, T.C. O'Haver, G. Hellinghausen, and D.W. Armstrong. Power Law Approach as a Convenient Protocol for Improving Peak Shapes and Recovering Areas from Partially Resolved Peaks. *Chromatographia*, 82:211–220, 2019.

[311] G. Wang, X. Marie, I. Gerber, T. Amand, D. Lagarde, L. Bouet, M. Vidal, A. Balocchi, and B. Urbaszek. Giant Enhancement of the Optical Second-Harmonic Emission of WSe_2 Monolayers by Laser Excitation at Exciton Resonances. *Physical Review Letters*, 114:097403, 2015.

[312] G. Wang, C. Robert, M.M. Glazov, F. Cadiz, E. Courtage, T. Amand, D. Lagarde, T. Taniguchi, K. Watanabe, B. Urbaszek, and X. Marie. In-plane propagation of light in transition metal dichalcogenide monolayers: optical selection rules. *Physical Review Letters*, 119:047401, 2017.

[313] G. Wang, C. Robert, A. Suslu, B. Chen, S. Yang, S. Alamdari, I.C. Gerber, T. Amand, X. Marie, S. Tongay, and Urbaszek. Spin-orbit engineering in transition metal dichalcogenide alloy monolayers. *Nature Communications*, 6:10110, 2015.

[314] L. Wang, I. Meric, P.Y. Huang, Q. Gao, Y. Gao, H. Tran, T. Taniguchi, K. Watanabe, L.M. Campos, D.A. Muller, J. Guo, P. Kim, J. Hone, K.L. Shepard, and C.R. Dean. One-Dimensional Electrical Contact to a Two-Dimensional Material. *Science*, 342:614–617, 2013.

[315] Q.H. Wang, K. Kalantar-Zadeh, A. Kis, J.N. Coleman, and M.S. Strano. Electronics and optoelectronics of two-dimensional transition metal dichalcogenides. *Nature Nanotechnology*, 7:699–712, 2012.

[316] S. Wang, J. Wang, W. Zhao, F. Giustiniano, L. Chu, I. Werzhbitskiy, J.Z. Yong, and G. Eda. Efficient Carrier-to-Exciton Conversion in Field Emission Tunnel Diodes Based on MIS-Type van der Waals Heterostack. *Nano Letters*, 17:5156–5162, 2017.

[317] T. Wang, Z. Li, Y. Li, Z. Lu, S. Miao, Z. Lian, Y. Meng, M. Blei, T. Taniguchi, K. Watanabe, S. Tongay, D. Smirnov, C. Zhang, and S.-F. Shi. Giant Valley-Polarized Rydberg Excitons in Monolayer WSe_2 Revealed by Magneto-photocurrent Spectroscopy. *Nano Letters*, 20:7635–7641, 2020.

[318] Y. Wang, Y. Chen, Y. Zhang, H. Chen, and S. Yu. Generalized Hermite-Gaussian beams and mode transformations. *Journal of Optics*, 18:05501, 2016.

[319] Z. Wang, K.F. Mak, and J. Shan. Strongly Interaction-Enhanced Valley Magnetic Response in Monolayer WSe_2. *Physical Review Letters*, 120:066402, 2018.

[320] Z. Wang, J. Shan, and K.F. Mak. Valley- and spin-polarized Landau levels in monolayer WSe_2. *Nature Nanotechnology*, 12:144–149, 2017.

[321] Z. Wang, L. Zhao, K.F. Mak, and J. Shan. Probing the spin-polarized electronic band structure in monolayer transition metal dichalcogenides by optical spectroscopy. *Nano letters*, 17(2):740–746, 2017.

[322] J. Wilson and A. Yoffe. The transition metal dichalcogenides discussion and interpretation of the observed optical, electrical, and structural properties. *Advanced Physics*, 18, 1969.

[323] F. Wither, O. Del Pozo-Zamudio, S. Schwarz, S. Dufferwiel, P.M. Walker, T. Godde, A.P. Rooney, A. Gholinia, C.R. Woods, P. Blake, S.J. Haigh, I.L. Watanabe, Aleiner, A.K. Geim, V.I. Fal'ko, A.I. Tartakovskii, and K.S. Novosolev. WSe_2 Light-Emitting Tunneling Transistors with Enhanced Brightness at Room Temperature. *Nano Letter*, 15:8223–8228, 2015.

[324] T. Woźniak, P.E. Faria Jr., G. Seifert, A. Chaves, and J. Kunstmann. Exciton g factors of van der Waals heterostructures from first-principles calculations. *Physical Review B*, 101:235408, 2020.

[325] S. Wu, C. Guang, G. Aivazian, J.S. Ross, D.H. Cobden, and X. Xu. VaporSolid Growth of High Optical Quality MoS_2 Monolayers with Near-Unity Valley Polarization. *ACS Nano*, 7:2768–2772, 2013.

[326] S.F. Wu, J.S. Ross, G.B. Liu, G. Aivazian, A. Jones, Z.Y. Fei, W.G. Zhu, D. Xiao, W. Yao, D. Codben, and X.D. Xu. Electrical tuning of valley magnetic moments through symmetry control in bilayer MoS_2. *Nature Physics*, 9:149–153, 2013.

[327] D. Xiao, G.B. Liu, W. Feng, X. Xu, and W. Yao. Coupled Spin and Valley Physics in Monolayer MoS_2 and Other Group-VI Dichalcogenides. *Physical Review Letters*, 108:196802–1–5, 2012.

[328] D. Xiao, W. Yao, and Q. Niu. Valley-contrasting physics in graphene: magnetic moment and topological transport. *Physical Review Letters*, 99:236809, 2007.

[329] Z.-Q. Xu, Y. Zhang, S. Lin, C. Zheng, Y.L. Zhong, X. Xia, Z. Li, P.J. Sophia, M.S. Fuhrer, Y.-B. Cheng, and Q. Bao. Synthesis and Transfer of Large-Area Monolayer WS_2 Crystals: Moving Towards Recyclable Use of Sapphite Substrates. *ACS Nano*, 9:6178–6187, 2015.

[330] F. Xuan and S.Y. Quek. Valley Zeeman effect and Landau levels in two-dimensional transition metal dichalcogenides. *Physical Review Research*, 2:033256, 2020.

[331] J. Xue, J. Sanchez-Yamagishi, D. Bulmash, P. Lacquod, A. Deshpande, K. Watanabe, T. Taniguchi, P. Jarillo-Herrero, and B.J. LeRoy. Scanning tunneling microscopy and spectroscopy of ultra-flat graphene on hexagonal boron nitride. *Nature Materials*, 10:282–285, 2011.

[332] J. Yan and K. Varga. Excited-state trions in two-dimensional materials. *Physical Review B*, 101:235435, 2020.

[333] Y. Yan, G. Xie, M.P. Lavery, G. Huang, N. Ahmed, C. Bao, Y. Ren, Y. Cao, Z. Zhao, A.F. Molisch, M. Tur, M.J. Padgett, and A.E. Willner. High-capacity millimetre-wave communications with orbital angular momentum multiplexing. *Nature Communications*, 5:4876, 2014.

[334] W. Yang, J. Shang, J. Wang, X. Shen, B. Cao, N. Peimyoo, C. Zou, Y. Chen, Y. Wang, C. Cong, W. Huang, and T. Yu. Electrically Tunable Valley-Light Emitting Diode (vLED) Based on CVD-Grown Monolayer WS_2. *Nano Letters*, 16:1560–1567, 2016.

[335] Alison M. Yao and Miles J. Padgett. Orbital angular momentum: origins, behavior and applications. *Adv. Opt. Photon.*, 3(2):161–204, Jun 2011.

[336] W. Yao, D. Xiao, and Q. Niu. Valley-dependent optoelectronics from inversion symmetry breaking. *Physical Review B*, 77:235406, 2008.

[337] P.-C. Yeh, W. Jin, N. Zaki, D. Zhang, J.T. Liou, J.T. Sadowski, A. Al-Mahboob, J.I. Dadap, I.P. Herman, P. Sutter, and R.M. Osgood. Layer-dependent electronic structure of an atomically heavy two-dimensional dichalcogenide. *Physical Review B*, 91:041407, 2015.

[338] H. Yu, G.-B. Liu, P. Gong, X. Xu, and W. Yao. Dirac cones and Dirac saddle points of bright excitons in monolayer transition metal dichalcogenides. *Nature Communications*, 5:3876, 2014.

[339] Hongyi Yu and Wang Yao. *Valley-Spin Physics in 2D Semiconducting Transition Metal Dichalcogenides*. Cambridge University Press, 2017.

[340] Y. Yu, G.-H. Nam, Q. He, X.-J. Wu, K. Zhang, Z. Yang, J. Chen, Q. Ma, M. Zhao, Z. Liu, F.R. Ran, X. Wang, H. Li, X. Huang, B. Li, Q. Xiong, Q. Zhang, Z. Liu, Y. Du, W. Huang, and H. Zhang. High phase-purity 1T-MoS_2- and 1T-$MoSe_2$-layered crystals. *Nature Chemistry*, 10:638–643, 2018.

[341] L. Yuan and L. Huang. Exciton dynamics and annihilation in WS_2 2D semiconductors. *Nanoscale*, 7:7402, 2015.

[342] Y. Yumeng, X.X. Zhang, T.C. Berkelbach, M.S. Hybertsen, D.R. Reichman, and T.F. Heinz. Observation of biexciton in monolayer WSe_2. *Nature Physics*, 11:477–481, 2015.

[343] P. Zeeman. Over de invloed eener magnetisatie op den aard van het door een stof uitgezonden licht [On the influence of magnetism on the nature of the light emitted by a substance]. *Verslagen van de Gewone Vergaderingen der Wis- en Natuurkundige Afdeeling (Koninklijk Akademie van Wetenschappen te Amsterdam) [Reports of the Ordinary Sessions of the Mathematical and Physical Section (Royal Academy of Sciences in Amsterdam)]*, 5:181–184, 1896.

[344] H. Zeng, J. Dai, W. Yao, D. Xiao, and X. Cui. Valley polarization in MoS_2 monolayers by optical pumping. *Nature Nanotechnology*, 7:490–493, 2012.

[345] D.K. Zhang, D.W. Kidd, and K. Varga. Excited biexcitons in transition metal dichalcogenides. *Nano Letters*, 15:7002–7005, 2015.

[346] F. Zhang, C. Erb, L. Runkle, X. Zhang, and N. Alem. Etchant-free transfer of 2D nanostructures. *Nanotechnology*, 29:025602, 2017.

[347] F. Zhang, Y. Fu, and X.-Y. Yu. *Physical Chemistry of Gas-Liquid Interfaces*. Developments in Physical & Theoretical Chemistry, 2018.

[348] X. Zhang, W.-Y. Shan, and D. Xiao. Optical Selection Rule of Excitons in Gapped Chiral Fermion Systems. *Physical Review Letters*, 120:077401, 2018.

[349] X.-X. Zhang, Y. You, S.Y.F. Zhao, and T.F. Heinz. Experimental evidence for dark excitons in monolayer WSe_2. *Physical Review Letters*, 115:257403, 2015.

[350] X.X. Zhang, T. Cao, Z. Lu, Y-C Li, F. Zhang, Y. Wang, L. Zhiqiang, J.C. Hone, J.A. Robinson, D. Smirnov, S.G. Louie, and T.F. Heinz. Magnetic brightening and control of dark excitons in monolayer wse_2. *Nature Nanotechnology*, 12:883–888, 2017.

[351] Y. Zhang, Y.-W.. Tan, H.L. Stormer, and P Kim. Experimental observation of the quantum Hall effect and Berry's phase in graphene. *Nature*, 438:201–204, 2005.

[352] Y. Zhang, Y. Zhang, Q. Ji, J. Ju, H. Yuan, and J. Shi. Controlled growth of high-quality monolayer WS_2 layers on sapphire and imaging of grain boundaries. *ACS Nano*, 7:8963–8971, 2013.

[353] G.-M. Zhao, M.B. Hunt, H. Keller, and K.A. Müller. Evidence for polaronic supercarriers in the copper oxide superconductors $La_{2x}Sr_xCuO_4$. *Nature*, 385:236–239, 1997.

[354] Y. Zheng, J. Gao, C. Han, and W. Chen. Ohmic Contact Engineering for Two-Dimensional Materials. *Cell Reports Physical Science*, 2:100298, 2021.

[355] Y. Zhou, G. Scuri, D.S. Wild, A.A. High, A. Dibos, L.A. Jauregui, C. Shu, K. De Greve, K. Pistunova, A.Y. Joe, T. Taniguchi, K. Watanabe, P. Kim, M. Lukin, and H. Park. Probing dark excitons in atomically thin semiconductors via near-field coupling to surface plasmon polariton. *Nature Nanotechnology*, 12:856–860, 2017.

[356] Y. Zhou, J. Sung, E. Brutschea, I. Esterlis, Y. Wang, G. Scuri, R.J. Gelly, H. Heo, T. Taniguchi, K. Watanabe, G. Zaránd, M.D. Lukin, P. Kim, E. Demler, and H. Park. Bilayer Wigner crystals in transition metal dichalcogenide heterostructure. *Nature*, 595:48–52, 2021.

[357] C.R. Zhu, G. Wang, B.L. Liu, X. Marie, X.F. Qiao, X. Zhang, X.X. Wu, H. Fan, P.H. Tan, T. Amand, and B Urbaszek. Strain tuning of optical emission energy and polarization in monolayer and bilayer MoS_2. *Physical Review B*, 88:12301, 2013.

[358] H. Zhu, J. Yi, M.-Y. Li, J. Xiao, L. Zhang, C.-W. Yang, R.A. Kaindl, L.-J. Li, Y. Wang, and X. Zhang. Observation of chiral phonons. *Science*, 359:579–582, 2018.

[359] X. Zhu, N.R. Monahan, Z. Gong, H. Zhu, K.W. Williams, and C.A. Nelson. Charge Transfer Excitons at van der Waals Interfaces. *Journal of the American Chemical Society*, 137:8313–8320, 2015.

[360] C. Zibrov, A.A. Kometter, H. Zhou, E.M. Spanton, T. Taniguchi, K. Watanabe, M.P. Zaletel, and A.F. Young. Tunable interacting composite fermion phases in half-filled bilayer-graphene Landau level. *Nature*, 549:360–364, 2017.

[361] J. Zipfel, K. Wagner, M.A. Semina, J.D. Ziegler, T. Taniguchi, K. Watanabe, M.M. Glazov, and A. Chernikov. Electron recoil effect in electrically tunable $MoSe_2$ monolayers. 2021.

[362] P.J. Zomer, S.P. Dash, N. Tombros, and B.J. van Wees. A transfer technique for high mobility graphene devices on commercially available hexagonal boron nitride. *Applied Physics Letters*, 99:232104, 2011.

[363] P.J. Zomer, M.H.D. Guimarães, J.C. Brant, N. Tombros, and B.J. van Wees. Fast pick up technique for high quality heterostructures of bilayer graphene and hexagonal boron nitride. *Applied Physics Letters*, 105:013101, 2014.